# Development and characterization of sensing layers based on molecularly imprinted conducting polymers for the electrochemical and gravimetrical detection of small organic molecules

Youssef Lattach

## To cite this version:

Youssef Lattach. Development and characterization of sensing layers based on molecularly imprinted conducting polymers for the electrochemical and gravimetrical detection of small organic molecules. Other. Conservatoire national des arts et metiers - CNAM, 2011. English. NNT : 2011CNAM0783 . tel-00699628

## HAL Id: tel-00699628
## https://theses.hal.science/tel-00699628

Submitted on 21 May 2012

le cnam | *CONSERVATOIRE NATIONAL DES ARTS ET METIERS*

***ÉCOLE DOCTORALE ED 415***

**Laboratoire de Conception de Capteurs Chimiques et Biologiques, LC3B**

# THÈSE

présentée par :

**Youssef LATTACH**

soutenue le : **18 octobre 2011**

pour obtenir le grade de :

**Docteur du Conservatoire National des Arts et Métiers**

Discipline/ Spécialité : Sciences et Techniques Analytiques

# Development and characterization of sensing layers based on molecularly imprinted conducting polymers for the electrochemical and gravimetrical detection of small organic molecules

# Développement et caractérisation de couches sensibles à base de polymères conducteurs à mémoire moléculaire pour la détection électrochimique et gravimétrique de petites molécules organiques

**THÈSE dirigée par :**

| | |
|---|---|
| **Mr REMITA Samy** | Professeur, Cnam |

**RAPPORTEURS :**

| | |
|---|---|
| **Mme JAFFREZIC Nicole** | Directeur de Recherche, CNRS, Université Claude Bernard |
| **Mr RANDRIAMAHAZAKA Hyacinthe** | Professeur, Université Paris Diderot |

**JURY :**

| | |
|---|---|
| **Mme FERROUD Clotilde** | Professeur, Cnam |
| **Mme REINAUD Olivia** | Professeur, Université Paris-Descartes |
| **Mr ARCHIREL Pierre** | Chargé de Recherche, CNRS, Université Paris-Sud |
| **Mr GOUBARD Fabrice** | Professeur, Université de Cergy-Pontoise |
| **Mr ZERROUKI Chouki** | Maître de Conférences, Cnam |

le cnam | CONSERVATOIRE NATIONAL DES ARTS ET METIERS

***ÉCOLE DOCTORALE ED 415***

**Laboratoire de Conception de Capteurs Chimiques et Biologiques, LC3B**

# THÈSE

présentée par :

**Youssef LATTACH**

soutenue le : **18 octobre 2011**

pour obtenir le grade de :

**Docteur du Conservatoire National des Arts et Métiers**

Discipline/ Spécialité : Sciences et Techniques Analytiques

# Development and characterization of sensing layers based on molecularly imprinted conducting polymers for the electrochemical and gravimetrical detection of small organic molecules

# Développement et caractérisation de couches sensibles à base de polymères conducteurs à mémoire moléculaire pour la détection électrochimique et gravimétrique de petites molécules organiques

| | |
|---|---|
| **THÈSE dirigée par :** | |
| **Mr REMITA Samy** | Professeur, Cnam |
| **RAPPORTEURS :** | |
| **Mme JAFFREZIC Nicole** | Directeur de Recherche, CNRS, Université Claude Bernard |
| **Mr RANDRIAMAHAZAKA Hyacinthe** | Professeur, Université Paris Diderot |

---

| | |
|---|---|
| **JURY :** | |
| **Mme FERROUD Clotilde** | Professeur, Cnam |
| **Mme REINAUD Olivia** | Professeur, Université Paris-Descartes |
| **Mr ARCHIREL Pierre** | Chargé de Recherche, CNRS, Université Paris-Sud |
| **Mr GOUBARD Fabrice** | Professeur, Université de Cergy-Pontoise |
| **Mr ZERROUKI Chouki** | Maître de Conférences, Cnam |

## Remerciements

Je remercie très sincèrement madame Christine Pernelle de m'avoir accueilli dans son laboratoire, le LC3B du cnam, et de m'avoir donné l'occasion d'y effectuer cette thèse.

Ces travaux n'auraient jamais été réalisés sans monsieur Samy Remita, mon directeur de thèse. Je souhaite donc te remercier pour ce travail passionnant. Je te suis très reconnaissant pour ton aide et toute l'attention quotidienne que tu as portée à mes travaux. Tes idées et ton ouverture d'esprit m'ont beaucoup apporté.

Je remercie particulièrement monsieur Francis Garnier pour m'avoir fait profiter de sa riche expérience scientifique. Sa constante disponibilité à mon égard et ses conseils précieux lui valent ma profonde gratitude.

Je tiens à remercier très sincèrement madame Najla Fourati (× 20 mille merci !) pour sa disponibilité, son enthousiasme et de m'avoir permis de « propager des ondes acoustiques » et d'améliorer mes connaissances dans le domaine des capteurs gravimétriques. Ton soutien efficace m'aura bien aidé à avancer dans le monde des capteurs.

J'adresse tous mes remerciements à monsieur Chouki Zerrouki pour son soutien et sa contribution indispensables au développement du capteur gravimétrique, mais aussi d'avoir accepté d'être dans le jury de ma thèse

Un grand merci à monsieur Jean-Marie Fougnion, « le père du petit capteur SAW » pour son soutien au niveau technique et informatique.

Que monsieur Pierre Archirel, du LCP d'Orsay, trouve ici l'expression de ma gratitude pour m'avoir fait découvrir le monde du calcul théorique lors de notre collaboration, pour sa sympathie et pour avoir accepté d'être dans mon jury de thèse.

Je tiens également à exprimer ma gratitude à madame Nicole Jaffrezic-Renault, et à monsieur Hyacinthe Randriamahazaka de me faire l'honneur d'être rapporteurs de ce manuscrit.

Merci également à monsieur Fabrice Goubard d’être parmi les examinateurs de ce travail, et pour m’avoir donné l’accès au profilomètre mécanique du Laboratoire de Physico-Chimie des Polymères et des Interfaces de Cergy-Pontoise.

Un grand merci à madame Clotilde Ferroud et à madame Olivia Reinaud d'accepter de faire partie de mon jury.

Merci à monsieur Michel Goldmann et à madame Emmanuelle Lacaze, de l'Institut des Nanosciences de Paris pour leur aide lors des études AFM.

Je tiens à remercier également monsieur Denis Limagne, de l'Institut des Nanosciences de Paris pour sa présence et son aide technique précieuse.

J’associe à mes remerciements madame Fanny Hauquier et madame Hélène Cheap pour m’avoir initié à l’électrochimie. Je les remercie pour leur sympathie et leur intérêt pour mon travail.

Je remercie l’ensemble du personnel du LC3B et du Service de Physique, en particulier « les géniaux » Patrick Boutin, Laurence Dallery, Claudine David, François Giraud, Muriel Mestre, Jean-Paul Monin, Petronille Agbo, Christelle Chapet, Patrick Lepeut, Françoise Lepage, Félix Nal, et Alain Changarnier. Un grand merci à vous tous.

Je tiens également à remercier tous mes amis passés et présents, pour leur bonne humeur et pour leur amitié, particulièrement : Michel, Georges et Omar.

Merci pour tout à ma famille : Souheil, Randa, Fadi, Naïla, Ram et Nadia-Rose. Sans votre soutien je ne serais jamais arrivé jusqu’à ce stade.

# Résumé

Dans le domaine des capteurs chimiques et biologiques, les besoins toujours croissants en termes de sensibilité, de rapidité et de sélectivité de l'analyse nécessitent le développement de couches sensibles transductrices de plus en plus performantes. Dans ce contexte et dans l'optique de pouvoir détecter de petites molécules non électroactives, telles que l'atrazine (ATZ), nous avons conçu, caractérisé et développé des couches sensibles constituées de polymères conducteurs fonctionnalisés à empreintes moléculaires (MICP) et les avons intégrées au sein de capteurs électrochimiques et gravimétriques. A partir de solutions d'acétonitrile contenant de l'ATZ, molécule empreinte en interaction avec des monomères fonctionnels dérivés du thiophène (FM = TMA, TAA, EDOT, TMeOH ou Th), différents polythiophènes FM-MICP de structures et de fonctionnalités différentes ont été électrosynthétisés sur substrats d'or et utilisés pour la détection de l'ATZ. Nous avons montré que les propriétés de reconnaissance des FM-MICP résultaient de la présence en leur sein d'empreintes moléculaires, fonctionnalisées par les résidus FM, qui conservaient la mémoire géométrique et fonctionnelle des molécules cibles. Néanmoins, une adsorption non-spécifique se produit systématiquement à la surface des couches sensibles et affecte par conséquent la sélectivité de la reconnaissance. Les techniques de caractérisation de surface employées nous ont permis de mettre en évidence l'influence de l'épaisseur et des propriétés structurales des couches sensibles sur l'efficacité de la détection. En outre, nous avons montré que du fait de la porosité de la couche polymère, le processus de reconnaissance se produisait en volume. Par ailleurs, des mesures électrochimiques corrélées à des calculs semi-empiriques ont permis de démontrer l'influence de la nature de FM d'abord sur la force de l'interaction ATZ-FM au sein de la solution de pré-polymérisation, ensuite sur le nombre d'empreintes moléculaires et enfin sur la sensibilité des FM-MICP vis-à-vis de l'ATZ. La couche TAA-MICP, qui présente un faible seuil de détection ($10^{-9}$ mol $L^{-1}$) ainsi qu'une large gamme dynamique ($10^{-8}$ à $10^{-4}$ mol $L^{-1}$), est la plus performante des couches sensibles puisqu'elle offre le meilleur compromis entre une détection spécifique de l'ATZ relativement efficace et une adsorption non-spécifique relativement faible. Enfin, le TAA-MICP a été utilisé comme couche sensible au sein d'un capteur électrochimique original à ondes acoustiques de surface (ESAW) dans l'optique de réaliser des mesures gravimétriques et électrochimiques couplées et simultanées.

**Mots clés :** Polymères conducteurs, polymères a empreinte moléculaire, atrazine, transduction gravimétrique, transduction électrochimique.

# Abstract

In the field of chemical and biological sensors, the increased need for better sensitivity, faster response and higher selectivity during an analysis process, requires the development of more and more efficient transducing sensing layers. In this context, and with the aim to detect small non-electroactive molecules, such as atrazine (ATZ), we designed, characterized and developed sensing layers constituted by functionalized Molecularly Imprinted Conducting Polymers (MICP) and we integrated them into electrochemical and gravimetrical sensors. Starting from acetonitrile pre-polymerization media containing ATZ as template molecules in the presence of thiophene-based functional monomers (FM, namely TMA, TAA, EDOT, TMeOH or Th), differently functionalized and structurally different polythiophene-based FM-MICP films were electrosynthesized onto gold substrates and used for ATZ detection. The sensing properties of FM-MICP layers were shown to result from the presence in their backbones of pre-shaped FM-functionalized imprinted cavities which keep the memory of the targets. Nevertheless, non-specific adsorption onto the surface of the sensing layers takes place systematically, which affects the selectivity of the recognition process. Thanks to surface characterization techniques, we highlighted the influence of the thickness and of the structural properties of the layers on the efficiency of the recognition process. Besides, this latter was shown to operate in the bulk of the polymer matrixes thanks to layers porosity. On another hand, electrochemical measurements correlated with semi-empirical calculations demonstrated the influence of the nature of FM on the strength of the ATZ-FM interaction in the pre-polymerization medium, and then on the number of ATZ molecular imprints and on the sensitivity towards ATZ of the FM-MICP layers. We showed that TAA-MICP, which presents a low limit of detection ($10^{-9}$ mol $L^{-1}$) and a large dynamic range ($10^{-8}$ to $10^{-4}$ mol $L^{-1}$), is the best sensing layer since it offers the best compromise between high level of specific detection of ATZ and low level of non-specific adsorption. Finally, TAA-MICP was used as sensitive layer in an original Electrochemical Surface Acoustic Wave sensor (ESAW) which enabled simultaneous coupled gravimetric and electrochemical measurements.

**Keywords :** Conducting polymers, molecularly imprinted polymers, atrazine, gravimetric transduction, electrochemical transduction.

# Index

**Chapter 1**

Chapter 2

Chapter 3

Chapter 4

## Chapter 5

## List of Abbreviations

| | |
|---|---|
| ACN | Acetonitrile |
| ADP | Adenosine diphosphate |
| AFM | Atomic Force Microscopy |
| AMP | Adenosine mono phosphate |
| AM1 | Semi-Empirical Austin Model |
| 3-APBA | 3-Aminophenylboronicacid |
| APM | Acoustic Plate Mode |
| ATP | Adenosine Triphosphate |
| ATR | Attenuated Total Reflectance |
| ATZ | Atrazine |
| BAW | Bulk Acoustic Wave |
| BSSE | Basis Set Superposition Error |
| CE | Capillary Eletrophoresis |
| CME | Chemically Modified Electrode |
| CP | Conducting Polymers |
| CV | Cyclic Voltammetry |
| CWE | Coated Wire Electrode |
| DCM | Dichloromethane |
| DEAEMA | Diethylaminoethyl Methacrylate |
| DFT | Density Functional Theory |
| DMF | Dimethyl Formamide |
| DPV | Differential Pulse Voltammetry |
| DRN | Diuron |
| DVB | Divinylbenzene |
| EDOT | Ethlyenedioxythiophene |
| EDTA | Ethylenediaminetetraacetic acid |
| EIS | Electrochemical Impedence Spectroscopy |
| EGDMA | Ethylene Glycol Dimethacrylate |
| ENFET | Enzyme FET |
| EQCM | Electrochemical Quartz Crystal Microbalance |
| ESAW | Electrochemical Surface Acoustic Wave |
| FET | Field Effect Transistor |
| FluM | Fluorescence Microscopy |
| FM | Functional Monomer |
| FM-MICP | Poly(EDOT-co-FM/ATZ) |
| FM-NICP | Poly(EDOT-co-FM) |
| FOCS | Fiber Optic Chemical Sensor |
| FPW | Flexural Plate Wave |
| FT-IR | Fourier Transform Infrared Spectrometry |
| HLB | Hydrophilic-Lipophilic-Balance |
| HOPG | Highly Ordered Pyrolytic Graphite |

| | |
|---|---|
| HPLC | High-Performance Liquid Chromatography |
| ISE | Ion-Selective Electrode |
| ISFET | Ion-Selective FET |
| ITO | Indium Tin Oxide |
| MAA | Methaacrylic Acid |
| ME | Micro Electrode |
| MICP | Molecularly Imprinted Conducting Polymer |
| MIP | Molecularly Imprinted Polymer |
| MISPE | Molecularly Imprinted SPE |
| MOSFET | Metal Oxide FET |
| MWCNT | Multi Wall Carbon Nanotubes |
| NA | Numerical Aperture |
| NICP | Non-imprinted Conducting Polymer |
| NIP | Non-imprinted Conducting Polymer |
| NMR | Nuclear Magnetic Resonance |
| N-VP | N-Vinylpyrrolidon |
| PBS | Phosphate Buffer Solution |
| PCM | Polarized Continuum Medium |
| *o*-PD | poly(*o*-phenylenediamine) |
| PPV | Poly(paravinylene) |
| PGE | Pencil Graphite Electrode |
| PLE | Pressurized Liquid Extraction |
| PEDOT | Poly(3,4-ethylenedioxythiophene) |
| PTAA | Poly(3-thiopheneacetic acid) |
| PTh | Poly(thiophene) |
| PTMA | Poly(3-thiophenemalonic acid) |
| PTMeOH | Poly(3-thiophenemethanol) |
| QCM | Quartz Crystal Microbalance |
| SAM | Self Assembled Monolayer |
| SAW | Surface Acoustic Wave |
| SEM | Scanning Electron Microscopy |
| SH | Shear Horizontal |
| SPE | Solid Phase Extraction |
| SPMTE | Solid Phase Membrane Tip Extraction |
| SPME | Solid Phase Micro Extraction |
| SPR | Surface Plasmon Resonance |
| STM | Scanning Tunneling Microscope |
| SWV | Square Wave Voltammetry |
| TBZ | Tetrabutylazine |
| 3,3-biTh | 3,3-bithiophene |
| TAA | 3-Thiopheneacetic acid |
| TBATFMS | Tetrabutylammonium trifluoromethanesulfonate |
| Th | Thiophene |
| TIR | Total Internal Reflection |

| | |
|---|---|
| TMA | 3-Thiophenemalonic acid |
| TMeOH | 3-Thiophenemethanol |
| TRIM | Trimethylolpropane Trimethacrylate |
| TSM | Thickness Shear Mode |
| UME | Ultra Micro Electrode |
| VOC | Volatile Organic Compounds |

# List of Tables

## Chapter 1

## Chapter 3

## Chapter 4

# Chapter 5

**Table 5.1**. Some experimental parameters calculated from ESAW response in the case of MICP film during voltammetric cycling measurements.

# List of Figures

## Chapter 1

## Chapter 2

**Figure 2.1.** Structure of thiophene Th, and substituted thiophene : EDOT, TMeOH, TAA and TMA, used as functional monomers. Pesticides used as templates and target molecules: ATZ, TBZ, and DRN.

**Figure 2.2.** Voltammogram of calibration of Ag/$AgNO_3$ reference electrode at 100 mV $s^{-1}$ in 0.1 M $LiClO_4$/ACN on Au electrode (3.14 $mm^2$).

**Figure 2.3.** (A) Schematic representation of conventional three electrode cell: working electrode (WE) counter electrode (CE) and reference electrode (RE); (B) Picture and (C) Scheme of the electrochemical cell used for electropolymerization over the HOPG surfaces (5mm × 5mm × 2mm). (1) Teflon cover; (2) Teflon container of the electrolyte and electrodes; (3) Teflon column to maintain the surface and the electrical connection; (4) Teflon gaskets used to ensure the isolation of the electrical connection and to control the active surface; (5) Stainless steel surface to hold the working surface and ensure the electrical connection; (6) Current entry. (D) Picture representing a deposited PEDOT film (dark zone in the center of the surface) over HOPG surface.

**Figure 2.**4. Electrosynthesis and use for ATZ detection of (A) FM-MICP. (B) FM-NICP. The FM functional monomers are TMA, TAA, TMeOH, EDOT or Th.

**Figure 2.5.** Cyclic voltammograms, (A) Potential linear sweep in function of time; (B) Reversible system composed of dissolved electroactive species; (C) Irreversible system; (D) Reversible system composed of adsorbed electroactive species over the electrode surface. Adapted from ref. Error! Bookmark not defined..

**Figure 2.6.** Waveform and measurement scheme for square wave voltammetry. In each cycle, a forward current sample is taken at the time indicated by the solid dot, and a reverse current sample is taken at the time marked by the white dot.

**Figure 2.7.** Transversal horizontal waves propagated on $LiTaO_3$ piezoelectric substrate: leaky surface acoustic wave and surface skimming bulk waves.

**Figure 2.8.** Representation of a delay line with the dimensional parameters; λ: periodicity of IDTs; L: length of the central zone; LCC: distance center to center.

**Figure 2.9.** (A) Metalized delay line deposited over lithium tantalate wafer; (B) single delay line cut and prepared to be used.

**Figure 2.10.** Schematic representation of impulsion measurement configuration.

**Figure 2.11.** (A) Common terms for high-frequency drive characterization, (B) Frequency response $S_{21}$ of a SAW functional at 104 MHz.

**Figure 2.12.** SAW dispositive placed over PID in the faraday cage.

**Figure 2.13.** A full potentiostatic system based on a BNC-2120 panel, SAW sensing surface acts as working electrode (WE), Pt electrode as counter electrode (CE) and an Ag/$AgNO_3$ as reference electrode (RE).

## Chapter 3

**Figure 3.1.** Schematic representation of MICP electrosynthesis by copolymerization of EDOT and TAA after the establishment of hydrogen bonds between TAA and ATZ in a pre-polymerization complex.

**Figure 3.2.** Cyclic voltammogram of 1 mM of EDOT in 0.1 M $LiClO_4$ aqueous solution at 25 mV $s^{-1}$ using HOPG working electrode.

**Figure 3.3. (A)** The first 2 seconds of choronoamperograms obtained at different potentials of PEDOT polymerization: +0.7, +0.8, +0.9, and +1V for $1 \times 10^{-3}$ mol $L^{-1}$ in 0.1 mol $L^{-1}$ of $LiClO_4$ in aqueous solutions; **(B)** Linear relationship between the coulombic charge of electropolymerization ($Q_s$) and potential values of electrodeposition ($E_p$) implied during 10 seconds.

**Figure 3.4.** AFM images and topography in tapping mode of PEDOT films electropolymerized from aqueous solution of $1 \times 10^{-3}$ mol $L^{-1}$ EDOT onto HOPG substrates over a period of ca. 10 seconds at different potentials; **(A)** +0.7V; **(B)** +0.8V; **(C)** +0.9V and **(D)** +1V

**Figure 3.5.** Variation of PEDOT film thickness deposited onto HOPG as a function of coulombic charge ($Q_s$) of electropolymerization. PEDOT films were electrosynthesized on HOPG substrates from 1 mmol $L^{-1}$ EDOT in 0.1 mol $L^{-1}$ $LiClO_4/H_2O$ . The thicknesses were measured by AFM.

**Figure 3.6.** Absorbance values at $\lambda_{max}$ = 280nm as a function of TAA concentration in $H_2O$ at natural pH. Pathlength was 1cm.

**Figure 3.7.** Cyclic voltammograms (six cycles) of 30 mmol $L^{-1}$ of TAA in 0.1 mol $L^{-1}$ $LiClO_4/H_2O$ over HOPG at a surface active area of 7 mm² and a scan rate of 25 mV $s^{-1}$.

**Figure 3.8.** Cyclic voltammograms of **(A)** characterization of EDOT at a concentration of 7.5mmol $L^{-1}$ in 0.1 mol $L^{-1}$ $LiClO_4$/ACN and formation of PEDOT film over Au at a surface active area of 3.14 mm² and a scan rate of 100mV $s^{-1}$; **(B)** PEDOT film over Au at different scan rates from 25 to 200 mV $s^{-1}$ in 0.1 M $LiClO_4$/ACN with linear dependency of the oxidation current peak ($I_P$) of PEDOT as a function of the scan rate.

**Figure 3.9.** Cyclic voltammograms of **(A)** characterization of TAA at a concentration of 30mmol $L^{-1}$ in 0.1 mol $L^{-1}$ $LiClO_4$/ACN and formation of PTAA film over Au at a surface active area of 3.14 mm² and a scan rate of 100mV $s^{-1}$; **(B)** PTAA film over Au at a scan rate of 25 mV $s^{-1}$ in 0.1 mol $L^{-1}$ $LiClO_4$/ACN.

**Figure 3.10. (A)** Cyclic voltammograms of atrazine in ACN solutions containing $LiClO_4$ (0.1 mol $L^{-1}$) and increasing concentrations of ATZ: **(a)** 0, **(b)** 5 $10^{-3}$, **(c)** $15 \times 10^{-3}$ mol $L^{-1}$. The scan rate was 25mV $s^{-1}$ on a bare gold electrode. **(B)** Cyclic voltammogram of atrazine in ACN solution containing $LiClO_4$ (0.1 mol $L^{-1}$) and a concentrations of ATZ of $15 \times 10^{-3}$ mol $L^{-1}$. The scan rate was 25mV $s^{-1}$ on a bare gold electrode.

point of the curves, represented with its error bar, corresponds to the mean value obtained from three experiments.

**Figure 3.22.** **(A)** Cyclic voltammograms of MICP in 0.1 mol $L^{-1}$ $LiClO_4$/ACN **(a)** after extraction of ATZ molecules. **(b)** after injection of $10^{-4}$ mol $L^{-1}$ in additional ATZ. The thickness of the film was 1140 nm, and the scan rate was 25 mV $s^{-1}$; **(B)** Variation of the "relative charge", $Q_r$, of MICP (thickness of 1140 nm) as a function of additional ATZ concentration. Each point of the curves, represented with its error bar, corresponds to the mean value obtained from three experiments.

**Figure 3.23.** Square wave voltammograms of MICP (thickness of 1140 nm) in 0.1 mol $L^{-1}$ $LiClO_4$/ACN, pulse amplitude = 100mV, potential step height = 10mV, and square wave frequency = 2.5 Hz. **(A)** evolution of square wave voltammograms upon detection. **(B)** dependence of current peak, $I_{pic}$, of square wave voltammograms of MICP on the different concentrations of the detected ATZ target molecules ranging from $10^{-9}$ to $10^{-4}$ mol $L^{-1}$. Each point of the curves, represented with its error bar, corresponds to the mean value obtained from three experiments.

**Figure 3.24**. Relative charges corresponding to the detection by MICP (thickness of 1140 nm) of Atrazine (ATZ), Terbutylazine (TBZ), and Diuron (DRN), pesticides at a concentration of $10^{-4}$ mol $L^{-1}$ in 0.1 mol $L^{-1}$ $LiClO_4$/ACN solutions. Relative charges were deduced from the cyclic voltammograms at 25mV $s^{-1}$. Each value of the histogram, represented with its error bar, corresponds to the mean value obtained from three experiments.

## Chapter 4

**Figure 4.1.** (A) Electrosynthesis and use for ATZ detection of FM-MICP. (B) Electrosynthesis of FM-NICP. The FM functional monomers are TMA, TAA, TMeOH, EDOT or Th.

**Figure 4.2.** (A) Cyclic voltammograms of TMA-MICP and TMA-NICP films (FM = TMA). (B) Cyclic voltammograms of Th-MICP and Th-NICP films (FM = Th). All cyclic voltammograms were recorded in 0.1M $LiClO_4$/ACN solutions at a scan rate of 25mV $s^{-1}$. (C) Relative charges, $Q_{FM}$, measured for the different FM functional monomers (FM = TMA, TAA, TMeOH, EDOT or Th). Each charge value, represented with its error bar, corresponds to the mean value obtained from three experiments.

**Figure 4.3** (A) Cyclic voltammograms of washed TMA-MICP (a) before and (b) after addition of $10^{-4}$ mol $L^{-1}$ in ATZ. (B) Cyclic voltammograms of washed Th-MICP (a) before and (b) after addition of $10^{-4}$ mol $L^{-1}$ in ATZ. All cyclic voltammograms were recorded in 0.1M $LiClO_4$/ACN solutions at a scan rate of 25mV $s^{-1}$. (C) Relative charges, $Q_{d\ FM\text{-}MICP}$, corresponding to ATZ detection by the different FM-MICP films (FM = TMA, TAA, TMeOH, EDOT or Th). Each charge value, represented with its error bar, corresponds to the mean value obtained from three experiments.

**Figure 4.4.** (A) Relative charges, $Q_{d\ FM\text{-}NICP}$, corresponding to the adsorption of ATZ onto the different FM-NICP films (FM = TAA, TMA, TMeOH, EDOT or Th). Each charge value, represented with its error bar, corresponds to the mean value obtained from three experiments. (B) Variation with FM of $Q_{d\ FM\text{-}MICP}$ - $Q_{d\ FM\text{-}NICP}$, which corresponds to the specific interaction of FM-MICP films with ATZ target molecules.

## Chapter 5

# Introduction

With the drastic growth in industrial development and in public health criterions, the modern tendency in health, chemistry, agro-alimentary field, and environmental science is to detect and to quantify various analytes and measurands in complex matrixes and sophisticated conditions at sub-micron concentrations. Thus, improved performances in analysis techniques for rapid and reliable monitoring systems are needed. In order to answer severe norms in worldwide legislation, rapid, sensitive and specific tests, need to be developed with the aim to achieve accurate results.

In this regard, the development of original analytical technologies is of prime importance in modern scientific research, specially, in chemical and biological sensors, where a considerable effort has to be paid to improve the performances of the sensors at the levels of both sensing layers and transduction technologies.

In this context, development of sensing layers based on molecularly imprinted polymers (MIP) knows a considerable interest in the detection of molecules of different types. These sensing layers mimic the natural bio-receptors, with interesting properties. In addition to their stability against a wide range of environments, the advantage of molecularly imprinted polymers based sensors is that the binding affinity of MIP is comparable to biological recognition elements. Besides, these materials are easily synthesized in a tailor–made manner for a given template (analyte) and they can be developed against various targets such as herbicides, pharmaceuticals, proteins and vitamins. The needed features in the MIP based sensing layers, particularly, in terms of minimization of the sensor, easiness of use and low cost of realization, are compatible with the use of electrochemical, piezoelectrical and optical transduction methods.

The introduction of a transduction functionality in the MIP based sensors can be achieved by using conducting polymers. Molecularly imprinted conducting polymers (MICP) can adhere to different kinds of substrates (electrodes) of any shape and size. In addition, these materials are easily synthesized by electrochemical techniques and offer the possibility to combine the interesting recognition properties of MIP layers with the electronic and optical transduction properties of conducting polymers.

The potential future applications of these materials in sensors are clearly very large. It is the view of LC3B laboratory in CNAM that the combination of conducting polymers to molecular imprinting technology can be one of the most promising solutions towards the development of miniaturized devices that enable rapid and direct analysis of the specific binding of small non-electroactive molecules.

In this work, an effort has been made to improve the sensing performance of a sensor based on MICP, dedicated for the detection of small organic molecules, through the combination of different approaches. The preparation of MICP sensing layers as well as the detection of atrazine pesticide molecules, by differently functionalized polythiophenes, as MICP based sensing films, was optimized and studied as a physico-chemical model for the involved recognition phenomena. Then, electrochemical, gravimetrical and original coupled electrochemical/gravimetrical, ESAW, transductions of the atrazine sensing process was developed in order to improve the performance of our sensor.

This effort has been discussed throughout this thesis. First chapter overviews the state of art of chemical sensors and sensing layers dedicated to the detection of small organic molecules and proposes an introduction to the role of MICP in the development of chemical sensors.

Second chapter demonstrates the different experimental procedures used for the preparation of the sensing layers, with a brief introduction to the theoretical method used in this work. In addition, the electrochemical, microscopic and spectroscopic characterization techniques used in this study are described. Also, the different electronic assemblies developed and used for the electrochemical, gravimetrical and simultaneous electrochemical/gravimetric transductions are presented.

Third chapter presents the optimization of both MICP layers electrosynthesis and atrazine targets detection. Also, this section discusses the influence of structural, chemical and electrochemical properties of the MICP based sensing layers on the recognition process and then on the performance of the sensor.

Fourth chapter outlines the influence of the chemical functionalities of the MICP films on their sensing properties through electrochemical measurements correlated with semi-empirical calculations of the involved interaction free energies.

Fifth chapter focuses on gravimetrical and simultaneous electrochemical/gravimetrical transductions of atrazine recognition process by the developed MICP based sensing layers. This section also proposes kinetic investigations on the growth mechanism of the film and on the recognition process.

Finally, the properties of the developed MICP as sensing layers in electrochemical and gravimetrical sensors are summarized and the perspectives based on this work are outlined and oriented towards overriding the actual limitations of MICP based sensors.

# Chapter 1

## State of art on chemical sensors and sensitive layers

## An introduction to molecularly imprinted conducting polymers, MICP

A study on the state of art of sensors with a special attention to the chemical sensors will be paid in this section. A brief demonstration of different types of sensors classified by their transduction methods will be followed by the role of conducting polymers in the chemical sensors field. Then a description of the role of molecularly imprinted conducting polymers in the sensing applications will be presented. The detection of “Atrazine” as an example of the application of molecularly imprinted polymers in the detection of small organic molecules will be studied in order to introduce our contribution in the detection of this kind of molecules by molecularly imprinted conducting polymers **MICP**.

## 1.1 Introduction

The evolution of the modern industry requires an exact and fast acquisition of different variables covering various areas and multiple applications. Sensors which are becoming more and more sophisticated and varied represent excellent candidates to answer this demand.

A Sensor is a dispositive or a device that provides a signal related to a measurand and converts the sensed chemical, biological or physical manifestation into measurable signals, generally converted into an electric signal. The electric signals are intended to deliver the necessary information of the recognition of the measured variable.

With a large panel of physical, chemical and biological phenomena, a classification of sensors can be proposed[1] (table 1.1):

**Table 1.1.** Classification of the different types of sensors with examples of applications.

| Sensor category | Applications | Mesurand |
|---|---|---|
| Physical sensors | Thermal sensors | temperature, heat, thermal flux |
| | Radiation sensors | $\gamma$ ray, X ray, UV, visible, IR |
| | Mechanical sensors | displacement, velocity, acoustic waves |
| | Magnetic sensors | magnetic field, permeability |
| | Electrical sensors | potential, current, charge, inductance. |
| Biological sensors | Recognition | cells, proteins, antigens, hormones |
| Chemical sensors | Recognition<br>pH<br>Humidity | pollutants, gas, vapors, VOC |

In order to precise the function of a sensor, a distinction must be made between the recognition interface and the transducer. The transducer is the element that converts a sensed chemical, biological or physical manifestation of a measurand into a measurable signal.

## 1.2 Development of chemical and biological sensors

The development of chemical and biological sensors represents one of the most promising objectives in the field of sensors, owing to the vast applications of these sensors in the characterization of complex samples in liquid or gas media. Their applications can be as varied as in food industry, quality control, process operations[2], in addition to environmental applications such as the analysis of fuel mixtures, identification of toxic wastes, and the detection of oil leaks[3], analysis of natural waters[4] and detection of heavy metals[5].

These devices are able to deliver qualitative as well as quantitative informations regarding the chemical, biological or physical state of a material. Chemio- and Biosensors involve a recognition layer and a transducer in an integrated system. A range of selective and specific recognition layers have been interfaced onto the surface of transduction system. The interaction of the target species, being measured by the recognition layers induces a change in the latter, which is transduced (converted) into a measurable electronic signal. In biosensors the recognition material is usually a natural biologically derived system such as microorganisms, enzymes, anti-bodies, oligonucleotides, or other natural molecular binding systems[6]. In chemical sensors, the recognition layer is a chemical (synthetic) recognition layer, such as a functionalized polymer film, a supramolecular host system, or a self assembled arrangement that is designed for selective interaction with the substance to be sensed.

A chemical sensor can be defined[7] as a device, which responds to a particular analyte in a selective way by means of a reversible chemical interaction and that can be used for the quantitative and qualitative determination of the analyte.

Sensors also involve the transduction of physicochemical properties at an interface into usable information[8]. Thus, two main features (Figure 1.1) define the detection process:

*i)* Chemio-, bio- or physico-sensitive layer which provides selectivity and sensitivity of the recognition process.

*ii)* Transducer, which converts the chemical, biological or physical information into an electrical signal.

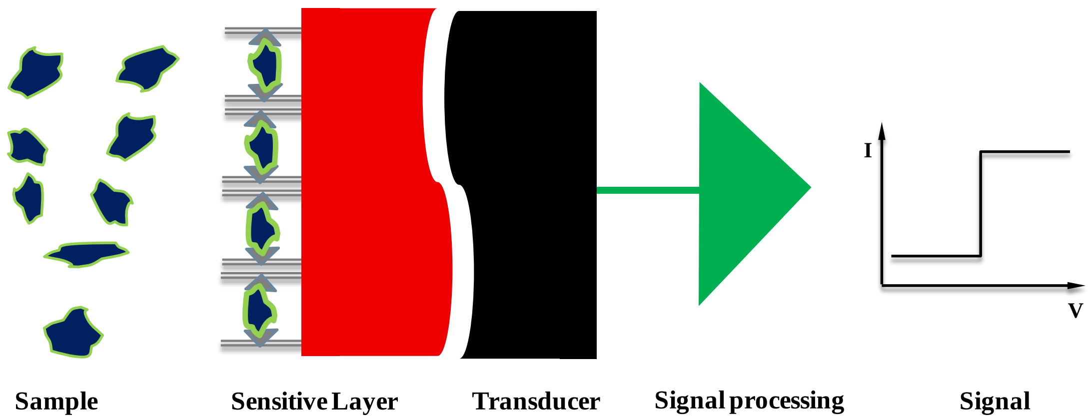

**Figure 1.1.** Chemical (biological) multistep sensing process: sensing of the target molecules by the recognition element (the sensitive layer), transduction of the recognition into a signal and processing of the signal, then exploiting the resulting signal.

Over the last decades, many types of sensors were developed. Table 1.2, adapted from ref. 9, gives a summary of some of the main developments in the field of chemical and biological sensors, starting with the pH glass electrode, which appeared early in the 1930s till the onward development of lab-on-chip and sensor arrays.

**Table 1.2.** Major Developments in the Sensor area

| **Year** | **Development** |
|---|---|
| 1930 | Glass pH electrode |
| 1956 | Clark oxygen electrode |
| 1959 | Piezoelectric mass deposition sensor |
| 1961 | Solid electrolyte sensor |
| 1962 | Enzyme electrode (first biosensor) |
| 1962 | Metal oxide semiconductor gas sensor (Taguchi sensor) |
| 1964 | Bulk acoustic wave (BAW) chemical vapor sensor |
| 1966 | Glucose sensor |
| 1966 | Fluoride ion-selective electrode |
| 1970 | Ion-selective field effect transistor (ISFET) |
| 1970 | Fiber optic gas sensor |
| 1975 | Palladium gate FET hydrogen sensor (MOSFET) |
| 1977 | Enzyme FET biosensor (ENFET) |
| 1979 | Surface acoustic wave (SAW) vapor/thin film sensor |

| | |
|---|---|
| 1982 | Surface Plasmon Resonance (SPR) sensor |
| 1984 | Evanescent wave fiber optic sensor |
| 1986 | BAW liquid-phase immunosensor |
| 1996 | Electronic tongue first reported |
| 1999 | Electronic nose used to identify the presence of pathogens in wine |
| 2000 onward | Developments in miniaturization (lab-on-chip) and sensor arrays |

The detection of large molecules systems such as biologically active entities like oligonucleotides involve a large set of probe-target interactions (hydrogen bonds), which enabled the development of various sensors showing high selectivity and sensitivity. On the other hand, the detection of small organic molecules, such as: gas molecules, volatile compounds, organic solvents, toxic substances, pesticides, herbicides, explosives or organophosphorus compounds, remains one of the most challenging questions in the sensor field, regarding the relative small molecular mass and the relative limited capacity of these molecules to interact specifically with the recognition sites on the sensing layer.

In the next sections the characteristics, the function and the role of the chemical sensors will be described in order to reach a better understanding of this problem.

## 1.3 Characteristics of the chemical sensors

A chemical sensor involves a sensing layer together with a transducer. The sensing layer represents the main part of the sensor. Many organic, inorganic or hybrid organic-inorganic based materials, can be used as active sensing layers, providing that analytes (or measurands) can diffuse into the sensing matrix and be trapped, thus modifying the physical or/and chemical properties of the material. The active layer can also be doped with specific probe-molecules able to interact selectively with the target analytes, thus providing the selectivity of the sensor. The role of the transducer is to convert the variation of a physical property (e.g. refraction index…), associated with a chemical interaction (e.g. H-bond formation, electrostatic interaction, establishment of covalent bond, etc.) into a measurable signal (optical, electrical, electrochemical, piezoelectrical, etc.) proportional to the measurand.

The required characteristic of a chemical sensor are:

### 1.3.1 Stability

The percent of change of the baseline and/or sensitivity in time.

### 1.3.2 Repeatability

The ability of a sensor to deliver an identical signal of the same value of the analyte recognition when the measurements are repeated in the same conditions.

### 1.3.3 Reproducibility

The closeness of replicate measurements on the same sample, using the same measuring technique, under the same conditions. It can be limited by many factors, including instrument stability, loss of the substance being measured during sample operation and contamination.

### 1.3.4 Resolution

The smallest variation in the input signal causing a measurable change in output.

### 1.3.5 Sensitivity (S)

The slope of the response (calibration) curve expressed as output per unit of concentration. The relation between the value of the obtained output signal (s) to the input signal (m).

$$S = ds/dm \qquad \text{Eq 1.1}$$

### 1.3.6 Limit of detection (LOD)

The lowest value (threshold) of the output signal where the variations in the input become measurable. Usually LOD is equal to 3 times the value of the standard deviation of the output signal ($\sigma$).

$$LOD = 3\sigma \qquad \text{Eq 1.2}$$

### 1.3.7 Response time ($t_\alpha$)

The length of time necessary to deliver a certain proportion $\alpha$ of the full amplitude of the signal (s).

$$s_{(t\alpha)} = \alpha \times s_{(t \to \infty)} \qquad \text{Eq 1.3}$$

### 1.3.8 Selectivity

The ability of the sensor to detect one chemical component in the presence of many different components in the same sample and to deliver a quantitative, non disturbed signal.

### 1.3.9 Dynamic range

The concentration interval over which the sensor provides a measurable changing response. The linear dynamic range (LDR) constrains this interval to that region in which a linear proportionality is maintained between response and concentration. Dynamic range is bounded by the limit of detection at the lower end and by saturation effects at the upper end.

## 1.4 Signal transduction by chemical sensors

The interactions between the analyte and the organic or inorganic sensing layers can cause variations in the physicochemical properties of the chemically interactive layers. As a consequence a classification of the sensors can be used by identifying the type of the transducing method. In this regard we can mainly distinguish:

### 1.4.1 Optical sensors

For this type of sensors the output transduced signal is light. Examples being optic fiber and devices making use of the principles of absorbance, reflectance, luminescence, and surface Plasmon resonance.

With optical sensors, evanescent wave technology is of prime importance. If the refractive index of one material is less than the other, there is a change of phase in the reflected ray with a corresponding energy loss. The lost energy is released as an evanescent wave, which decays rapidly outside the first medium and penetrates one wavelength. In addition, any modulation of the evanescent wave via absorption, polarization, or refraction leads to changes in the properties of transmitted light[9]. This allows measurements to be made through the wall of optic fibers or SPR chip. One can measure large number of chemical quantities, such as: chemical species, pH, humidity, etc. Techniques by which the measurements are made can be classified in three categories depending on[10]:

*i)* How the sensing process is accomplished.

*ii)* The physical extent of the sensing process.

#### 1.4.1.1 Means of sensing

In this category, sensors are generally based either on measuring an intensity change in one or more light beams or on looking at phase changes in the light beams by causing them to interact or interfere with one another. Thus sensors in this category are termed either *intensity sensors* or *interferometric sensors*. Techniques used in the case of intensity sensors include light scattering (both Rayleigh and Raman), spectral transmission changes (i.e., simple attenuation of transmitted light due to absorption), microbending or radiative losses, reflectance changes, and changes in the modal properties of the fiber. Interferometric sensors have been demonstrated based upon the magneto-optic, the laser-Doppler, or the Sagnac effects, to name a few

### 1.4.1.2 Extent of sensing

This category is based on whether sensors operate only at a single point or over a distribution of points. Thus, sensors in this category are termed either *point sensors* or *distributed sensors*. In the case of a point sensor, the transducer may be at the end of a fiber the sole purpose of which is to bring a light beam to and from the transducer. Examples of this sensor type are interferometers bonded to the ends of fibers to measure temperature and pressure. In the case of a distributed sensor, as the name implies, sensing is performed all along the fiber length. Examples of this sensor type are fiber Bragg gratings distributed along a fiber length to measure strain or temperature.

### A) Surface Plasmon Resonance, SPR

SPR is refractive index-based detection technique which helps for real time and label free monitoring of interactions on a metal surface and is a widely used optical transducing technique[11,12]. The SPR can occur when plane-polarized light hits a metal film under total internal reflection conditions, thus, when a light beam hits a half circular prism, the light is bend towards the plane of interface, when it is passing from a denser medium to a less dense one (figure 1.2 A). Changing the incidence angle changes the outcoming light until a critical angle is reached. At this point, all the incoming light is reflected within the circular prism. This is called total internal reflection (TIR). The prism is coated with a thin film of a noble metal on the reflection site; gold is used because it gives a SPR signal at convenient combinations of reflectance angle and wavelength. In addition, gold is chemically inert to solutions and solutes. When the energy of the photon electrical field is just right, it can interact with the free electron constellations in the gold surface. These are the outer shell and conduction-band electrons. The incident light photons are absorbed and the energy is transferred to the electrons, which convert into surface plasmons. In TIR, the reflected photons create an electric field on the opposite site of the interface. The plasmons create a comparable field that extends into the medium on either side of the film. This field is called the evanescent wave because the amplitude of the wave decreases exponentially with increasing distance from the interface surface, decaying over a distance of about one light wavelength (black curved line in figure 1.2A). The depth of the evanescent wave which is useful for measurements is within ~300 nm of the sensor surface. The wavelength of the evanescent field wave is the same as that of the incident light. The energy of the evanescent wave is dissipated by heat.

The introduction of sensitive layers onto the SPR chip (e.g. molecularly imprinted polymers) transduces and transforms the interactions with the target analytes into measurable physical signals with high sensitivity and rapidity. Certain real-time detection methodologies were developed[13]. Simultaneous electrochemical and SPR measurements are possible (figure 1.2B) affording additional information and insights into various electrochemical processes. The SPR chip (gold film) serves as working electrode. Also a gas detection module to study molecular adsorption and desorption processes in the gas phase (figure 1.2C) is available. It allows the detection of various chemical vapors in applications like toxic molecules in the environments or the chemical analysis of human breaths for medical research.

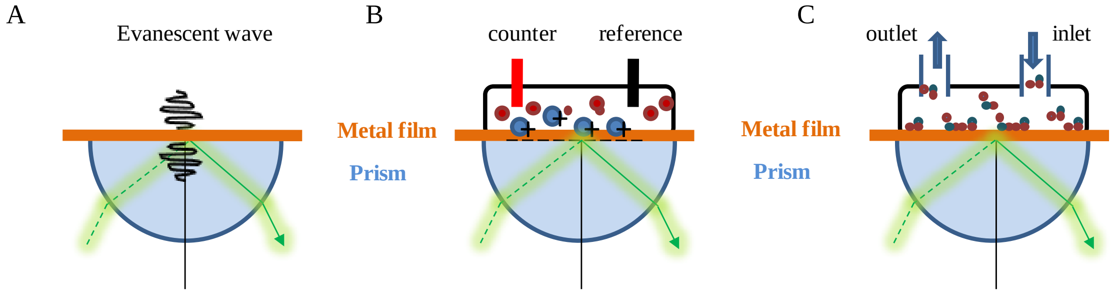

**Figure 1.2.** Surface plasmon resonance configurations. A) SPR with a presentation of the evanescent wave field. B) Electrochemical SPR where the metal film serves as working electrode. C) Chemical vapor sensing module where the chip is provided with a functionalized sensing layer.

### B) Fiber-Optic Chemical Sensors, FOCS

An optical fiber is a flexible, transparent cylindrical cable whose diameter can range from less than one µm to several hundred µm. The materials most commonly used in the fabrication of the fibers are plastics, glasses, and quartz. The choice of material depends on the spectral range of the radiation to be transmitted along the fiber. For example, if visible radiation is to be transmitted, glass or plastic fibers work well, whereas for guiding UV radiation, the more expensive quartz or fused silica fibers can be used. As shown in figure 1.3, the fiber consists of an inner shaft, known as the core, of a given refractive index, surrounded by a second material of slightly lower refractive index, known as cladding. To give mechanical strength and flexibility to the fiber, a jacket or buffer, generally made of a polymeric and flexible material, is used. The principle of transmission of light along optical fibers is that of total internal reflection, which can be described using different rays as illustrated in figure 1.3. In order for a ray to be effectively “trapped” within the fiber core, it must strike the core/cladding interface at an angle $\alpha_2$ greater than the critical angle $\alpha_c$. This critical angle is related to the refractive indice of the core $\eta_1$ and the cladding $\eta_2$ by Snell’s law and can be calculated as (Eq 1.4):

— Eq 1.4

This requirement means that any ray entering the fiber with an incidence angle α between 0 and ±Θ will be internally reflected along the fiber core[14]. This angle Θ is known as semiaperture angle, or acceptance angle and is related to the numerical aperture, NA, a typical parameter used in the characterization of an optical fiber as follows (Eq 1.5):

Eq 1.5

where $\eta_0$: is the refractive index of the medium surrounding the fiber.

The radiation cone trapped within the core will exit the fiber with an aperture angle of ±Θ. The greater the value for the NA, the wider the angle Θ and thus the larger the cone of radiation accepted. The electromagnetic field does not fall abruptly to zero at the core/cladding interface. Instead, the overlap of the incoming beam and the internally reflected beam leads to a field that penetrates into the medium next to the core. This electromagnetic field, which tails but does not propagate into the second medium, is called the evanescent field; its intensity decays exponentially with the distance to the interface.

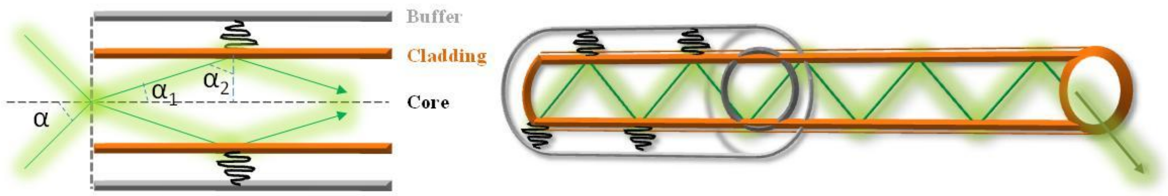

**Figure 1.3.** Principle of propagation of light in an optical fiber, and optical fiber components with schematic representation of light transmission.

The coupling of the light-transmitting properties of optical fibers with optical spectroscopic methods of analysis has resulted in the development of fiber-optic chemical sensors, FOCS, which are becoming conventional tools in chemical analysis. A distinction is often made in the case of FOCS as to whether measurands act externally or internally to the fiber. If the transducers are external to the fiber and the fiber registers and transmits the sensed quantity, the sensors are termed extrinsic sensors. When the sensors are embedded in or as parts of the fiber, the sensors are termed internal or intrinsic sensors. Examples of extrinsic sensors are moving gratings to sense strains, fiber-to-fiber couplers to sense displacement, and absorption cells to sense chemistry effects. Examples of intrinsic sensors are the sensors that use microbending losses in the fiber to sense strain, modified fiber claddings to make spectroscopic measurements, and counter-propagating beams within a fiber coil to measure rotation.

### C) Mach-Zehnder interferometer

Another mode of optical transduction using the variation of the optical index of the mediums upon the adsorption of the target analytes is the Mach-Zehnder interferometer. The principal of the technique is based on the separation of the wave by a Y junction into a reference and detection waves using a sensitive membrane[14] (figure 1.4). After the recombination, the resulting interference due to different optical paths will serve as an indication to the optical index variations. These variations are related to the detection of the target analytes by the sensitive layer deposited on the optical path of the detection hand of the interferometer.

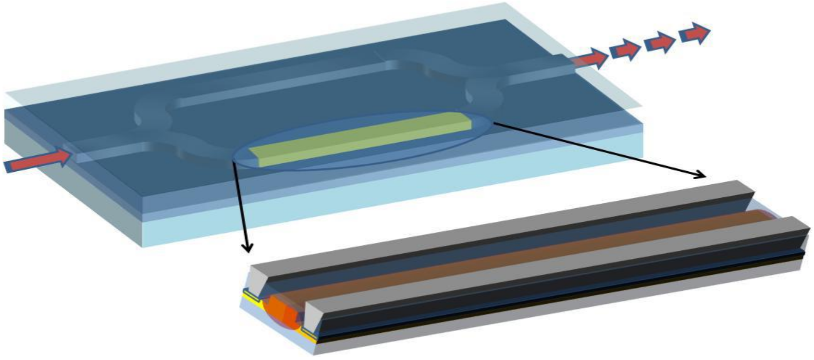

**Figure 1.4.** Schematic representation of Mach-Zehnder interferometer with an optical modulator.

Even if the optical sensors present interesting properties, LC3B laboratory usually uses piezoelectric and electrochemical sensors. As a consequence, in this work we will focus on the use of these types of sensors.

### 1.4.2 Piezoelectric sensors

Piezoelectricity is defined as “electric polarization” produced by mechanical strain in particular crystals (belonging to certain classes), the polarization being proportional to the strain and changing sign with it. A mechanical deformation gives rise to the polarization of a dielectric material. Piezoelectric materials tend to be sensitive to changes in mass, density, or viscosity, which explains that frequency can be used as a sensitive transduction parameter[6]. The most widely used piezoelectric material is quartz. Devices based on piezoelectric crystals have been constructed in a number of configurations for sensor applications and materials characterization, including the thickness-shear mode (TSM) resonator, the surface acoustic wave (SAW) device, the acoustic plate mode (APM) device, and the flexural plate wave (FPW) device. Each of these devices, (figure 1.5) uses a unique acoustic mode[15].

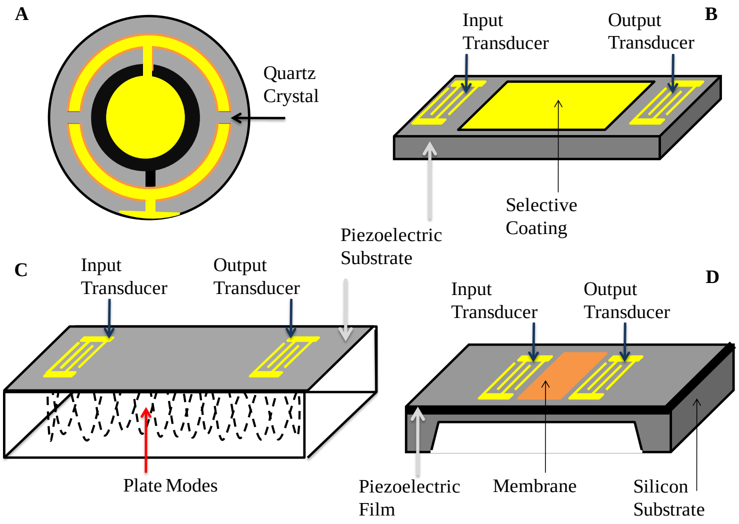

**Figure 1.5.** Schematic sketches of the four types of acoustic sensors. A) Thickness-Shear Mode resonator; B) Surface Acoustic Wave (SAW) sensor; C) Shear-Horizontal Acoustic Plate Mode (SH APM) sensor; and D) Flexural Plate Wave (FPW) sensor.

A distinction can be made between one-port acoustic devices, such as the Thickness-Shear Mode resonator, TSM, and two-port devices, including the Surface Acoustic Wave, SAW, Shear-Horizontal Acoustic Plate, SH-APM sensor, and Flexural Plate Wave, FPW devices. In one-port acoustic devices, a single port acts as both the input and the output port. The input signal excites an acoustic mode which in turn generates charges on the input electrode. These signals combine to produce an *impedance variation* that constitutes the TSM resonator response. In two-port devices, one port is used as the input port and the other as an output port; these are typically interchangeable. The input signal generates an acoustic wave that propagates to a receiving transducer, which regenerates a signal on the output port.

### 1.4.2.1 Thickness-Shear Mode (TSM) Resonator

The TSM resonator, widely referred to as a quartz crystal microbalance (QCM)[16], typically consists of a thin disk of AT-cut quartz crystal disk with circular electrodes patterned on both sides, as shown in figure 1.6. When an electric field is applied between the electrodes, the crystal is mechanically deformed and in an AC field the crystal can be made to oscillate. The resonance frequency can be measured precisely. Even a tiny mass change of the sensor causes a measurable frequency shift. The mass sensitivity can be expressed by the Sauerbrey equation[16] (Eq 1.6).

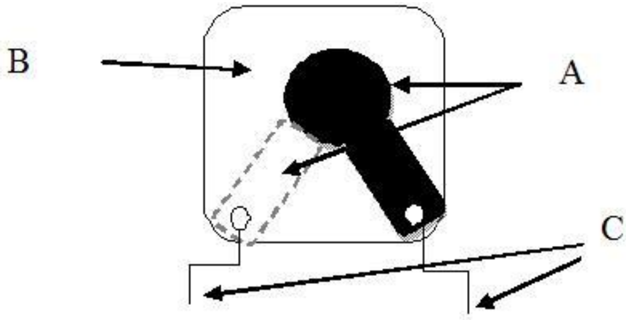

**Figure 1.6.** Schematic representation of QCM (Quartz Cristal Microbalance): **(A)** Metallized electrodes; **(B)** Quartz plaque; (**C)** Electrical connections.

The equation that relates the mass variations *Δm* with the resonance frequency of the uncoated device $f_0$:

$$\frac{\Delta f}{f_0} = -\frac{2 f_0 \Delta m}{\sqrt{\mu\rho}} \qquad \text{Eq 1.6}$$

where:

*Δf:* is the frequency variations due to mass deposition.

*μ:* the elastic rigidity modulus.

*ρ:* the quartz density.

In order to improve the gravimetrical sensitivity, one need to increase the functional frequency of the propagated acoustic wave by decreasing the thickness of the piezoelectric disc. However, this decrease in thickness reduces the mechanical stability of the disc.

Deposition of foreign material on the quartz crystal surface results in an increase in the plate thickness, thus causing a change in the resonant frequency. The Sauerbrey equation applies only to AT-cut crystals vibrating in the thickness shear mode, and assumes that the resulting frequency change is caused only by a change in the thickness of the crystal and that the crystal operates in the vacuum. However, this equation provides a basic mathematical expression for the system but ignores the viscoelastic properties of the deposited material and the difference between its density and that of the crystal[6]. The Sauerbrey equation strictly applies in the vacuum or in the gas phase. When the QCM is in contact with a solution, there is a decrease in frequency that is dependent upon the viscosity and density of the solution. For example, immersing a QCM in water leads to a decrease in frequency of about 750 Hz. Similar effects are also observed for viscoelastic films immobilized on the crystal surface. Therefore, the rigidity of a polymer film must be first established (by e.g. crystal impedance or a linear correlation between film thickness and $\Delta f$) in order to validate the interpretation of QCM measurements using the Sauerbrey equation[17]. Furthermore, since electron transfer reactions of electroactive films are necessarily accompanied by charge transport in or out the film (in order to maintain electroneutrality) and often by solvent transport and morphological changes, it is not uncommon for the density and/or viscosity of a polymer to vary significantly as a result of electron transfer reactions, leading to changes in the rigidity of the film. Thus, the rigidity of the film must be established for all the observed oxidation states.

One of the most interesting applications of QCM is its coupling with electrochemical measurements (EQCM) in order to measure mass changes associated with electrochemical processes such as adsorption, electrodeposition, corrosion, and equilibration of redox polymers undergoing charge transfer reactions[18]. The application of the QCM to mass changes occurring during electrochemical processes is relatively simple. The QCM electrode that is in contact with the solution also acts as the working electrode in the electrochemical cell and processes under investigation like adsorption, deposition, mass transport, etc., pass over this electrode. The combination of the QCM and commercial potentiostats to build an electrochemical QCM (EQCM) has required some modifications of the potentiostat electronics related to the grounding of the working electrode[17,18]. Quantitative interpretation of EQCM data is based on the combination of the Sauerbrey equation and Faraday’s Law. The former relates changes in frequency to changes in mass, whereas the latter ($Q = nFN$) relates charge (Q) passed in an electrochemical experiment to the number of moles of material electrolyzed (N) and (n = number of electrons involved in the electrochemical reaction).

Therefore, frequency changes can be related to the total passed charge. However, before any calculations can be performed, the EQCM must be calibrated in order to derive the proportionality constant of the Sauerbrey equation, which is done using a well-behaved electrochemical reaction (typically the electrodeposition of copper or silver) under experimental conditions similar to those used for the reaction of interest.

#### 1.4.2.2 Surface Acoustic Waves

The surface acoustic waves are propagated and guided along the surface of an elastic layer, with most of the energy density confined to a depth of about one wavelength below the surface. Two main categories of surface waves exist: the Rayleigh waves and the Bleustein-Gulyaev wave (shear horizontal wave).

#### A) Rayleigh wave

Rayleigh waves have longitudinal and vertical components that can couple with the medium placed in contact with the device’s surface. The Rayleigh mode SAW has predominantly two particle displacement components in the sagittal plane[15]. The surface particles move in elliptical paths characterized by surface normal and surface parallel components. The surface parallel component is parallel to the wave propagation direction. The generated electromechanical field travels in the same direction. The velocity of the wave depends on the substrate material and the cut of the crystal. An example of piezoelectric substrate is lithium niobiate ($LiNbO_3$), where the dominant acoustic mode propagating on a Y-cut Z propagating $LiNbO_3$ is the Rayleigh mode (figure 1.7). The use of Rayleigh SAW sensors is applicable only to the gas media as the Rayleigh wave is severely attenuated in liquid media.

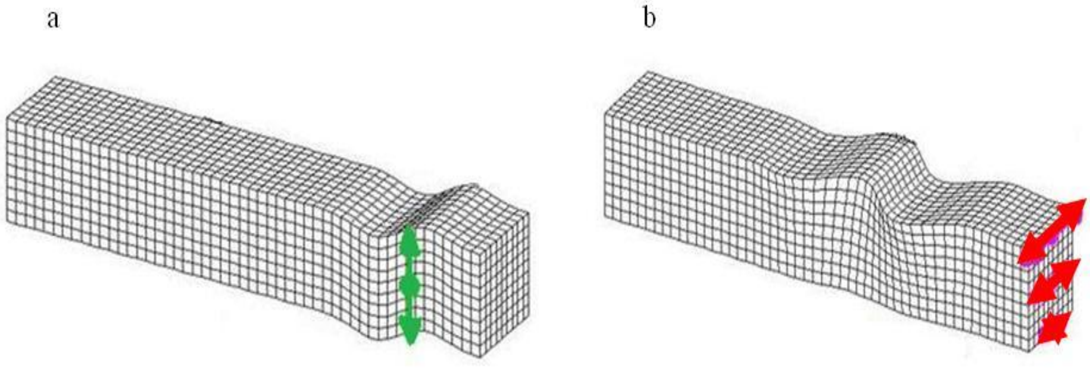

**Figure 1.7.** Acoustic wave propagation in elastic media **(a)** Rayleigh wave propagation in Y-Z $LiNbO_3$, **(b)** Shear horizontal wave propagation in 36°-rotated Y-X $LiTaO_3$.

### B) Shear horizontal wave

The selection of a different piezoelectric material and appropriate crystal cut yields shear horizontal waves instead of Rayleigh waves. An example of piezoelectric substrate is lithium tantalate ($LiTaO_3$), where the dominant acoustic mode propagating on a 36°-rotated Y-cut X propagating $LiTaO_3$ is the SH mode[19]. The particle displacements in this type of wave are transverse to the wave propagation direction and parallel to the plane of the surface (figure 1.7). This makes SH-SAW devices suitable for operation in liquid media, where propagation at the solid-liquid interface can be attained with minimal energy losses. The appearance of these devices is very similar to that of Rayleigh mode devices, but a thin solid film or grating is added to prevent wave diffraction into the bulk[19]. When the surface is metalized and electrically shorted, the potential on the surface is zero. In this case, only the normalized displacement ($u_2$) interacts with the liquid loading, and the phenomenon is called mechanical perturbation. If the surface is free and electrically open, then both $u_2$ and normalized electric potential ($\Phi$) interact with the adjacent liquid medium. Interactions of $\Phi$ and the electrical properties of the liquid constitute the acoustoelectric interaction.

The nature of all of the parameters involved with sensor applications concerns either mechanical or electrical perturbations[19,20]. An acoustic device is thus mainly sensitive to the physical parameters, which may interact with the mechanical properties of the wave and/or its associated electrical field. For chemical or biosensing applications, a transduction layer is used to convert the value of desired parameter (e.g. analyte concentration) into mechanical and electrical perturbation that can disturb the acoustic wave properties. The acoustic wave velocity is affected by several factors, each of which possesses a potential sensor response.

$$\frac{}{} = \frac{}{} \quad \frac{}{}\mathit{\Delta mass} + \frac{}{}\mathit{\Delta elec} + \frac{}{}\mathit{\Delta mech} + \frac{}{}\mathit{\Delta envir}) \qquad \text{Eq 1.7}$$

equation 1.7 illustrates the perturbation of acoustic velocity due to various factors.

$V_0$: acoustic wave velocity

$\Delta V$: perturbation of acoustic velocity

*Δmass:* mass variations

*Δelec:* electrical perturbation

*Δmech:* mechanical perturbation

*Δenvir:* perturbations due to temperature and/or pressure

A sensor response may be due to a combination of these factors. Understanding the acoustic wave perturbation due to each of the above factors would help gain insights into the sensing mechanism as well as in designing efficient sensors.

The development of chemical or biochemical wave sensors needs the development of a sensing layer deposited over the sensitive zone of the acoustic wave dispositive. Interacting then binding between the analyte and the probe will increase the mass of the system so we can define the process as a gravimetrical transduction.

### 1.4.3 Electrochemical sensors

Most electrochemical sensors are based on potentiometry, voltammetry, or amperometry although coulometry and conductimetry have also been used. Interfaces and devices such as solid electrolyte gas sensors, semiconductor-based gas sensors, ion-selective electrodes (ISE), ion-selective field effects transistors (ISFET), and conducting polymer sensors have been reported. These sensors are widely used in many branches of industry, environmental and medical monitoring, together with control of biological processes. The selectivity of these sensors depends on the chemical nature of the used electrode. Thus, metallic electrodes and surface modified metallic electrodes are sensitive to chemical equilibria involving electron transfer, such as oxido-reduction (redox) equilibria, or electrodes that are sensitive in the media involving mobile ions, such as ion-selective electrodes (ISEs).

Due to the large diversity of this type of sensors, a classification based on the operating principal can be established (Table 1.3)[21].

**Table 1.3.** Principal electrochemical sensors

| Electrochemical method | Electrode's Type | Example of the sensitive element | Example of measured species |
|---|---|---|---|
| Potentiometric | Redox | -Pt, Graphite, Au, etc. | -Redox systems like $Fe^{2+}/Fe^{3+}$ |
| | pH sensitive | -Glass with special composition<br>-Metal oxides<br>-$Si_3N_4$ | -$H^+$ |
| | Specific | -Glass with special composition | -$Na^+$,$K^+$ |
| | | -Ionic exchange membrane | -$Na^+$, $K^+$, $NH_4^+$, $Ca^{2+}$, $NO_3^-$, $ClO_4^-$, $BF_4^-$ |
| | | -Gas diffusion membrane+ pH electrode | -$NH_3$, $CO_2$, $SO_2$, $N_xO_y$, $H_2S$ |
| Amperometric | Redox | - Hg, Pt, C, Au, etc. | -Redox species in solution |
| | Oxygen | -Gas diffusion membrane+ redox electrode | -$O_2$ |
| | Enzymatic | -Grafted enzyme membrane+ redox electrode | -Glucose, Urea |

| | | | |
|---|---|---|---|
| Conductimetric | Resistivity or conductivity cell | -Pt, Stainless steel, C, etc. | -Ionisable species in solution |

Three principal groups of electrochemical sensors can be referenced:

### 1.4.3.1 Potentiometric sensors

There are three basic types of potentiometric sensors: ion-selective electrodes (ISEs), coated wire electrodes (CWEs) and field effect transistors (FETs). The utility of these sensors is based on the determination of the difference in potential established between a measuring electrode and a reference electrode (electrode with a constant and reproducible value of potential in the implicated working conditions). This difference in the potential is related to the activity of the ion (or ions) involved in the recognition event. The response is measured under conditions of essentially zero current or at a given value of the current intensity. The potential that develops in a potentiometric measurement is the result of the free energy change that would occur if the chemical phenomena were to proceed until the equilibrium condition has been satisfied. In these measurements the potential difference can be calculated by using the Nernst equation:

— —— Eq 1.8

where:

*E:* measured potential.

*E*°: standard potential.

*R:* gas constant.

*T:* absolute temperature.

*F:* Faraday constant.

*n:* number of the electrons involved in the redox process

$\alpha_{(Ox)}$ and $\alpha_{(Red)}$ activities of the oxidation and the reduction species respectively.

Physical phenomena which do not involve explicit redox reactions and whose initial conditions have a non-zero free energy, also generate a potential as would be the ion concentration gradients across a semi-permeable membrane. The following equation is generally used to determine the concentration of the analyte in test solutions:

— Eq 1.9

where:
*k:* constant
$T$: absolute temperature
$Z_i$: charge of the ion.
$\alpha_i$: activity of the ion.

Ion-selective electrodes (ISEs) are mainly membrane-based devices, consisting of permselective ion-conducting materials, which separate the samples from the inside of the electrode[22,23]. Depending on the nature of the membrane, ISEs can be divided into three groups: glass, liquid or solid electrodes[24], which are widely used for the analysis of organic ions, as well as in the medical monitoring of drugs[25]. The most widely used potentiometric sensor is the glass electrode for measurements of pH and activities of alkali ions[24].

In coated wire electrodes (CWEs), a conducting wire is directly coated with an appropriate ion-selective polymer membrane, usually poly(vinyl chloride) or, poly(acrylic acid) to form an electrode system that is sensitive to electrolyte concentrations. The great advantage of CWEs is that the design eliminates the need for an internal reference electrode which is particularly useful for the miniaturization of the sensor device and for biomedical and environmental monitoring of different kinds of analytes[26].

Ion-selective field effect transistors (ISFET) work as an extension of CWE. ISFET incorporate the ion sensing membrane directly on the gate area of a field effect transistor (FET)[27]. The FET is a solid-state device (figure 1.8) that exhibits high-input impedance and low-output impedance and therefore is able to monitor charge buildup on the ion-sensing membrane. The operation of ISFET is based on the application of a gate voltage ($V_{GS}$) through the electrolyte medium that causes a change in the channel current ($I_{\mathrm{DS}}$). More specifically, upon the application of a small gate voltage, ions from the electrolyte medium migrate into or out of the membrane film altering the doping level of the active area. This causes a change of the channel conductivity that can be detected by an $I_{\mathrm{DS}}$ current measurement. In order to reach maximum current modulation between the redox states of the active area, the area of the gate electrode must be considerably larger compared with the area of the channel[21].

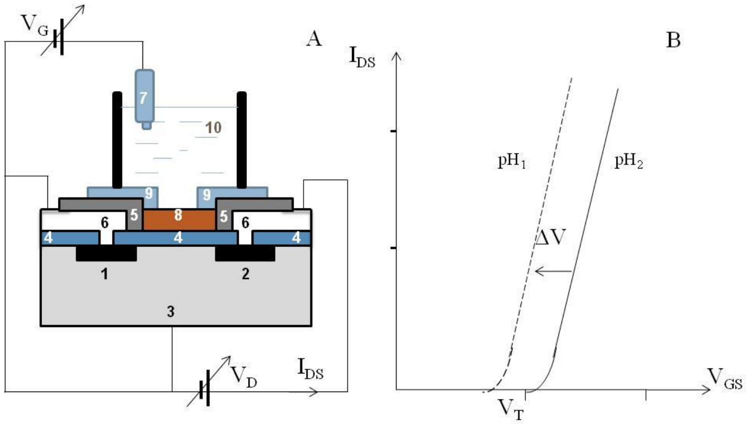

**Figure 1.8** ISFET device for pH measurement using $Si_3N_4$ or $Al_2O_3$ insulating gate. A) Structure of the transistor: 1-Source; 2-Drain; 3-Substrate (p Silicon); 4-Insulator ($SiO_2$); 5-Insulator ($Si_3N_4$ or $Al_2O_3$); 6- Metal contacts; 7- Reference electrode; 8-Ion-selective membrane; 9- Encapsulate; 10- Electrolyte solution. B) Example of the pH influence on the characteristics of the transistor.

Glass pH electrodes can also be used as gas sensing electrodes, where the glass pH electrode is protected from the test solution by a polymer diaphragm. Between the glass membrane and the diaphragm is a small volume of electrolyte. Small molecules, such as $SO_2$, $NH_3$, and $CO_2$, can penetrate the membrane and interact with the trapped electrolyte by reactions that produce changes in pH (figure 1.8). The glass electrode responds to the alteration in acidity[24]. The oxygen content of gases at high temperature is measured by an electrochemical cell using a solid electrolyte composed of zirconium dioxide containing $Y_2O_3$ (yttria—stabilized zirconia). In fact, sensors of this type are widely used to monitor the exhaust gas from the internal combustion engines. And it is used in order to control air-to-fuel mixture to minimize the emission of pollutants such as CO and $NO_x$.

Many commercially available ion-sensing potentiometric devices testify the increasing interest of the researchers in this kind of sensors. These systems tend to be low in cost, simple to use, with low interference from the matrix, and can be applied to small volumes. These advantages make potentiometric sensors an ideal choice for both clinical and industrial measurements.

### 1.4.3.2 Amperometric sensors

In these sensors, a difference in potential is applied between a working electrode (e.g. metallic electrodes) and a reference electrode. The signal transduction process is accomplished by monitoring the current as a function of time. On the other hand, a voltammetric measurement is made when the potential difference is scanned between two values and the current is recorded as a function of the applied potential. In both measurements the applied potential creates a driving force for the electron transfer reaction of the electroactive species. The resulting current is a direct measure of the electron transfer reaction. It is thus reflecting the rate of the recognition event, and is proportional to the concentration of the target analyte. The essential operational feature of voltammetric or amperometric devices is the transfer of electrons to or from the analyte. The basic instrumentation requires controlled-potential equipment and the electrochemical cell consists of two electrodes immersed in a suitable electrolyte, or a three electrode electrochemical cell. First, reference electrode (e.g. Ag/AgCl, $Hg/Hg_2Cl_2$) provides a stable potential compared to the working electrode, at which the reaction of interest usually occurs. Second, an inert conducting material (e.g. Pt, stainless steel) is used as auxiliary electrode. A supporting electrolyte is required in controlled-potential experiments to eliminate electromigration effects, to decrease the resistance of the solution and to maintain the ionic strength constant. The theoretical aspects and experimental procedures are well documented[24]. The performance of an amperometric sensor is strongly influenced by the working electrode material. Mercury was very attractive as an electrode material for many years because it has an extended cathodic potential range window, high reproducibility and a renewable surface. The hanging mercury drop electrode or mercury film electrode was the most suitable for stripping analysis[24]. However, the limited anodic potential of mercury electrodes and its toxicity are the principal disadvantages which limited its use. Solid electrodes (e.g. Carbon, Pt, Au, Ag, Ni) have been used as electrode materials because of their versatile potential windows, low back ground currents, chemical inertness, and suitability for various sensing and detection applications.

The miniaturization of the working electrodes has gained much attention where microelectrodes (ME) and ultra microelectrodes (UME) are widely used. Chemically modified electrodes (CME) result from the immobilization of an interface onto the electrode surface through chemical reaction, chemisorption, composite formation or polymer coating. These systems possess many applications, including for instance: the development of electrocatalytic systems with high chemical selectivity and activity, the coating of semiconducting electrodes with anticorrosive properties, electrochromic displays, microelectrochemical devices and electrochemical sensors. One of the common approaches for CME is to use a polymer based interface. Most polymers are applied to electrode surfaces by a combination of adsorptive attraction and low solubility in the electrolyte solution, using pre-formed polymers or electrochemical polymerization. Also different types of inorganic films, such as metal oxide or metal ferrocyanide can also be formed on electrode surface.

### 1.4.3.3 Conductimetric sensors:

A potential or an alternative current is imposed between two inert electrodes in the measuring cell. Using alternative current limits the errors resulting from the polarization of the electrodes. In order to determine the resistance or the conductivity of the measured medium, there are two possibilities[21]: in the case of imposed potential, the parameter is the current intensity or the potential in the case of implication of an alternative current. From Ohm's law it is apparent that the electric current (I) is inversely proportional to the resistance (R). E represents the potential difference:

Eq 1.10

The inverse of the resistance is the conductance (G) which is proportional to the surface of the conducting material (S) and inversely proportional to its length (L):

– Eq 1.11

where γ is constant.

In conductometry, the electrical conductivity of a sample is used to determine the components and their concentrations. However, conductivity measurements are difficult, due to the variable ionic background of the samples and the relatively small conductivity changes that are observed in high ionic strength solutions.

### 1.4.4 Thermal sensors

These systems use the enthalpy of a chemical reaction involving the analyte and monitored with a transducer. The example can be a thermistor[28]. A thermistor is a contraction of a term "thermal resistor". It is composed of semiconductor materials and can be used in applications that involve measurements in the range of -60°C to 15°C, with a resistance ranging from 0.50Ω to 0.75 MΩ. The emission or the absorption of heat in biological or chemical reaction can also be exploited and transduced through the change in the resistance of the thermistor, which acts as a temperature transducer[29].

## 1.5 Chemically sensitive layers

The coupling of the chemically selective layer to the transducer part of the sensor is very important, since it can have a profound effect on the overall performance of the sensor. Generally, we can distinguish two types of interactions between the chemical species and the sensor: a *surface interaction* in which the species of interest is adsorbed at the surface, and a *bulk interaction* in which the species of interest partitions between the sample and the sensor. The classification of the interaction as either surface or bulk is relative with respect to the size of the species. Large molecules, such as proteins, may adsorb at the surface of the sensor layer, whereas smaller ions can penetrate and absorb in the bulk[30].

With only a few exceptions, such as enzyme containing layers and some ion-selective membranes, the selective layers are on the order of a few micrometers thick. Therefore, common thin-film preparation techniques can be used, particularly if the uniformity of preparation is important. For layers prepared from solvents, spin-coating offers good control of both the thickness and uniformity. Dip-coating and drop-casting are often used for preparation of individual sensors. The rate of evaporation of the solvent influences the porosity and density of the film. Vacuum deposition techniques, such as sputtering, electron beam evaporation, and plasma deposition are common. Electrodeposition, photopolymerization and laser-assisted depositions are used for preparation of specialized layers, particularly in the fabrication of sensing arrays.

Electrodeposition of conducting polymer films at the surface of an electrode has opened a field at the convergence between two rich domains: electrochemistry of modified electrodes and conjugated systems[31]. Consequently, applications of modified electrodes in electrocatalysis, electrochromism, energy storage, electroanalysis, and sensors have been enriched by the properties of conducting polymers[32].

Given the impressive progress in the sensors area, the emphasis of this study will be concentrated on the role played by conducting polymers in electrochemical and piezoelectrical sensors with a special interest to molecularly imprinted conducting polymers.

## 1.6 Conducting polymers in chemical sensors

Over the last decades, organic electronic materials based on conducting polymers (CP) and their uses in semiconducting devices have attracted enormous attention. The interest in developing this class of materials is due to the many advantages this technology can offer.

Above all, these materials provide a bridge between the chemical (biochemical) molecular world and electronic devices. Beside their unique features allow flexible electronic devices to be fabricated, by the use of low-cost manufacturing processes, such as electropolymerization, spin coating, spray coating, inkjet printing, and screen printing. These materials offer compatibility with biological systems, and in addition, their electronic properties can be tuned via chemical synthesis or doping. The large application potential of CP in chemical and biological sensors is one of the main trends for the development of these materials. Most CPs were synthesized by modification of the structures shown in figure 1.9. The intrinsic conductivity of the CP results from the formation of charge carriers upon oxidizing (*p*-doping) or reducing (*n*-doping) their conjugated macromolecular chains. Oxidation of the CP in its neutral state (uncharged state), and following internal relaxation processes, causes the generation of localized electronic states, leading to the formation of so-called polaron. After the saturation of the CP chain with polarons, removing additional electrons leads to the formation of bipolaron rather than two polarons which is more favored energetically[33] (figure 1.9). Doping or charge injection in CP leads to interesting variations in these structures beside the variations in the conductivity of the CP, which leads to a modification in the electrochemical behavior. Thus, applications in electrochemical devices were realized since the pioneer work of Wrighton et al.[34]. Also, the change of the CP electronic band structure is accompanied by a change of the optical properties in the UV-vis and NIR-region. This is used in electrochromic displays and optical sensors like in the work of Ho and Leclerc[35].

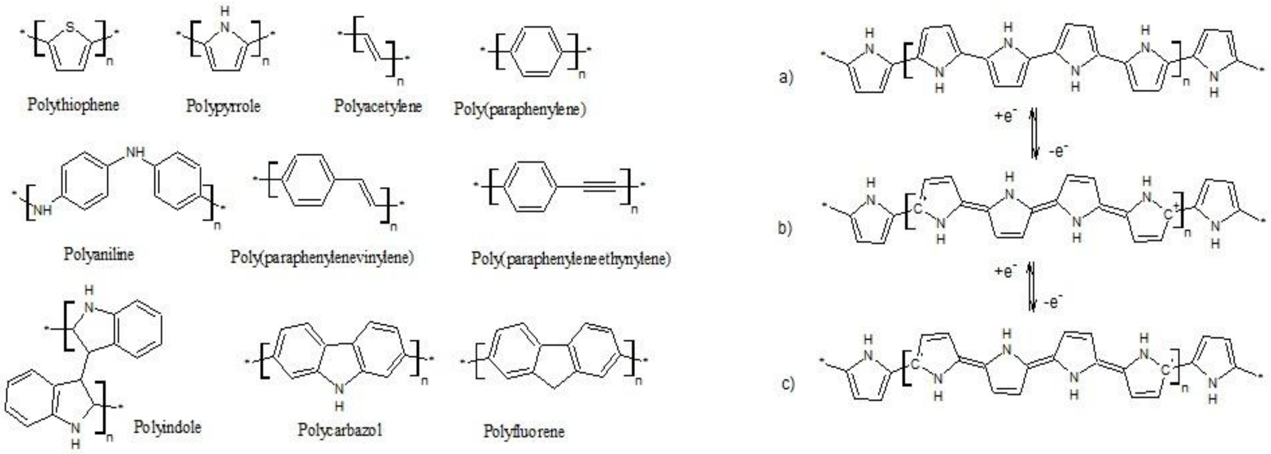

**Figure 1.9.** Main Classes of conducting polymers, and electronic structures of a) neutral state; b) polaron in partially doped; c) bipolaron in fully doped poly(pyrrole).

Doping of CP can be done either chemically or electrochemically. In chemical doping the oxidation is accomplished by exposing the CP to oxidizing vapors, like iodine. Another unique chemical doping procedure is the doping of polyaniline due to protonation. This leads to an internal redox reaction converting the semiconducting form of polyaniline (emeraldine base) to a metallic form (emeraldine salt). The reaction between the different forms is adapted from ref. 36 and is shown in figure 1.10.

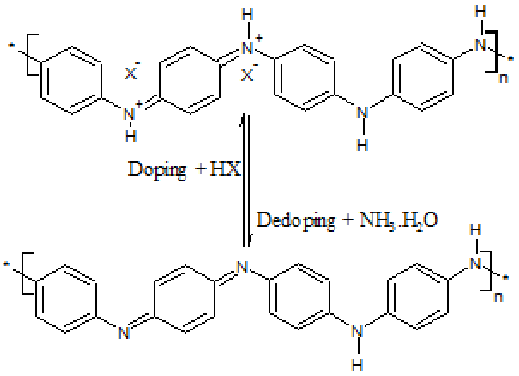

**Figure 1.10.** Polyaniline in its doped emeraldine salt state that then can be dedoped by a base to its emeraldine base form.

Contrarily to chemical doping which is effective but poorly reproducible quantitavely, electrochemical doping provides fine tuning of the doping level by adjusting the electrical potential. The polymers can be synthesized either by addition of an external agent (chemical synthesis of CP) or by electrochemical reaction. Chemical synthesis of CP is performed using oxidants like $(NH_4)_2S_2O_7$ or $FeCl_3$ and usually used for the preparation of CP solutions, while electrochemical deposition is used mainly for deposition of CP films on conducting substrates. An advantage of this method is the possibility to control the film thickness by the charge passed through the electrochemical cell during the film growth. Other techniques can be used for the deposition of thin films over various substrates as the spin coating of a solution of a chemically synthesized CP, the deposition of one or more monomolecular layers of CP by Langmuir-Blodgett technique, or coating of substrates by bilayers of CP and opposed charged polymers by the layer-by-layer technique.

In the next section the application of CP in chemical sensors will be demonstrated with special interest to their role in the development of molecularly imprinted polymers based chemical sensors.

### 1.6.1 Conducting polymers as sensing layers

A description of the role of CP as sensing layer for the detection of metallic ions, organic molecules and gases and electronic noses and tongues also, a special attention will be paid for the molecularly imprinted polymers based on CP, **MICP**.

#### 1.6.1.1 Recognition of metallic ions

Unmodified CP films can display some intrinsic affinity to metal ions, a film of poly-3-octylthiophene (P3OTH) show a selective Nernstian response towards $Ag^+$ ions. It was proposed that the ions interact with the sulphur atoms and the $\pi$-electrons in the conjugated structure of P3OTH[37]. Also potentiometric $Ag^+$ sensors have been prepared by galvanostatic electropolymerization of 3,4-ethylenedioxythiophene on glassy carbon electrodes[38]. Electropolymerization of Polypyrrole in presence of Erichrome Blue-Black B as the counter anion was suggested as a potentiometric and voltammetric $Ag^+$ sensor. A selective recognition for silver ions and improved response were realized by pretreatment of the CP by electrochemical doping/dedoping in $AgNO_3$ solution, the process that rearranges the binding sites and generates recognition sites in the polymer and improves the detection limits into 6 nM [39]. Electrochemical properties of PEDOT poly(3,4-ethylenedioxythiophene) doped with hexacyanoferrate (II, III) ions, was used to detect $Cu^{2+}$ ions with a relative low detection limit of 0.1 µM [40]. A chelating agent like Ethylenediaminetetraacetic acid, widely abbreviated EDTA, to modify the structure of the monomers was used to detect heavy metals. EDTA was covalently bonded to diamino-terthiophene on glassy carbon electrode and used for a simultaneous determination of $Pb^{2+}$, $Cu^{2+}$, $Hg^{2+}$ by combining an extraction of the ions from the sample by EDTA and a stripping voltammetry for the quantification[41]. The detection limits are approximately 0.6 nM, 0.2 nM, and 0.5 nM, for $Pb^{2+}$, $Cu^{2+}$, and $Hg^{2+}$ respectively. The same combination of extraction-stripping voltammetry was used for the detection of $Pb^{2+}$, $Cu^{2+}$, $Cd^{2+}$ with a film of poly(pyrrole) based on pyrrole monomers modified with EDTA[42]. The selectivity towards $Cd^{2+}$ was enhanced by synthesizing the conducting polymer in presence of these ions. Probably some molecular imprinted effects contributed into the selectivity (see *section 1.6.2*). Ionic selectivity can be also introduced in PEDOT by doping the films with *p*-Tetrasulfonated calix[4]aren as potentiometric $Ag^+$ ion selective electrodes[43]. Crown ether modified polythiophenes have been used for the selective coordination of alkali metal ions like $Na^+$ and the performance was investigated by spectroscopic, electrochemical and electrochemical Quartz microbalance (EQCM) techniques[44].

### 1.6.1.2 Recognition of gases

Interaction of gases with CP can be divided in two main classes: gases which chemically react with CP and gases which physically adsorb on CP. Chemical reactions lead to changes in the doping level of CP and modify therefore their physical properties like resistance or optical absorption. Electron acceptors like $NO_2$, $I_2$, $O_3$, and $O_2$ are able to oxidize partially reduced CP and therefore increase their doping level. To oxidize CP, the gas should have a higher electron affinity than the CP[45]. An NO sensor based on a carbon fiber microelectrode modified by a poly(N-methylpyrrole) incorporating $[(H_2O)FePW_{11}O_{39}]^{4-}$ as sublayer and coated by a Nafion external layer has been reported[46]. $NO_2$ was found to increase the number of charge carriers in Poly(aniline)[47] and Poly(3-hexyl-thiophene)[48] through oxidative doping with $NO_2^-$ ions and therefore to decrease the resistance. $SO_2$ also increase the number of charge carriers in poly(pyrrole) thus decreasing the resistance[49]. CO gas sensor has been fabricated using nanocomposite film consists of poly(aniline)-$SnO_2$ and poly(aniline)-$TiO_2$. In these films, CO acts as an oxidant for poly(aniline)-metal oxide nanocomposites films and decreases the resistance values when its concentration gets higher[50]. Metal oxide particles are assumed to form *n-p* hetero junctions with the CP with a depletion region. Adsorbed gases change the depletion region and thus modulate the conductivity of the junction[50]. Electron donating gases like $H_2S$, $NH_3$, and $N_2H_4$ reduce and therefore dedope CP, which leads to an increase in resistance. The behavior, including sensitivity, reproducibility, and reversibility, to various ammonia gas concentrations ranging from 8 ppm to 1000 ppm are investigated using poly(pyrrole) films as sensing layers[51]. The reduction of Poly(3-hexyl-thiophene)[52], and poly(aniline)[53], by hydrazine vapors was reported. Weak physical interactions of non-reactive volatile organic compounds (chloroform, acetone, aliphatic alcohols, benzene, toluene, etc.) with the polymer may lead to modification of CP resistance. An increase in the resistance due to adsorption of chloroform, acetone, ethanol, acetonitrile, toluene and hexane on poly(aniline), poly(pyrrole) and poly(thiophene) and their derivatives were explained by CP swelling leading to higher distance between the chains[54] or by modification of dielectric constant of CP[55]. The major drawback of gas sensor is their poor selectivity and strong interference with humidity which can be overcome by combination of different sensors into arrays[45].

### 1.6.1.3 Recognition of organic molecules

Sensitivity of CP towards organic molecules can be based on the intrinsic affinity of the CP backbone, on affinity of side groups or on binding to immobilized receptors. Synthetic (e.g. cyclodextrines, calixarene, phenyl boronic acid) or biological (e.g. nucleic acids, antibodies, enzymes) receptors can be used. Electroactive molecules such as dopamine were detected in presence of excess of ascorbic acid using a CP matrix of PEDOT[56]. The difference in energy in the hydrophilic and in the hydropobic regions of the PEDOT electropolymerized in phosphate buffer solution (PBS) over a glassy carbon electrode, explained the significant separation between the oxidation peak potentials of dopamine and ascorbic acid (figure 1.11). Dopamine tends to reside on the hydrophobic regions and ascorbic acid on the hydrophilic regions. This difference leads to their preferential oxidation at these sites.

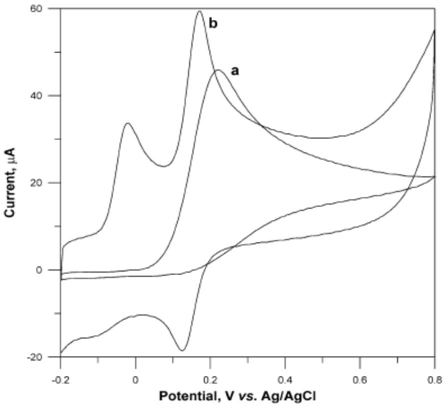

**Figure 1.11.** Cyclic voltammetric behavior of dopamine (1 mM) + ascorbic acid (1 mM) at **(a)** bare glassy carbon electrode, **(b)** PEDOT electrodes in PBS of pH 7.4. Scan rate of 50 mV $s^{-1}$. (Adapted from[56])

A hybrid inorganic redox material-organic CP for the detection of dopamine and 4-nitrophenol was developed by Lupu et al.[57]. Hybrid inorganic-organic coatings based on prussian blue, polyazulene, PEDOT and poly(3-[(E)-2-azulene-1-yl)vinyl]thiophene) have been prepared onto Pt substrate and 4-nitrophenol was detected in concentrations from 30 to 90 µM, with a detection limit of 8.23 µM, whereas, dopamine attended a sensitivity of 0.116 µA/µM with a dynamic range from 2 to 100 µM. An introduction of γ-cyclodextrine into poly(3-methyl-thiophene)[58] or β-cyclodextrine into polypyrrole[59], leads to sensitivity to dopamine, ascorbic acid, chlorpromazine and neurotransmitters derived from pyrogallol and catechol. A number of new chemosensitive receptors modified with cyclodextrines were reported by Radi et al.[60] A copolymer of polyaniline and poly(3-aminophenylboronic acid) was used as sensing film with a potentiometric response to sugars[61]. The stabilization of the polyemeraldine salt form of poly(3-aminophenylboronic acid) upon binding of sugars explain the changes in the $H^+$ activity which is detected as potentiometric response. Simultaneously, changes of resonance frequency of quartz microbalance were measured[62].

#### 1.6.1.4 Electronic noses and tongues

Integrating electronic noses (gas sensors) with electronic tongues (liquid analytes sensors) to improve the detection abilities and to compensate the poor selectivity of single sensors is a rich domain of research. An integrated system has been proposed by Taguchi et al.[63] for the detection of gases and volatile liquids. The detection was based on changes in electrical resistance, which occurs when a poly(aniline) or a poly(pyrrole) coated microelectrodes were exposed to the different samples. NaCl and pH were sensed, and it was claimed that this approach may even be used to detect color for display device applications. This may lead to further development of an electronic eye. The poly(pyrrole) and poly(aniline) are widely used in the development of electronic noses and tongues sensors[64]. The main reasons for the use of CP as odor-sensing devices are the following[9]:

*i)* Rapid adsorption and desorption phenomena at room temperature.
*ii)* Low Power consumption.
*iii)* Sensitive for humidity.
*iv)* Resistive to contaminants.
*v)* Specificity is achieved by modifying the structure of the polymer.

However, the major problem of the electronic noses and tongues is the poor selectivity and the limited ability to distinguish the target molecule among different components of the sample.

In the next section a demonstration of the molecularly imprinted polymers will be presented, and then the role of these polymers in the chemical sensors will be exposed with a special interest to conducting polymers based molecularly imprinted polymers **MICP**.

### 1.6.2 Molecularly Imprinted Conducting Polymers, MICP

Molecular imprinting has been recognized as a powerful technique to prepare specific binding sites for given molecules in appropriate matrices. The shape and functionality of a template can be transcribed onto the cavities in the matrix. The configuration of the functional groups in the template can be memorized by these cavities. The essential driving force to imprint the template (or the target) molecules can be either covalent or non-covalent, includes electrostatic interactions, hydrogen bonding and hydrophobic interactions. Covalent bonds interactions based MIPs were first demonstrated by Shea[65] and Wulff[66] groups. On the other hand, an approach based on non-covalent bonds has been demonstrated by Mosbach et al.[67]

### 1.6.2.1 Molecularly Imprinted Polymers, MIP

MIP Preparation involves polymerization of monomers in presence of target analyte (template) and a porogenic solvent. The functional monomers initially form pre-polymerization complexes with the target molecules and after polymerization, their functional groups are held in position by the cross-linked polymeric structure. Upon removal of the molecular template, the matrix retains binding sites that hold the size and shape of the analyte. This process is similar to the “lock and key” model of enzymes. As a result, a molecular memory is introduced into the polymer matrix, in which the analyte is now able to rebind on the same imprinted material with very high specificity. The porogenic solvent helps to dissolve all the ingredients and to create pores in the final polymer, through which the binding sites will be accessible to the analyte. A schematic representation of the two approaches of MIP preparation was reproduced from ref. 68 and is depicted in figure 1.12. The pre-polymerization complex between the target molecule and the functional monomer determines the type of interactions involved between the binding sites and the analyte in the MIP. Owing to the greater stability of covalent bonds, the imprinting efficiency (yield of binding sites relative to the amount of imprint molecules) is higher for covalent imprinting than for non-covalent one. However, non-covalent imprinting is more flexible enabling a large choice of monomers, target molecules, and the use of the imprinted materials. Moreover, it is very similar to natural processes in a sense that most of biomolecular bindings are non-covalent in nature[67].

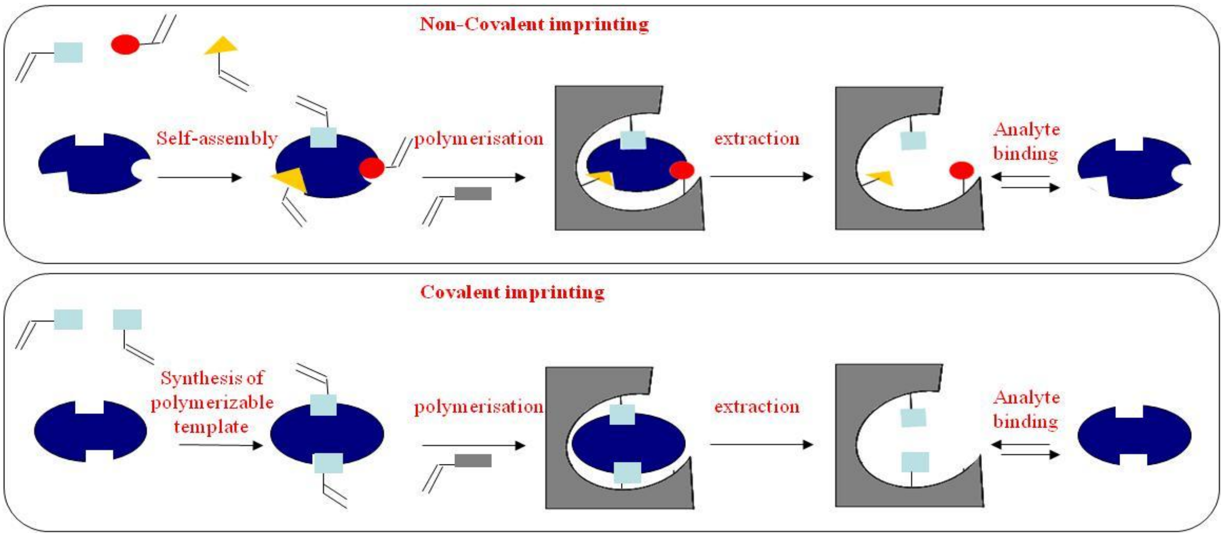

**Figure 1.12.** Schematic representation of the Covalent and Non-covalent Molecular imprinting procedures.

#### 1.6.2.2 Molecularly Imprinted Polymers based sensors

Molecular imprinted polymers acquired a major position as materials in various sensor devices among other materials. Either the conducting polymers is being used on an electrode surface, or non-conducting polymers is being used for immobilization of specific receptor agents on the sensor device. MIP can be used in gas sensors, pH sensors, ion-selective sensors, alcohol sensors, and for the detection of a great number of organic molecules, such as drugs, hormones, explosives, organophosphorus and toxins[69].

Pesticides belong to an interesting class of analytes frequently probed by sensors due to their increasing impact as contaminants in water or in agriculture products. Atrazine is the most extensively used as a template for the detection of herbicides and pesticides, due to its relatively high mobility in soil, and it is often detected in surface and ground waters[70]. Also it is highly persistent in soil: the half life of atrazine in loamy soils ranges from 60 to 150 days. Under dry or cold conditions it can persist for longer than 1 year. It has a low adsorption rate to soil particles with a high potential for ground water contamination, despite its moderate solubility in water, about 1.5 µM or 33 mg $L^{-1}$ at 20 °C[70]. Some analytical methods such as chromatography[71], capillary enzyme immunoassay[72], flow injection immunoanalysis[73], also an impedimetric immunosensor based on N-substituted poly(pyrrole) film[74], has been developed for atrazine detection.

Among the different techniques, The MIPs for the detection of atrazine were reported by many researchers (table 1.4). Three types of polymers can be observed in this table: MIPs realized as a film or thin layer over a substrate, as a membrane, or as a powder used as steady phase in liquid or gas chromatography. The detection of atrazine was carried out using different techniques and low detection limits were obtained. However, the questions concerning the in-field detection and the miniaturization of the sensors are still a challenge in this domain. Beside some other problems like poor stability and moderated selectivity of the MIP based sensors, which limit their application, and open an interesting field for developing new sensing layers with better performance and more robust detection techniques.

#### 1.6.2.3 Sensors based on Molecularly Imprinted Conducting Polymers MICP

Typically molecularly imprinted polymers, MIP, are prepared by photo- or thermally-induced radical polymerization[75]. However, there are a number of reports on MIP preparation by electropolymerization that was developed first by Hutchins and Bachas[76], and later reproduced in many laboratories. This technique was used for preparation of insulating or conductive chemosensistive films.

Films of conducting polymers were generally formed by electropolymerization of pyrrole, aniline, anilineboronic acid, porphyrine and substituted thiophene (table 1.5). The detection of analytes bonded to molecularly imprinted conducting polymers, MICP, were realized by different techniques. Electrical conductance of the sensing layers allowed electrochemical detection of redox active analytes, like dopamine, and was applied for the detection of non electroactive analytes like atrazine. Other detection techniques were used for non-conductive as well as for conductive electro-polymerized layers like electrical capacitance, by impedance measurements, and changes of resonance frequency of quartz microbalance (table 1.5).

**Table 1.4.** Detection of atrazine by molecularly imprinted polymers MIP.

| FM | cross linker | Solvent | Transduction method | Dynamic range | LOD | Ref |
|---|---|---|---|---|---|---|
| MAA | EGDMA | DMF | Amperometric | 9.3-42 µM | 9.4 µM | 77 |
| MAA | EGDMA | ACN | SPR |  | 5pM | 78 |
| MAA | EGDMA | MeOH | Spectroscopic | $10^{-10}$ - 1 µM | $10^{-8}$ ng/mL | 79 |
| MAA | EGDMA | Toluene | Potentiometric | $10^{-4}$ - 10 mM | 0.5 µM | 80 |
| MAA | EGDMA | EDGMA | Potentiometric | 30 µM-1mM | 20 µM | 81 |
| MAA | EGDMA | DMF | Amperometric | 1-10 µM |  | 82 |
| MAA | EGDMA | $CHCl_3$ | Gravimetric (QCM) |  | 2 µM | 83 |
| MAA | EGDMA | DMF | Conductometric | 1-100 nM | 5 nM | 84 |
| TAA | 3,3-bithiophene | $CHCl_3$ |  |  |  | 85 |
| TAA | EDOT | DCM | Amperometric | 1 nM- 15 mM | 0.1 µM | 86 |
| MWCNT |  |  | SPMTE/HPLC | 1-100 µg/L | 0.2-0.5 µg/L | 87 |
| MAA | EGDMA | ACN | SPME/GC and GC/MS | 100-9000 ng/mL | 43 ng/mL | 88 |
| N-VP | Divinylbenzene | Toluene | MISPE/HPLC | 0.1-10 ng/mL | 0.02 ng/mL | 89 |
| MAA | EGDMA-TRIM-DVB | Toluene | HPLC | 5-50 µg/L | 2 µg/L | 90 |
| MAA | EGDMA | ACN | MISPE/HPLC |  | 0.028 µg/g | 91 |
| MAA | EGDMA | Toluene | HPLC |  | 0.1 mg/L | 92 |
| MAA | EGDMA-TRIM-DVB | Toluene | HPLC | 1-40 µg/L | 0.2 µg/L | 93 |
| MAA | EGDMA | ACN | SPME/GC and GC/MS | 100-5500 ng/mL | 56 ng/mL | 94 |
| MAA | EDGMA | DMF | HPLC-MS | 1 nM- 0.1 mM |  | 95 |
| MAA | EGDMA | ACN | MISPE/HPLC |  | $10^{-2}$ µg/mL | 96 |
| MAA | EGDMA | ACN | SPME/GC and GC/MS | 50-9000 ng/mL | 20 ng/mL | 97 |
| MAA | EGDMA | DCM | PLE/ LC- MS/MS |  | 0.03 ng/g | 98 |
| MAA | EGDMA | $CHCl_3$ | HPLC & NMR |  |  | 99 |
| MAA | EGDMA | Toluene | HPLC |  |  | 100 |
| MAA | EGDMA | DCM | HPLC |  |  | 101 |
| MAA | EGDMA | $CHCl_3$ | HPLC & NMR |  |  | 102 |
| MAA | DEAEMA | DMF | Conductometric | 0.01-0.5 mg/L |  | 103 |

**Table 1.5.** Molecularly imprinted conducting polymers designed as sensing layers.

| **Analyte** | **Polymer** | **Transduction method** | **Notes** | **Ref** |
|---|---|---|---|---|
| (T-2) toxin | Poly(3-APBA) | SPR/EIS | LOD= 0.1 fM | 13 |
| Atrazine | Poly(TAA) | XPS | crosslinked by (3,3-bTh) | 85 |
| Atrazine | Poly(EDOT-co-TAA) | CV | LOD= 0.1 µM | 86 |
| L-Glutamic acid | PPy | EQCM | overoxidized film | 104 |
| L-lactate | PPy | HPLC | | 105 |
| L-tryptophan | PPy | EQCM | overoxidized film | 106 |
| Caffeinne | PPy | DPV | | 107 |
| L-aspartic | PPy | FluM | labeled with Av-FITC | 108 |
| Paracetamol | PPy | DPV | polymerization on PGE | 109 |
| Histamine | Poly(biTh) | EQCM | LOD= 5 nM | 110 |
| L-nicotine | PPV/Poly(MAA-co-EDGMA) | EIS | | 111 |
| Avidine | PEDOT/PSS | FluM | labeled with Av-FITC | 112 |
| Protein | PEDOT/PSS | EQCM | labeled with Av-FITC | 108 |
| ATP/ADP/AMP | PAN | HPLC | multiple detection | 113 |
| Glucose | poly(*o*-PD) | EIS | studied in presence of $[Fe(CN)_6]^{3-}$ /$[Fe(CN)_6]^{4-}$ | 114 |
| Glucose | poly(*o*-PD) | QCM | electropolymerization of *o*-PD by CV | 115 |
| Phenylalanine | Phenol | EIS | Predeposition of mercaptophenol SAM on Au and alkanthiol over polymer | 116 |

## 1.7 Use of MICP as a sensitive layer in the LC3B laboratory

Molecularly Imprinted Conducting Polymers can be considered as a promising technology for the preparation of chemosensitive surfaces. It is very attractive for the fabrication of sensors and sensor arrays in many applications. However, it is difficult to evaluate, if it is competitive with other sensors approaches. Nevertheless, one of the advantages of the electropolymerization of MICP is the possibility to control the thickness of the polymer layer. Additionally, it is well compatible with the configuration of the used electrode. Electrical, optical and mass properties of these materials may provide interesting possibilities for binding detection.

In this regard a sensing layer based on functionalized polythiophenes was recently developed by our laboratory[117,118]. This sensitive layer was electrosynthesized over an electrode dedicated for the detection of small organic molecules such as atrazine. The transduction of the sensing process was carried out by an electrochemical method (cyclic voltammetry) and enhanced with a selectivity study[86].

In This work we will present more profound investigations about MICP based sensitive layer. Characterizations and structure investigations of the sensing layer will take place in order to improve the performance of the sensor, also electrochemical and gravimetrical transductions will be presented with an original transduction method based on coupled electrochemical/gravimetric transduction.

In the next chapter, experimental techniques and procedures will be presented with a brief introduction to the DFT calculations carried out in this work.

## References

---

[1] Ichinose N., Kobayashi T., *Guide pratique des capteurs*, Paris, Masson, 1990.

[2] Deisingh A. K., Stone D. C., and Thompson M., applications of electronic noses and tongues in food analysis, *Int. J. Food Sci. Technol.*, 39, 587-604, 2004.

[3] Giese J., Electronic noses, *Int. J. Food Sci. Technol*. 54(3), 96-98, 2000.

[4] Hasan J., States S., and Deininger R., Safeguarding the security of public water supplies using early warning systems: A brief review, *J. Contemp. Water Research and Education*, 129, 27-33, 2004.

[5] Biran I., Babai R., Levcov K., Risphon J., and Ron E. Z., Online and in situ monitoring of environmenetal pollutants: electrochemical biosensing of cadmium, *Environ. Microbiol*. 2, 3, 285-290, 2000.

[6] Gizeli E. and Lowe C. R., *Biomolecular Sensors,* New York, FL: CRC Press, 180-183, 2002.

[7] Cattrall R. W., *Chemical sensors,* Oxford: Oxford University Press, 1-2, 1997.

[8] Thompson M. and Stone D. C., *Surface-launched Acoustic Wave Sensors,* New York: Wiley-Interscience, 15-25, 1997.

[9] Deisingh A. K., in *Sensors for Chemical and Biological Applications*, Boca Raton, FL: CRC Press, 173-189, 2010.

[10] http://www.wtec.org/loyola/opto/c6_s3.htm

[11] Otto A., Excitation of non-radiative surface plasma waves by the method of frustrated total reflection, *Z. Physik,* 216-398, 1968.

[12] Otte M. A., Sepulveda B., Ni W., Juste J. P., Liz-Marzan L. M., Lechuga L. M. Identification of the optimal spectral region for plasmonic and nanoplasmonic sensing, *ACS Nano* 4, 349-357, 2009.

[13] Gupta G., Bhaskar A. S. B., Tripathi B. K., Pandey P., Boopathi M., Lakshmana Rao P. V., Singh B., Vijayaraghavan R., Supersensitive detection of T-2 toxin by the in-situ synthesized π-conjugated molecularlu imprinted nanopatterns. An in-situ investigation by surface Plasmon resonance combined with electrochemistry, *Biosensors and Bioelectronics*, 26, 2534-2540, 2011.

[14] Maillart E., *Développement d'un système optique d'imagerie en résonance de plasmons de surface pour l'analyse simultanée de multiples interactions biomoléculaires en temps réel.*, thèse université de Paris XI Orsay, 2004.

[15] Ballantine D. S., White R. M., Martin S. J., Ricco A. J., Zellers E. T., Frye G. C., Wohltjen H., *Acoustic Wave Sensors: Theory, Design, and Physico-Chemical Applications*, New York: Academic Press, 1997.

[16] Sauerbrey G., Use of quartz oscillators for weighing thin layers and for micro-weighing, Z. Phys, 155, 206-222, 1959.

[17] Bott A. W., Characterization of films immobilized on an electrode surface using the electrochemical quarz crystal microbalance, *Bionanalytical Systems*, INC. Current Separations 18:3, 1999.

[18] Buttry D., Ward M. D., Measurement of interfacial processes at electrode surfaces with the electrochemical quartz microbalance, *Chem. Rev.* 92, 1355-11379, 1992.

[19] Grate J. W., Martin S. J., White R. M., Acoustic wave microsensors. Part I, Anal. Chem. 65, 941A-948A, 1993.

[20] Grate J. W., Martin S. J., White R. M., Acoustic wave microsensors. Part II, Anal. Chem. 65, 987A-996A, 1993.

[21] Asch G., *Les capteurs en instrumentation industrielle*, 5e ed., Dunod, Paris, 749-772, 1998.

---

[22] Bakker E., Bühlmann P. and Pretsch E., Carrier-based ion-selective electrodes and bulk optodes. 1. General characteristics, *Chem. Rev.*, 97, 3083-3132, 1997.

[23] Bühlmann P., Pretsch E., and Bakker E., Carrier-based ion-selective electrodes and bulk optodes. 2. Ionophores for potentiometric and optical sensors, *Chem. Rev.*, 98, 1593-1687, 1998.

[24] Bard A. J. and Faulkner L. R. in *Electrochemical Methods Fundamentals and Applications*, 2nd ed., Wiley-Interscience, New York, 79-82, 2001.

[25] Ashok K. S., Rupam S., Singh R. P. and Saxena P., Novel potentiometric sensor for monitoring barium(II) based on 2,3,4-pyridine-1,3,5,7,12-pentaazacyclopentadeca-3-ene, *Sensors and Actuators B*, 106, 2, 779-783, 2005.

[26] Cross G. G., Fylest T. M., Suresh V. V., Coated-wire electrodes containing polymer immobilized Ionophores blended with poly(vinyl chloride) , *Talanta*, 41, 9, 1589-1596, 1994.

[27] Bergveld P., Development of an Ion-Sensitive Solid-State Device for Neurophysiological Measurements. *IEEE Transactions on Biomedical Engineering*, 1970. BME-17(1): p.70-71.

[28] Rajkumar R., Katterle M., Warsinke A., Mohwald H., Thermometric MIP sensor for fructosyl valine, *Biosensors and Bioelectronics*, 23, 7, 1195-1199, 2008.

[29] Blum L., Marquette C., in *Les Nanosciences, Vol. 3, Nanobiotechnologies et nanobiologie*, Belin, Paris, 855-892, 2007.

[30] Janata J., *Principles of chemical sensors*, Springer, New York, 2009.

[31] Cosnier S., Karyakin A., *Electropolymerization* Wiley-VCH Verlag & Co. KGaA, Weinheim, Germany, 2010.

[32] Garnier F., Functionalized conducting polymers-towards intelligent materials. *Angew. Chem*. 101 (4), 529-533, 1989.

[33] Stafström S., in *Hand book of conducting polymers*, 3ed. Boca Raton, FL: CRC Press, 2-3 to 2-8, 2007.

[34] White H. S., Kittlesen G. P., Wrighton M. S., Chemical derivatization of an array of three gold microelectrodes with polypyrrole: fabrication of a molecule based transistor. *J. Am. Chem. Soc*., 106, 18, 1984.

[35] Ho H. and Leclerc M., Optical sensors based on hybrid aptamer/conjugated polymer complexes. *J. Am. Chem. Soc*. 126, 1384- 1387, 2004.

[36] Huang J., and Kaner R. B., in *Hand book of conducting polymers*, 3ed. Boca Raton, FL: CRC Press, 7-2, 2007.

[37] Vàzquez M., Bobaka J., Ivaska A., Potentiometric sensors for $Ag^+$ based on poly(3-octylthiophene) (POT), *J. Solid State Electrochem*. 9, 865-873, 2005.

[38] Mousavi Z., Bobacka J., Lewenstam A., Ivaska A., Response mechanism of potentiometric $Ag^+$ sensor based on poly(3,4-ethylenedioxythiophene) doped with silver hexabromocarborane. *J. Electroanal. Chem. 593,* 219-226, 2006.

[39] Zanganeh A. R., Amini M. K., A potentiometric and voltammetric sensor based on polypyrrole film with electrochemically induced recognition sites for detection of silver ion. *Electrochim. Acta*, *52,* 3822-3830, 2007.

[40] Ocypa M., Michalska A., Maksymiuk K., Accumulation of Cu(II) cations in poly(3,4-ethylenedioxythiophene) films doped by hexacyanoferrate anions and its application in $Cu^{2+}$ selective electrodes with PVC based membranes. *Electrochim. Acta*, *51,* 2298-2305, 2006.

[41] Rahman M. A., Won M. S., Shim Y. B., Characterization of an EDTA bonded conducting polymer modified electrode: its application for the simultaneous determination of heavy metal ions. *Anal. Chem. 75*, 1123-1129, 2003.

---

[42] Heitzmann M., Bucher C., Moutet J. C., Pereira E., Rivas B. L., Royal G., Saint-Aman E., Complexation of poly(pyrrole-EDTA like) film modified electrodes: Application to metal cations electroanalysis, *Electrochim. Acta*, 52, 3082-, 2007.

[43] Vàzquez M., Bobaka J., Luostarinen K., Lewenstam A., Ivaska A., Potentiometric sensors based on poly(3,4-ethylenedioxythiophene) (PEDOT) doped with sulfonated calix[4]arene and calix[4]resorcarenes , *J. Solid State Electrochem*. 9, 312-319, 2005.

[44] Berlin A., Zotti G., Zecchin S., Schiavon G., EQCM analysis of the alkali metal ion coordination properties of novel poly(thiophene)s 3,4-functionalized with crown-ether moieties, *Synth. Met*., 131, 149-161, 2002.

[45] Lange U., Roznyatovskaya N. V., Mirsky V. M., Conducting polymers in chemical sensors and arrays, *Anal. Chim. Acta.* 614, 1-26, 2008.

[46] Fabre B., Burlet S., Cespuglio R., Bidan G., Voltammetric detection of NO in the rat brain with an electronic conducting polymer and Nafion bilayer-coated carbon fibre electrode. *J. Electroanal. Chem.*426, 75-83, 1997.

[47] Xie D. Jiang Y., Pan W., Li D., Wu Z., Li Y., Fabrication and characterization of polyaniline-based gas sensor by ultra-thin film technology, *Sens . Actuators B*, 81, 158-164, 2002.

[48] Ram M. K., Yavuz O., Aldissi M., $NO_2$ gas sensing based on ordered ultrathin films of conducting polymer and its nanocomposites, *Synth. Met.* 151, 77-84, 2005.

[49] Prissanaron L., Ruangchuay L., Sirivat A., Schwank J., Electrical conductivity response of dodecylbenzene sulfonic acid-doped polypyrrole films to $SO_2$–$N_2$ mixtures, *Synth. Met*. 114, 65-72, 2000.

[50] Ram M. K., Yavuz O., Lahsangah V., and Aldissi M., CO gas sensing from ultrathin nano-composite conducting polymer film, *Sens. Actuators B*, 106, 750-757, 2005.

[51] Carquigny S., Sanchez J. B., Berger F., Lakard B., Lallemand F., Ammonia gas sensor based on electrosynthesized polypyrrole films, *Talanta*, 78(1),199-206, 2009.

[52] Ellis D. L., Zakin M. R., Bernstein L. S., Rubner M. F., Conductive Polymer Films as Ultrasensitive Chemical Sensors for Hydrazine and Monomethylhydrazine Vapor, *Anal. Chem*. 68, 817-822, 1996.

[53] Virji S., Huang J., Kaner R. B.,Weiller B. H., Polyaniline Nanofibre Gas Sensors : Examination of response Mechanisms, *Nano Lett*. 3, 491-496, 2004.

[54] Li B., Santhanam S., Schultz L., Jeffries-El M., Iovu M. C., Sauve G., Cooper J., Zhang R., Revelli J. C., Kusne A. G., Inkjet printed chemical sensor array based on polythiophene conductive polymers *Sens. Actuators B*, 123, 651-660, 2007.

[55] Vercelli B., Zecchin S., Comisso N., Zotti G., Berlin A., Dalcanale E., Groenendaal L. B., Solvoconductivity of Polyconjugated polymers: The roles of polymer oxidation degree and solvent electrical permittivity, *Chem. Mater.* 14, 4768-4774, 2002.

[56] Kumar S. S., Mathiayarasu J., Phani K. L. N., Yegnaraman V., Simultaneous determination of dopamine and ascorbic acid on poly(3,4-ethylenedioxythiophene) modified glassy carbon electrode, *J. Solid State Electrochem*, 10, 905-913, 2006.

[57] Lupu S., Lete C., Marin M., Totir N., Balaure P. C., Electrochemical sensors based on platinum electrodes modified with hybrid inorganic-organic coatings for determination of 4-nitrophenol and dopamine, *Electrochim. Acta*. 54, 1932-1938, 2009.

[58] Bouchta D., Izaoumen N., Zejli H., Kaoutit, M. E., Temsamani K. R., A novel electrochemical synthesis of poly-3-methylthiophene-γ- cyclodextrin film: Application for the analysis of chlorpromazine and some neurotransmitters, *Biosens. Bioelectron.* 20, 2228, 2005.

[59] Izaoumen N. Bouchta D. Zejli H. Kaoutit M. E., Stalcup A. M., Temsamani K. R., Electrosynthesis and analytical performances of functionalized poly(pyrrole/beta cyclodextrine) films, *Talanta*, 66, 111-117, 2005.

---

[60] Radi A. E., Eissa S., Electrochemistry of Cyclodextrin Inclusion Complexes of Pharmaceutical Compounds, *The Open Chemical and Biomedical Methods Journal,* 3, 74-85, 2010.

[61] Shoji E., Freund M. S., Potentiometric saccharide detection based on the p$K_a$ changes of Poly(anilineboronic acid), *J. Am. Chem. Soc*. 124, 12486-12493, 2002.

[62] Deore B. A., Braun M. D., Freund M. S., pH Dependent Equilibria of Poly(anilineboronic acid)-Saccharide Complexation in thin films, *Macromol. Chem. Phys.,* 207, 660-664, 2006.

[63] Taguchi T., Romagnoli J. A., Talaie A., Lee J. Y., Eisazadeh H., Adaehi K., Towards a Conducting Polymer-based Electronic Nose and Electronic Tongue, *Iranian Polymer Journal*, 9, 3, 2000.

[64] Deisingh A. K., Stone D. C., and Thompson M., Applications of electronic noses and tongues in food analysis, *Int. J. Food Sci. Technol.*, 39, 587-604, 2004.

[65] Shea K. J., Molecular Imprinting of Synthetic Network Polymers: The De Novo Synthesis of Macromolecular Binding and Catalytic Sites, *Trends in Polymer Science*, 2, 166-173, 1994.

[66] Wulff G., Molecular Imprinting in Cross-Linked Materials with the aid of Molecular Templates-A Way towards Artificial Antibodies, *Angew. Chem. Int. Ed. Engl.*, 34, 1812-1832, 1995.

[67] Mosbach K., Ramström O., The Emerging Technique of Molecular Imprinting and Its Future Impact on Biotechnology, *Bio Technol.,* 14, 163-170, 1996.

[68] Haupt K., Mosbach K., Molecularly Imprinted Polymers and Their Use in Biomimetic Sensors, Chem. Rev., 100, 2495-2504, 2000.

[69] Adhikari B., Majumdar S., Polymers in sensor applications, *Prog. Polym. Sci.* 29, 699-766, 2004.

[70] Di Palma L., Ferrantelli P., Petrucci E., Experimental study of the remediation of atrazine contaminated soils through soil extraction and subsequent peroxidation, *J. Hazard. Mater.* B99, 265-276, 2003.

[71] Zhou Q. X., Xiao J. P., Wang W. D., Determination of atrazine and simazine in environmental water samples using multiwalled carbon nanotubes as the adsorbents for preconcentration prior to high performance liquid chromatography with diode array detector, *Talanta,* 68, 1309-1315, 2006.

[72] Jiang T. B., Halsall H. B., Heineman W. R., Capillary enzyme-immunoassay with electrochemical detection for the determination of atrazine in water, *J. Agric. Food Chem.*, 43, 1098-1104, 1995.

[73] Wortberg M., Middendorf C., Katerkamp A., Flow-injection immunosensor for triazine herbicides using Eu(Iii) chelate label fluorescence detection. *Anal. Chim. Acta.,* 289, 177-186, 1994.

[74] Ionescu R. E., Gondran C., Bouffier L., Jaffrezic-Renault N., Martelet C., Cosnier S., Label-free impedemetric immunosensor for sensitive detection of atrazine. *Electrochim. Acta.,* 55, 6228-6232, 2010.

[75] Gam-Derouich S., Nguyen M. N., Madani A., Maouche N., Lang P., Perruchot C., Chehimi M. M., Aryl diazonium salt surface chemistry and ATRP for the preparation of molecular imprinted polymer grafts on gold substrates, *Surf. Interface Anal.* 42, 1050-1056, 2010.

[76] Hutchins R. S., Bacahs L. G., Nitrate-selective electrode developed by electrochemically mediated imprinting/doping of polypyrrole, *Anal. Chem.* 67, 1654-1660, 1995.

---

[77] Pesavento M., D'Agostino G., Biesuz R., Alberti G., Molecularly imprinted polymer-based sensors for amperometric determination of nonelectroactive substances. *Elactroanalysis*, 21, 604-611, 2009.

[78] Matsui J., Takayose M., Akamatsu K., Nawafune H., Tamaki K., Sugimoto N., Molecularly imprinted nanocomposites for highly sensitive SPR detection of a non-aqueous atrazine sample, *Analyst*, 134, 80-86, 2009.

[79] Wu Z., Tao C., Lin C., Shen D., Li G., Label-Free Colorimetric Detection of Trace Atrazine in Aqueous Solution by Using Molecularly Imprinted Photonic Polymers. *Chem. Eur. J.* 14, 36, 11358-11368, 2008.

[80] Prasad K., Prathish K. P., Mary Gladis J., Naidu G. R. K., Prasada Rao T., Molecularly imprinted polymer (Biomimetic) based potentiometric sensor for atrazine. *Sensors and actuators B*, 123, 65-70, 2007.

[81] D'Agostino G., Alberti G., Biesuz R., Pesavento M., Potentiometric sensor for atrazine based on molecular imprinted membrane. *Biosens. Bioelectron.* 22, 145-152, 2006.

[82] Shoji R., Takeuchi T., Kubo I., Atrazine sensor based on molecularly imprinted polymer-modified gold electrode. *Anal. Chem.* 75, 4882-4886, 2003.

[83] Luo C., Liu M., Mo Y., Qu J., Feng Y., Thickness-shear mode acoustic sensor for atrazine using molecularly imprinted polymer as recognition element. *Anal. Chim. Acta.* 428, 143-148, 2001.

[84] Sergeyeva T. A., Piletsky S. A., Brovko A. A., Slinchenko E. A., Sergeeva L. M., El'skaya A. V., Selective recognition of atrazine by molecularly imprinted polymer membranes. Development of conductometric sensor for herbicides detection. *Anal. Chim. Acta.* 392, 105-111, 1999.

[85] Malitesta C., Guascito M. R., Mazzotta E., Picca R. A., X-ray photoelectron spectroscopy characteriazation of electrosynthesized poly(3-thiophene acetic acid) and its application in molecularly imprinted polymers for atrazine. *Thin Solid Films*, 518, 3705-3709, 2010.

[86] Pardieu E., Cheap H., Vedrine C., Lazerges M., Lattach Y., Garnier F., Remita S., Pernelle C., Molecularly imprinted conducting polymers based on electrochemical sensor for detection of atrazine. *Anal. Chim. Acta.* 649, 236-245, 2009.

[87] See H. H., Sangai M. M., Wan Ibrahim W. A., Naim A. A., Determination of triazine herbicides using membrane-protected carbon nanotubes solid phase membrane tip extraction prior to micro-liquid chromatography. *J. Chromatogr. A.* 1217, 1767-1772, 2010.

[88] Djozan D., Ebrahimi B., Mahkam M., Farajzadeh M. A., Evaluation of a new method for chemical coating of aluminum wire with molecularly imprinted polymer layer. Application for the fabrication of triazines selective solid-phase microextraction fiber. *Anal. Chim. Acta.* 674, 40-48, 2010.

[89] Boonjob W., Yu Y., Miro M., Segundo M. A., Wang J., Cerdà V., Online hyphenation of multimodal microsolid phase extraction involving renewable molecularly imprinted and reversed-phase sorbents to liquid chromatography for automatic multiresidue assays. *Anal. Chem.* 82, 3052-3060, 2010.

[90] Zhang Y., Liu R., Li G., Micro wave heating in preparation of magnetic molecularly imprinted polymer beads for trace triazines analysis in complicated samples. *Anal. Chem.* 81, 967-976, 2009.

[91] Mhaka B., Cukrowska E., Tse Sum Bui B., Ramström O., Haupt K., Tutu H., Chimuka L., Selsctive extraction of trizine herbicides from food samples based on a combination of a liquid membrane and molecularly imprinted polymers. *J. Chromatogr. A.* 1216, 6796-6801, 2009.

---

[92] Le Noir M., Plieva F. M., Mattiasson B., Removal of endocrine-disrupting compounds from water using macroporous molecularly imprinted cryogels in a moving-bed reactor. *J. Sep. Sci.* 32, 1471-1479, 2009.

[93] Hu Y., Liu R., Zhang Y., Li G., Improvement of extraction capability of magnetic molecularly imprinted polymer beads in aqueous media via dual-phase solvent system. *Talanta*, 79, 576-582, 2009.

[94] Djozan D., Mahkam M., Ebrahimi B., Preparation and binding study of solid-phase microextraction fiber on the basis of ametryn imprinted polymer. Application to the selective extraction of persistent triazine herbicides in tap water, rice, maize and onion. *J. Chromatogr. A.* 1216, 2211-2219, 2009.

[95] Sergeyeva T. A., Piletska O. V., Piletsky S. A., Sergeeva L. M., Brovko O. O., El'skaya G. V., Data on the structure and recognition properties of the template-selective binding sites in semi-IPN-based molecularly imprinted polymer membranes. *Materials Science and Engineering: C*, 28, 8, 1472-1479, 2008.

[96] Koohpaei A. R., Shahtaheri S. J., Ganjali M. R., Forushani A. R., Golbabaei F., Molecular imprinted solid Phase extraction for determination of atrazine in environmental samples. Iran. J. Environ. Health. Sci. Eng. 5, 4, 283-296, 2008.

[97] Djozan D., Ebrahimi B., Preparation of new solid phase micro extraction fiber on the basis of atrazine-molecular imprinted polymer: Application for GC and GC/MS screening of triazine herbicides in water, rice and onion. *Anal. Chim. Acta.* 616, 2, 152-159, 2008.

[98] Amalric L., Mouvet C., Pichon V., Bristau S., Molecularly imprinted polymer applied to the determination of the residual mass of atrazine and metabolites within an agricultural catchment (Brevilles, France). *J. Chromatogr. A.* 1206, (2), 95-104, (2008).

[99] Matsui J., Kubo H., Takeuschi T., Design and preparation of molecularly imprinted atrazine-receptor polymers: Investigation of functional monomers and solvents. *Anal. Sci.* 14, 4, 699-702, 1998.

[100] Siemann M., Andersson L. I., Mosbach K., Selective recognition of the herbicide atrazine by noncovalent molecumarly imprinted polymers. *J. Agric. Food Chem.* 44, 141-145, 1996.

[101] Dauwe C., Sellegren B., Influence of template basicity and hydrophobicity on the molecular recognition properties of molecularly imprinted polymers. *J. Chromatogr. A.* 753, 191-200, 1996.

[102] Matsui J., Miyoshi Y., Doblhoff-Dier O., Takeuchi T., A molecularly imprinted synthetic polymer receptor selective for atrazine. *Anal. Chem.* 67, 4404-4408, 1995.

[103] Piletsky S. A., Piletskaya E. V., Elgersma A. V., Yano K., Karube I., Parhometz Y. P., El'skaya A. V., Atrazine sensing by molecularly imprinted membranes, Biosens. Bioelectron. 10, 959-964, 1995.

[104] Deore B., Chen Z., Nagaoka T., Overoxidized Polypyrrole with dopant complementary cavities as a new molecularly imprinted polymer matrix, *Anal. Sci.* 15, 827-828, 1999.

[105] Okuno H., Kitano T., Yakabe H., Kishimoto M., Deore B., Siigi H., Nagaoka T., Characterization of overoxidized Polypyrrole colloids imprinted with L-Lactate and their application to enantioseparation of aminoacids, *Anal. Chem.* 74, 4184-4190, 2002.

[106] Kong Y., Zhao W., Yao S., Xu J., Wang W., Chen Z., Molecularly imprinted Polypyrrole prepared by electrodeposition for the selective recognition of Tryptophan enentiomers, *J. App. Polym. Sci.* 115, 1952-1957, 2010.

[107] Choong C. L., Milne W. I., Dynamic modulation of detection window in conducting polymer based biosensor, *Biosen. Bioelectron.* 25, 10, 2384-2388, 2010.

---

[108] Öpik A., Menaker A., Reut J., Syritski V., Molecularly imprinted polymers: a new approach to the preparation of functional materials. Proceedings of the Estonian academy of sciences, 58, 1, 3-11, 2009.

[109] Özcan L., Sahin Y., Determination of paracetamol based on electropolymerized-molecularly imprinted polypyrrole modified pencil graphite electrode, *Sens. Actuators B: Chem.*, 127, 362-369, 2007.

[110] Pietrzyk A., Suriyanarayanan S., Kutner W., Chitta R., D'Souza F., Selective histamine piezoelectric chemosensor using a recognition film of the molecularly imprinted polymer of bis(bithiophene) derivatives. *Anal. Chem.* 81, 2633-2643, 2009.

[111] Thoelen R., Vansweevelt R., Duchateau J., Horemans F., D'Haen J., Lutsen L., Vanderzande D., Ameloot M., vandeVen M., Cleij T. J., Wagner P., A MIP-based impedimetric sensor for the detection of low-MW molecules, *Biosen. Bioelectron.* 23, 913-918, 2008.

[112] Menaker A., Syritski V., Reut J., Öpik A., Horvàth V., Gyurcsanyi R. E., Electrosynthesized surface-imprinted conducting polymer microrods for selective protein recognition, *Adv. Mater.* 21, 2271-2275, 2009.

[113] Sreenivasan K., Synthesis and evaluation of multiply template molecularly imprinted polyaniline, *J. Mater. Sci.* 42, 7575-7578, 2007.

[114] Cheng Z., Wang E., Yang X., Capacitive detection of glucose using molecularly imprinted polymers, *Biosen. Bioelectron.* 16, 179-185, 2001.

[115] Malitesta C., Losito M., Zambonin P. G., Molecularly imprinted electrosynthesized polymers: New materials for Biomimetic sensors, *Anal. Chem.* 71, 1366-1370, 1999.

[116] Panasyuk T. L., Mirsky V. M., Piletsky S. A., Wolfbeis O., Electropolymerized molecularly imprinted polymers as receptor layers in capacitive chemical sensors, *Anal. Chem.* 71, 4609-4613, 1999.

[117] Pardieu, E. *Conception et développement d'un capteur électrochimique à base de polymères conducteurs à mémoire de forme pour la détection de petites molécules : application au cas de l'atrazine*. Sciences et Techniques Analytiques, Conservatoire National des Arts et Métiers CNAM, 2010.

[118] Pernelle, C. Pardieu, E. Garnier, F. Remita, S. *Détecteur électrochimique d'une petite molécule cible à base polymères conjugués à effet mémoire et procédé de détection utilisant un tel détecteur* » dépôt de brevet d'invention, référence : 9A-4963 cas 5, 2009.

# Chapter 2

## Experimental techniques and theoretical methods

A presentation of the different techniques and experimental protocols as well as calculation methods used in the present work will be given in this chapter. Chemicals and electrochemical measurements with spectroscopic and microscopic characterization techniques are demonstrated with the preparation procedures of electrodes and solutions. Then, gravimetric transduction and coupled electrochemical/gravimetrical transduction will be described with a brief presentation of the different electronic configurations and used procedures.

## 2.1 Chemicals

The 3,4-Ethylenedioxythiophene, EDOT, used as linker and/or as functional monomer (FM) purchased from AKSCI, was distilled under reduced pressure before use. 3-Thiopheneacetic acid, TAA, was provided from Acros. 3-Thiophenemalonic acid, TMA, 3-Thiophenemethanol, TMeOH, Thiophene, Th, used as functional monomers, and Lithium perchlorate, $LiClO_4$, utilized as supporting electrolyte, were purchased from Aldrich and used without further purification (figure 2.1). Pesticides used as target molecules (figure 2.1): atrazine (2-chloro-4-(ethylamino)-6-(isopropylamino)-1,3,5-triazine), ATZ, terbutylazine (2-chloro-4-(ethylamino)-6-(tertiobutylamino)-1,3,5-triazine), TBZ, and diuron (3-(3,4-dichlorophenyl)-1,1-dimethyl-urea), DRN, were obtained from Sigma. Acetonitrile, ACN, was obtained from Acros Chemicals and was used as solvent. ACN was distilled prior to use and purged with argon for 30 min. Double-distilled deionized water was used for the aqueous medium experiments and was purged with argon for 30 min prior to use. Methanol (MeOH) and acetic acid ($CH_3COOH$) used as extraction solvents were purchased from VWR and Acros respectively.

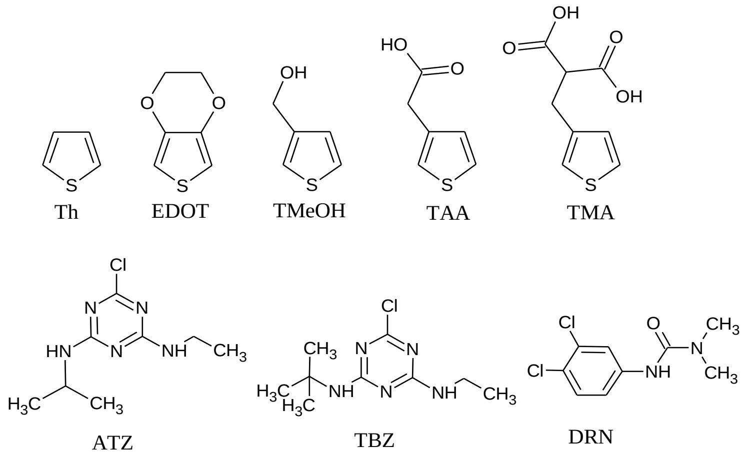

**Figure 2.1.** Structure of thiophene Th, and substituted thiophene : EDOT, TMeOH, TAA and TMA, used as functional monomers. Pesticides used as templates and target molecules: ATZ, TBZ, and DRN.

In order to study the solubility of the different components (monomers and/or template) in ACN or in $H_2O$, UV-Vis absorption spectra were recorded with a Shimadzu, model UV-160A spectrophotometer. The spectra were recorded between 200-800 nm at a scan rate of 30 nm $s^{-1}$ in a 1 cm quartz cell.

## 2.2 Electrodes and electrochemical apparatus

Different types of working electrodes were used: gold and platinum electrodes with a surface area of 3.14 $mm^2$ were purchased from BioAnalytical System (BAS). Homemade gold substrates with a surface area of (7 mm × 10 mm) were obtained by evaporating gold under secondary vacuum over a Chromium layer deposited on glass slide. Highly ordered pyrolytic graphite, HOPG, substrates (5 mm × 5 mm × 2 mm) were purchased from Goodfellow Company.

Gold and platinum (BAS) electrodes with a surface area of 3.14 $mm^2$ were rinsed with distilled water and ethanol, then polished and ultrasonically cleaned (in distilled water for 5 min). These substrates were finally rinsed with the used solvent, before being used as working electrodes. Gold substrates with a surface area of 70 $mm^2$ were cleaned using "piranha" solution (0.4:0.6) v/v of $H_2O_2$ and $H_2SO_4$ respectively. In order to design clean and plane surfaces, the HOPG electrodes were regularly cleaved prior to use.

The electrochemical set involved a three-electrode cell, where one of the above mentioned electrodes acted as working electrodes, and a stainless steel sheet as counter electrode. All potentials were controlled *vs.* $Ag/AgNO_3$ reference electrode for ACN (+0.170 *vs.* Ag/AgCl)[1], which was first calibrated with the ferricinum/ferrocene couple using gold working electrode at 100 mV $s^{-1}$ in 0.1M $LiClO_4$ in ACN (figure 2.2). All measurements were performed at room temperature. Prior to all experiments, the solutions were purged with argon, and an argon atmosphere was maintained over the solutions during the measurements.

Cyclic voltammetry, square wave voltammetry and amperometric measurements were performed on an EG&G model 263A potentiostat/galvanostat (Princeton Applied Research).

Electrochemical procedures were carried out using conventional three electrode cells, except for HOPG where a homemade cell was designed and developed thanks to the help of Denis Limagne in Institut des Nanosciences de Paris (figure 2.3).

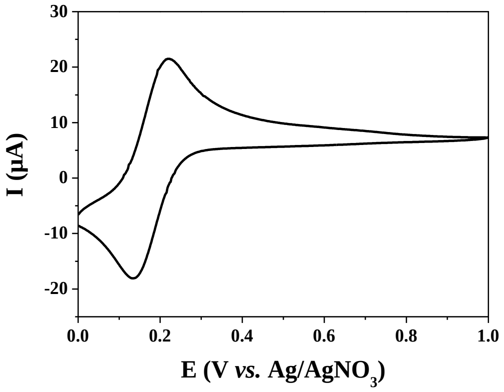

**Figure 2.2.** Voltammogram of calibration of Ag/AgNO$_3$ reference electrode at 100 mV s$^{-1}$ in 0.1 M LiClO$_4$/ACN on Au electrode (3.14 mm²).

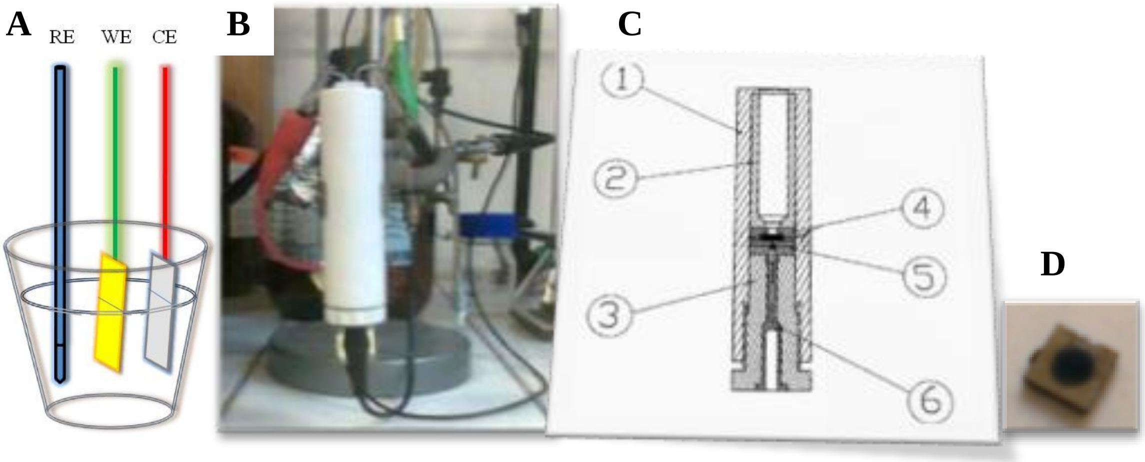

**Figure 2.3. (A)** Schematic representation of conventional three electrode cell: working electrode (WE) counter electrode (CE) and reference electrode (RE); **(B)** Picture and **(C)** Scheme of the electrochemical cell used for electropolymerization over the HOPG surfaces (5mm × 5mm × 2mm). **(1)** Teflon cover; **(2)** Teflon container of the electrolyte and electrodes; **(3)** Teflon column to maintain the surface and the electrical connection; **(4)** Teflon gaskets used to ensure the isolation of the electrical connection and to control the active surface; **(5)** Stainless steel surface to hold the working surface and ensure the electrical connection; **(6)** Current entry. **(D)** Picture representing a deposited PEDOT film (dark zone in the center of the surface) over HOPG surface.

## 2.3 Electrosynthesis and electrochemical characterization

In this work, molecularly imprinted conducting polymers or copolymers, MICP-based sensitive layers, were electrochemically obtained by polymerization of EDOT monomers in the presence of ATZ target molecules (functional monomer, FM = EDOT) or by copolymerization of EDOT with another kind of functional monomers (FM = TAA, TMA, TMeOH or Th) associated by non covalent interactions with ATZ target molecules (figure 2.4A, electrosynthesis). For clarity, for all functional monomers (FM) used, the obtained Poly(EDOT/ATZ) polymers and Poly(EDOT-co-FM/ATZ) copolymers are noted FM-MICP (or MICP).

For FM-MICP preparation, FM functional monomers (EDOT, TAA, TMA, TMeOH or Th) at a concentration of $30 \times 10^{-3}$ mol $L^{-1}$ (except contrary mentioned) were dissolved in solvent (ACN or $H_2O$), in the presence of $LiClO_4$ (0.1 mol $L^{-1}$, as supporting electrolyte), together with ATZ molecules at a concentration of $15 \times 10^{-3}$ mol $L^{-1}$ (except contrary mentioned). A sufficient lap of time of 10 minutes was used in order to favor the association between FM and ATZ, through non covalent interactions, in FM/ATZ pre-polymerization complexes. Then, EDOT, at a concentration of $7.5 \times 10^{-3}$ mol $L^{-1}$ (except contrary mentioned), was added as a linker, before electropolymerization, to each FM/ATZ solution.

Another type of films, non-imprinted conducting polymers or copolymers, NICP, was also electrochemically prepared, but in the absence of target molecules in the pre-polymerization media (figure 2.4B, electrosynthesis). NICP polymers were synthesized by polymerization of EDOT monomers (FM = EDOT), while NICP copolymers were obtained from the copolymerization of EDOT monomers with another kind of functional monomers (FM = TAA, TMA, TMeOH or Th). For clarity, in the case of all functional monomers (FM) used, the obtained poly(EDOT) polymers and poly(EDOT-co-FM) copolymers are noted FM-NICP (or NICP).

For FM-NICP preparation, FM functional monomers (EDOT, TAA, TMA, TMeOH or Th) at a concentration of $30 \times 10^{-3}$ mol $L^{-1}$ (except contrary mentioned) were dissolved in solvent (ACN or $H_2O$), in the presence of $LiClO_4$ (0.1 mol $L^{-1}$) but in the absence of ATZ molecules. Then, EDOT, at a concentration of $7.5 \times 10^{-3}$ mol $L^{-1}$ (except contrary mentioned) was added as a linker to each FM solution, before electropolymerization.

Note that the above mentioned concentrations and their effect on the corresponding polymers and copolymers were already studied and optimized by spectroscopic and electrochemical investigations using TAA as functional monomer in the previous works of Elodie Pardieu[2,3].

Electropolymerizations were carried out in a conventional three-electrode electrochemical cell. The electrodes were prepared (as mentioned in *section 2.2*) and immersed in the pre-polymerization solutions, before being used for the electropolymerization.

In order to study the electrochemical behaviors of FM functional monomers as well as those of synthesized FM-MICP and FM-NICP films, cyclic voltammograms were recorded at different scan rates. All cyclic voltammograms were obtained by subtracting the background current corresponding to the electrolyte. Several preliminary experiments were also performed in order to determine the oxidation potentials of the different FM functional monomers.

Electrosynthesis of FM-MICP and FM-NICP films at the surface of the electrodes, under potentiostatic conditions, were realized using a 2-steps chronoamperometry technique in the electrochemical cell. In the first step, the potential was switched from 0.0 to 0.8 V for a period of ca. 10 s. Polymerization was achieved by a second step at a constant potential (see *chapter 3*). Specific times were used during this second chronoamperometric step in order to adjust the electropolymerization charge.

## 2.4 Electrochemical measurements and target detection

Contrarily to non-imprinted conducting FM-NICP films, molecularly imprinted FM-MICP layers were electrosynthesized in the presence of atrazine (figure 2.4A, electrosynthesis). In order to remove the target molecules from FM-MICP matrixes, by destroying the non covalent intermolecular interactions which involve ATZ and polymerized functional monomers, a methanol/acetic acid solution (0.7:0.3 v/v) was used to wash the polymer-coated electrodes for 10 min[4] with a continuous mechanical agitation (180 rpm) at room temperature. This washing step leads to the desired creation of molecular imprinted cavities within the copolymer matrixes of FM-MICP (figure 2.4A, extraction). These cavities keep the memory of the interactions between FM functional monomers and ATZ molecules[4]. Indeed, the spatial distribution of the polymerized functional monomers into the polymer matrixes allows the precise matching of additional ATZ molecules. Thus the so-prepared washed FM-MICP modified electrodes can act as sensors to quantify the presence of new additional ATZ pesticides thanks to the establishment of new intermolecular FM/ATZ interactions between the probe-functionalized monomer units and the target molecules (figure 2.4A, ATZ detection).

In order to check the ability of FM-MICP to interact with newly added pesticide targets (figure 2.4A, ATZ detection), the modified electrodes were immersed for 10 min in ACN (or $H_2O$) solutions containing ATZ at a given concentration in the presence of $LiClO_4$ 0.1 mol $L^{-1}$. A continuous mechanical agitation was maintained at a stable velocity (180 rpm) at room temperature. The presence of added pesticide targets and consequently the specific recognition process was then analyzed using an electrochemical (*chapters 3 and 4*), a gravimetrical, or a coupled electrochemical/gravimetrical methods (*chapter 5*).

Contrarily to FM-MICP, FM-NICP layers are synthesized in the absence of ATZ molecules. As a consequence, no specific cavities are presented in the structure of FM-NICP layers. In order to check the ability of FM-NICP to interact with newly added ATZ target molecules (figure 2.4B ATZ detection). The modified electrodes were immersed for 10 min in ACN (Or $H_2O$) solution containing ATZ. The presence of added pesticides and consequently the non-specific recognition process was analyzed using an electrochemical method (*chapter3 and 4*).

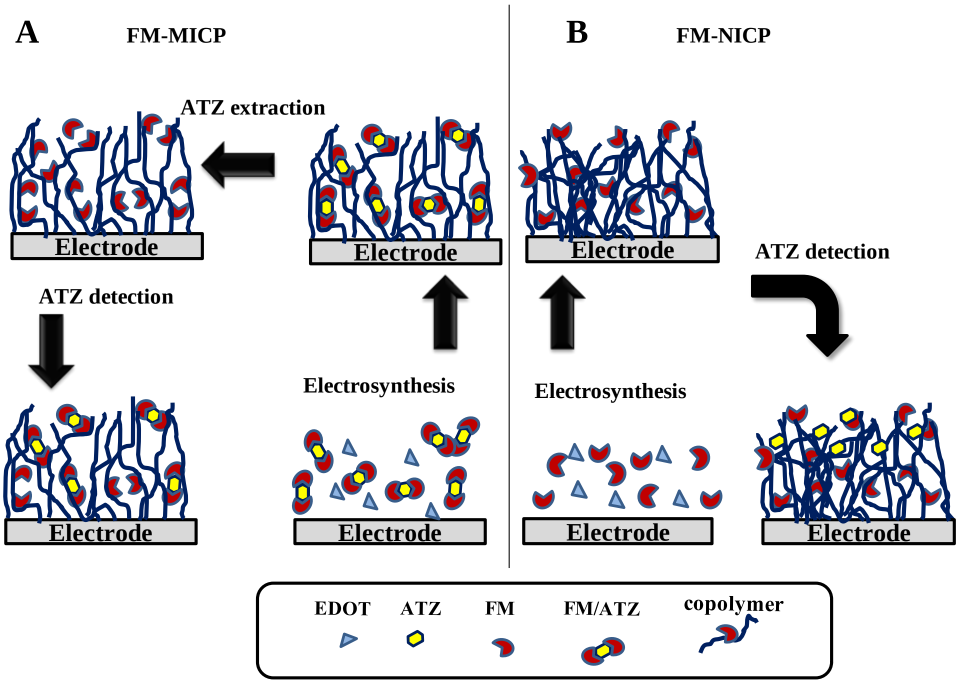

**Figure 2.4**. Electrosynthesis and use for ATZ detection of **(A)** FM-MICP. **(B)** FM-NICP. The FM functional monomers are TMA, TAA, TMeOH, EDOT or Th.

In this work, two electrochemical techniques were used to evaluate the sensing process: cyclic voltammetry (CV) and square wave voltammetry (SWV).

### 2.4.1 Cyclic Voltammetry

The experiment is a linear scan of the potential as a function of time. The direction of the scan is “switched” at the switching potential $E_f$. This potential sweep reversal technique is considered as a symmetrical triangular wave (figure 2.5A). Thus, the potential is given at any time $t$ by the equation 2.1:

$E = E_i - vt$ Eq 2.1

where

$E$ : the potential at $t$ (V)

$E_i$ : the initial potential (V)

$v$ : the scan rate (V $s^{-1}$)

If $i$ is the current, thus, $i$-$E$ curves are obtained by scanning the potential of the working electrode as a function of time. Usually the user controls the potential window ($E_i$ and $E_f$) beside the scan rate, $v$.

In the case of a reversible system, composed of an electroactive species in solution, the electrochemical behavior of the redox couple is translated in a reversible voltammogram (figure 2.5B). The theoretical expression of the peak current $I_p$ is given by the resolution of the Fick second law of diffusion as a boundary condition at interface of Nernst equation:

$I_p = (2.69 \times 10^5)n^{3/2}AD^{1/2}C_0v^{1/2}$ Eq 2.2

where

$n$: the number of electrons involved in the redox process

$A$: the active surface of the electrode ($cm^2$)

$D$: the diffusion coefficient of the electroactive species ($cm^2$ $s^{-1}$)

$C_0$: the concentration of the electroactive species in solution (mol $L^{-1}$)

$v$: the scan rate (V $s^{-1}$)

In the case of an irreversible system, where the oxidized (or the reduced) species is unstable towards another species present in the solution (figure 2.5C), the theoretical expression of the current is given by the resolution of the Fick second law of diffusion with the Buttler-Volmer law as a boundary condition at the interface:

$I_p = (2.99 \times 10^5)n(\alpha p)^{1/2}AD^{1/2}C_0v^{1/2}$ Eq 2.3

where

p: the number of the transferred electrons per mol of the substrate ($mol^{-1}$)

α: the anodic transfer coefficient

The scan rate is powered to (½) that corresponds to power of time of (-½) which is characteristic of diffusion controlled kinetics. We can conclude that $t^{-1/2}$ is available for both above mentioned cases.

In the case of a reversible system of an adsorbed species over the working electrode (figure 2.5D), the evolution of the superficial concentration can be predicted by the Nernst equation

$I_p = n^2F^2vA\Gamma/4RT = (9.39 \times 10^5)n^2vA\Gamma$ Eq 2.4

where

$\Gamma$ : the superficial concentration of an electroactive species adsorbed on the surface of an electrode ($mol\ cm^{-2}$).

In the equation 2.4 the implied power of the scan rate is 1, which means that the electroactive species is adsorbed at the electrode surface. Thus, in the light of this discussion, we can distinguish the nature of the redox systems: $I_p = f(v^{1/2})$ if the electroactive species is dissolved in the solution and $I_p = f(v)$ if the electroactive species is adsorbed at the electrode surface.

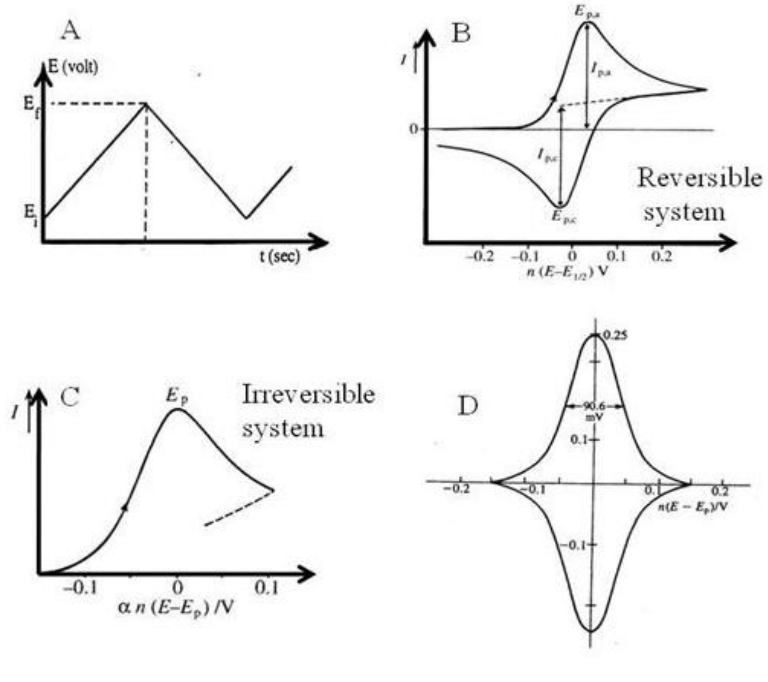

**Figure 2.5.** Cyclic voltammograms, **(A)** Potential linear sweep in function of time; **(B)** Reversible system composed of dissolved electroactive species; **(C)** Irreversible system; **(D)** Reversible system composed of adsorbed electroactive species over the electrode surface. Adapted from ref. 5.

### 2.4.2 Square Wave Voltammetry

Figure 2.6 helps to define the principal parameters of the square wave voltammetry SWV. The square wave is characterized by a pulse height, $\Delta E_p$, measured with respect to the corresponding tread of the staircase, and a pulse width $t_p$. Alternatively, the pulse width can be expressed in terms of the square wave frequency, $f = 1/2t_p$. The staircase shifts by $\Delta E_s$ at the beginning of each cycle; thus the scan rate $v = \Delta E_s/2t_p = f\ \Delta E_s$. The scan begins at an initial potential, $E_i$, which can be applied for an arbitrary time to initialize the system as desired.

Current samples are taken twice per cycle, at the end of each pulse. The forward current sample, $i_f$, arises from the first pulse per cycle, which is in direction of the staircase scan. The reverse current sample, $i_r$, is taken at the end of the second pulse, which is in the opposite direction. A difference current $\Delta i$ is calculated as $i_f - i_r$. There is diagnostic value in the forward and reverse currents; hence they are preserved separately. Consequently, the result of a single SWV run is three voltammograms showing forward, reverse, and difference currents *vs.* the potential on the corresponding staircase tread.

In general, $t_p$ defines the experimental time scale; $\Delta E_s$ fixes the spacing of data points along the potential axis, and these parameters together determine the time required for a full scan. In normal practice, $\Delta E_s$ is significantly less than $\Delta E_p$, which defines the span of interrogation in each cycle and therefore determines the resolution of voltammetric features along the potential axis. Only $t_p$ is varied over a wide range, typically 1-500 ms ($f$ = 1-500 Hz). All the above discussion was adapted from ref. 5.

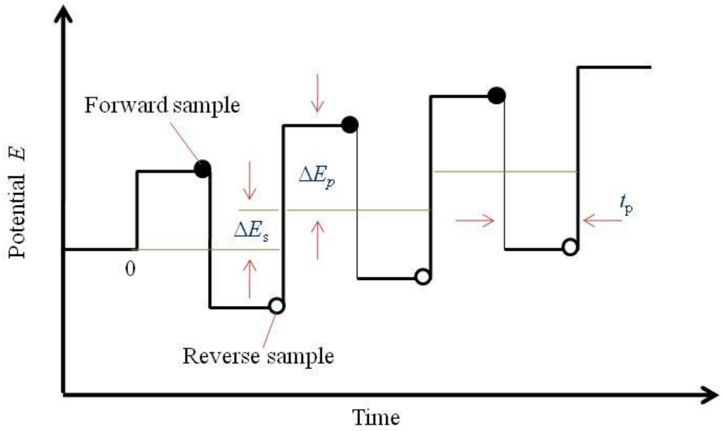

**Figure 2.6.** Waveform and measurement scheme for square wave voltammetry. In each cycle, a forward current sample is taken at the time indicated by the solid dot, and a reverse current sample is taken at the time marked by the white dot.

## 2.5 Gravimetric measurements and target detection

The gravimetric sensor consists of a delay line fabricated on a 36°rot lithium tantalate ($LiTaO_3$) piezoelectric substrate, which favors the propagation of two types of transversal horizontal waves: leaky surface acoustic wave, LSAW, and surface skimming bulk waves, SSBW, (figure 2.7). This substrate represents a good compromise between the relative weak coefficient of temperature (-32 ppm/°C for the LSAW, and -45 ppm/°C for SSBW), and high electromechanic coupling coefficient ($K^2 = 4.7\%$) with high dielectric constant ($\varepsilon_r = 47$)[6].

**Figure 2.7.** Transversal horizontal waves propagated on $LiTaO_3$ piezoelectric substrate: leaky surface acoustic wave and surface skimming bulk waves.

The used gravimetric sensor consists of a delay line shear horizontal surface acoustic wave (SH-SAW) fabricated over the tantalate piezoelectric substrate, with an interdigitated transducers (IDTs) made of chromium/gold (20 nm Cr/80 nm Au), structured with a periodicity of $\lambda = 40$ µm, corresponding to an operating frequency of 104 MHz (figure 2.8). The length of the acoustic track (the central zone) was L = 8 mm and the distance from center to center $L_{CC} = 9.2$ mm. The sensing area was metalized (20/80 nm Cr/Au) to favor leaky SAW propagation[7], and thus the acoustic energy confinements close to the surface substrate, making the sensor highly sensitive to any perturbation occurring in the propagating medium. A Teflon fluidic cell was placed on the region between the IDTs, to contain solutions, and to avoid any short circuit.

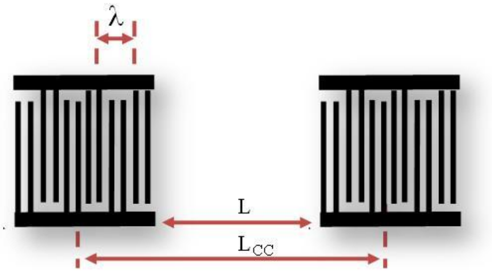

**Figure 2.8.** Representation of a delay line with the dimensional parameters; λ: periodicity of IDTs; L: length of the central zone; LCC: distance center to center.

The observation of fast dynamics reactions requires the use of a fast interrogation system. Standard techniques employing continuous wave systems, such as the network analyzer, measure the single transit signal, which may contains unwanted contributions from edge reflections and triple transit echoes. We have thus developed a home-made time-of-flight resolved information system, which gives rapid amplitude and phase informations. Moreover, phase detection can be performed even if the insertion loss is very high[8].

A pulse excitation technique was used to monitor both amplitude (A) and phase (φ) changes versus time. It enables time-of-flight resolved information to be obtained and spurious reflections to be identified[9]. Homemade software was developed for monitoring gravimetric experiments.

The interdigital pins realized by optic-photolithography, consisted of 30 pairs of double digits with an interdigital space of 5µm with a metallization rate of 50%. The physical parameters that influence the response of the sensor are based on the disturbances made over the sensitive zone, which will drive to variations in the output signal S. Beside the mass effect (m), other parameters can influence the output signal: viscosity (η), conductivity (σ), ionic strength (I), temperature (T) and pressure (P). Equation 2.5 represents the dependence of the output signal S of the sensor with these different parameters:

$$\Delta \boldsymbol{S},\boldsymbol{A} = \frac{\partial \mathrm{S,A}}{\partial \mathrm{m}}\,\Delta \boldsymbol{m} + \frac{\partial \mathrm{S,A}}{\partial \sigma}\,\Delta \boldsymbol{\sigma} + \frac{\partial \mathrm{S,A}}{\partial I}\,\Delta \boldsymbol{I} + \frac{\partial \mathrm{S,A}}{\partial \eta}\,\boldsymbol{\Delta\eta} + \frac{\partial \mathrm{S,A}}{\partial T}\,\Delta \boldsymbol{T} + \frac{\partial \mathrm{S,A}}{\partial P}\,\Delta \boldsymbol{P} \qquad \text{Eq. 2.5}$$

In order to overcome the different parameters and limit the response of the sensor at the influence of mass variations, a metallization of the central zone was one of the proposed solutions[10]. The metallization of the central zone of the sensor allows the elimination of the effects of ionic strength (I) and conductivity (σ)[11]. Also the metallization of the sensitive zone offers the advantage to ensure the fixing of the chemical and biological molecules, generally substituted thiols, and to favor the propagation of one type of surface wave: the LSAW[12]. The metallization also allows the realization of dual delay line, therefore differential measurements that cancel viscosity, temperature and pressure effects. Finally, the central zone of the sensor is related to the mass by a contact electrode which allows minimizing the direct coupling of the different systems of interdigitated pins. The metallization of the sensing area with a gold layer was displayed on a surface area of 22 mm$^2$ (figure 2.9).

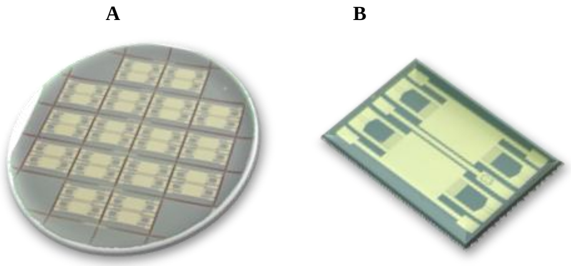

**Figure 2.9. (A)** Metalized delay line deposited over lithium tantalate wafer; **(B)** single delay line cut and prepared to be used.

In the next paragraphs a brief presentation will be given on the electronic configurations used for the characterization and for the test of the surface acoustic wave sensor SAW.

### 2.5.1 Impulsion configuration

The assembly of impulsion measurements is demonstrated in figure 2.10. The principle of the configuration of pulse excitation technique is to generate rectangular pulses with holders, and to measure the modulus (amplitude) and the phase of the transmitted pulses. Pulse generator (Agilent 33220A) and continuous RF generator (Rhode and Schwarz) related to an RF amplifier with an activation function “enabled” to generate pulses. The generated frequency is about 104 MHz, corresponding to the characteristic frequency of the SAW sensor. The pulse was varied between 1.5 and 2µs, which allows measuring a stable signal after the transients. The repetition frequency is about 10 kHz. The phase comparator gives beside the phase an indication about the amplitude values of the transmitted pulses. The integrator boxcar (SRS 250) allows the integration and the averaging of the signal corresponding to the desired delay period. After the boxcar, the signal is transmitted via a digital/analogical converter (DAC) into a computer.

The impulsion assembly offers the possibility to make a filter of the transmitted waves. Homemade software was developed for monitoring the received signal *vs.* time. As for phase-detection, the magnitude output of the AD8302 device is directed to a signal independent boxcar to record the signal amplitude variations.

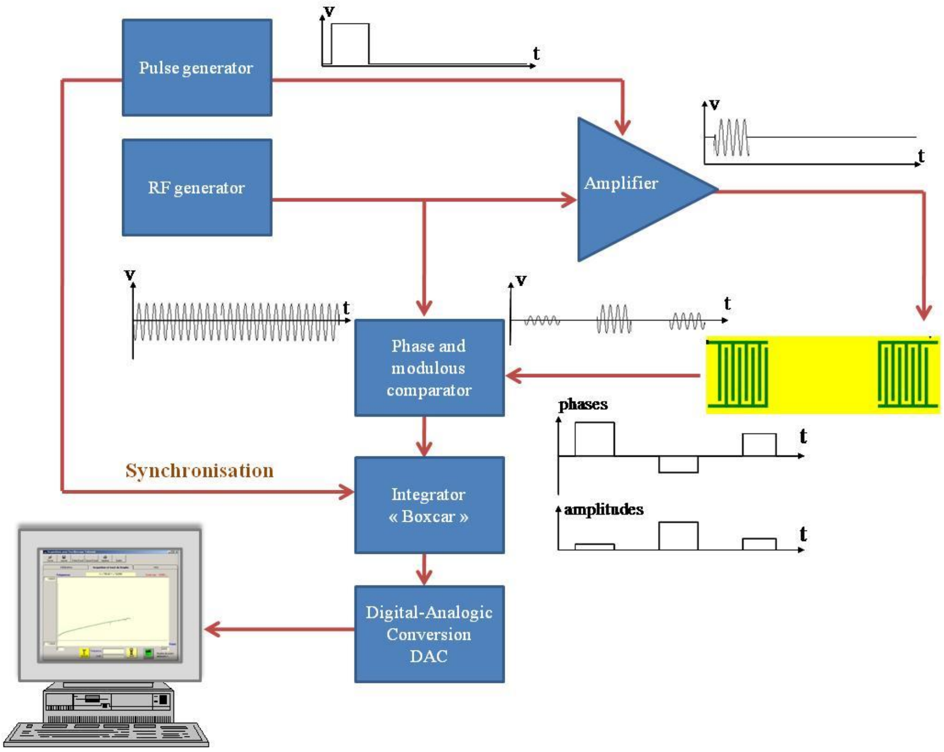

**Figure 2.10.** Schematic representation of impulsion measurement configuration.

### 2.5.2 Network analyzer

Network analysis is the process by which measurements of the electrical performance of the components and circuits used in complex systems take place. When these systems are conveying signals with information content, we are most concerned with getting the signal from one point to another with maximum efficiency and minimum distortion.

Network analyzer terminology generally denotes measurements of the incident wave with the reference channel. The reflected wave is measured with the B channel (figure 2.11A). With the amplitude and phase information in these waves, it is possible to quantify the reflection and transmission characteristics. These latter can be expressed as vector (magnitude and phase), scalar (magnitude only), or phase only quantities.

The network analyzer is the principal tool of high frequency measurements. It allows measuring the scattering parameters of the transmitted and the reflected waves of the dispositive under test, thus describing the electric behavior of the linear network as a function of the input signals. The used analyzer, HP8711C, allows the determination of the entry reflection coefficient ($S_{11}$), the input-output transmission coefficient ($S_{21}$) and the following at a constant frequency, of the modulus and the phase variations of the parameter $S_{21}$ after the different procedures made over the sensitive zone of the sensor. Figure 2.11B represents the frequency of a SAW dispositive functional at 104 MHz.

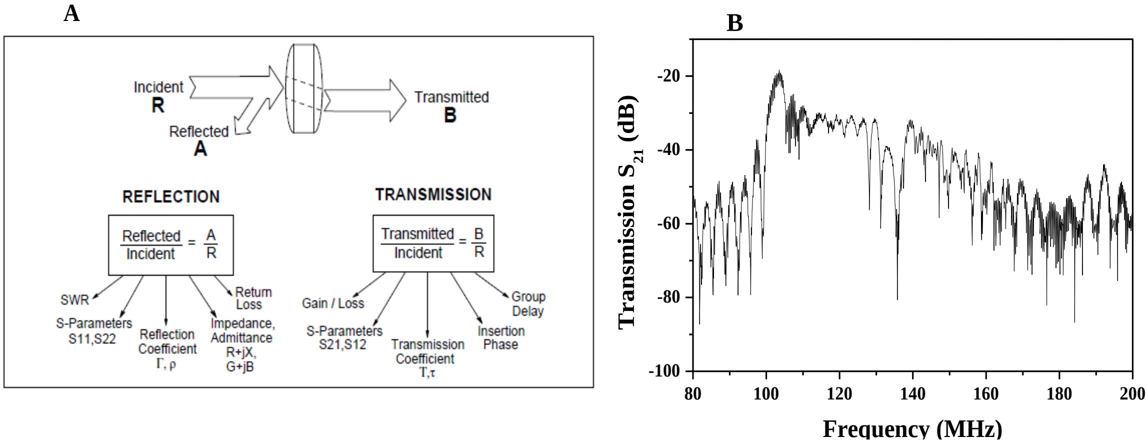

**Figure 2.11. (A)** Common terms for high-frequency drive characterization, **(B)** Frequency response $S_{21}$ of a SAW functional at 104 MHz.

The above mentioned techniques were developed and designed using a SAW dispositive presented in the next paragraph.

### 2.5.3 SAW device

The used dispositive is dedicated for the detection in liquid media (figure 2.12). This dispositive is composed of:

*i)* A metallic platform, where the delay line is placed.

*ii)* A printed circuit board (PCB) equipped with pins to ensure the electrical contact.

*iii)* Karlez gaskets with 1mm thickness, and teflon gasket of 5mm thickness to ensure the sealing and to maintain the tubes of the fluidic assembly.

*iv)* A metallic lid to enhance the sealing and fix the assembly.

The dispositive is disposed over a PID element allowing to control the temperature. The whole configuration is placed in a metallic box to form a Faraday cage (figure 2.12). The circulation of the solutions is ensured by peristaltic pump (Gilson Minipuls 3) with a low flow rate of 0.19 mL $min^{-1}$.

The electronic configurations and the different piloting programs were developed in the “Service de Physique” in LC3B laboratory at Conservatoire National des Arts et Métiers in Paris. More detailed description of the mentioned techniques and configurations can be found in ref. 10.

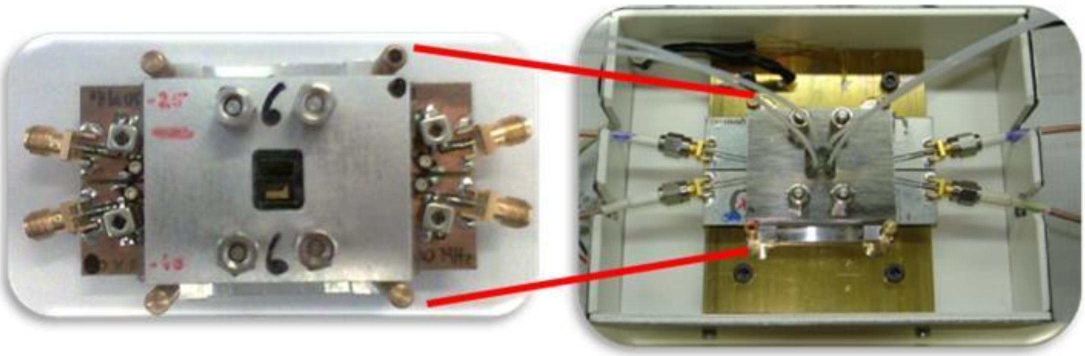

**Figure 2.12.** SAW dispositive placed over PID in the faraday cage.

In the next paragraph a brief description of the original electrochemical/gravimetric coupled technique, ESAW, developed in LC3B in the cadre of this thesis will be presented.

## 2.6 Electrochemical/gravimetric coupled transduction: ESAW

The configuration of ESAW (figure 2.13) consists of electrochemical cell related to the acoustic wave surface where the working electrode is SAW sensing surface. The sensing surface is related to the mass of the sensor. Working frequency was 104 MHz, hence it is necessary to relay this surface to the mass for isolation purposes.

The proposed configuration of the potentiostat uses a series of capacitors and resistances, positioned in a special distribution in order to isolate the SAW surface with deriving the high frequency towards the mass. The potentiostat was realized using BNC connector[13] taking the next remarks in consideration:

*i)* The number of measurements per second

*ii)* The acquisition device National Instrument 6014 is a stable precise and fast acquisition device with a good confidence in the generated and measured potential values.

*iii)* The National Instrument 6014 related to a BNC-2120 box was used to generate and to measure the potentials.

*iv)* The power is supplied to the system with a programmed potential generated by the BNC-2120 box.

*v)* The system consists of series of known resistances related to the electrochemical cell.

*vi)* Measurements were carried out to determine the potential of the reference electrode and all the electrodes during experiments.

*vii)* The generated potential and the measured one of the cell (versus the reference) were used to calculate the current passed in the resistance series which is equal to the current passed in the electrochemical cell.

*viii)* The position of the different electrodes is a primordial matter

The realized ESAW sensor thus gives us access to complementary gravimetrical and electrochemical measurements and to parameters which characterize the kinetics of recognition processes. All electronic configurations and software were developed in our laboratory for monitoring both electrochemical and gravimetric experiments simultaneously. Grounded gold SAW sensing area ($S \approx 22\ mm^2$) was used as working electrode; while coiled Pt and Ag/$AgNO_3$ wires were used as counter and reference electrodes, respectively.

Homemade program was developed to control the different parameters of the different techniques (chronoamperometry, cyclic voltammetry, pulse voltammetry), also to have a real time follow up of electrochemical/gravimetrical coupled procedures.

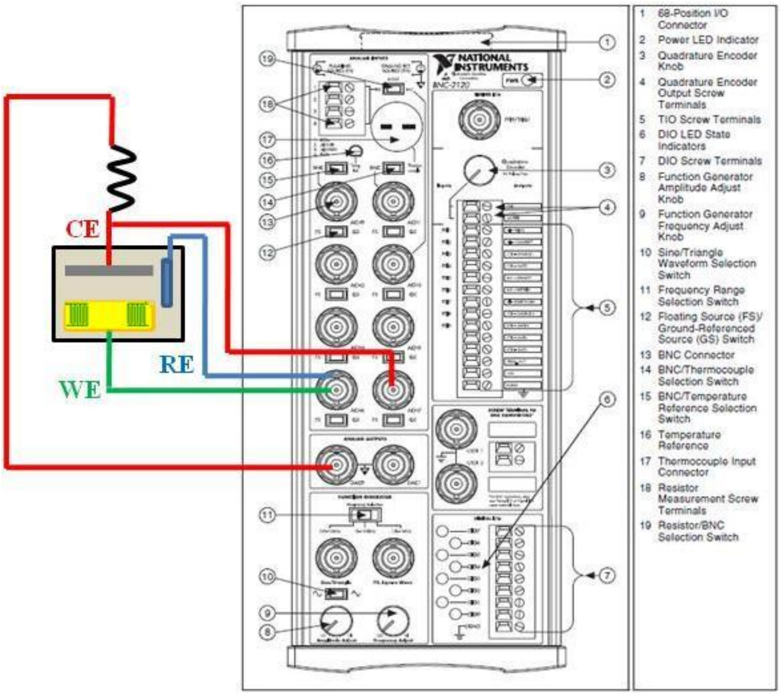

**Figure 2.13.** A full potentiostatic system based on a BNC-2120 panel, SAW sensing surface acts as working electrode (WE), Pt electrode as counter electrode (CE) and an Ag/$AgNO_3$ as reference electrode (RE).

## 2.7 Surface characterization techniques

In order to characterize the different conducting polymer films deposited onto solid substrates, different surface characterization techniques, microscopic and spectroscopic, were used in this work.

### 2.7.1 Structural characterization

Topography of the different samples was imaged using Atomic Force Microscopy, AFM, operating in the tapping mode using a silicon cantilever. The AFM observations were carried out in air at atmospheric pressure with a Nanoscope 3100 Veeco at the Institiut des NanoSciences de Paris, INSP. The obtained images were treated using WsXM program[14].

Thickness measurements of the polymer layers were realized using a DEKTAK 150 Veeco surface profilometer (radius of stylus: 12.5 µm, force: 1mg, resolution: 0.33 µm/sample) at the Institut des NanoSciences de Paris, INSP, and at Laboratoire de Physico-chimie des Polymères et des Interfaces, LPPI, in the university of Cergy-Pontoise.

### 2.7.2 Chemical charaterization

Chemical structures of the films were investigated by Attenuated Total Reflectance, ATR spectroscopy. Measurements were performed using a Brucker EQUINOX 55 FTIR spectrometer equipped with ATR accessory. ATR-FTIR spectra were carried out on the solid films by applying the pressure tower, in close contact with the crystal of ZnSe ($6 \times 6 \times 6$ $mm^3$). The IR absorption spectra were recorded at a nominal resolution of 4 $cm^{-1}$. Each reported spectrum is the result of accumulation of 256 scans. Between each spectrum acquisition, the ATR crystal was cleaned with ethanol, and an air background spectrum was recorded. ATR spectra obtained were corrected for optical effects. ATR-FTIR measurements were carried out at Laboratoire des Matériaux Industriels Métalliques et Polymères in CNAM.

## 2.8 Density Functional Theory, DFT

In order to evaluate the dimerization energies involving the species present in the pre-polymerization acetonitrile medium, in particular those of functional monomers and atrazine, DFT calculations were performed.

The DFT, is a quantum mechanical modeling method used in physics and chemistry to investigate the electronic structure (principally the ground state) of many-body systems, in particular atoms, molecules, and the condensed phases. A very easy way for understanding how DFT works is as follows:

The exact energy of a quantum system ($E^{\text{exact}}$) is given by (Eq 2.6):

$$E^{\text{exact}} = \langle \boldsymbol{\Psi^{exact}}, \boldsymbol{H^{exact}\Psi^{exact}} \rangle \qquad \text{Eq 2.6}$$

where:

$\Psi^{exact}$: the exact wave function of the system

$H^{\text{exact}}$ : the following Hamiltonian (Eq 2.7 and Eq 2.8):

$$H^{\text{exact}} = \sum_{\boldsymbol{i}} \boldsymbol{h}(\boldsymbol{i}) + \sum_{\boldsymbol{i<j}} \frac{\boldsymbol{1}}{\boldsymbol{rij}} + \sum_{\boldsymbol{N<N}} \frac{\boldsymbol{Z_N Z_{N\prime}}}{\boldsymbol{R_{NN\prime}}} \qquad \text{Eq 2.7}$$

$$\boldsymbol{h}(\boldsymbol{i}) = -\frac{\boldsymbol{1}}{\boldsymbol{2}} \Delta_{\boldsymbol{i}} - \sum_{\boldsymbol{N}} \frac{\boldsymbol{Z_N}}{\boldsymbol{riN}} \qquad \text{Eq 2.8}$$

with:

$r_{ij}$: the distance between electrons i and j

$\frac{\boldsymbol{1}}{\boldsymbol{r_{ij}}}$: the electronic repulsion

$Z_N$: the nuclei charge

$R_{NN'}$: the distance between nuclei

$\Delta_i$: the laplacian of electron *i*

$r_{iN}$: the distance between electron *i* and nuclei *N*

Since the beginning of quantum chemistry, quantum chemists have developed very sophisticated methods for calculating these wave functions (CI, CASPT2, CCSD…). The basic idea of the DFT is to postulate that the wave function is a single Slater determinant (Eq 2.9):

$$\Psi^{1D} = |\boldsymbol{\Phi_1(1)\Phi_1(2)} \ldots . \boldsymbol{\Phi_n(2n-1)\Phi_n(2n)}| \qquad \text{Eq 2.9}$$

with:

$\Phi$: the spin orbital

If we now write in full generality (Eq 2.10) :

$$\Psi^{exact} = U\,\Psi^{1D} \qquad \text{Eq 2.10}$$

where: U is unknown.

the energy can be read (Eq 2.11):

$$E^{exact} = \langle \boldsymbol{U\,\Psi^{1D}}, \boldsymbol{H^{exact}\,U\,\Psi^{1D}} \rangle \qquad \text{Eq 2.11}$$

$$= \langle \boldsymbol{\Psi^{1D}},\ \boldsymbol{{}^{t}U\,H^{exact}\,U\,\Psi^{1D}} \rangle \qquad \text{Eq 2.12}$$

$$= \langle \boldsymbol{\Psi^{1D}}, \boldsymbol{H^{DFT}\,\Psi^{1D}} \rangle \qquad \text{Eq 2.13}$$

with:

$$\boldsymbol{H^{DFT}} = \ \boldsymbol{{}^{t}U\,H^{exact}\,U} \qquad \text{Eq 2.14}$$

This shows that the exact energy can be extracted from the very simple one determinant wave function, provided a modified form of the Hamiltonian is used. This Hamiltonian is written as follows (Eq 2.15):

$$\boldsymbol{H^{DFT}} = \sum\nolimits_{\boldsymbol{i}} \boldsymbol{h^{DFT}}(\boldsymbol{i}) \qquad \text{Eq 2.15}$$

where:

$$\boldsymbol{h^{DFT}}(\mathbf{1}) = -\frac{\mathbf{1}}{\mathbf{2}}\,\Delta_{\mathbf{1}} - \sum\nolimits_{\boldsymbol{N}} \frac{\boldsymbol{Z_N}}{\boldsymbol{r1_N}} + \int \frac{\boldsymbol{\rho(r_2)}}{\boldsymbol{r_{12}}}\,\boldsymbol{dv_2} + \boldsymbol{V_{XC}} \qquad \text{Eq 2.16}$$

with :

$\rho(r_2)$: the electronic density

$V_{XC}$: the exchange correlation potential

The whole difficulty lies in the $V_{XC}$ term. From the early beginning of DFT, many forms of this potential were proposed. In the present work we have chosen the B97D form in order to take the Van-der-Waals interactions into account.

All the above experimental techniques, procedures and theoretical methods will be used to improve our understanding of the mode of operation of the sensing layers based on molecularly imprinted conducting polymers, MICP. Electrochemical and gravimetrical transductions and the coupled electrochemical/gravimetrical transduction will be studied and presented in details.

# References

---

[1] Meites, L. *Handbook of analytical chemistry*. McGraw-Hill, New York, **1963**.

[2] Pardieu, E. *Conception et développement d’un capteur électrochimique à base de polymères conducteurs à mémoire de forme pour la détection de petites molécules : application au cas de l’atrazine*. Sciences et Techniques Analytiques, Conservatoire National des Arts et Métiers CNAM, 2010, p 88-97.

[3] Pernelle, C. Pardieu, E. Garnier, F. Remita, S. *Détecteur électrochimique d’une petite molécule cible à base polymères conjugués à effet mémoire et procédé de détection utilisant un tel détecteur* » dépôt de brevet d’invention, référence : 9A-4963 cas 5, 2009.

[4] Pardieu E., Cheap H., Vedrine C., Lazerges M., Lattach Y., Garnier F., Remita S., Pernelle C., Molecularly imprinted conducting polymers based on electrochemical sensor for detection of atrazine. *Anal. Chim. Acta.* 649, 236-245, 2009.

[5] Bard, A. J., Faulkner, L. R., *Electrochemical methods fundamentals and applications*, 2nd Ed, Wiley interscience, New York, 2002.

[6] Nakamura, K. Horizontal piezoelectric surface acoustic waves. *J. App. Phys*, 46, 7B, 4421-4427, 2007.

[7] Harding, G. L., Du, J. Design and properties of quartz-based Love wave acoustic sensors incorporating silicon dioxide and PMMA guiding layers, *Smart Mater. Struct*. 6, 716-720, 1997.

[8] F. Martin a, M. I. Newton, G. McHalea, K. A. Melzak and E. Gizeli, *Pulse mode shear horizontal-surface acoustic wave (SH-SAW) system for liquid based sensing applications*, Biosens. Bioelec 19 (2004) 627–632.

[9] Bergaoui, Y., Zerrouki, C., Fougnion, J. M., Fourati, N., Abdelghani, A. Sensitivity Estimation and Biosensing Potential of Lithium Tantalate Shear Horizontal Surface Acoustic Wave Sensor, *Sen. letters*, 7, 1000-1005, 2009.

[10] Bergaoui, Y. *Réalisation de structures tests de capteurs capacitifs et à ondes acoustiques de surface.* INSAT, 2010.

[11] Kondoh, J. Simultaneous measurements of liquid properties using multichannel shear horizontal surface acoustic wave microsensor, *Jpn. J. Appl. Phys.,* 35, 5B, 3093-3096, 1996.

[12] Venkata, S., Chivuka, M., Shur, S., Ciplys, D. Recent advances in application of acoustic, acousto-optic and photoacoustic methods in biology and medicine, *phys. stat sol.(a),* 204,10, 3209-3236, 2007.

[13] BNC-2120 Connector accessory for E series devices, user guide, *National Instruments Co*, 1999.

[14] Horcas I., Fernandez R. Gomez-Rodriquez J. M., Colchero J., Gomez-Herrero J., Baro A. M. *Rev. Sci. Instrum*. 78, 013705, **2007.**

# Chapter 3

## Influence of electrochemical, chemical and structural properties of MICP on the recognition process

In this chapter experimental protocols and results will be discussed in order to optimize the synthesis as well as the properties of the sensing layers based on molecularly imprinted conducting polymers. A detailed discussion will be presented on the characteristics of the sensing layers which lead to the obtained properties of the sensor. Also, the electrochemical transduction of the sensor will be demonstrated with a study of the recognition properties, selectivity, and degradation of the sensor.

## 3.1 Recall

An original electrochemical sensor based on “shape memory polymer” was developed in LC3B laboratory in the frame of PhD thesis of E. Pardieu[1,2]. The recognition of atrazine (ATZ) target molecules was achieved by using the sensing properties of molecularly imprinted functionalized polymers, together with the electrical conduction of conducting polymers. This sensor has been realized following two steps:

- First, electropolymerization of two co-monomers: 3-Thiopheneacetic acid, TAA, (already associated through hydrogen bonds with the atrazine template, ATZ), and 3,4-ethylenedioxythiophene, EDOT, which is intended to play the role of conjugated link between the TAA moieties.
- Second, removal of atrazine from the resulting conjugated copolymer, leaving free recognition sites dedicated to the detection of additional ATZ molecules.

The obtained sensor demonstrates remarkable properties: a high selectivity towards the triazinic family, a large detection dynamic range ($2.5 \times 10^{-6}$ to $5 \times 10^{-3}$ mol $L^{-1}$) and a low detection threshold ($10^{-6}$ mol $L^{-1}$).

The design of the sensor was developed after spectral (NMR and FTIR) as well as electrochemical studies, carried out on the TAA/ATZ pre-polymerization complex, in order to favor the interaction between TAA and ATZ by H-bonding. The best TAA/ATZ/EDOT ratio was found to be 2/1/0.5. Thus, this ratio was adapted in this work.

Also the sensing layer developed in the work of E. Pardieu was electrosynthesized over a Pt electrode (BAS electrodes with active surface of 3.14 $mm^2$). We changed the type of the electrode for two reasons. First, the development of the sensors performances requires characterization of the solid polymer film deposited over the electrode. Hence, larger flat surfaces are needed. Second, an important part of the present work was dedicated to the gravimetric transduction and coupled electrochemical/gravimetric transduction where a delay line metalized with a gold layer was used. Thus the characterization and performance investigations were essentially carried out in this work on gold electrodes.

Platinum reference electrode was replaced by $Ag/AgNO_3$ reference electrode in this work, regarding the best stability of these electrodes, beside the miniaturized size of these electrodes which plays an important role when a small volume of solvents has to be used.

Also, the solvent and the electrolyte were changed. We passed from dichloromethane solvent, DCM, and tetrabutylammonium trifluoromethanesulfonate, TBATFMS, to acetonitrile solvent, ACN, and lithium perchlorate, $LiClO_4$, in order to avoid the fast evaporation of the solvent especially when a small volume of electrolyte is needed (in particular for the gravimetric and coupled transductions).

## 3.2 Experimental

Three kinds of conducting polymers are studied and prepared in this work as already mentioned in *section 2.3*:

*i)* Molecularly imprinted conducting copolymers (poly(EDOT-co-TAA), noted **MICP**) were prepared by electrochemical copolymerization of EDOT and TAA in the presence of pesticides target molecules (figure 3.1).

*ii)* Non-imprinted conducting copolymers (poly(EDOT-co-TAA), noted **NICP**) were electrochemically obtained by copolymerization of EDOT and TAA in the absence of target molecules

*iii)* Conducting homopolymers (polyEDOT, noted **PEDOT**) or (polyTAA, noted **PTAA**) were synthesized by electropolymerization of the corresponding monomers in the absence of the targets

For MICP preparation, TAA and ATZ ($3\times10^{-2}$ mol $L^{-1}$ and $1.5\times10^{-2}$ mol $L^{-1}$ respectively) were dissolved in ACN, in the presence of $LiClO_4$ (0.1 mol $L^{-1}$) as supporting electrolyte. A sufficient lap of time of 10 minutes was used for the association, through hydrogen bonds, between TAA and ATZ molecules (in the work of E. Pardieu[1,2], this lap of time was optimized by an electrochemical and FT-IR methods). Then, EDOT at a concentration of $7.5\times10^{-3}$ mol $L^{-1}$ in ACN was added before electropolymerization.

For NICP preparation, TAA ($3\times10^{-2}$ mol $L^{-1}$) and EDOT ($7.5\times10^{-3}$ mol $L^{-1}$) were dissolved in ACN solutions containing 0.1 mol $L^{-1}$ in $LiClO_4$ as supporting electrolyte. In this case, atrazine was not present before the electropolymerization step.

For PEDOT synthesis, EDOT was dissolved in ACN (or in $H_2O$) in the presence of $LiClO_4$ (0.1 mol $L^{-1}$), but in the absence of AAT and of any target molecule.

For PTAA synthesis, TAA was dissolved in ACN (or in $H_2O$) in the presence of $LiClO_4$ (0.1 mol $L^{-1}$), but in the absence of EDOT and of any target molecule.

The different kinds of conducting polymers were electrodeposited onto different substrates (gold, HOPG), in order to allow their physico-chemical characterization thanks to different techniques (ATR-FTIR, UV-Vis, AFM, profilometry, electrochemistry).

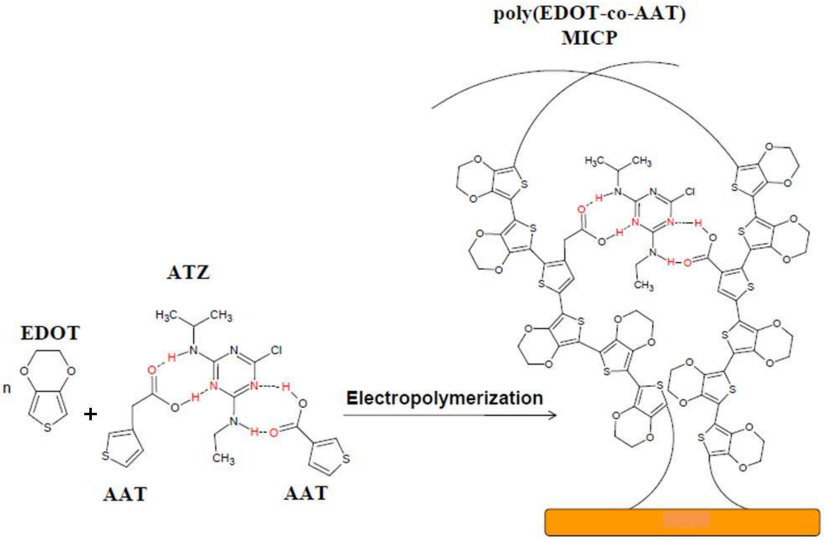

**Figure 3.1.** Schematic representation of MICP electrosynthesis by copolymerization of EDOT and TAA after the establishment of hydrogen bonds between TAA and ATZ in a pre-polymerization complex.

Constant potential electropolymerization is conducted with a three electrode system consisting of a working electrode (indicated for each electropolymerization) and counter electrode a stainless steel sheet with $Ag/AgNO_3$ electrode as reference electrode. A cyclic voltammogram of each monomer in the used electrolyte provides the appropriate range of potentials for this monomer, consequently the oxidation and reduction potentials. In electropolymerization, lower current densities are desirable and positions one-quarter or half-way up the rising curve are chosen. Hence, the electrochemical behavior of the monomers determined by cyclic voltammograms lead to the appropriate potential of electro-copolymerization of the comonomers.

## 3.3 Characterization of monomers, homopolymers, and template molecules in aqueous media.

In this section, a detailed study will be carried out on the behavior of the monomers and the template molecules in an aqueous medium. Electrochemical investigations will be enhanced by spectral and AFM studies.

### 3.3.1 EDOT in aqueous media

3,4-Ethylendioxythiophene is poorly soluble in aqueous solutions (2.1 g $L^{-1}$ at 20 °C). It is more preferable to use low enough concentrations in order to guarantee homogeneous media. EDOT concentrations around $1 \times 10^{-3}$ mol $L^{-1}$ and 1/100 ratio of $C_{EDOT}/C_{LiClO_4}$ provided the clearest and most reproducible results as already investigated by Pigani et al.[3] using EQCM.

Figure 3.2 shows the cyclic voltammogram recorded at a scan rate of 25mV $s^{-1}$ of $1 \times 10^{-3}$ mol $L^{-1}$ EDOT aqueous solution containing 0.1 mol $L^{-1}$ $LiClO_4/H_2O$ on HOPG surface (active surface area of 7 mm²). Two oxidation peaks, $P_1$ and $P_2$, are apparent around +0.75 and +1.25 V *vs.* $Ag/AgNO_3$, respectively. The two peak potential values are in agreement with previously reported data. According to them, the first peak ($P_1$) has been related to the oxidation of monomer, adsorbed[4] or not[5] on the electrode surface. The second peak ($P_2$) has been related either to the oxidation of EDOT species diffusing close to the electrode (and/or dimers or oligomers formed during the first step)[4] or to the overoxidation of the PEDOT film[5] if an enough amount of polymer was deposited on the electrode.

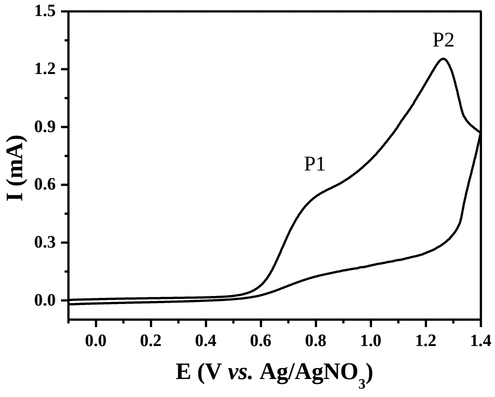

**Figure 3.2.** Cyclic voltammogram of 1 mM of EDOT in 0.1 M $LiClO_4$ aqueous solution at 25 mV $s^{-1}$ using HOPG working electrode.

The value of the applied potential ($E_p$) is one of the most significant parameters in an electropolymerization process; therefore, experiments dedicated to establish the highest and lowest potential values at which it is possible to obtain PEDOT polymer films with satisfactory characteristics were carried out. The highest potential value is conditioned by the fact that the polymer has not to be overoxidized; therefore, after the results shown in figure 3.2, potentials lower than +1.1 V *vs.* Ag/$AgNO_3$ have to be used.

Chronoamperograms were performed at +0.7, +0.8, +0.9 and +1 V *vs.* Ag/$AgNO_3$, for EDOT monomers at a concentration of $1 \times 10^{-3}$ mol $L^{-1}$ in presence of 0.1 mol $L^{-1}$ of $LiClO_4$ in $H_2O$ on HOPG surfaces with active area of 7 mm² (figure 3.3A). At deposition potential ($E_p$) of +1 V, the current can be seen to rapidly rise with time over a period of ca. 60 ms, this corresponds to the growth of particles which are initially sufficiently small and well separated that the individual diffusion fields (feeding the growth) do not overlap. The particles grow in size, and may increase in number[6], so that both the electroactive area and corresponding current increase. The current then reaches a maximum (3 mA) and subsequently decreases with time due to the overlap of diffusion fields of neighboring particles. A characteristic *i-t* decay curve is obtained at longer times, with current values that are consistent with linear diffusion of EDOT to the electrode surface. Indeed, it has been pointed out that a process limited by the resistance of a growing conducting polymer film may give a similar type of current decay curve[7].

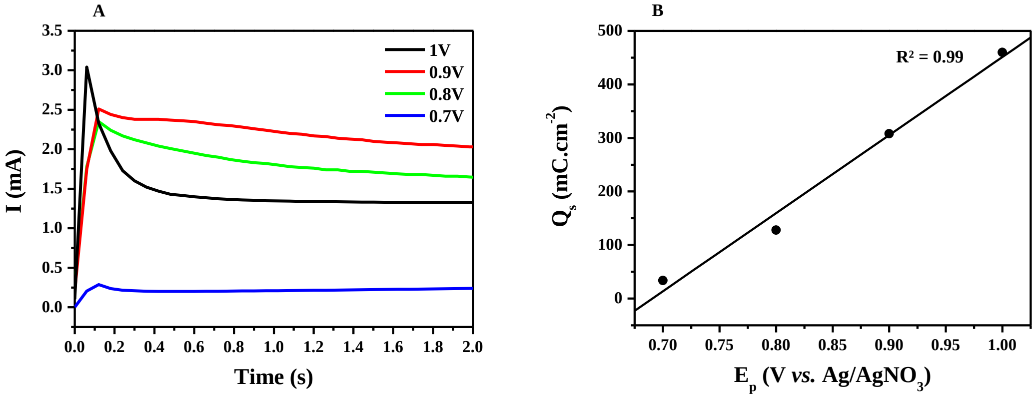

**Figure 3.3. (A)** The first 2 seconds of choronoamperograms obtained at different potentials of PEDOT polymerization: +0.7, +0.8, +0.9, and +1V for $1 \times 10^{-3}$ mol $L^{-1}$ in 0.1 mol $L^{-1}$ of $LiClO_4$ in aqueous solutions; **(B)** Linear relationship between the coulombic charge of electropolymerization ($Q_s$) and potential values of electrodeposition ($E_p$) implied during 10 seconds.

In contrast, at lower $E_p$ potentials, +0.9 V, +0.8 V and +0.7 V a slower rise of the current with time was observed. The current reaches a maximum (2.5 mA, 2.3 mA, and 0.3 mA) over a period of ca. 120 ms (for the electrodepositions at +0.9 V, +0.8 V, and +0.7 V respectively). This change in the initial values of time indicates that there is a different characteristic initial process at these potentials when compared to the electrodeposition at +1 V, and the rate of the process is clearly potential dependent. Also, the linear relationship observed between the implied potential ($E_p$) and the coulombic charge of PEDOT electropolymerization ($Q_s$) calculated from the chronoamperograms (figure 3.3B) enhances this argument.

To obtain further insight into the electrodeposition process, AFM was employed to characterize the morphology of the surfaces after deposition time of 10 seconds for each deposition potential (figure 3.4). Also, the AFM images were used to estimate the thicknesses of PEDOT films (figure 3.5).

The AFM data are consistent with the *i-t* curves (figure 3.3A), and suggest that at low deposition potential, $E_p$, of +0.7 V the electrode isn't completely covered by PEDOT (figure 3.4A) at the implied conditions (electropolymerization potential about +0.7 V for $1 \times 10^{-3}$ mol $L^{-1}$ of EDOT during 10 seconds). Beside, the formation of nucleation centers over the surface corresponds to a 2D mechanism[6].

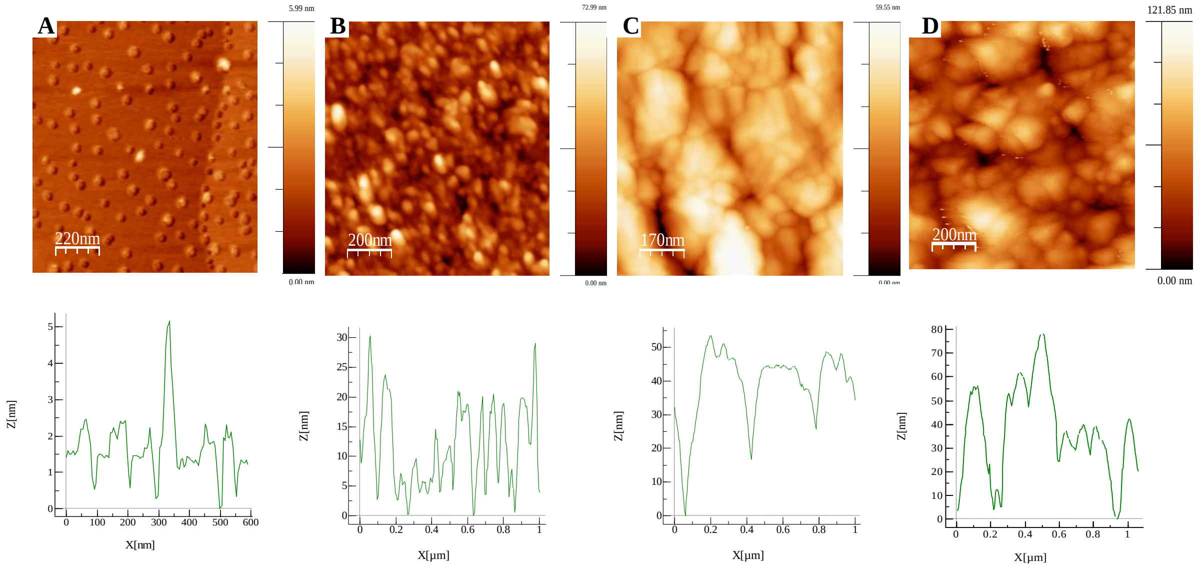

**Figure 3.4.** AFM images and topography in tapping mode of PEDOT films electropolymerized from aqueous solution of $1 \times 10^{-3}$ mol $L^{-1}$ EDOT onto HOPG substrates over a period of ca. 10 seconds at different potentials; **(A)** +0.7V; **(B)** +0.8V; **(C)** +0.9V and **(D)** +1V

The height of the formed nuclei at +0.7 V was deduced from AFM data and found to be included between 2 and 5 nm (figure 3.4) with a RMS roughness about 0.5 nm evaluated by AFM measurements.

At higher electrodeposition potentials, the HOPG electrodes are completely covered (figure 3.4 B, C, and D). The particles grow on the previously formed nuclei following a 3D growth regime, with associated roughening which can be calculated from the AFM data.

Thicknesses of PEDOT films deduced from AFM data were plotted as a function of the electropolymerization charge ($Q_s$) deduced from the chronoamperograms. A linear relationship can be obtained between the charge of electropolymerization and the thicknesses of films (figure 3.5), thus the thickness of PEDOT film can be adjusted by adjusting the electropolymerization charge.

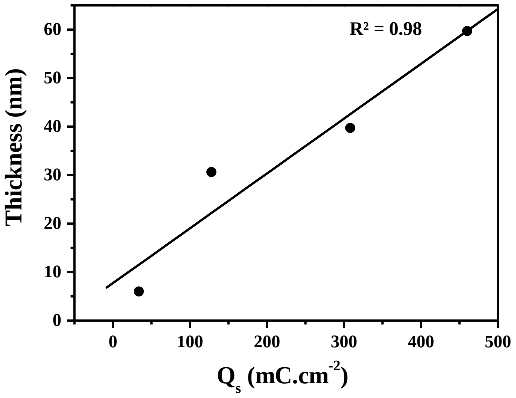

**Figure 3.5.** Variation of PEDOT film thickness deposited onto HOPG as a function of coulombic charge ($Q_s$) of electropolymerization. PEDOT films were electrosynthesized on HOPG substrates from 1 mmol $L^{-1}$ EDOT in 0.1 mol $L^{-1}$ $LiClO_4/H_2O$ . The thicknesses were measured by AFM.

RMS roughness values measured by AFM are found to be 17 nm, 10 nm, and 9 nm for deposition potentials of +1 V, +0.9 V and +0.8 V respectively. Thus, we can conclude that thick layers are accompanied with rougher surfaces (table 3.1). Values of $E_p$, $Q_s$, thickness and roughness cited in table 3.1 suggest that an increased potential of electropolymerization of PEDOT film results in higher values of electropolymerization charges, hence a thicker and rougher surfaces of these films.

**Table 3.1.** Charge of electropolymerization ($Q_s$) (in mC $cm^{-2}$), thicknesses (in nm) and roughness values (RMS in nm) of PEDOT layers electrosynthesized on HOPG from 1 mmol $L^{-1}$ EDOT in 0.1 mol $L^{-1}$ $LiClO_4/H_2O$ at different potentials of electopolymerization.

| Deposition Potential $E_p$ (V *vs.* $Ag/AgNO_3$) | Charge of electrosynthesis Qs (mC $cm^{-2}$) | Thickness of the layer (nm) | RMS roughness (nm) |
|---|---|---|---|
| +0.7 | 34 | 5 | 0.5 |
| +0.8 | 228 | 30 | 9 |
| +0.9 | 308 | 40 | 10 |
| +1 | 460 | 60 | 17 |

The electropolymerization at constant potential of EDOT on HOPG in aqueous solution has been studied at different potentials using AFM and chronoamperograms measurements. There is a potential dependent initial step in which the nucleation of the film is propagated. Two different mechanisms govern the growth depending on the applied potential. A two dimensional progressive mechanism agrees the investigations of E. Ventosa et al.[6] at low potential, then the film grows in a layer by layer fashion which leads to flat modified surfaces. On the other hand, a three dimensional progressive mechanism occurs at higher potentials of electrodeposition and rough surfaces with thicker layers are obtained.

### 3.3.2 TAA in aqueous media

Poly(3-Thiopheneacetic acid), PTAA, is an interesting material largely used in several applications ranging from solar cells[8], to optical sensors[9]. PTAA application in electrochemical sensors appears particularly interesting. Among few proposed examples, an amperometric sensor for ascorbic acid, cathecol and dopamine based on permselectivity properties of PTAA was developed[10]. Also a covalent immobilization of glucose oxidase on films prepared by electrochemical copolymerization of TAA with 3-methylthiophene was reported[11]. Other works were conducted on the use of PTAA as sensing layer for atrazine[12] beside to our work[13] with an important difference concerning the performance and the development of the sensor.

Despite of the interesting properties of PTAA, the solubility of TAA in aqueous solutions is relatively limited, due to the H-bonding interactions between the carboxylic residues of the TAA molecules. In order to dissolve TAA in $H_2O$, the samples were agitated using ultrasound for 20 min at room temperature. In order to determine the hydrosolubility of TAA at room temperature, we performed UV-vis absorption spectroscopy measurements. The UV-vis spectra of TAA in aqueous solution (at natural pH) exhibit a main band centered a

$\lambda_{max}$ = 280 nm, the intensity of which increases with concentration till a maximum value of about 0.9 (figure 3.6). From figure 3.6, one can deduce the solubility of TAA: 60 × $10^{-3}$ mol $L^{-1}$ and the molar extinction coefficient at 280 nm : $\varepsilon$ = 17 L $mol^{-1}$ $cm^{-1}$.

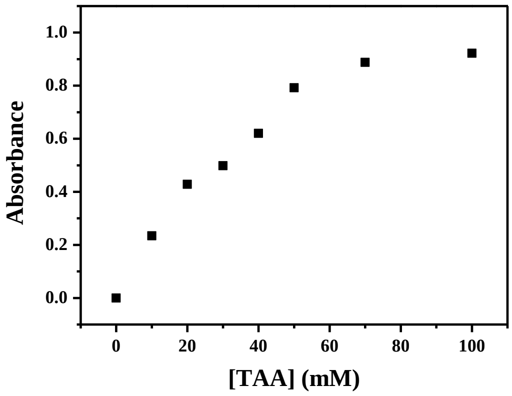

**Figure 3.6.** Absorbance values at $\lambda_{max}$ = 280nm as a function of TAA concentration in $H_2O$ at natural pH. Pathlength was 1cm.

Given the solubility values of TAA in $H_2O$ we decided to work at a concentration smaller than 60 × $10^{-3}$ mol $L^{-1}$. Thus, in order to study the electrochemical behavior of TAA in aqueous media a concentration of 30 × $10^{-3}$ mol $L^{-1}$ was used. Figure 3.7 displays six cyclic voltammograms of 30 × $10^{-3}$ mol $L^{-1}$ of TAA in 0.1 mol $L^{-1}$ $LiClO_4/H_2O$ (natural pH) over HOPG substrates at a surface active area of 7 mm² and at a scan rate of 25 mV $s^{-1}$.

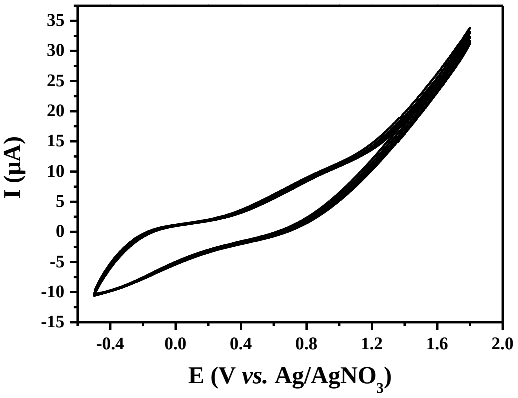

**Figure 3.7.** Cyclic voltammograms (six cycles) of 30 mmol $L^{-1}$ of TAA in 0.1 mol $L^{-1}$ $LiClO_4/H_2O$ over HOPG at a surface active area of 7 mm² and a scan rate of 25 mV $s^{-1}$.

The absence of oxidation peaks from the voltammograms of figure 3.7 suggests that in the implicated conditions no polymer layer was deposited over the HOPG surface.

The electropolymerization of TAA in aqueous solution was already checked in the work of Liaw et al.[14]. They suggested that the deposition of PTAA film above a given thickness isn't possible. The loss in the electroactivity of the conducting polymer is observed when an electropolymerization is operated by cyclic voltammetry. Liaw et al. referred this behavior to the loss in the conjugation length over the macromolecular chains. This phenomenon is attributed first to the cycling of the (–COOH) groups of the TAA molecules due to the electrophilic substitution by $H_2O$ molecules, then the formation of (C=O) groups on the β` site on the thiophene moiety, thus a loss in the conjugation length of PTAA macromolecular chains, associated to the extent of quinoidal structure. Thus, we can conclude that in the implied conditions, polymerization of PEDOT was carried out; however, the electrodeposition of PTAA film above a given thickness was not realized which was already indicated in the literature.

### 3.3.3 ATZ in aqueous solutions

The UV-vis absorption spectrum of atrazine in aqueous solution (at natural pH) exhibits a main band centered at 222 nm with a molar extinction coefficient $\varepsilon = 39400$ L mol$^{-1}$ cm$^{-1}$. Variation of the absorbance at 222 nm as a function of ATZ concentration (results not shown), indicates that the solubility in water of atrazine is limited at $15 \times 10^{-4}$ mol L$^{-1}$ (or 33 mg L$^{-1}$ at room temperature), which is similar to the value already obtained in ref. 15.

The limited solubility of ATZ in $H_2O$ is due to H-bonding interactions between ATZ molecules. This limited solubility prevents using $H_2O$ as solvent for the MICP polymerization, where relative higher concentrations of ATZ need to be used in order to have enough interactions between template and functional monomers in the pre-polymerization complexes. Consequently, in order to electrosynthesize the MICP based sensitive layers dedicated to the ATZ detection, organic media are preferred.

In the next sections a study of the electropolymerization process in ACN will be developed. We can note that, even if electropolymerization is carried out in ACN, the further detection of target molecules can be carried out either in organic media or in aqueous solutions.

## 3.4 Electrochemical characterization of monomers, homopolymers, and template molecule in acetonitrile.

An electrochemical study of EDOT, TAA and their homopolymers beside ATZ in ACN will be presented in this section, in order to determine the convenient conditions of electropolymerization of MICP sensitive layer which depends on the electrochemical behavior of the different components present in the pre-polymerization medium.

### 3.4.1 Electrochemical behavior of EDOT and PEDOT in acetonitrile

EDOT monomers were first characterized using Au working electrodes (BAS electrodes) with an active surface area of 3.14 mm². Electrodes were prepared as already mentioned in *section 2.2*. Stainless steel sheet and $Ag/AgNO_3$ were used as counter and reference electrodes respectively.

The electrochemical behavior of EDOT molecules at a concentration of $7.5 \times 10^{-3}$ mol $L^{-1}$ in 0.1 mol $L^{-1}$ $LiClO_4$/ACN was investigated by cyclic voltammetry at a scan rate of 100 mV $s^{-1}$ (figure 3.8A). Cyclic voltammograms were obtained by subtracting the background current corresponding to supporting electrolyte 0.1 mol $L^{-1}$ $LiClO_4$/ACN solution from the current of the samples containing EDOT monomers. Cyclic voltammograms of EDOT in 0.1 mol $L^{-1}$ $LiClO_4$/ACN show an anodic potential peak corresponding to the monomer oxidation at +1.3 V *vs.* $Ag/AgNO_3$ at a scan rate of 100mV $s^{-1}$. The trace crossing on the reverse sweep (nucleation loop) in the first cycle is typical in voltammograms of formation of conducting polymers. This nucleation loop has been ascribed to the nucleation process requiring an activation energy provided by an overpotential[16]. The nucleation loop is a characteristic feature and is considered as a proof of the initiation of the nucleation process of the polymer film. Multisweep experiments show an increasing current with each cycle, resulting in the formation of conducting polymer film. After 4 cyclic voltammograms, a dark blue PEDOT film was formed on the gold surface.

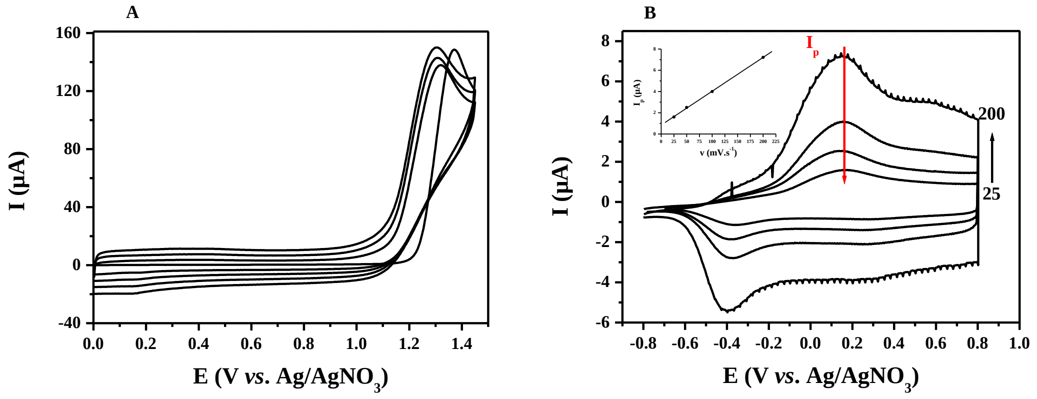

**Figure 3.8.** Cyclic voltammograms of **(A)** characterization of EDOT at a concentration of 7.5mmol $L^{-1}$ in 0.1 mol $L^{-1}$ $LiClO_4$/ACN and formation of PEDOT film over Au at a surface active area of 3.14 mm² and a scan rate of 100mV $s^{-1}$; **(B)** PEDOT film over Au at different scan rates from 25 to 200 mV $s^{-1}$ in 0.1 M $LiClO_4$/ACN with linear dependency of the oxidation current peak ($I_P$) of PEDOT as a function of the scan rate.

The electrochemical behavior of PEDOT was investigated in monomers free electrolyte solution (figure 3.8B). The cyclic voltammetric response of PEDOT at different scan rates from 25 to 200mV $s^{-1}$ shows two oxidation peaks, the first around -0.23 V followed by another with higher amplitude around +0.15 V *vs.* $Ag/AgNO_3$. Also two reduction peaks can be distinguished around -0.4 V and +0.25 V *vs.* $Ag/AgNO_3$. These results are similar to those found in literature[17,18]. General accepted explanation for the appearance of two reduction peaks is that the polymer un-doping process starts at the electrode/film interface and some of the anions ($ClO_4^-$) that have to be migrated from the reduced film to the electrolyte upon reduction may stay trapped, delaying and originating the reduction in two successive reduction processes occurring at different potentials[4]. The oxidation peak current $I_p$ (figure 3.8B) shows a linearly dependent behavior on the scan rate indicating that the current is not limited by the diffusion of counteranions[18,19].

### 3.4.2 Electrochemical behavior of TAA and PTAA in acetonitrile

The redox behavior of TAA ($30 \times 10^{-3}$ mol $L^{-1}$) in 0.1 mol $L^{-1}$ $LiClO_4$/ACN over Au working electrodes (active area surface of 3.14 mm²) was also studied. Potential scanning was performed between 0.0 V and +2.0 V *vs.* $Ag/AgNO_3$, with a scan rate of 100mV $s^{-1}$. The voltammograms exhibit an oxidation peak at +1.8 V *vs.* $Ag/AgNO_3$, which refers to the oxidation of the monomer. The current of the first oxidation peak was rapidly decreased in the next cycles (figure 3.9A). This observation can be referred to the formation of a PTAA film after the first voltammogram; this film looses rapidly its electroconductivity in the implied conditions, and causes the insulation of the electrode surface. This phenomenon is probably due to the loss in the conjugation length of the PTAA chains owing to the relative high oxidation potential of the molecule. Thus, polymerization on the site β of the thiophene ring beside the polymerization on α and α` sites of this ring takes place, which induces this loss in the mean conjugation length due to the irregular structure (a comparable behavior of TAA was observed in aqueous medium but in a different mechanism).

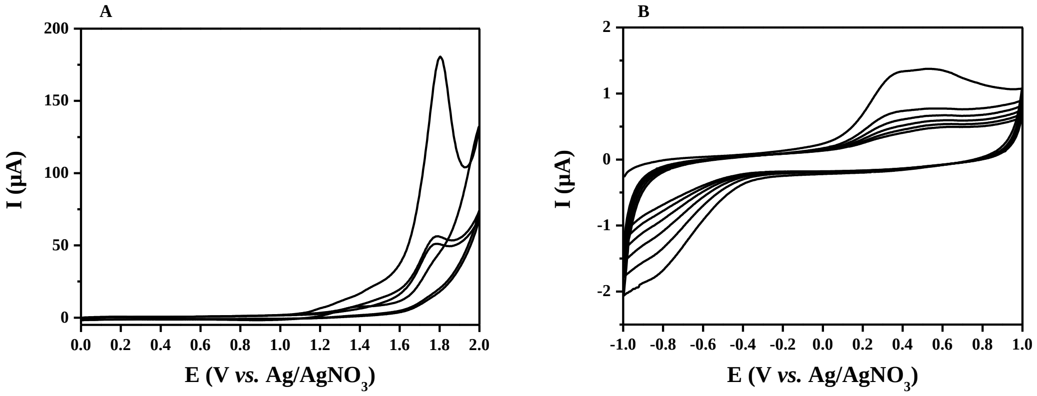

**Figure 3.9.** Cyclic voltammograms of **(A)** characterization of TAA at a concentration of 30mmol $L^{-1}$ in 0.1 mol $L^{-1}$ $LiClO_4$/ACN and formation of PTAA film over Au at a surface active area of 3.14 mm² and a scan rate of 100mV $s^{-1}$; **(B)** PTAA film over Au at a scan rate of 25 mV $s^{-1}$ in 0.1 mol $L^{-1}$ $LiClO_4$/ACN.

Figure 3.9B shows six cyclic voltammograms of PTAA modified Au electrode surface at a scan rate of 25 mV $s^{-1}$ in 0.1 mol $L^{-1}$ $LiClO_4$/ACN. A loss in the deposited mass is observed after six voltammograms, indicating the formation of unstable film after the three cycles appeared in figure 3.9A.

Cyclic voltammograms of EDOT and TAA in ACN indicated an electrochemical behavior comparable to that already observed in ref. 1 but different to the behavior of these molecules in $H_2O$. More reproducible voltammograms of these molecules in ACN was obtained when compared to the voltammograms of these molecules in $H_2O$. Thus, we decided to use the same potential of electropolymerization already used in ref. 1, 2, and 13, ($E_p$ = +1.45 V *vs.* $Ag/AgNO_3$). Taking into account that the obtained results that were discussed and justified by electrochemical and spectral means [1,2], allow the copolymerization of EDOT and TAA. Therefore, a study of the electrochemical behavior of atrazine molecules at this potential is and remains necessary.

### 3.4.3 Electrochemical behavior of atrazine

Electrochemical behavior of atrazine was checked using a bare gold electrode in the absence of any monomer and polymer. This electrochemical study was performed by cyclic voltammetry at a scan rate of 25mV $s^{-1}$. For this study, ACN solutions containing 0.1 mol $L^{-1}$ $LiClO_4$ and various concentrations of atrazine ($5 \times 10^{-3}$ and $15 \times 10^{-3}$ mol $L^{-1}$) were used. Figure 3.10A displays the cathodic currents measured on a gold electrode in the absence of ATZ (curve a) and for two different concentrations of atrazine (curves b and c).

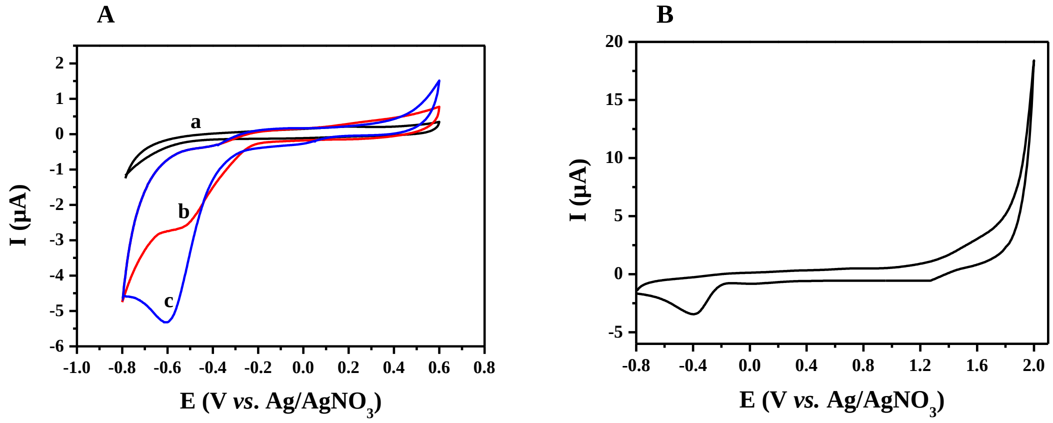

**Figure 3.10. (A)** Cyclic voltammograms of atrazine in ACN solutions containing $LiClO_4$ (0.1 mol $L^{-1}$) and increasing concentrations of ATZ: **(a)** 0, **(b)** 5 $10^{-3}$, **(c)** $15 \times 10^{-3}$ mol $L^{-1}$. The scan rate was 25mV $s^{-1}$ on a bare gold electrode. **(B)** Cyclic voltammogram of atrazine in ACN solution containing $LiClO_4$ (0.1 mol $L^{-1}$) and a concentrations of ATZ of $15 \times 10^{-3}$ mol $L^{-1}$. The scan rate was 25mV $s^{-1}$ on a bare gold electrode.

As expected, the measured current clearly increases with the pesticide concentration. This result is in agreement with those obtained by Shoji *et al.* in the case of atrazine reduction on gold electrode[20]. In the presence of atrazine, cyclic voltammograms (figure 3.10A) display reduction peaks, while no oxidation peak is observed. This indicates that atrazine is reduced, in our experimental conditions on gold electrode, at about -0.6 V *vs* Ag/$AgNO_3$ in an irreversible process, following the same behavior as that observed on other types of electrodes, such as platinum electrode[13], gold electrode[20], or mercury electrode[21].

In the next section, electrochemical copolymerization of TAA and EDOT in presence of ATZ will be achieved at a constant potential of +1.45 V *vs.* Ag/$AgNO_3$, thus, the electrochemical behavior of ATZ at this potential should be studied. Figure 3.10B represents potential scanning between -0.8 V and +2.0 V *vs.* Ag/$AgNO_3$ of $15 \times 10^{-3}$ mol $L^{-1}$ of ATZ in 0.1 mol $L^{-1}$ $LiClO_4$/ACN at a scan rate of 25mV $s^{-1}$. The electrochemical behavior of the molecule in this potential range shows a similarity with its behavior which was indicated in figure 3.10A, and no degradation of ATZ molecules was observed.

We can conclude that the electrochemical behaviors of EDOT, TAA and ATZ over gold electrodes in acetonitrile using 0.1 mol $L^{-1}$ $LiClO_4$ as supporting electrolyte should allow the electrodeposition at a constant potential ($E_p$ = +1.45 V *vs.* Ag/$AgNO_3$) of PEDOT and of poly(EDOT-co-TAA) in the presence of ATZ without inducing any overoxidation of the conducting polymer film or any alteration of the ATZ template molecule.

## 3.5 Electrosynthesis and electrochemical characterization of MICP, NICP and PEDOT films in ACN

By electropolymerization of EDOT and TAA monomers in the presence or in the absence of ATZ target molecules in ACN, three types of conducting polymers, used as sensitive layers were synthesized on gold electrode surfaces: MICP, NICP and PEDOT.

*i)* For MICP copolymer preparation, an ACN solution containing $LiClO_4$ as supporting electrolyte, TAA, EDOT and ATZ was prepared.

*ii)* For NICP copolymer synthesis, an ACN solution containing $LiClO_4$ as supporting electrolyte, TAA and EDOT was prepared in the absence of ATZ. NICP films were used to exhibit and to compare the influence of the functionalized cavities on the recognition process of ATZ molecules by MICP.

*iii)* For PEDOT homopolymer electrosynthesis, EDOT was dissolved in ACN in the absence of TAA and of ATZ, but in the presence of $LiClO_4$ as supporting electrolyte. PEDOT films were used in order to study the effect of the presence of TAA functional monomer on the recognition process.

### 3.5.1 Synthesis of conducting polymers

Electropolymerization of MICP, NICP and PEDOT under potentiostatic conditions was realized in the same conditions, using a 2-steps chronoamperometry technique in the electrochemical cell. This technique afforded more reproducible chronoamperograms of electropolymerization and cyclic voltammograms of characterization, when compared to the 1-step chronoamperometry technique used in ref. 13. Thus, in the first step, the potential was switched from 0.0 to 0.8 V *vs.* Ag/$AgNO_3$. The initial step was intended to build the double-layer charging of the Au|solution interface. By this way, the distortion of the transient polymerization current by the double-layer charging was minimized and the electropolymerization process was controlled by the electrochemical step rather than by the diffusion of the monomers to the electrode surface[18,22,23,24,25,26]. Polymerization was then achieved by a further step at a constant potential of +1.45 V *vs*. Ag/$AgNO_3$ as already mentioned in *section 2.3*. Due to the atrazine redox behavior (figure 3.10), no oxidation of the target molecules, present exclusively during MICP synthesis, can occur at such a potential. Moreover, the time used for this second chronoamperometric step was chosen in order to adjust the total electropolymerisation charge to 3.14 mC (100 mC $cm^{-2}$, the area of gold surfaces was 3.14 $mm^2$) for the synthesis of MICP, NICP as well as PEDOT.

Even if all the films are synthesized in ACN medium, their characterizations can be carried out either in ACN medium or in aqueous solution.

### 3.5.2 Characterization of conducting polymers in aqueous media

After the electrosynthesis step, the obtained MICP film exhibits voltammograms which are represented, at a scan rate of 25mV $s^{-1}$ in 0.1 mol $L^{-1}$ $LiClO_4/H_2O$, on figure 3.11. As illustrated in this figure, a fast decrease in the cyclic voltammogram intensity takes place upon cycling of MICP in aqueous medium. The film lost 34% of its electroactivity after six cyclic voltammograms in 0.1 M $LiClO_4/H_2O$ carried out on MICP electrosynthesized in the above mentioned conditions. This loss in the electroactivity can be referred to a degradation of the film in the aqueous medium.

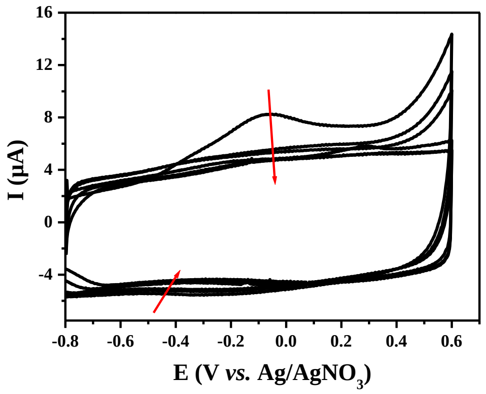

**Figure 3.11.** Six cyclic voltammograms of MICP (in 0.1 mol $L^{-1}$ $LiClO_4/H_2O$) at a scan rate of 25mV $s^{-1}$. The electropolymerization charge was 100mC $cm^{-2}$, red arrows show the decrease in the current intensity induced by voltammetric cycling.

The competitive interactions of ATZ and $H_2O$ with the carboxylic residues in the structure of the MICP can also be one of the reasons of this behavior, where these interactions affect the conjugation mean length on the macromolecular chain, hence the electrochemical activity of the conducting polymer film (see *section 3.8*).

For these reasons all electrochemical characterizations were carried out in ACN medium rather than in aqueous solutions.

### 3.5.3 Characterization of conducting polymers in acetonitrile

After the electrosynthesis step, the obtained MICP, NICP and PEDOT films exhibit voltammograms which are represented, at the same scan rate of 25mV $s^{-1}$, on Figure 3.12. PEDOT voltammogram (curve a) exhibits oxidation peaks at +0.15 V and -0.23 V (*vs.* Ag/$AgNO_3$) corresponding to the conjugated polymer oxidation and concomitant $ClO_4^-$ anions insertion as charge compensators, During reduction, two cathodic peaks are observed at +0.25 V and -0.4 V (*vs.* Ag/$AgNO_3$) as already observed in figure 3.8B.

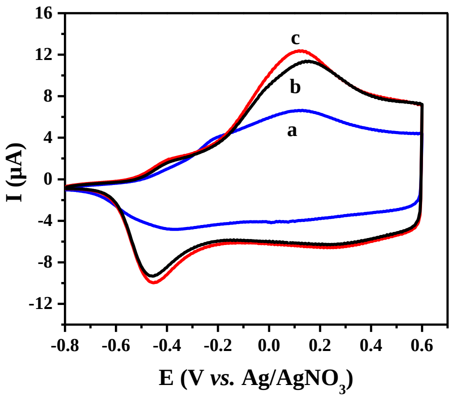

**Figure 3.12.** Cyclic voltammograms of **(a)** PEDOT, modified electrode, **(b)** MICP, modified electrode and **(c)** NICP, modified electrode, in ACN containing 0.1 mol $L^{-1}$ of $LiClO_4$. MICP, NICP and PEDOT were electrosynthesized by a 2-steps chronoamperometry technique. The electropolymerization charge was 100mC $cm^{-2}$ and the scan rate was 25mV $s^{-1}$

During PEDOT electrosynthesis, only EDOT monomers are present, while TAA is also present as comonomer during MICP and NICP formation. The voltammograms of MICP and NICP are different from that of PEDOT homopolymers (figure 3.12, curves b and c respectively). This result confirms the presence of TAA, in addition to EDOT, in the polymer matrix of electrosynthesized MICP and NICP. The copolymer nature of these latter conducting polymers is also demonstrated in the *chemical and structural characterization* *section 3.6* below. MICP and NICP voltammograms indicate that conformational strain, due to the presence of ATZ (figure 3.1), has an effect, in our experimental conditions, on the electrochemical response of the electrosynthesized polymers.

In order to better understand the redox process implicated during the electrosynthesis of MICP, NICP and PEDOT, the voltammograms of these conducting polymers were recorded at different scan rates. Figure 3.13A displays the voltammograms obtained in the case of MICP at different scan rates ranging from 25 to 200mV $s^{-1}$. The MICP electroactivity as well as the intensity of the oxidation peak, $I_p$, located around +0.1 V *vs.* $Ag/AgNO_3$ clearly vary with the scan rate, following a linear increase of $I_p$ with the scan rate (figure 3.13B). Such a behavior, also observed for NICP and PEDOT modified electrodes (figure 3.8) indicates that the redox process implicated in the MICP, NICP and PEDOT conducting polymers is not limited by diffusion but by the adsorption onto the electrode surfaces[27]. Figure 3.13B shows a slight increase of the anodic peak potentials with the scan rate. This may indicate that the MICP electrochemical processes are not reversible but follow quasi-reversible mechanisms.

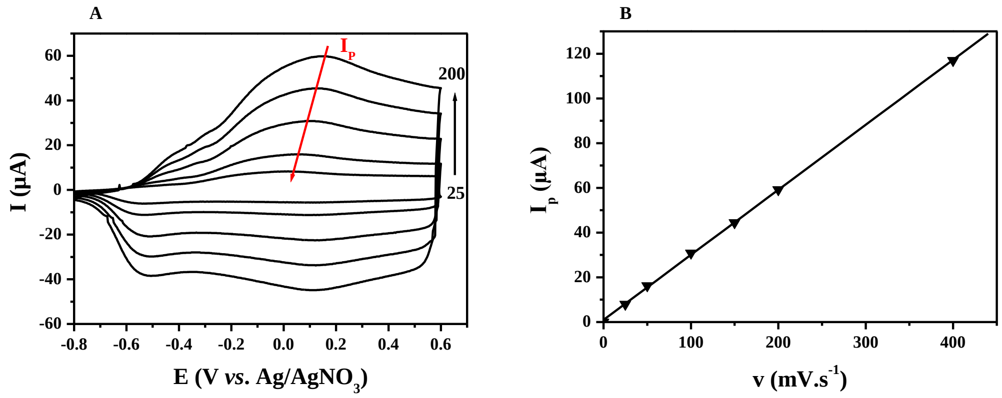

**Figure 3.13. (A)** Cyclic voltammograms of MICP (in 0.1 mol $L^{-1}$ $LiClO_4$/ACN) at different scan rates: 25, 50, 100, 150 and 200mV $s^{-1}$. The electropolymerisation charge was 100mC $cm^{-2}$. **(B)** Variation of the intensity of the oxidation peak, $I_p$, as a function of the scan rate.

In order to study the electrochemical stability of MICP towards the successive cycling in 0.1 mol $L^{-1}$ $LiClO_4$/ACN between -0.8 V and +0.6 V *vs.* $Ag/AgNO_3$, 90 successive voltammograms at a scan rate of 25mV $s^{-1}$ were recorded (figure 3.14). The electrochemical charges passed in the first and the ninetieth cycles were calculated in respect to the scan rate, and the MICP film kept 86% of its electroactivity after 90 cycles.

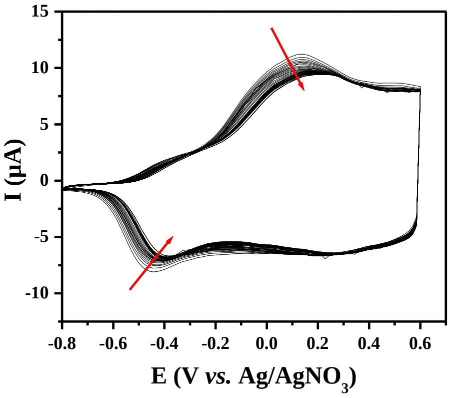

**Figure 3.14.** Ninety cyclic voltammograms of MICP (in 0.1 mol L$^{-1}$ LiClO$_4$/ACN) at a scan rate of 25mV s$^{-1}$. The electropolymerisation charge was 100mC cm$^{-2}$, red arrows show the decrease in the current intensity induced by voltammetric cycling.

The MICP film lost less than 4% of its electroactivity (regarding the first cycle) after 10 cycles and the electrochemical charge calculation gives constant value between the third and the tenth cycle. Thus, the third cycle of voltammograms will be systematically employed for different purposes in this work, whenever the cyclic voltammetry is used (films characterization, detection of target molecules and selectivity studies). NICP films exhibited a comparable electrochemical behavior towards cycling, whereas PEDOT films demonstrated better stability, which was also demonstrated in ref. 18.

The electrosynthesis of MICP, NICP and PEDOT under potentiostatic conditions using a 2-steps chronoamperometry technique was carried out in 0.1 mol L$^{-1}$ LiClO$_4$/ACN. Electrochemical characterization and voltammetric cycling stability of the MICP film in acetonitrile medium reflect good properties of the film from an electrochemical point of view, but additional characterizations should be carried out in order to develop conducting layers performance as electrochemical sensors.

## 3.6 Chemical and structural characterization of MICP, NICP and PEDOT films

In order to chemically and structurally characterize the polymer layers, the three kinds of conducting polymers, MICP, NICP and PEDOT, were synthesized in the same electrochemical conditions as before (electropolymerization charge of 100 mC cm$^{-2}$), on flat gold electrodes (area of 70 mm²). The use of such substrates allowed performing surface analysis techniques, such as ATR-FTIR spectroscopy and AFM microscopy.

### 3.6.1 ATR-FTIR spectroscopy of MICP, NICP and PEDOT films

ATR-FTIR measurements were carried out in order to confirm the chemical composition of the films. The IR spectra corresponding to MICP, NICP and PEDOT were then recorded (figure 3.15). The spectrum obtained in the case of PEDOT is in very good agreement with the main vibrations reported for this homopolymer and for other polythiophenes in the literature[28,29,30,31,32,33,34,35]. Vibrations at 1518, 1483 and 1339 cm$^{-1}$ are attributed to the stretching modes of C=C and C-C in the thiophene ring. The vibration modes of the C-S bond in the thiophene ring can be observed at 977, 842 and 691 cm$^{-1}$. The bands at 1213 and 1093 cm$^{-1}$ are assigned to the stretching modes of the ethylenedioxy group, and the band around 920 cm$^{-1}$ is due to the ethylenedioxy ring deformation mode.

The ATR-FTIR spectra of MICP and NICP are very similar to each other. Contrarily to PEDOT, MICP and NICP specifically display bands at 3560 and 3520 cm$^{-1}$ referred as O-H bond of the carboxylic group present in the TAA residue. Bands at 1620 and 1320 cm$^{-1}$ can be attributed to C=O and C-O bonds of the carboxylic group of the TAA functional monomer[36]. The 1620 cm$^{-1}$ band is also characteristic of the C=N, O-H and N-H vibrations present only for ATZ molecules. This can explain the fact that this band intensity is higher in the case of MICP IR spectrum than in the NICP case.

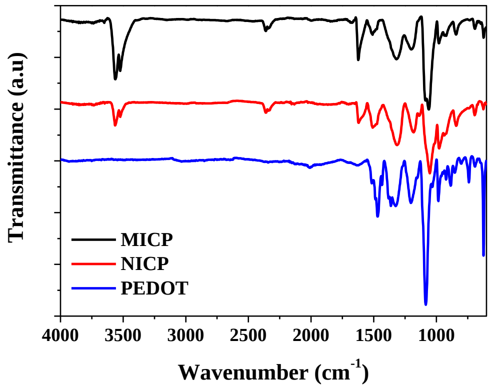

**Figure. 3.15.** ATR-FTIR spectra of MICP, NICP and PEDOT films, all electrosynthesized in 0.1 mol L$^{-1}$ $LiClO_4$/ACN by 2-steps chronoamperometry at a constant potential of 1.45 V vs. Ag/$AgNO_3$, charge of electropolymerization was 100 mC cm$^{-2}$.

Besides, and contrary to PEDOT, MICP and NICP IR spectra present a peak at 2300 cm$^{-1}$ which corresponds to the $C \equiv N$ functional group. The existence of this band can be attributed to the presence of residual molecules of ACN in both MICP and NICP matrixes.

Without any ambiguity and in good agreement with what has already been suggested in *Section 3.5*, this observation confirms the copolymer nature of both MICP and NICP. The mixing of TAA and EDOT residues in the copolymer matrixes can also explain the shift of the vibration bands of MICP and NICP in comparison with those of PEDOT homopolymers.

Figure 3.16 represents the FTIR spectra of acetonitrile and of atrazine in acetonitrile. A non-identified band with two shoulders at 3560 and 3520 cm$^{-1}$ is present. As a consequence, the appearance of this double band in MICP and NICP spectra at the same wavenumbers in figure 3.15 should indicate the presence of residual ACN molecules in both conducting polymers. However, since ATZ is also characterized by such bands, the difference in the intensity of the "double bands" between MICP and NICP is maybe due to the presence of trapped ATZ in MICP since this target molecule is necessarily absent from NICP matrix.

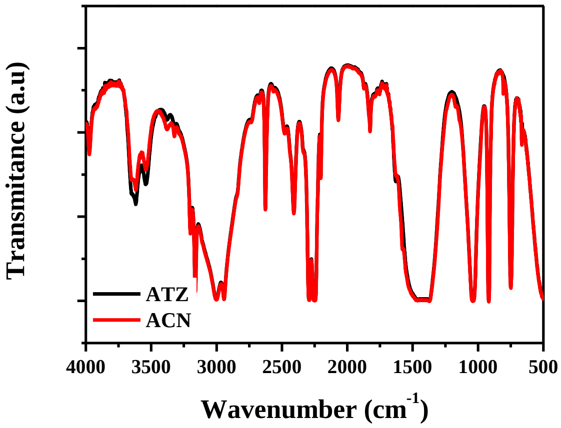

**Figure. 3.16.** FTIR spectra of acetonitrile (red line), and atrazine in acetonitrile (black line).

As a conclusion we can note that, MICP and NICP spectra are relatively similar and differ only by the intensity of bands at 3560, 3520 and 1620 cm$^{-1}$ which were assigned to ATZ molecules in ACN solvent. Both MICP and NICP spectra are different from PEDOT spectrum, which confirms the copolymer nature and the presence of TAA in their structure.

### 3.6.2 AFM microscopy of MICP, NICP and PEDOT films

AFM observations in tapping mode were carried out in order to investigate the surface of the polymer films which were electrodeposited onto gold substrates (70 mm²) with an electropolymerisation charge of 100 mC cm$^{-2}$. AFM images corresponding to MICP and NICP copolymers and to PEDOT homopolymers were recorded (figure 3.17). AFM images of PEDOT, NICP and MICP films (Figure 3.17A, B and C respectively) show a granular structure of the polymers chains, indicating that all the electrosynthesized homopolymers and copolymers grow layer by layer, perpendicularly to the electrode surface[18,37]. Even if the measure of the rough thickness of MICP, NICP and PEDOT layers was not possible by AFM in our experimental conditions, section analysis of the images (Figure 3.17) indicates that the mean height of the granules obtained for an electropolymerisation charge of 100mC cm$^{-2}$ is of several hundreds of nanometers for PEDOT, and around 800 nm for NICP, and can reach 1.3 µm for MICP. Besides, section analysis shows that the diameters of the columns depend on the chemical nature of the polymers. The mean diameter is of 650 nm, 1µm and 2µm respectively for PEDOT, NICP and MICP.

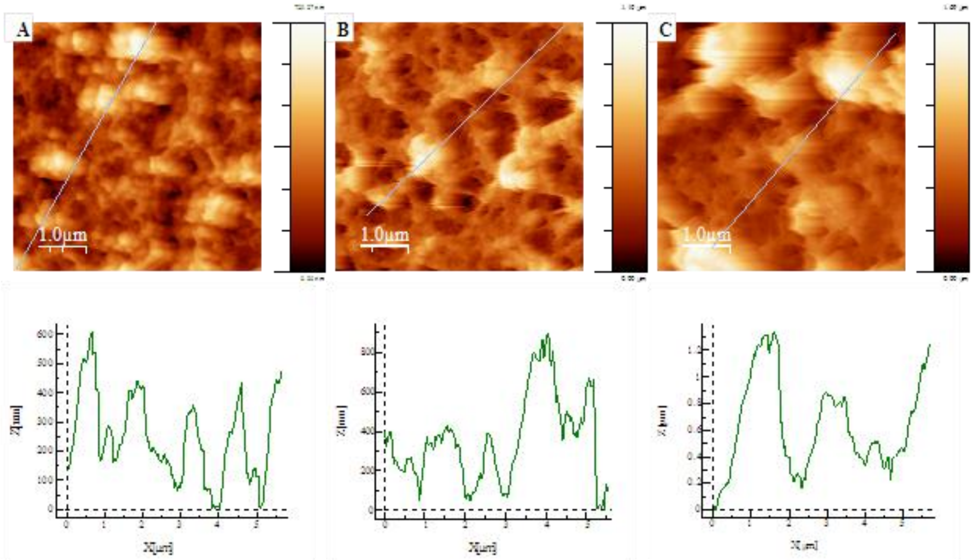

**Figure 3.17.** AFM images in tapping mode of: **(A)** PEDOT, **(B)** NICP and **(C)** MICP with section analysis of each (co)polymer. The conducting polymers were electrosynthesized on gold substrates by a 2-steps chronoamperometry technique. The electropolymerisation charge was 100 mC cm$^{-2}$.

The roughness (RMS) values, as measured by AFM, are different for PEDOT, NICP and MICP surfaces: 115, 180, and 305 nm respectively. The surface roughness is higher in the case of MICP and NICP copolymers films. In addition, comparing AFM images and section analysis of the polymer layers (figure 3.17) with the measured thicknesses of the films (*Section 3.7*) suggests that MICP and NICP are characterized by a more porous structure than PEDOT. The presence of TAA residues which can interact by hydrogen bonds with other TAA monomer units (in the case of MICP and NICP) or with ATZ target molecules (only in the case of MICP) during the growth of the films can explain the more porous structure and the higher surface roughness of the copolymers, when compared to those of PEDOT homopolymers.

The above ATR-FTIR and AFM characterizations demonstrate that MICP, NICP and PEDOT films are structurally and chemically different. First, the more porous structure of MICP and NICP in comparison with that of PEDOT can favor the diffusion of ATZ target molecules from and into the polymer matrixes. Second, the presence of TAA monomers in the copolymer structure of MICP and NICP can favor the interaction with ATZ target molecules thanks to hydrogen bonds. These chemical and structural considerations will explain the different behaviors of PEDOT, NICP and MICP when all these polymer films are used as sensitive layers for the recognition of ATZ target molecules (*see section 3.8*).

## 3.7 Influence of electropolymerization charge on the structure of MICP, NICP and PEDOT films

The growth layer by layer of MICP, NICP and PEDOT conducting polymers, deduced from the previous AFM observations, suggests that the modulation of the electropolymerization charge enables the control of the thickness of the polymer layers. This is an important parameter, which should allow concluding if the sensor operates in a 2D or a 3D (on the surface or in the bulk of the sensing layer) recognition process.

In order to study the dependence of polymer layers thickness as a function of electropolymerization charge, MICP, NICP and PEDOT polymers were electrosynthesized, as before, on flat gold electrodes (area of 70 mm²) using a 2-steps chronoamperometry technique. Polymerization was achieved by a second step at a constant potential of 1.45 V *vs.* Ag/AgNO$_3$. The time used for this second chronoamperometric step was varied in order to adjust the coulombic charge of electropolymerization, Q$_s$. Optical profilometry was then used to measure the thickness, of the polymer layers.

As expected, PEDOT, NICP and MICP films, electrogenerated using the above mentioned conditions, display a linear variation of their average thickness (in nm) as a function of the electropolymerization charge (in mC cm$^{-2}$, referred to electrode surface) as observed on figure 3.18. On this latter, each point of the curve corresponds to a mean value obtained from three independent measurements. Besides, the uncertainty bars corresponding to each point were displayed on the graph. As observed, the variation of the thickness is more pronounced in the case of MICP and NICP (11.4 and 10.7 nm/mC cm$^{-2}$ respectively) than for PEDOT (4.5 nm/mC.cm$^{-2}$). When the electropolymerisation charge used for polymer synthesis is adjusted to 100 mC cm$^{-2}$, the thicknesses measured in the implied conditions are 1100, 1000 and 450 nm respectively for MICP, NICP and PEDOT. The fact that, for a given electropolymerisation charge, MICP and NICP films are thicker than PEDOT layers implies that PEDOT homopolymers are more compact than NICP and MICP copolymers in the implied conditions, assuming that the electrical yields of polymerization are comparable.

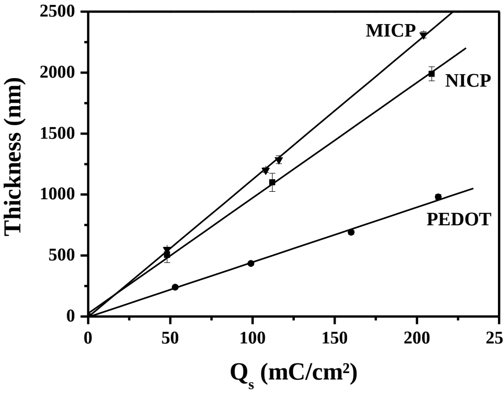

**Figure 3.18.** Variation of the thickness of the polymer films as a function of the coulombic charge ($Q_S$) of electropolymerization: MICP (▼), NICP (■) and PEDOT (●). The conducting polymers were electrosynthesized on gold substrates by a 2-steps chronoamperometry technique. The thicknesses were measured by optical profilometry. Each point of the curves, represented with its error bar, corresponds to the mean value obtained from three experiments.

This is in agreement with the AFM observations of MICP and NICP deduced from figure 3.17 and should be due, once again, to the presence of TAA residues which can interact by hydrogen bonds with other TAA monomers or with ATZ target molecules during the growth of the copolymer films.

## 3.8 Sensing properties of MICP, NICP and PEDOT films

The aim was to compare the sensing properties of MICP, NICP and PEDOT films of different thicknesses towards atrazine target molecules, in order to better understand the influence of the chemical and structural properties of these conducting polymers. Nevertheless, contrarily to NICP and PEDOT polymers, MICP films were always electrosynthesized in the presence of atrazine (figure 3.1). Thus, if we want to compare the recognition properties of all these polymers, the extraction of ATZ from MICP matrix is necessary.

In order to remove the target molecules from the MICP matrix, a mixture of protic solvents, a methanol/acetic acid solution, was used to wash all the MICP polymer-coated electrodes (as already mentioned in *section 2.4*). Then ATZ-free MICP layers were used to detect additional ATZ targets either in aqueous or ACN media.

### 3.8.1 Sensing properties of MICP in aqueous medium

After this washing step, which is intended to ATZ extraction, MICP voltammograms were recorded in aqueous solution in presence of 0.1 mol $L^{-1}$ $LiClO_4$ at a scan rate of 25mV $s^{-1}$. Figure 3.19 exhibits the cyclic voltammogram of washed MICP synthesized with an electropolymerisation charge of 100 mC $cm^{-2}$, corresponding to a thickness of 1140 nm. One can observe that the cyclic voltammogram is different from that of MICP before extraction (figure 3.11) by the charge quantity passed in the film. This observation can be related to the loss in the mass of the film upon extraction and cycling in aqueous medium, which induces a decrease in the intensity of cyclic voltammograms of the conducting polymers.

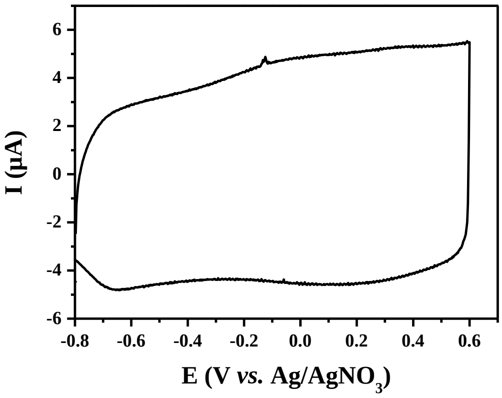

**Figure 3.19.** Cyclic voltammograms of MICP in 0.1 mol $L^{-1}$ $LiClO_4/H_2O$ after extraction of ATZ molecules in 0.1 M $LiClO_4/H_2O$ solution. The thickness of the film was 1140 nm, and the scan rate was 25mV $s^{-1}$.

However, the observed degradation behavior of the MICP film in aqueous media afforded a random behavior of the voltammograms upon different processes. Thus, we can conclude that in the implicated conditions detection of ATZ by MICP in aqueous media was not possible. Therefore, detection process will be systematically carried out in 0.1 mol $L^{-1}$ $LiClO_4$/ACN, in order to avoid the eventual degradation of the film in aqueous media.

### 3.8.2 Sensing properties of MICP in ACN medium

After the washing step and ATZ extraction, MICP voltammograms were recorded at a scan rate of 25mV $s^{-1}$, this time, in ACN in the presence of 0.1 mol $L^{-1}$ $LiClO_4$. Figure 3.20 (curve a) exhibits the cyclic voltammogram of washed MICP synthesized with an electropolymerisation charge of 100mC $cm^{-2}$, corresponding to a thickness of 1140 nm. One can observe that this cyclic voltammogram is different from the MICP before extraction by the charge quantity passed in the film (figure 3.12). This observation can be related to the decreased quantity of ATZ present in the matrix after the extraction procedure, which induces conformational variations in the macromolecular chains of the conducting polymers.

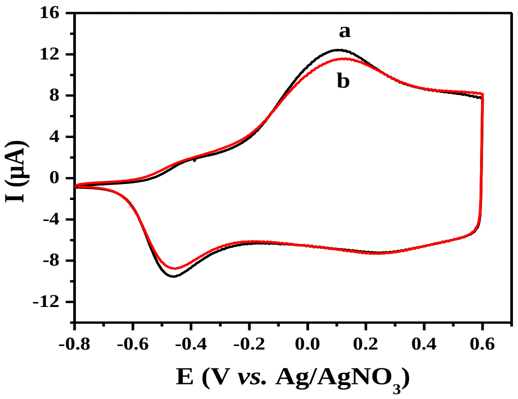

**Figure 3.20.** Cyclic voltammograms of MICP electrosynthesized in ACN containing 0.1 mol $L^{-1}$ $LiClO_4$. **(a)** after extraction of ATZ molecules. **(b)** after injection of $10^{-4}$ M in additional ATZ. The electropolymerization charge was 100mC $cm^{-2}$ (thickness of 1140 nm) and the scan rate was 25mV $s^{-1}$.

After the extraction step, one can suppose that the quantitative removal of atrazine enables the formation of free cavities, within the washed MICP copolymer matrix, these cavities hold the geometrical shape of the atrazine molecule with a specific distribution of the functionalities dedicated to the specific recognition of additional ATZ molecules, through the establishment of new interactions between the probe functional monomers and the target molecules. In order to check whether washed MICP is able to detect newly added target molecules, the modified gold electrodes were immersed in ACN solutions containing 0.1 mol $L^{-1}$ $LiClO_4$. Then, $10^{-4}$ mol $L^{-1}$ of ATZ was added to the electrolytic solution. This quantity was much lower than that used for MICP electrosynthesis ($15 \times 10^{-3}$ mol $L^{-1}$). Cyclic voltammetry was then used at a scan rate of 25mV $s^{-1}$ to check the modification of MICP voltammograms and to quantify the pesticide detection by the washed MICP. Figure 3.20 (curve b) exhibits the cyclic voltammogram of the previously studied washed MICP (curve a) once in the presence of $10^{-4}$ mol $L^{-1}$ in ATZ. In the electrolytic medium, the washed MICP displays a higher electroactivity in the absence of atrazine. The significant decrease in current, observed when atrazine is added to the solution, can be associated to the conformational variations occurring in the polymer during its redox activity. Two forms of polymer chains exist: the neutral state, which is polyaromatic, and the oxidized state which is polyquinoid. In the neutral state, there is a free rotation around the simple exocyclic bonds between thiophene units. The polymer chain can twist for adapting to the steric strain imposed by the presence of atrazine linked to the pendent acetic acid groups. On the other hand, the electroxidation of the polymer imposes the coplanarization of the polymer chains, owing to the required exocyclic double bonds between the thiophene units. In this case, the electroxidation of the polymer chain will become much more difficult, owing to the steric strain brought by the presence of associated atrazine. When compared to atrazine-free MICP, the redox currents will decrease, all the more as the quantity of complexed atrazine along the polymer chains will be higher. Thus, according to the results which concerned atrazine sensing by polythiophenes-based MICP[13], and oligonucleotide recognition by ODN functionalized polypyrroles[38,39,40], these considerations indicate that a quantitative characterization of atrazine can be obtained from the analysis of the redox currents (or the involved redox charges) as a function of the concentration of atrazine in the analyzed solution.

In order to quantify the current modification due to the addition of ATZ target molecules, electroxidation charges, can be calculated from cyclic voltammograms by area integration under the curves of current *versus* time. Hence, first, a charge $Q_0$ is calculated for the washed MICP in the absence of any target molecules; second, a charge Q is calculated for the MICP in the presence of additional ATZ molecules. Finally, a relative variation of the electroxidation charge $Q_r$ can be calculated according to equation (3.1):

$$Q_r = \frac{Q_0 - Q}{Q_0} \qquad \text{Eq 3.1}$$

Such a “relative charge” depends, as previously demonstrated[13], on the atrazine amount associated with the polymer matrix and must obviously be related to the sensing properties of the conducting polymers. A better recognition of the target molecules by the sensing layer induces a higher value of $Q_r$. Now, the sensing properties of the electrosynthesized conducting polymers should depend on their chemical functionalities and their structural properties, such as thickness and porosity.

In order to study the influence of the chemical and structural properties of the different conducting polymers on their sensing ability, MICP, NICP and PEDOT films of various thicknesses (285, 570, 1140 and 2280 nm) were electrosynthesized (with the adjusted electropolymerization charges, according to figure 3.18) onto gold substrates. We decided to avoid the synthesis of polymers of higher thicknesses since it is well known that the structural and electronic characteristics (stereoregularity, conductivity…) of conjugated polymers strongly depend on their thickness. In particular, above several micrometers in thickness, the polymers become too loose and too irregular for maintaining a satisfying reliability on their properties. The MICP films were systematically washed as previously described. In order to check and to compare the ability of washed MICP, NICP and PEDOT to detect the presence of newly added pesticide molecules, all the modified gold electrodes were immersed in ACN solutions containing $LiClO_4$ 0.1 mol $L^{-1}$. Then, $10^{-4}$ mol $L^{-1}$ of ATZ was added to the electrolytic solutions (as mentioned in *section 2.4*). Cyclic voltammetry was used at a scan rate of 25 mV $s^{-1}$ to check the modification of the voltammograms of the polymers and to quantify the current variations due to the addition of ATZ target molecules. Then, electroxidation charges, $Q_0$ and Q, were calculated from the cyclic voltammograms obtained respectively before and after the addition of atrazine. Finally, for each conducting polymer and for each thickness, a “relative charge” $Q_r$ was deduced according to equation (3.1).

The variation of the “relative charge” was reported on figure 3.21 as a function of the film thickness for each kind of conducting polymers: atrazine-free MICP, NICP and PEDOT. Each point of the curve corresponds to a mean value obtained from three independent measurements. Besides, the uncertainty bars corresponding to each point were displayed on the graph. Whatever the conducting polymer layer, the “relative charge”, $Q_r$, and thus the sensing properties increase with the thickness. While the value of the “relative charge” remains very low in the case of PEDOT homopolymer, the variation of $Q_r$ is much more pronounced in the case of MICP and NICP copolymers. The increase in $Q_r$ value could result from the amplification of the electrochemical transduction signal when the conducting polymer layer is thicker. Indeed, in the presence of atrazine target molecules, the conformational variations occurring in the polymer during its redox activity should depend on its structural properties, such as its thickness. In addition, such an increase in $Q_r$ can be assigned to the enhancement of the number of recognition sites in the polymer backbones: a thicker sensing layer displays more recognition sites, enabling the interaction with a higher fraction of target molecules. Since the electrode area covered by the polymer layer is a constant parameter during our experiments, this result indicates that the interaction between the target molecules and the sensing groups of the sensor layers takes place, not only at the surface, but also into the bulk of the conducting polymer matrixes. Thus, these results suggest that the recognition process operates as a 3D sensing device.

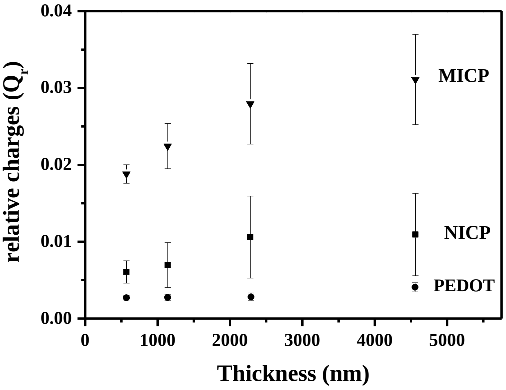

**Figure 3.21**. Evolution of the "relative charge", $Q_r$, as a function of the polymer film thickness of MICP (▼), NICP (■) and PEDOT (●). The conducting polymers were electrosynthesized on gold substrates by a 2-steps chronoamperometry technique. The "relative charges" were deduced from the cyclic voltammograms obtained before and after the addition of $10^{-4}$ mol $L^{-1}$ in ATZ. The thicknesses were measured by optical profilometry. Each point of the curves, represented with its error bar, corresponds to the mean value obtained from three experiments.

The variation of $Q_r$ is very pronounced in the case of MICP and NICP copolymers (figure 3.21). However, for thicknesses higher than 1140 nm, the "relative charge" values remain nearly constant, at about 3 $10^{-2}$ and $10^{-2}$ respectively in the cases of MICP and NICP. The non-linear dependence of $Q_r$ with the thickness indicates that the recognition process does not occur homogeneously in the polymer matrix. On the contrary, this process is limited by the diffusion of the target molecules into the polymer matrixes.

For a given thickness, the "relative charge" corresponding to MICP is higher than that of NICP, and much higher than that of PEDOT (figure 3.21). In other words, whatever the thickness, MICP copolymers correspond to the sensing layers which present the best sensing properties towards atrazine target molecules. On the contrary, although the ethylenedioxy residues of the EDOT monomer are able to interact with the pyridine cycle based molecules, through hydrogen bonds, as already demonstrated by Lomas et al.[41], in the present implied conditions, PEDOT films are bad sensing layers since the corresponding values of the "relative charge" remain very low in the implied conditions. This observation can be explained in terms of structural and chemical properties of the three kinds of conducting polymers considered in this work: MICP, NICP and PEDOT. First, the more porous structure of MICP and NICP, in comparison with that of PEDOT as deduced from AFM and optical profilometry, favors the diffusion of ATZ target molecules into the polymer matrixes. Second, the presence of TAA monomers in the copolymer structure of MICP and NICP, as observed by ATR-FTIR spectroscopy, can favor the interaction with ATZ target molecules thanks to hydrogen bonds between the carboxylic residues and the side amino groups and the nitrogen of the triazin cycle of ATZ with a pair of hydrogen bonds (figure 3.1). This was already investigated by $^1$H NMR study in the work of Matsui et al[42]. On the contrary, the TAA-free compact structure of PEDOT layer does not favor the diffusion and the recognition of atrazine. In this case, only weak "π- π" stacking interactions and a very limited number of hydrogen bonds, localized at the surface of PEDOT layers, can be involved between EDOT residues and aromatic atrazine target molecules. The London interactions with aromatic groups of the copolymers seem to be so weak in the case of PEDOT that they can be logically neglected in the cases of MICP and NICP in the implied conditions.

The difference in the behaviors of MICP and NICP can be understood not only in terms of structural properties, nor in terms of chemical functionalities, since TAA is present in both copolymers. The observed difference between MICP and NICP can be explained as follows: while NICP is synthesized in the absence of ATZ, MICP is electrosynthesized in the presence of target molecules. The following washing-step of MICP creates, only in the copolymer matrix of this kind of conducting polymers, free molecular imprinted cavities, where pendent acetic acid groups are spatially distributed for matching precisely the presence of bonding sites in the target ATZ molecules (figure 3.1). The pre-shaped imprinted cavities created in the MICP backbone keep the precise functional and geometrical memory of the targets at the molecular level and allow a 3D recognition process for the ATZ molecules. This enables the high selective chemical detection of additional atrazine molecules, leading to high values of the "relative charge". Such functional cavities do not exist in NICP layers. In these latter copolymers, TAA residues exist. However, since their spatial distribution is not optimal, these functional monomers interact with additional atrazine molecules only thanks to non-specific hydrogen-bonds interactions mostly at the specific surface of polymer, leading to lower values of the "relative charge".

Despite the lower relative charges values of NICP when compared to those of MICP, these values represent an important indication of the contribution of non-specific interactions implied during the recognition process at each film thickness. Table 3.2 represents the ratio of the relative charges $Q_{r\ NICP}/Q_{r\ MICP}$ as a function of the thickness. This ratio represents the relative contribution of non-specific adsorption at each thickness. We can conclude that, whatever the thickness of the film, a constant relative contribution of 33 % of non-specific adsorption is to be considered; assuming that the only difference between the MICP and NICP structures is the presence of functionalized cavities in the matrix of MICP film.

**Table 3.2.** An evaluation of non-specific adsorption contribution onto MICP layers based sensor measured by the ratio of NICP and MICP relative charges of detection of ($10^{-4}$ mol $L^{-1}$ of ATZ in 0.1 M $LiClO_4$/ACN) at different thicknesses.

| Thickness (nm) | 285 | 570 | 1140 | 2280 |
|---|---|---|---|---|
| $Q_{r\ NICP}/Q_{r\ MICP}$ (%) | 32 | 32 | 36 | 33 |

## 3.9 Range of atrazine detection by MICP in ACN

Among the different kinds of conducting polymers studied in this work, MICP films constitute the best sensing layers dedicated to the detection of ATZ, since their structure enables, first, the diffusion of the target molecules, and since their functionalized cavities imbedded into the polymer matrix enable, secondly, the precise matching of pesticides. As a consequence, the “relative charge” measured when $10^{-4}$ mol $L^{-1}$ in ATZ is added to the medium is much higher in the case of MICP than in the other cases.

As demonstrated, the “relative charge” depends on the sensing properties of the conducting polymers, but should also be related to the amount of additional atrazine[13]. Indeed, the sensitivity of an affinity-based sensor is first determined by the association constant between the probe and the target, i.e., between TAA and ATZ. Second, for a given probe, the quantity of associated ATZ targets will increase with the amount of TAA probes deposited on the sensor film.

Atrazine concentration used during the electrosynthesis of MICP was $15 \times 10^{-3}$ mol $L^{-1}$. Then, ideally, this concentration corresponds to the maximal number of preformed functionalized cavities present into the MICP matrix after the washing step. Thus, one can expect the ability of the MICP-based sensor to detect atrazine targets at concentrations lower than $15 \times 10^{-3}$ mol $L^{-1}$. However, if we suppose that all atrazine molecules do not act as molds during electropolymerisation, and if we assume that the washing step does not allow the release of all pesticides trapped into the MICP matrix, we can then consider that the concentration of preformed functionalized cavities can be much lower than that corresponding to 15 × $10^{-3}$ mol $L^{-1}$. Therefore, it was important to check whether the MICP-based sensor is able to detect decreasing amounts of atrazine. In addition, the characterization of our sensor in terms of detection range and limit of detection was essential.

In order to study the recognition properties of “our” best MICP sensing layer as a function of additional ATZ concentration, MICP films with a thickness of 1140 nm were all electrosynthesized in the same conditions onto gold substrates, then washed as previously described. Afterwards, these modified electrodes were immersed in different ACN solutions containing both 0.1 M $LiClO_4$ and ATZ at various concentrations ranging from 3 × $10^{-9}$ to 15 × $10^{-3}$ mol $L^{-1}$. For each sample, that is to say for each additional pesticide concentration, cyclic voltammetry was used at a scan rate of 25mV $s^{-1}$ to quantify the current modifications (an example for the detection of ATZ at $10^{-4}$ mol $L^{-1}$ is displayed in figure 3.22A). Then, electroxidation charges, $Q_0$ and Q, were calculated from the cyclic voltammograms obtained respectively before and after the addition of atrazine. Finally, for each MICP conducting polymer, a “relative charge” $Q_r$ was deduced according to equation 3.1. The “relative charge” was then plotted as a function of the atrazine concentration in solution (figure 3.22B).

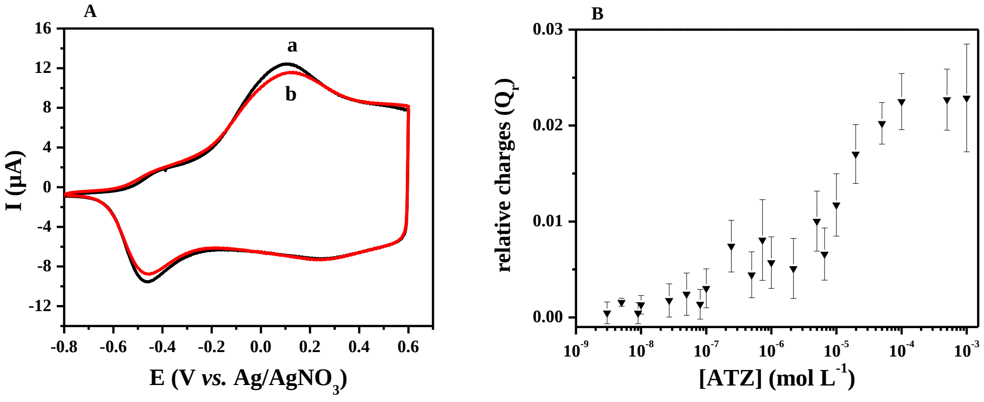

**Figure 3.22. (A)** Cyclic voltammograms of MICP in 0.1 mol $L^{-1}$ $LiClO_4$/ACN **(a)** after extraction of ATZ molecules. **(b)** after injection of $10^{-4}$ mol $L^{-1}$ in additional ATZ. The thickness of the film was 1140 nm, and the scan rate was 25 mV $s^{-1}$; **(B)** Variation of the “relative charge”, $Q_r$, of MICP (thickness of 1140 nm) as a function of additional ATZ concentration. Each point of the curves, represented with its error bar, corresponds to the mean value obtained from three experiments.

Once again, each point of the curve corresponds to a mean value obtained from three independent measurements. In addition, the uncertainty bars corresponding to each point are displayed on the graph. As expected for a sensing device, $Q_r$ increases with atrazine concentration following a sigmoid curve, as shown in figure 3.22B. This evolution can be understood in terms of variation in MICP electroactivity in the presence of increasing amounts of targets. First, at very low atrazine concentrations, the "relative charge" value is close to 0 and no detection can be foreseen. The $Q_r$ values become significant for atrazine concentrations higher than about $10^{-7}$ mol $L^{-1}$. This latter concentration can then be considered as the detection threshold of our MICP-based electrochemical sensor. Second, above $10^{-7}$ mol $L^{-1}$, a roughly linear steep increase of the relative charge can be observed up to a concentration of about $10^{-4}$ mol $L^{-1}$ in atrazine. Third, for higher concentrations, only a very slight increase is observed still about $10^{-3}$ mol $L^{-1}$ in atrazine, the response then tends to an asymptotic limit. This constant response indicates the saturation of the sensor, due first to the limited diffusion of the target molecules into the bulk of the polymer matrix and second to the limited number of accessible functionalized cavities.

Square wave voltammetry was also used to quantify the current modifications (figure 3.23A). Since square wave voltammetry has a much higher current sensitivity and better resolution than cyclic voltammetry, it was employed for the determination of ATZ concentration at MICP modified electrodes and for the estimation of lower limit of detection.

Optimized parameters used for square wave voltammograms were as follows: pulse amplitude was 100mV, potential step height was 10mV, and square wave frequency was 2.5 Hz. The peak current ($I_{pic}$) of the voltammogram was used to evaluate the detected concentration of ATZ target molecules. Increasing the concentration of the detected molecules results in the decrease of the peak current of the MICP situated at 0.3 V *vs.* Ag/$AgNO_3$ (figure 3.23A). These decreases in $I_{pic}$ value can be related to the conformational modification, as already discussed (*section 3.8*).

The peak current ($I_{pic}$)of the square wave voltammograms were plotted as a function of ATZ concentration in figure 3.23B. Once again, each point of the curve corresponds to a mean value obtained from three independent measurements. In addition, the uncertainty bars corresponding to each point are displayed on the graph. The evolution can be understood in terms of variation in MICP electroactivity in the presence of increasing amounts of targets. First, for higher concentrations, only a very slight difference is observed still about $10^{-4}$ mol $L^{-1}$ in atrazine. The anodic peak current is linear with ATZ concentration in the range of $10^{-8}$-$10^{-4}$ mol $L^{-1}$ (figure 3.23B) with a linear regression coefficient of ($R^2$ = -0.99) and the calculated detection limit (S/N = 3) is $10^{-9}$ mol $L^{-1}$.

The response then tends to an asymptotic limit indicating the saturation of the sensor response, due first to the limited diffusion of the target molecules into the bulk of the polymer matrix and second to the limited number of accessible functionalized cavities. Nevertheless, the dynamic range, as experimentally observed by SWV, should allow the use of MICP as selective sensitive layers integrated into electrochemical sensors for the detection of atrazine molecules, the concentration of which must be comprised between $10^{-8}$ and $10^{-4}$ mol $L^{-1}$. The dynamic ratio obtained thanks to our MICP-based atrazine sensing device is about $10^4$ ($10^{-4}$ / $10^{-8}$), value which is close to that of the dynamic ratios often mentioned for sensing devices in literature[43].

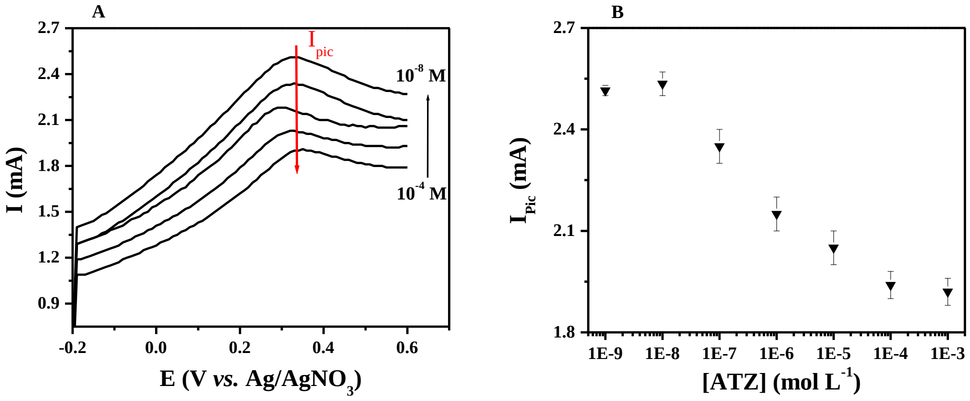

**Figure 3.23.** Square wave voltammograms of MICP (thickness of 1140 nm) in 0.1 mol $L^{-1}$ $LiClO_4$/ACN, pulse amplitude = 100mV, potential step height = 10mV, and square wave frequency = 2.5 Hz. **(A)** evolution of square wave voltammograms upon detection. **(B)** dependence of current peak, $I_{pic}$, of square wave voltammograms of MICP on the different concentrations of the detected ATZ target molecules ranging from $10^{-9}$ to $10^{-4}$ mol $L^{-1}$. Each point of the curves, represented with its error bar, corresponds to the mean value obtained from three experiments.

## 3.10 Selectivity of MICP towards ATZ in ACN

The MICP-based sensitive layer enables the quantitative detection of ATZ, due to the presence of pre-shaped functionalized cavities in the MICP backbone. The washing step of MICP allows the extraction of ATZ molecules from the polymer, which leaves molecular prints of ATZ in the matrix of the copolymer. These prints are specific, and possess a precise 3-Dimensional distribution of the functionalities able to engage hydrogen bonding with their counterparts, in ATZ target molecules. In order to check the selectivity of recognition of the sensor towards ATZ, other triazinic molecule belonging to the atrazine family: terbutylazine (TBZ), and another molecule: diuron (DRN), that belongs to another class of pesticides: halogenophenylurea family, were chosen (figure 2.1). TBZ differs from ATZ by the nature of one of the two lateral alkylamino groups linked to the aromatic structure: tertiobutylamino, and isopropylamino, respectively. Consequently, the two molecules differ by their molecular size and structure, although presenting the same chemical functionalities able to establish hydrogen-bonds with two carboxylic groups present in the MICP cavities. Diuron molecule is able to establish hydrogen-bonds with the preformed functionalized cavities by the functional carbonyl and amino groups linked to the aromatic structure, but its size, its structure and the spatial distribution of the functionalities are very different from those of ATZ molecule.

In order to check and to compare the ability of "washed MICP" to detect the presence of these molecules, ACN solutions containing 0.1 M of $LiClO_4$ and $10^{-4}$ mol $L^{-1}$ of pesticide were injected as already mentioned in *section 2.4*. Then, cyclic voltammetry in 0.1 mol $L^{-1}$ $LiClO_4$/ACN was carried out, as previously indicated, in order to quantify the detection of these target molecules. Hence, the relative charges corresponding to each target molecule were calculated using Eq (3.1) and displayed on histogram in Figure 3.24.

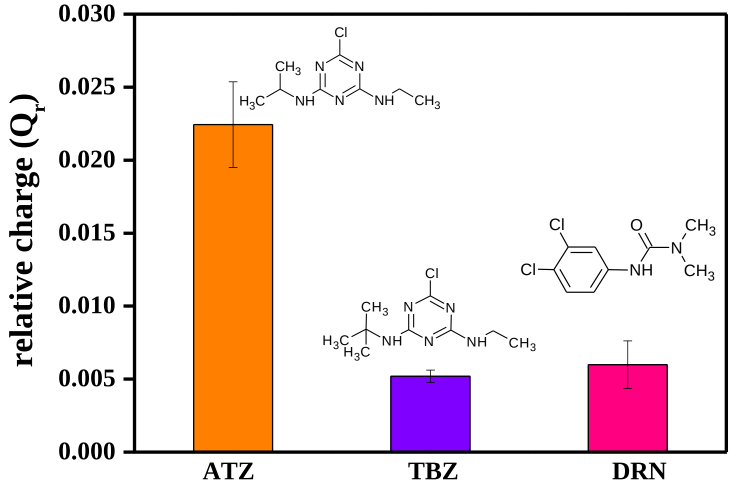

**Figure 3.24**. Relative charges corresponding to the detection by MICP (thickness of 1140 nm) of Atrazine (ATZ), Terbutylazine (TBZ), and Diuron (DRN), pesticides at a concentration of $10^{-4}$ mol $L^{-1}$ in 0.1 mol $L^{-1}$ $LiClO_4$/ACN solutions. Relative charges were deduced from the cyclic voltammograms at 25mV $s^{-1}$. Each value of the histogram, represented with its error bar, corresponds to the mean value obtained from three experiments.

As shown in figure. 3.24, the affinity of the MICP-based sensor depends on the nature of pesticide target. The high relative charge of detection of ATZ molecules indicates that the recognition of ATZ is more important when compared to TBZ and DRN molecules. Results suggest that the steric bulkyness of the targets plays an important role on the recognition process. The weaker recognition of TBZ when compared to ATZ can be understood in terms of molecular size of the lateral chain, tertiobutylamino, which is larger in comparison with isopropylamino group of ATZ. Although the presence of the same functionalities on TBZ and ATZ molecules, the larger size of TBZ prevents the specific recognition of these molecules by MICP films.

When comparing the relative charges of detection of ATZ and TBZ over MICP film, we obtain the ratio ~ 25 % which is smaller than that corresponding to the non-specific interaction ratio (~ 33%) estimated in *section 3.8*. Thus, we can conclude that TBZ molecules are only adsorbed non-specifically over MICP film and no specific recognition takes place.

In spite of smaller molecular size of DRN molecules, we note that the detection ratio of DRN to ATZ is only about 30% which is also inferior to the estimated ratio (33%) of non specific adsorption over MICP film (table 3.1).

As a conclusion, TBZ and DRN adsorb only at the polymer surface and are not specifically detected by imprinted cavities, thus, we can consider a good selectivity of MICP towards ATZ molecules.

## Conclusion

In this chapter, the effect of the nature of the functionalized polymer and the structural properties (thickness, roughness, and porosity) of MICP, NICP and PEDOT films were studied. The first objective was to understand the physical chemistry of the interaction between targets and the conducting polymer matrix. The second objective was to improve the sensitivity of the overall sensing process.

MICP, NICP and PEDOT conducting polymers were electrochemically grown layer by layer, which enables a precise control of their thickness through the adjustment of the electropolymerization charge. The observed dependence of the recognition properties of the conducting layers with their thickness and roughness indicates that the interaction between the target molecules and the sensing groups of the sensor layers takes place, not only at the surface, but also into the bulk of the conducting polymer matrixes in a tri-dimensional geometry. However, this 3D recognition process appears to be limited by the diffusion of the target molecules into the polymer matrixes.

In the case of PEDOT polymer, which does not bear a carboxylic probe moiety, the polymer layers do not favor the recognition of atrazine, since only weak "π- π" stacking interactions and limited number of hydrogen bonding sites of ethylenedioxy residues at the surface of the film can be involved between the EDOT units in the copolymer and the atrazine target molecules. On the contrary, the presence of TAA residues in the copolymer structure of MICP and NICP, indirectly favors the diffusion of the targets into the polymer matrixes, which enables a direct recognition of ATZ target molecules, thanks to hydrogen bonds. In comparison with NICP, the superior and remarkable sensing properties of MICP films result from the presence in their backbones of pre-shaped imprinted cavities which keep the precise functional and geometrical memory of the targets. Therefore, the presence of well spatially distributed pendent TAA groups enables matching of additional ATZ target molecules.

In addition to their sensitivity, the so-developed MICP electrochemical sensing layers, when used for the detection of atrazine, present a low limit of detection ($10^{-9}$ mol $L^{-1}$) and a large dynamic range ($10^{-8}$ to $10^{-4}$ mol $L^{-1}$).

Neverthless, non-specific adsorption of ATZ target molecules take also place in parallel with specific adsorption, which induces the non-specific recognition of different molecules. Thus, we can consider MICP layers as a selective sensor towards ATZ molecules if the influence of the non-specific adsorption is minimized or even eliminated. A complementary selectivity study on adsorption phenomenon will be carried out in *chapter 5* thanks to gravimetric transduction.

In the next chapter, the influence of the nature of the functional monomer present in MICP matrix on the recognition process will be studied, thanks to correlated experimental and theoretical investigations.

## References

---

[1] Pardieu, E. *Conception et développement d’un capteur électrochimique à base de polymères conducteurs à mémoire de forme pour la détection de petites molécules : application au cas de l’atrazine*. Sciences et Techniques Analytiques, Conservatoire National des Arts et Métiers CNAM, 2010.

[2] Pernelle, C. Pardieu, E. Garnier, F. Remita, S. *Détecteur électrochimique d’une petite molécule cible à base polymères conjugués à effet mémoire et procédé de détection utilisant un tel détecteur* » dépôt de brevet d’invention, référence : 9A-4963 cas 5, 2009.

[3] Pigani, L., Heras, A., Colina, A., Seeber, R., Lopez-Palacios, J., Electropolymerization of 3,4ethylenedioxythiophene in aqueous solutions. *Electrochem. Comm*. 6, 1192-1198, 2004.

[4] Sakmeche, N., Aeiyach, S., Aaron, J.J., Jouini, M., Lacroix, J.C., Lacaze, P.C., Improvement of the Electrosynthesis and Physicochemical Properties of Poly(3,4-ethylenedioxythiophene) Using a Sodium Dodecyl Sulfate Micellar Aqueous Medium *Langmuir*, 15, 2566-2574,1999.

[5] Du, X., Wang, Z. Effects of polymerization potential on the properties of electrosynthesized PEDOT films, *Electrochim. Acta*, 48, 1713-1717, 2003.

[6] Ventosa, E., Palacios, J.L., Unwin, P.R. Nucleation and growth of poly(3,4-ethylenedioxythiophene) thin films on highly oriented pyrolytic graphite (HOPG) electrodes. *Electrochem. Comm*. 10, 1752-1755, 2008.

[7] Scharifker, B.R., Garcia-Pastoriza, E., Marino, W. The growth of polypyrrole films on electrodes, *J. Electroanal. Chem.* 300, 85-98, 1991.

[8] Jorgensen, M., Norman, K., Krebs, F.C. Stability/degradation of polymer solar cells, *Sol. Energy Mater. Sol. Cells* 92, 686-714 ,2008.

[9] Constantine, C.A., Mello, S.V., Dupont, A., Cao, X., Santos, D., Oliveira, O.N., Strixino, F.T., Pereira, E.C., Cheng, T.C., Cheng, Defrank, J.J., Leblanc, R.M. Layer-by-layer self-assembled chitosan/poly(thiophene-3-acetic acid) and organophosphorus hydrolase multilayer, *J. Am. Chem. Soc*. 125, 1805-1809, 2003.

[10] Chan, H.S.O., Toh, C.S., Gan, L.M. Use of polythiophene and poly(thiophene-3-acetic acid) as charge-selective films for amperometric flow-cell detectors. *J. Mater. Chem*. 5, 631-637, 1995.

[11] Liu, C., Kuwahara, T., Yamazaki, R., Shimomura, M., Covalent immobilization of glucose oxidase on films prepared by electrochemical polymerization copolymerization of 3-methylthiophene and 3-thiophene-3-acetic acid for amperometric sensing of glucose: effects of polymerization conditions on sensing properties. *J. Eur. Polym*. 43, 3264-3276, 2007.

[12] Malitesta C., Guascito M. R., Mazzotta E., Picca R. A., X-ray photoelectron spectroscopy characteriazation of electrosynthesized poly(3-thiophene acetic acid) and its application in molecularly imprinted polymers for atrazine. *Thin Solid Films*, 518, 3705-3709, 2010.

[13] Pardieu E., Cheap H., Vedrine C., Lazerges M., Lattach Y., Garnier F., Remita S., Pernelle C., Molecularly imprinted conducting polymers based on electrochemical sensor for detection of atrazine. *Anal. Chim. Acta.* 649, 236-245, 2009.

[14] Liaw, D.J., Liaw, B.Y., Gong, J.P., Osada, Y. Synthesis and properties of poly(3-thiopheneacetic acid) and its networks via electropolymerization. *Synth. Met*. 99(1), 53-59, 1999.

[15] Gouzy, A., ATRAZINE, Données technico-économique sur les substances chimiques en France, Rapport INERIS n° DRC-07-86334-03509A, p4, 2007.

[16] Heinze, J., Rasche, A., Pagels, M., Geschke, B. On the origin of the so-called nucleation loop during electropolymerization of conducting polymers, *J. Phys. Chem. B* 111, 989-997, 2007.

---

[17] Dietrich, M., Heinze, J., Heywang, G., Jonas, F., Electrochemical and spectroscopic characterization of polyalkylenedioxythiophene. *J. Electroanal. Chem*. 369, 87-92 , 1994.

[18] Randriamahazaka, H., Noël, V., Chevrot, C. nucleation and growth of poly(3,4-ethylenedioxythiophene in acetonitrile on platinum under potentiostatic conditions. *J. Electroanal. Chem.* 472, 103-111, 1999.

[19] Hillman, A.R., Daisley, S.J., Bruckenstein, S. Kinetics and mechanism of the electrochemical p-doping of PEDOT. *Electrochim. Comm*. 9.1316-1322, 2007.

[20] Shoji, R., Takeuchi, T., Kubo, I. Atrazine sensor based on molecularly imprinted polymer-modified gold electrode. *Anal. Chem*. 75, 4882-4886, 2003.

[21] Pospisil, L., Trskova, R., Fuoco, R., Colombini, M. P. Electrochemistry of s-triazine herbicides: reduction of atrazine and terbutylazine in aqueous solutions. *J. Electroanal. Chem. 395*, 189-193, 1995.

[22] Li, F., Albery, W. J. A novel mechanism of electrochemical deposition of conducting polymers: two-dimensional layer-by-layer nucleation and growth observed for poly(thiophene-3-acetic acid). *Electrochim. Acta, 37,* 393-401, 1992.

[23] Chao, F., Costa, M., Tian, C. different steps in electrodeposition of poly(3-methylthiophene) films on platinum electrodes studied by ellipsometry, SEM, and AFM techniques. *Synth. Met. 53*, 127-147, 1993.

[24] Schrebler, R., Grez, P., Cury, P., Veas, C., Merino, M., Gomez, H., Cordova, R., del Valle, M. A. Nucleation and growth mechanisms of poly(thiophene) Part 1. Effect of electrolyte and monomer concentration in dichloromethane. *J. Electroanal. Chem. 430*, 77-90, 1997.

[25] Tamburri, E., Orlanducci, S., Toschi, F., Terranova, M. L., Passeri, D. Growth mechanisms, morphology, and electroactivity of PEDOT layers produced by electrochemical routes in aqueous medium. *Synth. Met. 15*9, 406-414, 2009.

[26] Randriamahazaka, H., Sini, G., Tran Van, F. Electrodeposition mechanisms and electrochemical behavior of poly(3,4-ethylenedithiathiophene). *J. Phys. Chem. C* 111, 4553-4560, 2007.

[27] Brown, A. P., Anson, F. C. Cyclic and differential pulse voltammetric behaviour of reactants confined to the electrode surface. *Anal. Chem.* **1977,** *49*, 1589-1595.

[28] Kvarnström, C., Neugebauer, H., Blomquist, S., Ahonen, H. J., Kankare, J., Ivaska, A. In situ spectroelectrochemical characterization of poly(3,4-ethylenedioxythiophene) *Electrochim. Acta 44*, 2739-2750, 1999.

[29] Hernandez, V., Ramirez, F.J., Otero, T. F., Lopez Navarrete J.T. An interpretation of the vibrational spectra of insulating and electrically conducting poly(3-methylthiophene) aided by a theoretical dynamical model. *J. Chem. Phys.* 100,114-129, 1994.

[30] Tran-Van, F., Garreau, S., Louarn, G., Froyer, G., Chevrot, C. Fully undoped and soluble oligo(3,4-ethylenedioxythiophene)s: spectroscopic study and electrochemical characterization. *J. Mater. Chem. 11*, 1378-1382, 2001.

[31] Li, J., Zhao, J., Wei, X. A sensitive and selective sensor for dopamine determination based on a molecularly imprinted electropolymer of *o*-aminophenol. *Sens. Actuat. B* 140, 663-669, 2009.

[32] Im, S. G., Gleason, K.K. Systematic control of the electrical conductivity of poly(3,4-ethylenedioxythiophene) via oxidative chemical vapor deposition. *Macromolecules*. *40*, 6552-6556, 2007.

[33] Neugebauer, H., Nauer, G., Neckel, A.,Tourillon, G., Garnier, F., Lang, P. In situ investigations of the 3-methylthiophene polymer with attenuated total reflection Fourier transform infrared spectroscopy. *J. Phys. Chem. 88* (4), 652, 1984

---

[34] Bazzaoui, E.A., Aeiyach, S., Lacaze, P.C. Electropolymerization of bithiophene on Pt and Fe electrodes in an aqueous sodium dodecylsulfate (SDS) micellar medium. *Synth. Met. 83*, 159-165, 1996.

[35] Seo, K. I., Chung, I. J. Reaction of 3,4-ethylenedioxythiophene with potassium persulfate in aqueous solution by using a calorimeter. *Polymer* 41, 4491–4499, 2000.

[36] Zhang, Z., Imae, T. Hydrogen-bonding stabilized self-assembled monolayer film of a functionalized diacid, protoporphyrin IX Zinc (II), onto a gold surface. *Nano Lett.* 1, 5, 241-243, 2001.

[37] O'Neil, K. D., Semenikhin, O. A. AFM phase imaging of electropolymerized polybithiophene films at different stages of their growth. *J. Phys. Chem. C*, 111, 14823-14832, 2007.

[38] Garnier, F., Youssoufi Korri, H., Srivastava, P., Yassar, A. Enzyme recognition by polpyrrole functionalized with bioactive peptides. *J. Am. Chem. Soc.* 116, 8813-8814, 1994.

[39] Garnier, F., Bouabdallaoui, B., Srivastava, P., Mandrand, B., Chaix, C. Conjugated polymer based DNA chip with real time access and femtomol detection threshold. *Sens. Actuat. B* 123, 13-20, 2007.

[40] Garnier, F., Torrence P.P., (Ed.), John Wiley & sons, New York, 2000, p. 349-359

[41] Lomas, J. S., Cordier, C. Diols as hydrogen bond acids: 1H NMR study of the hetero-association of pyridine with sterically hindered EDOT diols. *J. Phys. Org. Chem*. 22, 289-297, 2009.

[42] Matsui, J.; Miyoshi, Y.; Doblhoff-Dier, O.; Takeuchi, T. A molecularly imprinted synthetic polymer receptor selective for atrazine. *Anal. Chem.* **1995**, 67, 4404-4408

[43] Janata, J. *Principles of Chemical Sensors,* Springer, New York, 2009.

# Chapter 4

## Influence of the chemical functionalities of a MICP on its sensing properties: electrochemical measurements and semi-empirical DFT calculations

This chapter aims to study the influence of chemical functionalities of conducting polymers onto their sensing properties. Indeed modifying the nature of the functional monomer (FM) into the pre-polymerization complex and into the MICP matrix is an interesting point which would enable the improvement of recognition properties of the MICP based sensors. On the other hand, variations of the nature of FM into NICP layers would enable an estimation of the systematic contribution of the non-specific adsorption.

Starting from thiophene-based functional monomers (FM), namely TMA, TAA, TMeOH, EDOT and Th, bonded to atrazine (ATZ) target molecules into FM/ATZ pre-polymerization dimers in acetonitrile solutions, differently functionalized Molecularly Imprinted Conducting Polymers (FM-MICP), and Functionalized Non-Imprinted Conducting Polymers (FM-NICP) will be electrosynthesized, then washed and used as sensitive layers for ATZ recognition. Sensitivity of FM-MICP and FM-NICP layers towards ATZ, will be quantified by cyclic voltammetric measurements.

Besides, in order to study the influence of the formation of FM/ATZ pre-polymerization complexes on the efficiency of the recognition process by FM-MICP as well as by FM-NICP, absolute values of the FM-ATZ dimerization free energies will be calculated with the help of DFT/PCM calculations.

## 4.1 Introduction

The detection of small organic molecules remains an open challenge since their interaction with pendent binding sites present in a MICP polymer matrix is not really understood. In addition, the factors which contribute to the binding, such as ionization state, polarity, hydrophobicity need to be identified and quantified. An ideal sensor must be able to specifically detect very small amounts of a target. This implies, in our case, the development of the more specific and the more sensitive MICP layer. In particular, this means that the functionalized probes present into the polymer matrix must be well spatially distributed and must present a very high specific affinity towards the target in a given medium (polar or apolar). The choice of the chemical functionalities of the monomers, as polymers starting-blocks, appears then determining. These functionalities are first involved during the association of the monomers with the targets in the pre-polymerization complexes. They are second implied during the binding of the targets with the polymer matrixes. A strong interaction of the probes with the targets must then lead to a MICP matrix with highly specific imprints and, as a consequence, to a very sensitive functionalized layer.

The literature describing molecularly imprinted polymers was to a large extent focused upon systems employing new template structures, monomers and polymerization formats and, significantly, presenting new areas for the application of these materials. The earliest attempts to describe aspects of the molecular imprinting process using physical or mathematical formalism involved the use of thermodynamic models[1,2,3,4,5,6]. Computational techniques were used to investigate both various aspects of the molecular imprinting process and of polymer performance. The characterization of molecular complexes formed by templates and monomers association (with the aim of achieving a clearer picture of the interactions that are the basis of the MIP technology), was the goal of numerous experimental as well as several theoretical studies. Examples of the latter include the use of the semi-empirical Austin model (AM1) method for the optimization of a complex between (S)-nilvadipine[7], the use of the parameter method (PM3) for describing complexes formed between (S)-naproxen and acrylamide molecules[8], and for the optimization of a complex between 2,4,6-trichlorophenol and four molecules of 4-vinylpyridine[9]. Furthermore, it was demonstrated that the binding energies calculated by the AM1 method for complexes of a cocaine molecule and 1 to 14 molecules of either methacrylic acid or 4-vinylpyridine can be used to optimize the composition of the polymerization mixture (template-functional monomer ratio)[10]. The proposed optimal ratio was subsequently validated by both NMR and rebinding studies on a series of synthesized MIPs, thus confirming the feasibility of the computational approach.

Quantum chemical calculations-based strategies were implied for the optimizing of MIP performance through the selection of suitable functional monomers. Generally, by modeling the complexes between the template and a set of different functional monomers, binding energies that can act as a guide for choosing an optimal functional monomer may be obtained. Further examples include the calculation of the structures of the complexes formed between series of compounds and two molecules of methacrylic acid[11]. In this case, the structural parameters obtained by AM1 calculations can be correlated to the results of experimental data in the form of chromatographic studies.

The main limitation in the application of quantum mechanics based methods to MIP systems is the ability to handle the large numbers of atoms necessary to provide a comprehensive picture of the pre-polymerization or polymer system, and the inclusion of any reasonable number of solvent molecules would make the calculations expensive by means of computational time. However, methods such as the polarisable continuum model (PCM), provide the possibility of including solvent effects without the inclusion of solvent molecules[12]. Nonetheless, the validity of this assumption appears limited in light of reports[13]. In PCM calculations the effect of the solvent is approximated by placing the system in a cavity with a surface that is polarisable according to the dielectric constant of the modeled solvent. An important limitation of the PCM method is that not all solvents can be modeled due to the inability of the PCM method to include the effect of hydrogen bounds to solvent molecules, which compete with the hydrogen bounds formed between the template molecules and functional monomers.

Small molecules simulation presents an interesting tool especially with newer force fields, such as GAFF[14], designed specifically to simulate small organic molecules, in particular structures of clinical significance. It was frequently observed that there exists a correlation between observed strength of monomer-template interactions in pre-polymerization mixtures and recognition properties of the final MIP product[3]. Thus, a theoretical means of evaluating the probability of monomers and templates interacting should assist in the selection of experimental conditions.

While quantum and semi-empirical approaches allow determination of the absolute energies of monomer-template interactions, these methods tend to be limited by a number of factors, e.g., the inability to explicitly simulate solvent or to account for dimerisation of mixture components. Molecular dynamic studies, in contrast, permit the qualitative evaluation of the types of interaction occurring in a mixture, the frequency of such interactions across a given time frame, and the lifetimes of complexes. All these factors provide indications to the suitability of a particular combination of monomer and solvent to a given MIP application. Evidence in the literature demonstrates that in non-covalent imprinting procedures, processes such as monomer-monomer interactions[15], template-template interactions[16,17], template self association induced by interaction with functional monomers[18,19] and template-cross linker interactions[20] can all have important consequences for the recognition properties of resultant MIPs. Naturally, more complex scenario involving the various components present in the polymerization mixture also exists, not least the role of the solvent/porogen. Thus, the complexity exhibited by pre-polymerization systems would suggest that stringent study is required, and simulations of these systems must exclude bias towards monomer-template complexation. For this reason, molecular dynamics is ideally suited to describe the evolution of these systems, allowing the researcher to examine the competing non-covalent processes observable in the simulated systems.

The use of molecular dynamics technique for describing monomer-template interactions was presented in reviews, such as: O'Mahony et al. 2005[21]; Karim et al. 2005[22]; Mayes and Whitcombe, 2005[23]. This underlines that the use of theoretical approaches in developing MIPs is best used as part of an integrated approach to polymer design and optimization, where they are complemented by spectroscopic and thermodynamic methods of examining the pre-polymerization mixture. The Piletsky group pioneered and refined a molecular dynamics based protocol (Piletsky et al. 2001[24]) for the selection of functional monomer for a given template by non-covalent imprinting only. Following the creation of a library of functional monomer molecules (21 functional monomer molecules were selected for the library), the template is then 'screened' against the components of the library in a fashion analogous to the ligand or fragment screening processes used in drug discovery research[25]. This involves allowing the monomer and template molecules to interact to find a minimum energy conformation. The Optimum monomer-template complex configurations can then be identified. This process is applied to a template molecule in a virtual box, rather than to multiple copies (thus excluding the possibility of template-template effects), and often with the use of limited numbers of functional monomers (thus limiting insight regarding functional monomer-functional monomer interactions), which may be considered a limitation of this procedure.

It's generally accepted in the field of MIP (and *a fortiori* in our case for MICP) that the increased number of the interactions in the pre-polymerization complex will increase the number of binding sites in the polymer matrix and account for greater fidelity of these sites, and impart greater affinity, specificity and selectivity to the sensor. However, this supposition is insufficient to develop the specificity of the MICP-based sensor, because the number of functional groups in the polymer binding site is not determined only by the solution phase pre-polymer complex; rather it is determined during polymerization. Because of the difficulty of characterizing the binding site structures during and after polymerization, the actual events determining the final binding site structure are still relatively difficult to be evaluated.

In the present chapter, we experimentally and theoretically study the influence of the nature of the chemical functionalities of a polythiophene-based MICP on its ability to bind and then to detect a target molecule, atrazine. Differently functionalized thiophene-based monomers are used in order to form pre-polymerization complexes with atrazine in acetonitrile solvent. The binding energies involved are calculated using a quantum chemical approach. The polymerization of the thiophene-based monomers in the presence of atrazine leads to differently functionalized MICP. The recognition of additional amounts of atrazine is quantified by electrochemical measurements. We finally propose in this chapter a correlation between the binding energy involved in the pre-polymerization complex and the sensitivity of the MICP-based sensor.

## 4.2 Electrochemical evaluation of the sensing properties

### 4.2.1 Electrochemical polymerization and electrochemical measurements

In this chapter, molecularly imprinted conducting polymers or copolymers, **MICP**-based sensitive layers were electrochemically obtained by polymerization of EDOT monomers in the presence of ATZ target molecules (FM = EDOT) or by copolymerization of EDOT with another kind of functional monomers (FM = TAA, TMA, TMeOH or Th) associated by non covalent interactions with ATZ target molecules (Figure 4.1A, electrosynthesis). For clarity, for all functional monomers (FM) used, the obtained Poly(EDOT/ATZ) polymers and Poly(EDOT-co-FM/ATZ) copolymers are noted **FM-MICP**.

For FM-MICP preparation, FM functional monomers (EDOT, TAA, TMA, TMeOH or Th) at a concentration of $30 \times 10^{-3}$ mol $L^{-1}$ were dissolved in acetonitrile solvent, in the presence of $LiClO_4$ (0.1 mol $L^{-1}$, as supporting electrolyte), together with ATZ molecules at a concentration of $15 \times 10^{-3}$ mol $L^{-1}$. A sufficient lap of time of 10 minutes was used in order to favor the association between FM and ATZ, through non covalent interactions, in FM/ATZ pre-polymerization complexes. Then, EDOT, at a concentration of $7.5 \times 10^{-3}$ mol $L^{-1}$, was added as a linker, before electropolymerization, to each FM/ATZ solution.

Another type of films, non-imprinted conducting polymers or copolymers, **NICP**, was also electrochemically prepared, but in the absence of target molecules in the pre-polymerization media (figure 4.1B, electrosynthesis). NICP polymers were synthesized by polymerization of EDOT monomers (FM = EDOT), while NICP copolymers were obtained from the copolymerization of EDOT monomers with another kind of functional monomers (FM = TAA, TMA, TMeOH or Th). For clarity, in the case of all functional monomers (FM) used, the obtained Poly(EDOT) polymers and Poly(EDOT-co-FM) copolymers are noted **FM-NICP**.

For FM-NICP preparation, FM functional monomers (EDOT, TAA, TMA, TMeOH or Th) at a concentration of 30 × $10^{-3}$ mol $L^{-1}$ were dissolved in acetonitrile solvent, in the presence of $LiClO_4$ (0.1 mol $L^{-1}$, as supporting electrolyte) but in the absence of ATZ molecules. Then, EDOT, at a concentration of $7.5\times10^{-3}$ mol $L^{-1}$, was added as a linker to each FM solution, before electropolymerization.

Electropolymerizations were carried out in a conventional three-electrode electrochemical cell. The working electrodes were gold surfaces with a surface area of 3.14 $mm^2$ (BAS electrodes), prepared as already indicated in *section 2.2*. Counter electrodes were stainless steel sheets, and all potentials were measured versus $Ag/AgNO_3$ reference electrodes. Prior to all the experiments, the solutions were purged with argon. Such an inert atmosphere was maintained over all the solutions during the measurements.

In order to study the electrochemical behaviors of FM functional monomers as well as those of synthesized FM-MICP and FM-NICP films, cyclic voltammograms were recorded at a scan rate of 25mV $s^{-1}$. All cyclic voltammograms were obtained by subtracting the background current corresponding to the electrolyte (0.1 mol $L^{-1}$ of $LiClO_4$ in ACN). Several preliminary experiments were performed in order to determine the oxidation potentials of the different FM functional monomers. Electrosynthesis of FM- MICP and FM-NICP films at the surface of gold electrodes, under potentiostatic conditions, was realized using a 2-steps chronoamperometry technique in the electrochemical cell. In the first step, the potential was switched from 0.0 to 0.8 V for a period of ca. 10 s. Polymerization was achieved by a second step at a constant potential of 1.45 V *vs*. $Ag/AgNO_3$. Specific times were used during this second chronoamperometric step in order to adjust the electropolymerization charges at 3.14 mC for 3.14 $mm^2$ of active surface of the working electrode (100 mC $cm^{-2}$).

Contrarily to non-imprinted conducting FM-NICP films, molecularly imprinted FM-MICP layers were electrosynthesized in the presence of atrazine (figure 4.1A, electrosynthesis). In order to remove the target molecules from FM-MICP matrixes, by destroying the non covalent intermolecular interactions which involve ATZ and polymerized functional monomers, a methanol/acetic acid solution (0.7:0.3 v/v) was used to wash the polymer-coated electrodes for 10 min (as already indicated in *section 2.4*). This washing step leads to the desired creation of molecular imprinted cavities within the copolymer matrixes of FM-MICP (figure 4.1A, ATZ extraction). These cavities keep the memory of the interactions between FM functional monomers and ATZ molecules (see *section 3.8*). Indeed, the spatial distribution of the polymerized functional monomers into the polymer matrixes allows the precise matching of additional ATZ molecules. Thus the so-prepared washed FM-MICP modified electrodes can act as electrochemical sensors to quantify the presence of new additional ATZ pesticides thanks to the establishment of new intermolecular FM/ATZ interactions between the probe-functionalized monomer units and the target molecules (figure 4.1A, ATZ detection).

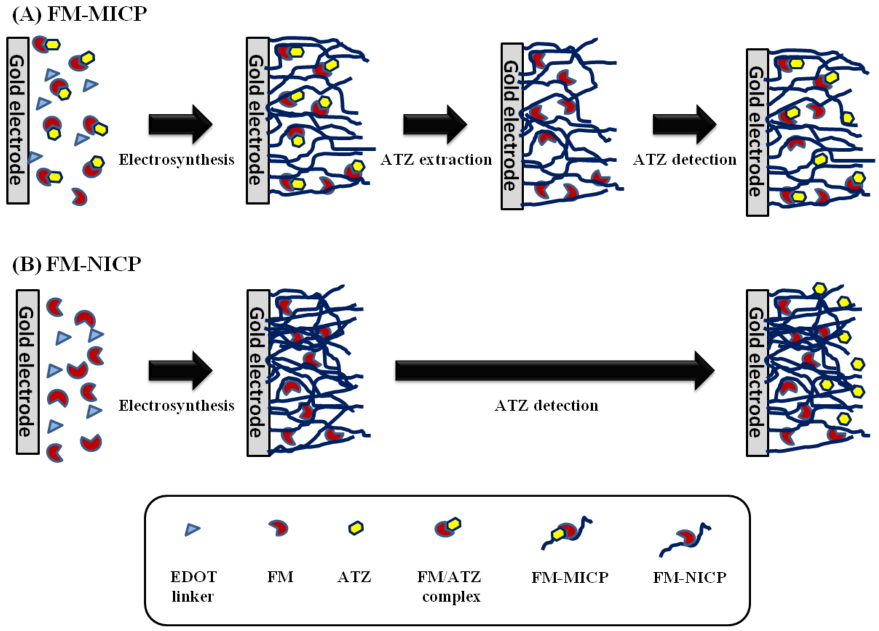

**Figure 4.1. (A)** Electrosynthesis and use for ATZ detection of FM-MICP. **(B)** Electrosynthesis of FM-NICP. The FM functional monomers are TMA, TAA, TMeOH, EDOT or Th.

Contrarily to FM-MICP films, FM-NICP layers don't display molecular imprinted cavities able to specifically interact with target molecules (figure 4.1B, electrosynthesis). Nevertheless, in both FM-MICP and FM-NICP cases, non specific adsorption of additional ATZ molecules is possible (figure 4.1A and B, ATZ detection). In order to check and to compare the ability of FM-MICP (by specific bounding and by adsorption) and FM-NICP (only by adsorption) to interact with newly added pesticide targets, the modified gold electrodes were immersed for 10 min in ACN solutions containing ATZ at a concentration of $10^{-4}$ mol $L^{-1}$ in the presence of $LiClO_4$ 0.1 mol $L^{-1}$. The presence of added pesticide targets and consequently the recognition process was then analyzed using an amperometric method. Modification of FM-MICP and FM-NICP conducting polymers electrochemical signatures was monitored by the use of cyclic voltammetry. To quantify the current modifications when targets were added to the solution, the oxidation and reduction charges were calculated from cyclic voltammograms, by area integration under the curve of current *versus* time, this latter being related to the applied potential and to the scan rate.

### 4.2.2 FM-MICP and FM-NICP electrosynthesis.

In order to determine the "ideal" electropolymerization potential, which can be used for FM-MICP and FM-NICP electrosynthesis, the redox behaviors of functionalized monomers were studied in ACN using cyclic voltammetry. FM oxidation potentials $E_p$, represented in Table 4.1, were determined *vs.* Ag/$AgNO_3$ electrode at a scan rate of 25 mV $s^{-1}$.

**Table 4.1.** Oxidation potentials of the different functional monomers. These potentials were determined by Cyclic Voltammetry *vs.* Ag/$AgNO_3$ at a sweep rate of 25 mV $s^{-1}$.

| **FM** | **TMA** | **TAA** | **TMeOH** | **EDOT** | **Th** |
|---|---|---|---|---|---|
| **$E_p$ (V *vs.* Ag/$AgNO_3$)** | 1.85 | 1.80 | 1.41 | 1.30 | 0.95 |

Although the relative high oxidation potentials obtained for TMA and TAA in comparison with those of the other functional monomers, an electropolymerization potential of 1.45 V *vs.* Ag/$AgNO_3$ was found to be sufficient to initiate EDOT polymerization as well as FM and EDOT copolymerization whatever the functional monomer. Applying such a potential enabled in all the cases the synthesis of the different FM-MICP and FM-NICP films respectively in the presence and in the absence of ATZ (Figure 4.1A and B, electrosynthesis). In all the cases, no polymer films overoxidation was observed. In addition, ATZ molecules didn't show any electroactivity in the used potential range as demonstrated in *section 3.4*.

### 4.2.3 FM-MICP and FM-NICP electrochemical characterization.

After the electrosynthesis step, the obtained FM-MICP and FM-NICP cyclic voltammograms were recorded for each FM functional monomer at the same scan rate of 25 mV $s^{-1}$. For illustration, Figure 4.2A displays voltammograms obtained in the case of TMA functional monomer, while Figure 4.2B displays those of Th.

The FM-MICP voltammograms are all different, as can be observed, for example, when comparing figures 4.2A and 4.2B in the cases of TMA and Th as FM functional monomers. This indicates that the structure of the electrosynthesized FM-MICP films depends on the nature of the FM functional monomer. This result demonstrates that in all the cases, in addition to EDOT, FM functional monomers are present into the polymer matrixes of FM-MICP. In our experimental conditions, the copolymerization is thus systematic. Since the FM-NICP voltammograms are also different from each others, one can deduce that FM functional monomers are also incorporated into the non-imprinted matrixes.

For each FM functional monomer, FM-MICP voltammogram differs from FM-NICP one, as can be observed on figures 4.2A and 4.2B respectively in the cases of TMA and Th. This is also the case for all the other FM functional monomers (TAA, TMeOH and EDOT). Such a difference between FM-MICP and FM-NICP voltammograms proves the incorporation of ATZ molecules into the matrixes of each molecularly imprinted conducting polymer, whatever the FM functional monomer. When present, ATZ molecules affect the conformation, the conductivity and then the electrochemical signature of the electrosynthesized polymers.

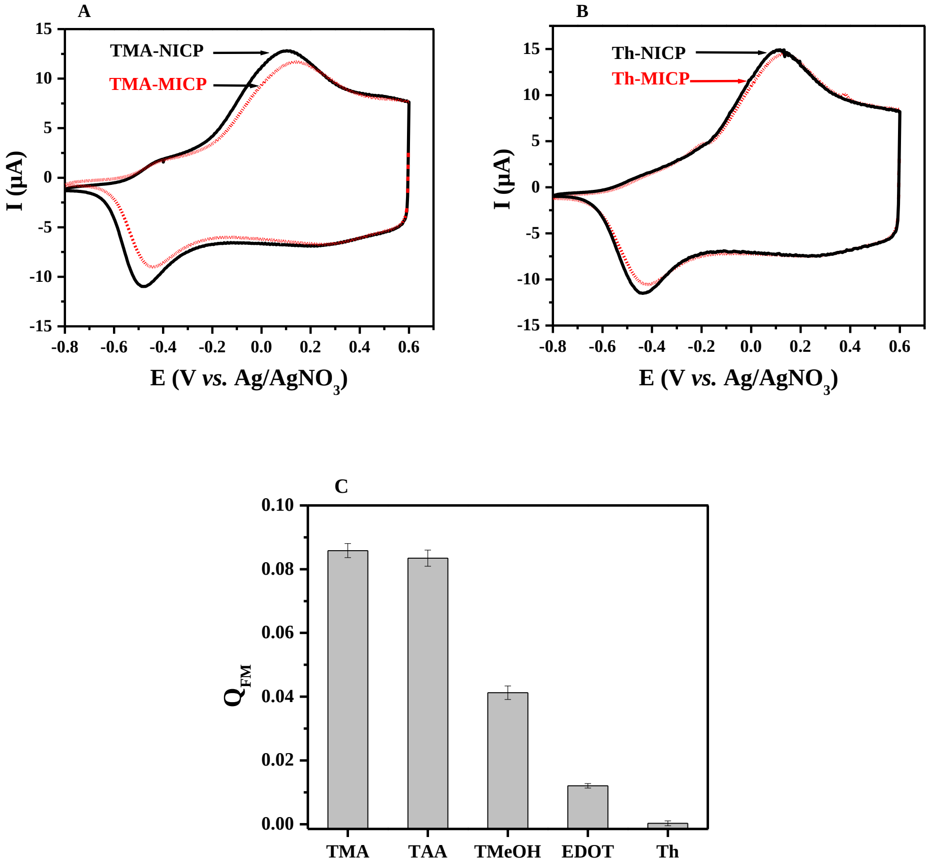

**Figure 4.2. (A)** Cyclic voltammograms of TMA-MICP and TMA-NICP films (FM = TMA). **(B)** Cyclic voltammograms of Th-MICP and Th-NICP films (FM = Th). All cyclic voltammograms were recorded in 0.1M $LiClO_4$/ACN solutions at a scan rate of 25mV $s^{-1}$. **(C)** Relative charges, $Q_{FM}$, measured for the different FM functional monomers (FM = TMA, TAA, TMeOH, EDOT or Th). Each charge value, represented with its error bar, corresponds to the mean value obtained from three experiments.

The electroactivity of FM-NICP films is always higher than that of FM-MICP layers, as observed for TMA and Th (Figures 4.2A and 4.2B). The decrease in the charge passed in the FM-MICP voltammograms is due to ATZ molecules which induce conformational strain in the imprinted films upon oxidation. Due to the hindrance exercised by the presence of ATZ molecules, the conjugation length over the FM-MICP macromolecular chains is reduced, which modifies the electrochemical behavior’[26,27] as well as the optical properties[28,29,30,31] of the conducting polymers based films.

Nevertheless, the observed difference between FM-MICP and FM-NICP voltammograms is more or less important depending on the nature of FM. In particular, the difference is more pronounced in the case of TMA than in the case of Th functional monomer (figure 4.2). This demonstrates that the quantity of ATZ incorporated into the FM-MICP depends on the nature of the FM functional monomer and thus on the strength of the intermolecular interaction between ATZ and FM in the pre-polymerization complex.

In order to quantify the relative difference between FM-MICP and FM-NICP voltammograms (due to the amount of incorporated ATZ molecules) for each FM functional monomer, electrooxidation charges are calculated, from cyclic voltammograms by area integration under the curves of current *versus* time. Charges $Q_{FM\text{-}NICP}$ and $Q_{FM\text{-}MICP}$ are first calculated from the FM-NICP and FM-MICP voltammograms respectively. Then, a relative variation of the electrooxidation charge, $Q_{FM}$, is deduced from equation (4.1):

$$Q_{FM} = \frac{Q_{FM-NICP} - Q_{FM-MICP}}{Q_{FM-NICP}} \qquad \text{Eq 4.1}$$

The so-calculated $Q_{FM}$ values are represented on the histogram of figure 4.2C as a function of the nature of the FM functional monomer. Each value corresponds to a mean value obtained from three independent measurements. Besides, the uncertainty bars corresponding to each point were displayed on the graph. It appears that $Q_{TMA}$ is a little bit higher than $Q_{TAA}$, these two values being higher than $Q_{TMeOH}$ and much higher than $Q_{EDOT}$ and $Q_{Th}$.

These results indicate a decreased amount of incorporated ATZ molecules in the following order of functional monomers-based MICP: TMA, TAA, TMeOH, EDOT and Th. Since a higher interaction between ATZ and FM functional monomer into the FM/ATZ pre-polymerisation complex lead to a better incorporation of ATZ into the FM-MICP polymerized matrix, one can suppose, at this stage of the work, that the non-covalent interactions between TMA and ATZ or between TAA and ATZ are stronger than the interactions involving TMeOH and much stronger than those implying EDOT and Th.

Note that in all the cases, for each FM-MICP electrosynthesis, EDOT is always present as linker. As a consequence, since EDOT interacts (even weakly) with ATZ, EDOT/ATZ pre-polymerization dimers are also to be considered. Thus, the embedded quantity of ATZ into the FM-MICP polymer matrix, in the cases of TMA, TAA, TMeOH and Th, depends not only on FM/ATZ complexes concentration, but also on EDOT/ATZ dimers number. However, in the case of EDOT-MICP, where EDOT plays the double role of linker and functional monomer, only EDOT/ATZ complexes quantity intervenes. Nevertheless, whatever the electrosynthesized FM-MICP, the study of the correlation between the $Q_{FM}$ charge and the sum of the pre-polymerization dimers concentrations, [FM/ATZ] + [EDOT/ATZ], seems to be interesting. This will be considered in *section 4.4*.

### 4.2.4 FM-MICP and FM-NICP sensing properties.

Unlike non-imprinted conducting FM-NICP films, molecularly imprinted FM-MICP layers were electrosynthesized in the presence of atrazine. In order to quantitatively remove the target molecules from FM-MICP matrixes, a methanol/acetic acid solution was used to wash the polymer-coated electrodes. After this washing step, the obtained FM-MICP cyclic voltammograms were recorded for each FM functional monomer at the same scan rate of 25mV $s^{-1}$. For illustration, Figures 4.3A and B (curves a) display the voltammograms obtained respectively in the cases of TMA and Th functional monomers. This washing step leads to the desired creation of free molecular imprinted cavities within the FM-MICP polymer matrixes, dedicated to the specific detection of additional ATZ molecules thanks to the establishment of new intermolecular FM/ATZ interactions between the probe-functionalized monomer units and the target molecules.

In order to check, for each kind of FM functional monomers, whether washed FM-MICP films are able to detect newly added target molecules, the modified gold electrodes were immersed in ACN solutions containing $LiClO_4$ 0.1 mol $L^{-1}$. Then, $10^{-4}$ mol $L^{-1}$ of ATZ was added to the electrolytic solution. This quantity was much lower than that used for FM-MICP electrosynthesis (1.5 $10^{-2}$ mol $L^{-1}$). Cyclic voltammetry was then used at a scan rate of 25mV $s^{-1}$ to check the modification of all FM-MICP voltammograms and to quantify the pesticide detection by the washed films. For illustration, figures 4.3A and B (curves b) exhibit cyclic voltammograms of the previously studied washed TMA-MICP and Th-MICP (curves a) after the addition of $10^{-4}$ mol $L^{-1}$ in ATZ.

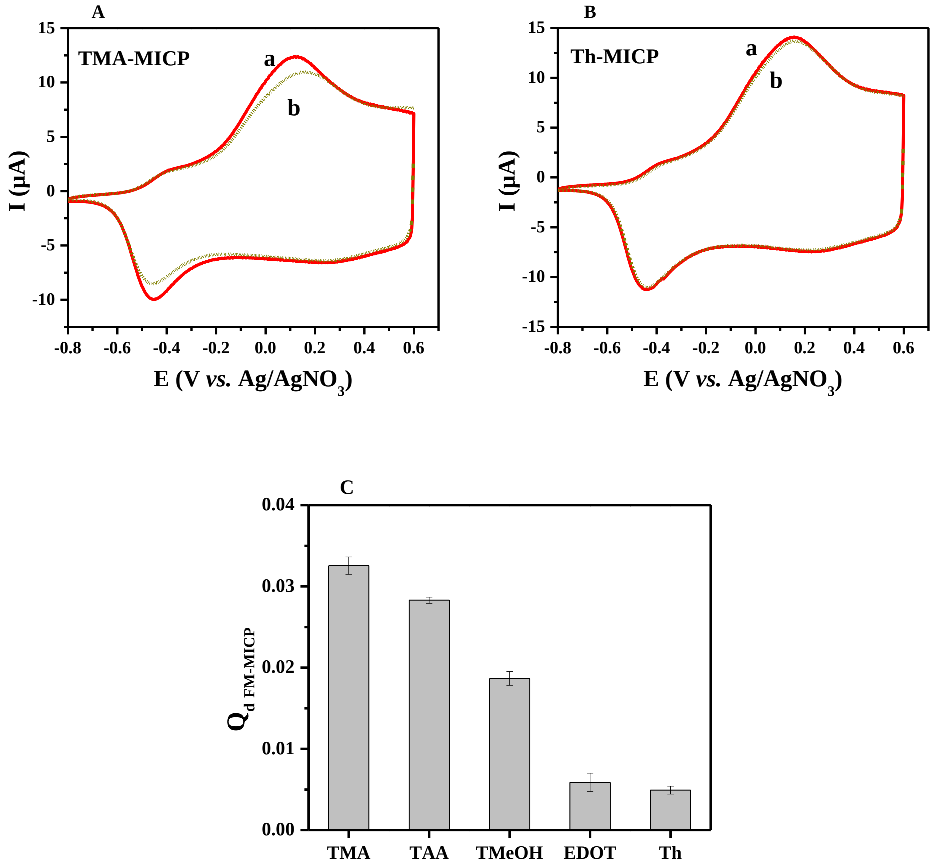

**Figure 4.3 (A)** Cyclic voltammograms of washed TMA-MICP (a) before and (b) after addition of $10^{-4}$ mol $L^{-1}$ in ATZ. **(B)** Cyclic voltammograms of washed Th-MICP (a) before and (b) after addition of $10^{-4}$ mol $L^{-1}$ in ATZ. All cyclic voltammograms were recorded in 0.1M $LiClO_4$/ACN solutions at a scan rate of 25mV $s^{-1}$. **(C)** Relative charges, $Q_{d\ FM\text{-}MICP}$, corresponding to ATZ detection by the different FM-MICP films (FM = TMA, TAA, TMeOH, EDOT or Th). Each charge value, represented with its error bar, corresponds to the mean value obtained from three experiments.

In the electrolytic medium, all the washed FM-MICP display a higher electroactivity in the absence of atrazine as observed for TMA and Th (figures 4.3A and B). Such a decrease in current, observed when atrazine is added to the solution, can be attributed once again to the interaction of ATZ molecules with FM functional monomers into the polymer matrixes. Indeed, in the presence of ATZ, the electroxidation of the polymer, which imposes the coplanarization of the chains, becomes much more difficult. Thus, a bigger quantity of detected targets induces a more important decrease in redox currents. These considerations indicate that a quantitative characterization of atrazine can be obtained from the analysis of the redox currents (or the involved redox charges) as a function of the concentration of atrazine in the analyzed solution.

The observed difference between FM-MICP voltammograms before and after addition of ATZ is more or less important depending on the nature of FM. In particular, this difference is more pronounced in the case of TMA than in the case of Th functional monomer (figure 4.3). This demonstrates that the quantity of ATZ detected by the FM-MICP films depends on the nature of the FM functional monomer.

In order to quantify the current modification due to the detection of ATZ target molecules by FM-MICP layers (for each FM functional monomer), electroxidation charges are calculated from cyclic voltammograms. First, a charge $Q'_{FM\text{-}MICP}$ is calculated for the washed FM-MICP in the absence of any target molecule; second, a charge $Q''_{FM\text{-}MICP}$ is calculated for the FM-MICP in the presence of additional ATZ molecules. Finally, a relative "detection" charge can be calculated according to equation (4.2):

$$Q_{d\ FM-MICP} = \frac{Q'_{FM-MICP} - Q''_{FM-MICP}}{Q'_{FM-MICP}} \qquad \text{Eq 4.2}$$

Such a relative detection charge depends, as previously demonstrated, on the ATZ amount associated with the FM-MICP polymer matrix and must obviously be linked to the sensing properties of the conducting polymers. A better recognition of the target molecules by the sensing layer induces a higher value of $Q_{d\ FM\text{-}MICP}$.

The so-calculated $Q_{d\ FM\text{-}MICP}$ values are represented on the histogram of figure 4.3C as a function of the nature of FM functional monomer. Each point corresponds to a mean value obtained from three independent measurements. Besides, the uncertainty bars corresponding to each point were displayed on the graph. It appears that $Q_{d\ TMA\text{-}MICP}$ and $Q_{d\ TAA\text{-}MICP}$ are higher than $Q_{d\ TMeOH\text{-}MICP}$ and much higher than $Q_{d\ EDOT\text{-}MICP}$ and $Q_{d\ Th\text{-}MICP}$. These results indicate a decreased amount of detected ATZ molecules in the following order of functional monomers-based MICP: TMA, TAA, TMeOH, EDOT and Th.

One can note that the dependence of $Q_{d\ FM\text{-}MICP}$ (which reflects the target detection quality) with the nature of FM parallels that of $Q_{FM}$ (which reflects the FM-MICP preparation quality). This can be explained as follows:

*i)* A stronger interaction between ATZ and FM functional monomer into the FM/ATZ pre-polymerization complex leads to a better incorporation of ATZ into the electrosynthesized FM-MICP matrix, leading to a higher $Q_{FM}$ value. This latter is then expected to increase with increasing concentrations of FM/ATZ pre-polymerization complexes (in addition to EDOT/ATZ dimers as already discussed). Considering the different $Q_{FM}$ experimental values, the non-covalent interactions between TMA and ATZ or between TAA and ATZ seem to be stronger than those involving TMeOH and much stronger than those implying EDOT and Th.

*ii)* Since the amount of incorporated ATZ molecules depends on the functional monomer used, one can suppose that the quantitative extraction of ATZ leads (into the washed FM-MICP matrixes) to a number of molecular imprints which also depends on the nature of FM. In particular, TMA-MICP and TAA-MICP should contain a higher number of functionalized cavities dedicated to ATZ detection.

*iii)* The strength of the interaction between ATZ and FM into the FM/ATZ pre-polymerization complex should vary as that between ATZ and FM into the FM-MICP polymer matrix. As a consequence, the sensing properties of washed FM-MICP layers do not depend only on the number of molecular imprints, but also on the FM ability to interact with ATZ. Then, TMA-MICP and TAA-MICP, which contain a high number of imprints and which are also built from TMA and TAA functional monomers (that seem to strongly interact with ATZ), are characterized by great sensing properties towards ATZ, as traduced by the high corresponding experimental $Q_{d\ TMA\text{-}MICP}$ and $Q_{d\ TAA\text{-}MICP}$ values.

While FM-MICP films are electrosynthesized in the presence of ATZ molecules, FM-NICP layers are electrochemically prepared in the absence of target molecules and are thus free from functionalized imprinted cavities able to specifically interact with target molecules. As a consequence, added ATZ molecules could only interact with FM-NICP layers by the way of a non specific adsorption thanks to the interaction with FM functional monomers localized close to the polymer surface.

In order to check, for each kind of FM functional monomers, whether non-imprinted FM-NICP films are able to interact with newly added ATZ molecules, the FM-NICP modified gold electrodes were immersed in ACN solutions containing $LiClO_4$ 0.1 mol $L^{-1}$. Then, $10^{-4}$ mol $L^{-1}$ of ATZ was added. Cyclic voltammetry was then used at a scan rate of 25 mV $s^{-1}$ to check the modification of all FM-NICP voltammograms and to quantify the interaction of pesticide molecules with the films (results not shown).

As it was observed in the case of FM-MICP films, all the FM-NICP layers display a lower electroactivity when atrazine is added (results not shown). In addition, the observed difference between FM-NICP voltammograms before and after addition of ATZ is more or less important depending on the FM functional monomer. This is attributable to the non specific adsorption of ATZ molecules onto the functionalized polymer matrixes, the strength of which should depend on the nature of FM.

In order to quantify the current modification due to the adsorption of ATZ target molecules onto FM-NICP layers (for each FM functional monomer), $Q'_{FM\text{-}NICP}$ and $Q''_{FM\text{-}NICP}$ electrooxidation charges are calculated from FM-NICP cyclic voltammograms, respectively in the absence and in the presence of additional ATZ molecules. Then, a relative “detection” charge can be calculated according to equation (4.3):

$$Q_{d\ FM-NICP} = \frac{Q'_{FM-NICP} - Q''_{FM-NICP}}{Q'_{FM-NICP}} \qquad \text{Eq 4.3}$$

The so-calculated $Q_{d\ FM\text{-}NICP}$ values are represented on the histogram of figure 4.4A as a function of the nature of the FM functional monomer. Each experimental value corresponds to a mean value obtained from three independent measurements. Besides, the uncertainty bars corresponding to each point are displayed on the graph. It appears that $Q_{d\ TMA\text{-}NICP}$ is higher than $Q_{d\ TAA\text{-}NICP}$ and $Q_{d\ TMeOH\text{-}NICP}$ and much higher than $Q_{d\ EDOT\text{-}NICP}$ and $Q_{d\ Th\text{-}NICP}$. These results indicate that the amount of non-specifically adsorbed ATZ molecules is directly related to the strength of the FM-ATZ interaction. In particular, ATZ molecules adsorb on TMA-NICP film more than on the other FM-NICP layers, since TMA-ATZ interaction seems to be the strongest. On another hand, since each TMA functional monomer contains two carboxylic groups (while one TAA residue contains just one –COOH), non covalent interactions of ATZ molecules with the surface of TMA-MICP layers is necessarily more favorable.

When comparing the values of the relative “detection” charges corresponding to FM-MICP (figure 4.3C) and to FM-NICP (figure 4.4A), it appears that $Q_{d\ FM\text{-}NICP}$ remains lower than $Q_{d\ FM\text{-}MICP}$ whatever the FM functional monomer. In particular, we can note that the ratio $Q_{d\ TAA\text{-}NICP}/Q_{d\ TAA\text{-}MICP}$ is close to 33%, value already specified in table 3.2 for the same film thickness. This implies that, for each functional monomer, a specific detection of ATZ by FM-MICP layers thanks to functionalized cavities is to be considered. Nevertheless, in all

FM-MICP cases the adsorption phenomenon does not seem to be negligible as already mentioned.

If the adsorption process intervenes in FM-NICP, it must also be considered in the case of FM-MICP layers. In other words, $Q_{d\ FM\text{-}MICP}$ values take into account, in addition to the specific detection of targets, the non specific adsorption of ATZ molecules. If we assume that, for a given FM functional monomer, ATZ adsorption is similar onto FM-MICP and FM-NICP layers, then subtracting $Q_{d\ FM\text{-}NICP}$ values from those of $Q_{d\ FM\text{-}MICP}$ should give access to specific detection data, according to:

$$Q_{d\ FM} = Q_{d\ FM-MICP} - Q_{d\ FM-NICP} \qquad \text{Eq 4.4}$$

$Q_{d\ FM}$ values must be related to the sensing properties of the FM-MICP films, thanks to the unique presence of functionalized imprinted cavities into the polymer matrixes.

$Q_{d\ FM}$ values are represented on the histogram of Figure 4B as a function of the nature of the FM functional monomer. As expected from the strength of the different functional monomers, the specific detection of ATZ molecules decreases in the following order of functional monomers-based MICP: TAA, TMeOH, EDOT and Th. However, due to the much higher $Q_{d\ TMA\text{-}NICP}$ value (ATZ quantitatively adsorbs onto TMA-MICP layers as discussed in further *section 4.4.2*) comparatively with that of $Q_{d\ TAA\text{-}NICP}$, $Q_{d\ TMA}$ finally appears lower than $Q_{d\ TAA}$, meaning that TAA-MICP based sensor is the more recommended for a specific detection of ATZ.

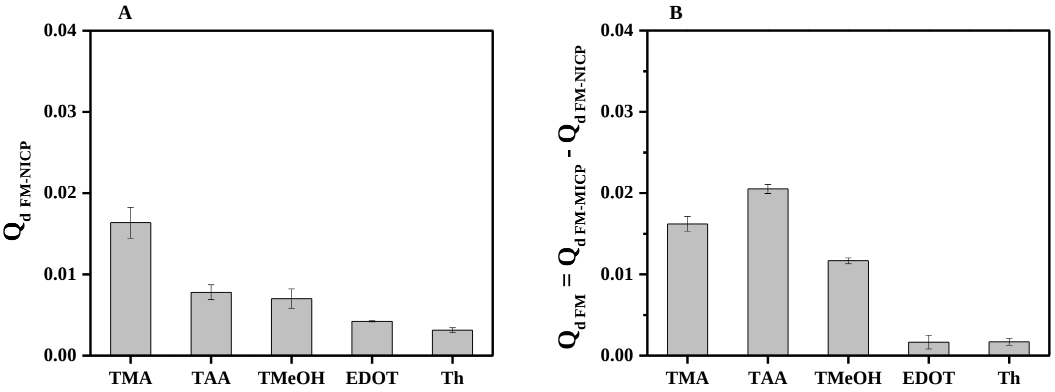

**Figure 4.4. (A)** Relative charges, $Q_{d\ FM\text{-}NICP}$, corresponding to the adsorption of ATZ onto the different FM-NICP films (FM = TAA, TMA, TMeOH, EDOT or Th). Each charge value, represented with its error bar, corresponds to the mean value obtained from three experiments. **(B)** Variation with FM of $Q_{d\ FM\text{-}MICP}$ - $Q_{d\ FM\text{-}NICP}$, which corresponds to the specific interaction of FM-MICP films with ATZ target molecules.

Note that in all the cases, for each FM-MICP electrosynthesis, EDOT is present as a linker. As a consequence, since EDOT interacts with ATZ and since EDOT/ATZ pre-polymerization complexes are to be considered, the number of functionalized cavities into the FM-MICP polymer matrix, in the cases of TMA, TAA, TMeOH and Th, depends also on EDOT/ATZ dimers quantity (in addition to FM/ATZ complexes number). On another hand, when considering sensing properties of washed FM-MICP or FM-NICP towards additional amounts of ATZ, EDOT-ATZ interactions must also be considered in addition to FM-ATZ intermolecular bonds. As a consequence, whatever the electrosynthesized FM-MICP or FM-NICP layer, the study of the correlation between $Q_{d\ FM\text{-}MICP}$, $Q_{d\ FM\text{-}NICP}$ as well as $Q_{d\ FM}$ with the sum of the pre-polymerization dimers concentrations, [FM/ATZ] + [EDOT/ATZ], seems to be very interesting. This will also be considered in *section 4.4.*

## 4.3 Calculation of the association free energies in solution

We demonstrated, in *section 4.2*, the clear effect of the nature of FM functional monomer, first, on the creation of ATZ molecular imprints into the polymer matrixes (through the $Q_{FM}$ values) and second, on the specific detection of ATZ targets (through the $Q_{d\ FM\text{-}MICP}$ values when the adsorption process is neglected). The obtained results were attributed to the strength of FM-ATZ interaction and then to the concentration of FM/ATZ (in addition to EDOT/ATZ) pre-polymerization complexes.

To investigate this hypothesis and in order to check whether $Q_{FM}$ and $Q_{d\ FM\text{-}MICP}$ (and eventually $Q_{d\ FM}$) values are correlated with the sum of dimers concentrations, [FM/ATZ] + [EDOT/ATZ], we need to determine the effective concentrations of the different pre-polymerization complexes present in the medium before each FM-MICP electrosynthesis.

For this purpose, we calculate in the present section the free energies of the following six competitive reactions:

ATZ + ATZ → ATZ/ATZ R 4.1

EDOT + ATZ → EDOT/ATZ R 4.2

EDOT + EDOT → EDOT/EDOT R 4.3

FM + FM → FM/FM R 4.4

FM + ATZ → FM/ATZ R 4.5

FM + EDOT → FM/EDOT R 4.6

These reactions (R 4.1 to R 4.6), involved during FM-MICP preparation, are to be considered for each of the FM functional monomers. However, during EDOT-MICP synthesis, EDOT molecule alone is associated to the ATZ, in the absence of any other FM functional monomer. Then, in the case of EDOT, only the first three reactions (R 4.1 to R 4.3) must be considered. Nevertheless, all these reactions are association reactions of the type:

$A_{sol} + B_{sol} \rightarrow AB_{sol}$ R 4.7

where *sol* means that the reaction takes place in solution in acetonitrile.

We have used the PCM (Polarized Continuum Medium) method[32] within the SMD formalism[33], available in the last version of the Gaussian code[34]. The PCM method is basically a method for calculating solvation free energies[32]. The SMD variant has been parameterized, so as to reproduce the standard solvation free energies, $\Delta G^{\circ}_{solv}$, of a large list of molecules and ions in several solvents[33], according to the formula:

$$\Delta G^{\circ\,smd}_{solv}(A) = \Delta G^{smd}_{solv}(A) + RT\ \mathrm{Ln}24.5 \qquad \text{Eq 4.5}$$

where $\Delta G^{smd}_{solv}(A)$ is the simple difference of the quantum energies of one molecule in the vacuum and in the SMD cavity, which can be transposed to one mol $L^{-1}$ systems of a perfect gas and an ideal solution:

$$\Delta G^{smd}_{solv}(A) = G^{smd}_{sol}(A, 1\,M) - G_{g}(A, 1\,M) \qquad \text{Eq 4.6}$$

The last term of equation 4.5 accounts for the different standard states in the gaz phase (1atm, concentration 1/24.5 mol $L^{-1}$) and in solution (concentration 1 mol $L^{-1}$)[35]. In consequence, addressing reaction (R 4.7) leads to consider the thermodynamic cycle of figure 4.5. From figure 4.5 and equation 4.5, the free energy change of reaction 4.7 in solution reads:

$$\begin{aligned}\Delta_r G^{\circ\,smd}_{sol} &= \Delta_r G^*_g + \Delta G^{\circ\,smd}_{solv}(AB) - \Delta G^{\circ\,smd}_{solv}(A) - \Delta G^{\circ\,smd}_{solv}(B) \\ &= \Delta_r G^*_g + \Delta G^{smd}_{solv}(AB) - \Delta G^{smd}_{solv}(A) - \Delta G^{smd}_{solv}(B) - RT\,Ln24.5\end{aligned} \qquad \text{Eq 4.7}$$

where $\Delta_r G^*_g$ is the standard reaction free energy in the gas phase and $\Delta_r G^{\circ\,smd}_{sol}$ the SMD value of the standard reaction free energy in solution.

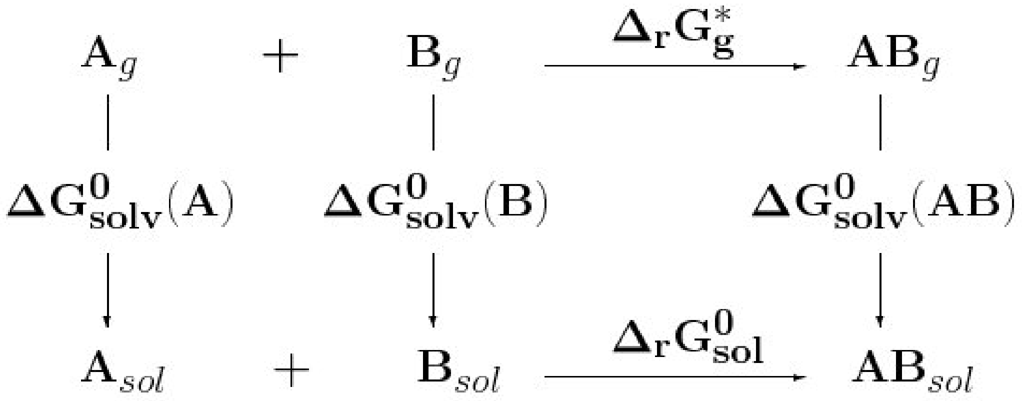

**Figure 4.5.** Thermodynamical cycle used for the calculation of the association free energies

### 4.3.1 Free energy change in the vacuum

It is well known that DFT calculations cannot describe van der Waals complexes; unless dispersion is taken into account and BSSE (Basis Set Superposition Error) is corrected. We have thus used the B97D functional, which includes the dispersion interactions[36], and the SDD core pseudopotentials and basis sets[37], supplemented with one d polarization Gaussians on all heavy atoms (exponents: 0.8 for C, N and O atoms, 0.65 for S and 0.7 for Cl atoms). All the calculations have been done with the Gaussian 09 package[34]. Since we expect that in our dimers the leading interactions are hydrogen bond and $\pi$ stacking, we have calculated the dimerization energies of benzene ($C_6H_6$), where $\pi$ stacking is essential and of water ($H_2O$), where hydrogen bond is predominant. For the benzene dimer, we have obtained for the dimerization energy the value 2.05 kcal mol$^{-1}$, to be compared with the CCSD(T)[38] value 2.6 kcal mol$^{-1}$. Our value is reasonable, though underestimated. For the water dimer, we have obtained the value 5.53 kcal mol$^{-1}$, to be compared with the experimental value[39]: 5.44 kcal mol$^{-1}$. Our description of the hydrogen bond is excellent, therefore.

The structures of the dimers of interest are shown in Figure 4.6. Most dimers are linked by one or two hydrogen bonds, those of thiophene by π stacking. The bonding modes are given in Table 4.2. It can be seen that the atrazine molecule links to itself by a double H bond, to EDOT by a single H bond, to TAA and TMA by a double H bond, to TMeOH by both H bonding and π stacking, and to Th by π stacking only.

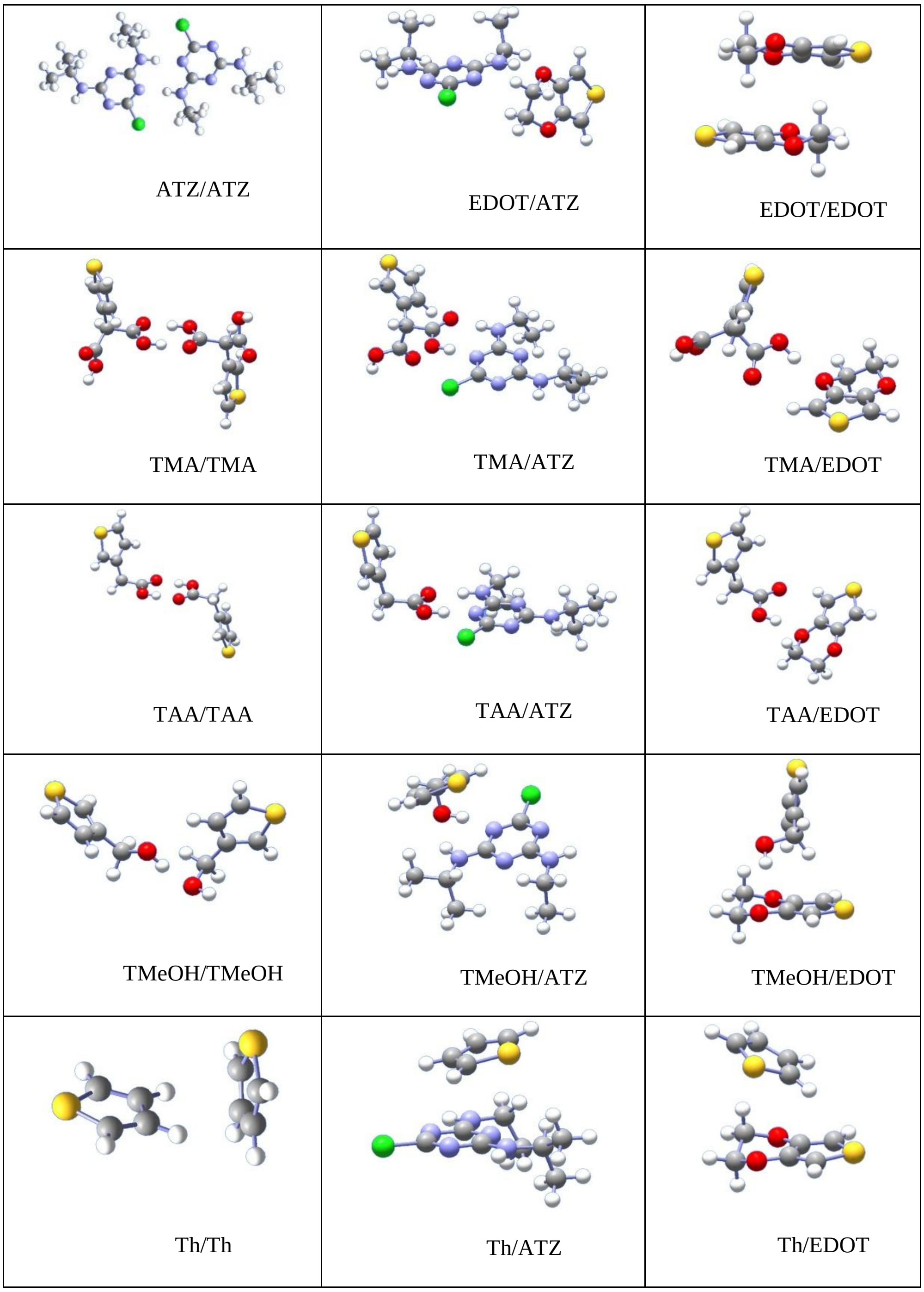
ATZ/ATZ
EDOT/ATZ
EDOT/EDOT
TMA/TMA
TMA/ATZ
TMA/EDOT
TAA/TAA
TAA/ATZ
TAA/EDOT
TMeOH/TMeOH
TMeOH/ATZ
TMeOH/EDOT
Th/Th
Th/ATZ
Th/EDOT

**Figure 4.6.** The dimers of atrazine (ATZ) and the different FM functional monomers (TMA, TAA, TMeOH, EDOT and Th).

**Table 4.2.** Conformation entropy for the formation of dimers and its contribution to free energy. a / b and l / r stand for the above / below and left / right alternatives.

| | **bonding mode** | **conformation effects** | **conformation entropy** | **contribution to free energy (eV)** |
|---|---|---|---|---|
| **ATZ/ATZ** | double H bond | C and T conformers of ATZ | +RLn (16/9) | -0.015 |
| **EDOT/ATZ** | H bond | C and T conformers of ATZ | +RLn (16/3) | -0.043 |
| **EDOT/EDOT** | dipole-dipole | a / b stacking | +RLn 2 | -0.018 |
| **TMA/ATZ** | double H bond | C and T conformers of ATZ two + two COOH on TMA | +RLn (8/3) | -0.025 |
| **TMA/TMA** | double H bond | two COOH on TMA | +RLn 4 | -0.036 |
| **TMA/EDOT** | H bond | two O on EDOT<br>+ two COOH on TMA | +RLn 4 | -0.036 |
| **TAA/ATZ** | double H bond | C and T conformers of ATZ | +RLn (4/3) | -0.007 |
| **TAA/TAA** | double H bond | - | 0 | 0. |
| **TAA/EDOT** | H bond | two O on EDOT | +RLn 2 | -0.018 |
| **TMeOH/ATZ** | double H bond<br>+ π stacking | C and T conformers of ATZ<br>+ a / b stacking | +RLn (8/3) | -0.025 |
| **TMeOH/TMeOH** | H bond | donor *vs* acceptor H bond | +RLn 2 | -0.018 |
| **TMeOH/EDOT** | H bond<br>+ π stacking | two O on EDOT<br>+ a / b stacking | +RLn 4 | -0.036 |
| **Th/ATZ** | π stacking | a / b and l /r stackings | +RLn 4 | -0.036 |
| **Th/Th** | π stacking | a / b and l /r stackings | +RLn 4 | -0.036 |
| **Th/EDOT** | π stacking | a / b and l / r stackings | +RLn 4 | -0.036 |

The translation, rotation and vibration contributions to entropy have been calculated in the usual way with the help of the Sackur-Tetrode formula, of the rigid rotor and harmonic analysis, respectively[40]. The $\Delta_r G_g^*$ values obtained in this way are given in Table 4.3 and shown in figure 4.7 ("in the vacuum" entry). In every case we have performed an extensive investigation of the possible energy minima. We found out that in most cases one single minimum is more stable than the other ones by 0.1 eV or more, so that the secondary minima can be neglected. In a few cases, we have found several minima with very close energies. This is the case, for instance, for the EDOT/ATZ case where we found out two structures, with the H bonding to EDOT on the ethyl *vs.* the isopropyl side yielding very close free energies (+0.056 and +0.059 eV respectively). In these cases, we have considered these structures equivalent and added RLn2 to the conformation energy.

**Table 4.3.** Formation free energies ($\Delta_r G_g^*$, $\Delta_r G_{sol}^{\circ\,smd}$, $\Delta_r G_{sol}^{\circ\,TRV\,mod\,smd}$, $\Delta_r G_{sol}^{\circ\,TR\,mod\,smd}$) and solvation free energies in acetonitrile ($\Delta G_{solv}^{smd}$) of the different dimers of interest (in eV). T, R and V allude to the translation, rotation and vibration of the molecules in the vacuum. In this table, the conformation entropies of Table 4.2 are not taken into account.

| | $\Delta_r G_g^*$ | $\Delta G_{solv}^{smd}$ | $\Delta_r G_{sol}^{\circ\,smd}$ | $\Delta_r G_{sol}^{\circ\,TRV\,mod\,smd}$ | $\Delta_r G_{sol}^{\circ\,TR\,mod\,smd}$ |
|---|---|---|---|---|---|
| **ATZ/ATZ** | -0.205 | -1.25 | +0.079 | -0.001 | -0.092 |
| **EDOT/ATZ** | +0.056 | -0.907 | +0.193 | +0.130 | +0.033 |
| **EDOT/EDOT** | +0.204 | -0.536 | +0.222 | +0.158 | +0.070 |
| **TMA/ATZ** | -0.261 | -1.106 | -0.062 | -0.129 | -0.225 |
| **TMA/TMA** | -0.196 | -0.872 | +0.008 | -0.058 | -0.151 |
| **TMA/EDOT** | +0.072 | -0.771 | +0.139 | +0.078 | -0.017 |
| **TAA/ATZ** | -0.232 | -0.942 | -0.039 | -0.110 | -0.197 |
| **TAA/TAA** | -0.201 | -0.556 | -0.021 | -0.095 | -0.172 |
| **TAA/EDOT** | +0.079 | -0.599 | +0.170 | +0.116 | +0.021 |
| **TMeOH/ATZ** | -0.121 | -0.884 | +0.085 | +0.013 | -0.071 |
| **TMeOH/TMeOH** | +0.043 | -0.556 | +0.133 | +0.078 | -0.010 |
| **TMeOH/EDOT** | +0.188 | -0.520 | +0.268 | +0.202 | +0.120 |
| **Th/ATZ** | +0.191 | -0.799 | +0.317 | +0.267 | +0.168 |
| **Th/Th** | +0.241 | -0.367 | +0.190 | +0.157 | +0.056 |
| **Th/EDOT** | +0.218 | -0.431 | +0.217 | +0.168 | +0.075 |

It can be seen that the double H bond is the most efficient bonding mode with very negative $\Delta_r G_g^*$ values: ATZ/ATZ (-0.205 eV), TAA/ATZ (-0.232 eV), TAA/TAA (-0.201 eV), TMA/ATZ (-0.262 eV). The single H bond is less efficient with slightly positive $\Delta_r G_g^*$ values: EDOT/ATZ (+0.056 eV), TAA/EDOT (+0.079 eV), TMeOH/TMeOH (+0.043 eV). The $\pi$ stacking binding mode yields very unfavorable binding free energies: Th/ATZ (+0.191 eV). Of course, these numbers will be modified by solvation, but roughly through a translation, so that this comparison will remain valid.

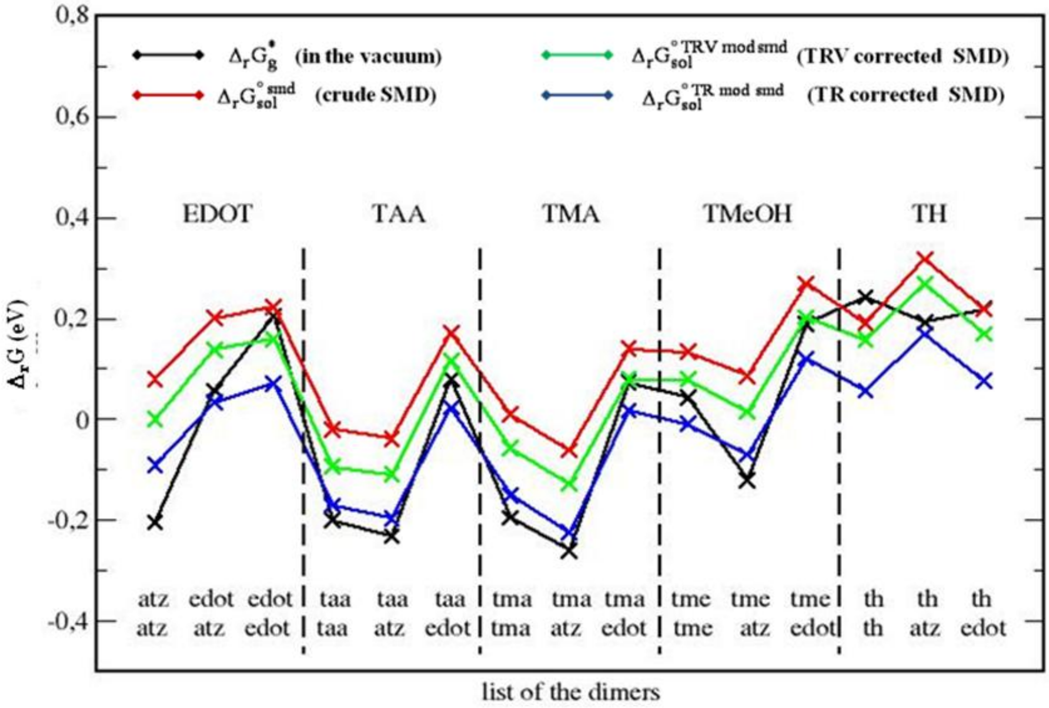

**Figure 4.7.** Dimerization free energies ( $\Delta_r G_g^*$ , $\Delta_r G_{sol}^{\circ smd}$ , $\Delta_r G_{sol}^{\circ TRV\ mod\ smd}$ and $\Delta_r G_{sol}^{\circ TR\ mod\ smd}$ ) obtained with several levels of approximation.

Note that the values of Table 4.3 are free from the conformation entropy. This effect has been addressed in the literature, see the work of Mammen[41]. Considering the present list of monomers (figure 2.1) and dimers (figure 4.6), conformation entropy can originate from the following features:

*i)* The free or partially restricted rotation of some substituents of the monomers may become more restricted in the dimer. This question arises mainly for the ethyl and isopropyl substituents of the ATZ molecule. We have considered that the rotation freedom of these groups is not modified by the dimer formation.

*ii)* Some conformers of the monomers do not participate to the formation of dimers.

*iii)* Several equivalent, but distinct structures may exist. In this case we add to the entropy the term RLn N, where N is the number of distinct structures. For example, in the case of π stacking of two molecules, one molecule can stack above or below the other one. In this case, we add RLn 2 to the entropy.

We now investigate the dimerization of the ATZ molecule in some details. If we first consider the ATZ molecule, the following points can be noted:

*i)* The monomer has two sides and each of them can be cis (C) or trans (T), see figure 2.1 showing one of the ATZ conformers. If we note Ce, Ci, Te and Ti the C and T sides of ATZ bearing the ethyl and isopropyl groups, respectively, then the ATZ molecule displays 4 distinct conformers: CeCi, CeTi, CiTe and TeTi. With these notations, figure 2.1 shows the CeTi conformer of ATZ. The CeCi and TeTi conformers can be simply noted CC and TT.

*ii)* We have calculated that, in solution, the TT conformer is the most stable, that the CeTi and CiTe conformers lie higher but within 0.02 eV only, and that the CC conformer lays 0.05 eV higher than TT. Considering that kT amounts to 0.025 eV (at 300K), we conclude that three conformers (TT, CeTi and CiTe) can be considered degenerate, and that the fourth one (CC) can be neglected.

*iii)* Since each monomer has three accessible conformers, then the conformation entropy of a pair of separated monomers amounts to +RLn9.

We now note that in the dimer:

*i)* the monomers are linked through a double H bond between their T sides. We have verified that binding the C sides leads to dimers with energies higher by at least 0.10 eV.

*ii)* The Ti and Te sides of each monomer are no more equivalent, so that the number of different dimers amounts to 4x4=16 and the conformation entropy amounts to +RLn16.

The conformation entropy of the ATZ dimerization is thus $\Delta S_{conf}$ = RLn(16/9) and the corresponding free energy must be added the value -RTLn(16/9) = -0.015 eV.

We have investigated the 14 other dimers in the same way. For the sake of concision, we only summarize our conclusions in Table 4.2, where we give the origins of conformation entropy and the corresponding contributions to dimerization entropies and free energies.

### 4.3.2 Free energy change in solution: the PCM paradox

We have calculated the solvation free energies, $\Delta G^{smd}_{solv}$, of all the monomers and dimers, relevant to the present study. Since the Gaussian package enables the BSSE correction in the vacuum only, we have evaluated the solvation free energies of the dimers (Table 4.3) with a single point electronic calculation at the geometry optimized in the vacuum with BSSE correction. For the sake of consistency, we have also calculated the solvation free energies of the monomers (Table 4.4) with single point calculations at the geometries optimized in the vacuum.

The SMD solvation free energies can be written[32]:

$$\Delta G_{solv}^{smd} = \Delta G_{solv}^{electr} + \Delta G_{solv}^{non\ electr} \qquad \text{Eq 4.8}$$

The first term of equation 4.8, $\Delta G_{solv}^{electr}$, is the interaction energy of the solute with the polarized solvent, modeled by a homogeneous dielectric medium with the dielectric constant of the solvent. The second term of equation 4.8, $\Delta G_{solv}^{non\ electr}$, gathers the cavitation, dispersion and Pauli repulsion effects[33]. Like most PCM methods, the SMD method uses atomic radii which have been optimized, so that the free energy of equation 4.5 reproduces the measured values of a list of molecules. For this reason we expect that the SMD solvation free energies, $\Delta G_{solv}^{smd}$, of the monomers, given in Table 4.4, are reliable.

**Table 4.4.** Solvation free energies in acetonitrile ($\Delta G_{solv}^{smd}$) of the monomers of interest (in eV).

| | $\Delta G_{solv}^{smd}$ |
|---|---|
| **ATZ** | -0.808 |
| **TMA** | -0.579 |
| **TAA** | -0.409 |
| **TMeOH** | -0.364 |
| **EDOT** | -0.318 |
| **Th** | -0.194 |

The SMD values of the solvation free energies of the dimers $\Delta G_{solv}^{smd}$ and of the dimerization standard free energies, $\Delta_r G_{sol}^{\circ smd}$, calculated according to equation (4.7), are given in Table 4.3 and shown in figure 4.7 (“crude SMD” entries). It can be seen on figure 4.7 that these crude SMD values are much more positive than the values in the vacuum ($\Delta_r G_g^*$).

We now emphasize that some terms are absent from equation 4.8. This can be easily seen if one takes the Bell formula for the solvation of a neutral dipole in a spherical cavity[42]:

$$\Delta G_{solv} = -\frac{\varepsilon - 1}{2\varepsilon + 1}\frac{\mu^2}{R^3} \qquad \text{Eq 4.9}$$

The corresponding solvation entropy is given by:

$$\Delta S_{solv} = -\left(\frac{\partial \Delta G_{solv}}{\partial T}\right)_p \qquad \text{Eq 4.10}$$

$$\Delta S_{solv} = \frac{3}{(2\varepsilon + 1)^2}\frac{\mu^2}{R^3}\varepsilon'_T \qquad \text{Eq 4.11}$$

where ε is the dielectric constant of the solvent and $\varepsilon'_T$ its derivative with respect to temperature. It is assumed here that the cavity radius does not depend on temperature, this is actually a very reasonable assumption, see for example ref. 43. From equations (4.9) and (4.11) we obtain:

$$\frac{T\Delta S_{solv}}{\Delta G_{solv}} = \frac{3T\varepsilon'_T}{(\varepsilon - 1)(2\varepsilon + 1)} \qquad \text{Eq 4.12}$$

The values for acetonitrile: ε = 36.64 (reference 52) and $\varepsilon'_T = 0.1862\ K^{-1}$ (ref. 45) give for this ratio the value 0.063, showing that the entropic contribution to the SCRF solvation free energy is small (6.3 %). Note that this entropic term gives the entropic contribution of the solvent only, specifically the decrease of the density of states of the solvent, due to the solute.

In the gas phase, the entropy of a molecule is usually separated in three components: translation, rotation and vibration. These effects are certainly present in the $\Delta_r G_g^*$ term of equation (4.7). According to the Sackur-Tetrode formula, the translation entropy varies exactly like the logarithm of the mass (M) of the molecule[40]. It has been noted that the rotation term roughly varies in the same manner[41]. This can be checked on figure 4.8 where we have plotted the translation rotation entropies of all the molecules of present interest (monomers and dimers, and acetonitrile) in the gas phase against the logarithm of their mass. It can be seen that the correlation is quite good (R=0.994). The question is now that the same effects, namely translation and rotation in solution, and also other effects such as solute solvent conformation entropy, are absent from equation (4.8), at least formally.

We here face the PCM paradox: the atomic radii have been optimized, so that the method reproduces the solvation free energies of a list of molecules. In consequence, the above mentioned entropy terms, lacking in the formalism, are numerically present in the PCM result. We think that the optimization of the atomic radii is made possible by the small scattering of the logarithm of the mass along the list of molecules, used for the optimization.

We also understand that the SMD solvation free energies of the dimers are inaccurate. Actually, one part of the entropy variation of the A+B→AB reaction should vary like $Ln[(M_A+M_B)/(M_AM_B)]$. This is not enabled by the PCM equation (4.8) and consequently the PCM solvation free energies have a poor additive behavior, mainly ruled by electrostatics. The loss of rotational and translational entropy due to the fixation of a ligand to a molecule has been discussed in the literature for a long time[41,46,47]. We decided to introduce an empirical correction to the solvation free energies, with a realistic mass dependence. Of course, we know that doing so, we lose the good accuracy of the solvation free energies of the monomers, but we expect that their additive behavior will be improved and the dimerization free energies as well.

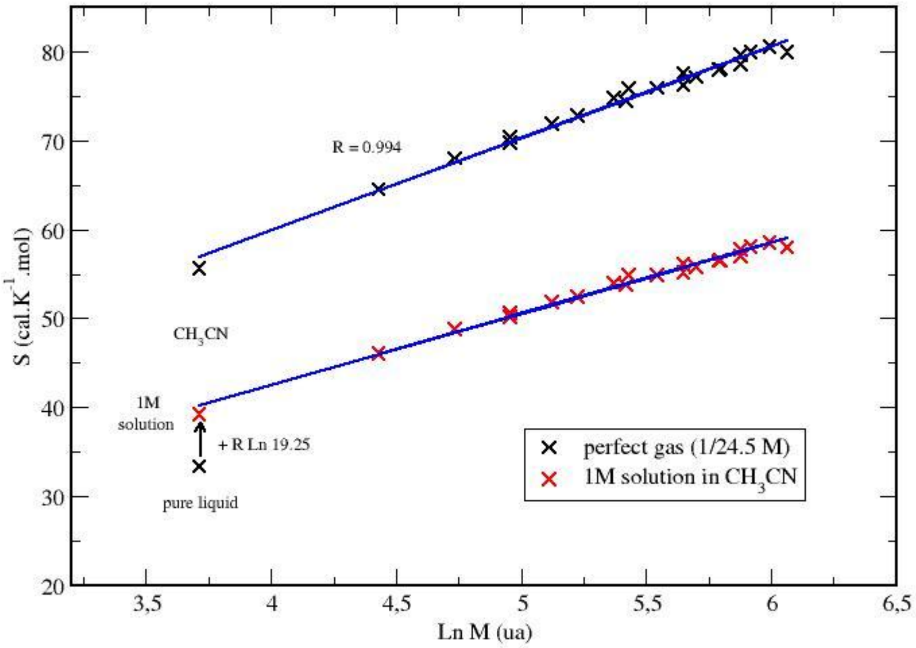

**Figure 4.8.** Entropy of the molecules of interest in the present chapter: translation rotation entropy in the gas phase and entropy deduced from the Wertz formula in solution.

### 4.3.3 Empirical treatment of solute entropies

We used the empirical formula given by D. Wertz in 1980[48]. Since 1980, the Wertz formula has been both severely criticized[49], and empirically used with success (ref. 50-54). D. Wertz noticed that the relative entropy loss of a molecule passing from the gas phase to the solution does not depend on the molecule, and that consequently it can be taken in the solvent molecule itself, provided the gas phase solute is brought to the standard state of the pure solvent.

We used the available values of the standard molar entropy of liquid acetonitrile: 35.76 cal $K^{-1}$ $mol^{-1}$ at $298.15^{o}C$ (ref. 55), and calculated the gas phase value with the help of the Sackur-Tetrode, harmonic analysis and rigid rotor formulas for translation, vibration and rotation, respectively. This yielded the value 58.0 cal $K^{-1}$ $mol^{-1}$ at $298.15^{o}C$ (ref. 34), in excellent agreement with the measured value: 58.2 cal $K^{-1}$ $mol^{-1}$ (ref. 55). According to D. Wertz, this gaz phase entropy must be brought to the standard state of the pure liquid, for which the concentration has the value 19.25 mol $L^{-1}$ (ref. 44). The total gaz phase entropy now amounts to:

$$\begin{aligned} S_g^{TRV}(19.25\,M) &= 58.0 - R\,Ln(24.5x19.25) \\ &= 58.0 - 12.24 = 45.7\,cal\,K^{-1}\,mol^{-1} \end{aligned} \qquad \text{Eq 4.13}$$

From these numbers we can deduce that for acetonitrile:

$$\frac{S_g^{TRV}(19.25\,M) - S_{sol}^{tot}(19.25\,M)}{S_g^{TRV}(19.25\,M)} = 0.22 \qquad \text{Eq 4.14}$$

In equations (4.13) and (4.14), the total entropy is noted $S_g^{TRV}$ (*TRV* for translation rotation vibration) in the gas phase, and $S_{sol}^{tot}$ (*tot* for total) in the solution. According to Wertz, the formula (4.14), exact for acetonitrile, can be used for any solute in acetonitrile and can be readily exploited with the help of the thermodynamic cycle of figure 4.9 (ref. 48). On this cycle, we use two intermediate states of the solute: first a 1 mol $L^{-1}$ perfect gas is compressed to a hypothetical 19.25 mol $L^{-1}$ perfect gas state, then solvated in a hypothetical 19.25 mol $L^{-1}$ ideal solution state and eventually diluted to 1 mol $L^{-1}$ ideal solution. Using this cycle, we obtain (in cal $K^{-1}$ $mol^{-1}$):

$$\begin{aligned}\Delta S_{solv}^{TRV} &= S_{sol}^{tot}(1\,M) - S_g^{TRV}(1\,M)\\ &= -5.88 - 0.22(S_g^{TRV}(1/24.5\,M) - 12.24) + 5.88 \qquad \text{Eq 4.15}\\ &= -0.22(S_g^{TRV}(1/24.5\,M) - 12.24)\end{aligned}$$

We now modify the solvation free energies:

$$\Delta G_{solv}^{TRV\,mod\,smd} = \Delta G_{solv}^{smd} - T\Delta S_{solv}^{TRV} \qquad \text{Eq 4.16}$$

and, eventually, the dimerization free energy for reaction 4.9:

$$\begin{aligned}\Delta_r G_{sol}^{\circ\,TRV\,mod\,smd} = {}& \Delta_r G_g^{*} + \Delta G_{solv}^{TRV\,mod\,smd}(AB)\\ & - \Delta G_{solv}^{TRV\,mod\,smd}(A) - \Delta G_{solv}^{TRV\,mod\,smd}(B) - RT\,Ln24.5\end{aligned} \qquad \text{Eq 4.17}$$

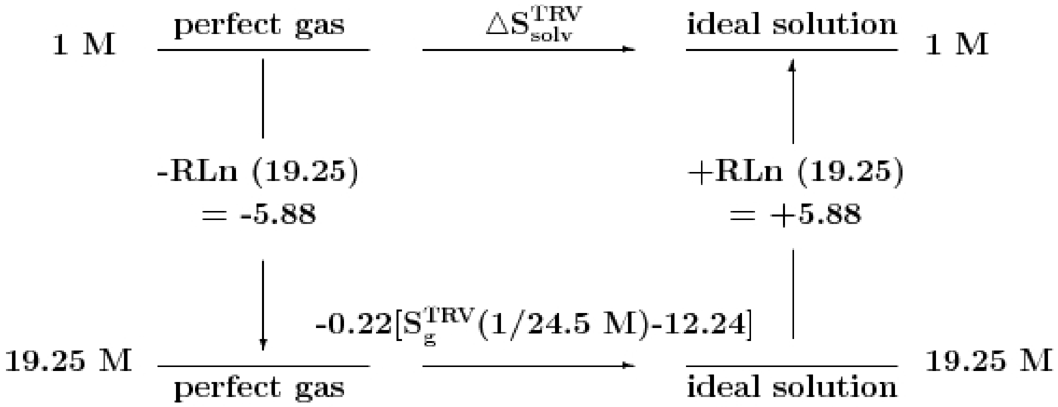

**Figure 4.9.** The thermodynamic cycle used for the Wertz formula in acetonitrile.

We have then considered that the Wertz formula is best justified when applied to only the translation rotation part of the entropy of the molecule in the gas phase. We here intuitively consider that, due to the potential created by the solvent, the densities of states for the translation and rotation of the solute do decrease, but that the density of internal vibration states of the solute is not affected. In consequence, we subtract the harmonic analysis entropies of acetonitrile in the vacuum and, for the sake of consistency, in the PCM cavity as well:

$$S_g^{TR}(19.25\,M) = 45.70 - 2.41 = 43.30\,cal\,K^{-1}\,mol^{-1} \qquad \text{Eq 4.18}$$

$$S_{sol}^{tot\text{-}V}(19.25\,M) = 35.76 - 2.35 = 33.40\,\text{cal}\,K^{-1}\,\text{mol}^{-1} \qquad \text{Eq 4.19}$$

where $S_g^{TR}$ is the translation rotation entropy in the gas phase and where $S_{sol}^{tot\text{-}V}$ is the corresponding entropy in the solution (*tot-V* for "total, minus internal vibration") because in solution not only two, but several effects remain: translation, rotation, solute-solvent vibration and conformation entropies. With these new values we obtain:

$$\frac{S_g^{TR}(19.25\,M) - S_{sol}^{tot\text{-}V}(19.25\,M)}{S_g^{TR}(19.25\,M)} = 0.23 \qquad \text{Eq 4.20}$$

and finally, in full analogy with equations 4.15, 4.16 and 4.17:

$$\begin{aligned}\Delta S_{solv}^{TR} &= S_{sol}^{tot\text{-}V}(1\,M) - S_g^{TR}(1\,M)\\ &= -0.23\left(S_g^{TR}(1/24.5\,M) - 12.24\right)\end{aligned} \qquad \text{Eq 4.21}$$

$$\Delta G_{solv}^{TR\,mod\,smd} = \Delta G_{solv}^{smd} - T\,\Delta S_{solv}^{TR} \qquad \text{Eq 4.22}$$

$$\begin{aligned}\Delta_r G_{sol}^{\circ\,TR\,mod\,smd} &= \Delta_r G_g^{*} + \Delta G_{solv}^{TR\,mod\,smd}(AB)\\ &\quad - \Delta G_{solv}^{TR\,mod\,smd}(A) - \Delta G_{solv}^{TR\,mod\,smd}(B) - RT\,\text{Ln}24.5\end{aligned} \qquad \text{Eq 4.23}$$

As stated at the end of section 4.3.2, equations 4.16 and 4.22 certainly deteriorate the SMD values of the solvation free energies of the monomers, but we expect that the dimerization free energies will be improved. We have used the two possibilities, using the total (TRV, from equation 4.17) and reduced (TR, from equation 4.23) values of the entropy in the gas phase. The corresponding values of the dimerization free energies, $\Delta_r G_{sol}^{\circ\,TRV\,mod\,smd}$ and $\Delta_r G_{sol}^{\circ\,TR\,mod\,smd}$ are given in Table 4.3 and shown in figure 4.7 ("TRV" and "TR corrected SMD" entries). It can be seen that the two ways of correcting the solvation entropy make the association free energies much more negative than the SMD values ($\Delta_r G_{sol}^{\circ\,smd}$), and that dropping the vibration entropy from the empirical treatment (TR correction) yields the largest correction. These features can be understood in the following way:

*i)* The sign of the TR correction can be easily predicted. From equations 4.21, 4.22 and 4.23, we can write:

$$\Delta_r G_{sol}^{\circ\,\mathrm{TR\,mod\,smd}} = \Delta_r G_{sol}^{\circ\,\mathrm{smd}} + 0.23\,T(S_g^{TR}(AB) - S_g^{TR}(A) - S_g^{TR}(B) + 12.24) \qquad \text{Eq 4.24}$$

From figure 4.8, it is seen that due to the small variation of the gas phase entropies with the mass M of the molecule, the second term of equation 4.24 is always negative.

*ii)* Concerning the TRV modification of the free energies, an equation quite similar to equation 4.24 can be written from equations 4.15, 4.16 and 4.17:

$$\Delta_r G_{sol}^{\circ\,\mathrm{TRV\,mod\,smd}} = \Delta_r G_{sol}^{\circ\,\mathrm{smd}} + 0.22\,T(S_g^{TRV}(AB) - S_g^{TRV}(A) - S_g^{TRV}(B) + 12.24) \qquad \text{Eq 4.25}$$

which can be written, thanks to the additivity of entropies in the gas phase:

$$\Delta_r G_{sol}^{\circ\,\mathrm{TRV\,mod\,smd}} = \Delta_r G_{sol}^{\circ\,\mathrm{TR\,mod\,smd}} + 0.22\,T(S_g^{V}(AB) - S_g^{V}(A) - S_g^{V}(B) + 12.24) \qquad \text{Eq 4.26}$$

where $S_g^V(A)$ is the vibrational entropy of A in the gas phase. We have found out that the vibrational correction to the free energies, second term of equation 4.26, is always positive. This is due to the fact that, unlike the translation rotation entropies, the vibrational entropies increase very rapidly with the mass of the molecules.

It is also striking that the TR correction yields values of the free energies rather close to the values in the vacuum. When passing from the gas phase to the solution, two effects modify the dimerization free energies:

*i)* The electrostatic stabilization of the dimers is smaller than that of the pair of the separated monomers. For example, it can be seen in tables 4.3 and 4.4 that the solvation free energy of two separate ATZ monomers amounts to -1.6 eV and that the value for the ATZ/ATZ dimer amounts to -1.25 eV only. This effect yields a positive contribution to the dimerization free energies in solution.

*ii)* As already mentioned, equation 4.24 shows that the TR correction to the SMD method is always positive.

The close performances of the two approaches ("in the vacuum" and "TR modified SMD") show that these two previous effects roughly cancel out. Note that this present agreement is fortuitous because each of the two canceling effects depends on the nature of the solvent in different ways.

We have also verified that the correction to the reaction free energies depends on the mass of the molecules: for the lightest dimer Th/Th, the correction amounts to -0.134 eV; for the heaviest dimer ATZ/ATZ, it amounts to -0.171 eV. This is exactly the order of magnitude given in ref. 46 for the entropy barrier to the binding of ligands to molecules.

The thermodynamic cycle of Figure 4.9 has been severely criticized[49], we emphasize here that this cycle is actually correct, only the hypothetical states may be said unreasonable. The Wertz formula is empirical and like any empirical formula, it can have fields of poor applicability, but it can be used so long as the results are satisfactory.

## 4.4 DFT calculations *versus* electrochemical measurements: a discussion

In section 4.2, we demonstrated the effect of the nature of FM functional monomers on the creation of ATZ molecular imprints into the polymer matrixes ($Q_{FM}$ values) and on the detection of ATZ targets ($Q_{d\ FM\text{-}MICP}$ and $Q_{d\ FM}$ values). The results were attributed to the strength of FM-ATZ interaction and then to the concentration of FM/ATZ (in addition to EDOT/ATZ) pre-polymerization complexes. In section 4.3, we calculated the free energies of formation of the different dimers in the vacuum ($\Delta_r G_g^*$) and in solution ($\Delta_r G_{sol}^{\circ\, smd}$, $\Delta_r G_{sol}^{\circ\, TRV\, mod\, smd}$ and $\Delta_r G_{sol}^{\circ\, TR\, mod\, smd}$).

In this section, we deduce from these free energies the values of the concentrations of the different pre-polymerization complexes present in the medium before each FM-MICP electrosynthesis. Since EDOT plays the same role as FM, we consider that the relevant quantity for the interpretation of the electrochemical results is the sum of the concentrations of the FM/ATZ and EDOT/ATZ dimers. We will therefore investigate whether the values of the $Q_{FM}$, $Q_{d\ FM\text{-}MICP}$ and $Q_{d\ FM}$ signals are correlated with the sum of the concentrations: [FM/ATZ] + [EDOT/ATZ].

### 4.4.1 Influence of the FM/ATZ interaction strength on the detection efficiency

For a given FM functional monomer, different from EDOT, there are nine unknown quantities, the concentrations of the monomer and dimer species involved in the pre-polymerization medium during FM-MICP preparation: ATZ, EDOT, FM, ATZ/ATZ, EDOT/ATZ, FM/ATZ, EDOT/EDOT, FM/EDOT and FM/FM. These unknowns are solutions of a system of three linear equations (conservation of matter for the monomers) and six non linear equations (law of mass action for the six dimers). When only EDOT is used for EDOT-MICP preparation, with no other FM functional monomer, there are only five unknowns and five equations. We have solved these systems of equations for each functional monomer, with the help of our own code, based on random variations of the concentrations. All the monomers and dimers concentrations have been determined according to the four different treatments of the free energies. The [FM/ATZ] and [EDOT/ATZ] concentrations involved during each FM-MICP preparation are given in Table 4.5.

We found out that for very negative free energies (say < -0.15 eV, mostly TAA and TMA cases) the concentrations of the FM/ATZ dimers are close to their maximum value (0.015 mol $L^{-1}$, initial value of the ATZ concentration) and are almost insensitive to small variations of the free energies. This is also true for the most positive values of the free energies (say > +0.15 eV, mostly Th and EDOT cases) for which the concentration of the FM/ATZ dimer is found close to zero.

On the other hand, when the free energy lies in between the extreme values (mostly TMeOH case), we found that the dimer concentration is highly sensitive to small variations of the free energy, as small as 0.02 eV. This is the order of magnitude of the conformation entropy. It has been noted that using simple thumb rules, like that of section 4.3.1 and Table 4.2, we can overestimate the conformation entropy by a factor two[41]. For this reason we worked in the following way:

*i)* we calculate the concentrations twice, with free energies including ($c_y$) and not including ($c_n$) the conformation entropies.

*ii)* we adopt for the concentration half the sum of the two values:

$$c = \frac{c_y + c_n}{2} \qquad \text{Eq 4.27}$$

*iii)* we also consider that the difference provides us with a kind of error bar:

$$\Delta c = c_y - c_n \qquad \text{Eq 4.28}$$

According to formulas 4.27 and 4.28, all the concentrations can be written c ± Δc/2. The [FM/ATZ] and [EDOT/ATZ] concentrations, calculated in this way, are given in Table 4.5. It can be seen that in all cases but one (Th), the [EDOT/ATZ] concentrations are always much smaller than the [FM/ATZ] concentrations. In the case of Th, the contrary is obtained. This feature can be easily understood from figure 4.7: in all cases but one (Th case) the value of the interaction free energy in the EDOT/ATZ dimer is more positive than the value for the FM/ATZ complex.

**Table 4.5.** Concentrations (in mol $L^{-1}$) of the FM/ATZ and EDOT/ATZ pre-polymerization complexes (corresponding to each FM-MICP preparation) obtained with different treatments of the free energies (thanks to $\Delta_r G_g^*$, $\Delta_r G_{sol}^{\circ\, smd}$, $\Delta_r G_{sol}^{\circ\, TRV\, mod\, smd}$ and $\Delta_r G_{sol}^{\circ\, TR\, mod\, smd}$ respectively). R is the correlation coefficient between the sum of concentrations ([FM/ATZ] + [EDOT/ATZ]) and the measured $Q_{FM}$ electrochemical charge.

| | | **in the vacuum** | **crude SMD** | **TRV corrected SMD** | **TR corrected SMD** |
|---|---|---|---|---|---|
| **TMA-MICP** | **[TMA/ATZ]** | $0.14\ 10^{-1}$ | $0.47\ 10^{-2}$ | $0.11\ 10^{-1}$ | $0.15\ 10^{-1}$ |
| | **[EDOT/ATZ]** | $0.62\ 10^{-6}$ | $0.91\ 10^{-7}$ | $0.86\ 10^{-6}$ | $0.88\ 10^{-6}$ |
| **TAA-MICP** | **[TAA/ATZ]** | $0.11\ 10^{-1}$ | $0.18\ 10^{-2}$ | $0.73\ 10^{-2}$ | $0.13\ 10^{-1}$ |
| | **[EDOT/ATZ]** | $0.16\ 10^{-5}$ | $0.13\ 10^{-6}$ | $0.20\ 10^{-5}$ | $0.31\ 10^{-5}$ |
| **TMeOH-MICP** | **[TMeOH/ATZ]** | $0.49\ 10^{-2}$ | $0.29\ 10^{-4}$ | $0.45\ 10^{-3}$ | $0.53\ 10^{-2}$ |
| | **[EDOT/ATZ]** | $0.18\ 10^{-4}$ | $0.15\ 10^{-6}$ | $0.38\ 10^{-5}$ | $0.12\ 10^{-4}$ |
| **EDOT-MICP** | **[EDOT/ATZ]** | $0.16\ 10^{-4}$ | $0.60\ 10^{-6}$ | $0.20\ 10^{-4}$ | $0.43\ 10^{-3}$ |
| **Th-MICP** | **[Th/ATZ]** | $0.30\ 10^{-5}$ | $0.12\ 10^{-6}$ | $0.40\ 10^{-5}$ | $0.38\ 10^{-4}$ |
| | **[EDOT/ATZ]** | $0.19\ 10^{-4}$ | $0.15\ 10^{-6}$ | $0.40\ 10^{-5}$ | $0.14\ 10^{-4}$ |
| **R** | | **0.983** | **0.809** | **0.910** | **0.992** |

In figures 4.10 and 4.11, we plot the experimental $Q_{FM}$ charges against the sum of the dimer concentrations: [FM/ATZ] + [EDOT/ATZ] (calculated with the four sets of values of the free energies). It can be seen that:

*i)* The crude SMD values yield very small concentrations and a poor correlation (R=0.809, figure 4.10 top). Actually the free energies in the vacuum yield more reasonable values of the concentrations and a stronger correlation with experimental values (R=0.983, figure 4.10 top).

*ii)* The TRV modified free energies yield a strong correlation between $Q_{FM}$ charges and concentrations (R=0.910, figure 4.10 bottom).

*iii)* The TR corrected SMD values yield the best correlation between the $Q_{FM}$ charges and the dimer concentrations (R=0.992, figure 4.11 top).

The strongest correlation is thus yielded by the $\Delta_r G_{sol}^{\circ\,TR\,mod\,smd}$ value. We emphasize that this value has been discussed in section 4.3.3 to be the best physically grounded. It is striking that the calculation in the vacuum (using $\Delta_r G_g^*$) yields quite honorable results. This can also be easily understood from figure 4.7, where "in the vacuum" and "TR corrected SMD" values of the free energies can be seen close to each others.

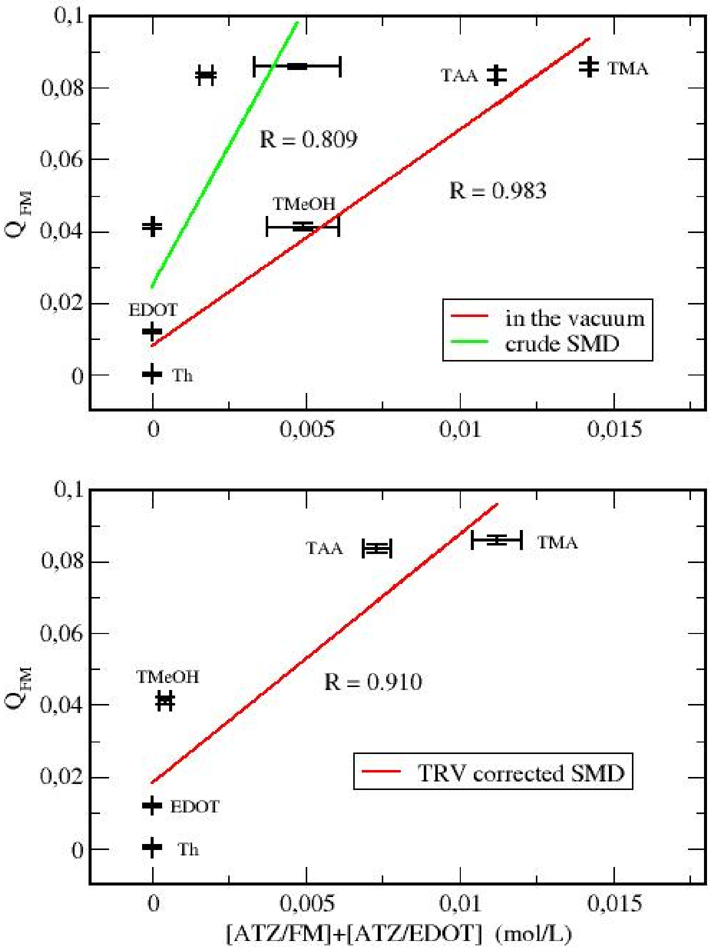

**Figure 4.10.** Correlation of the experimental $Q_{FM}$ charge with the total concentration of ATZ hetero-dimers. Concentrations are obtained with different calculations of the dimerization free energies (top: $\Delta_r G_g^*$ and $\Delta_r G_{sol}^{\circ\,smd}$, bottom: $\Delta_r G_{sol}^{\circ\,TRV\,mod\,smd}$). The error bars are defined in the text.

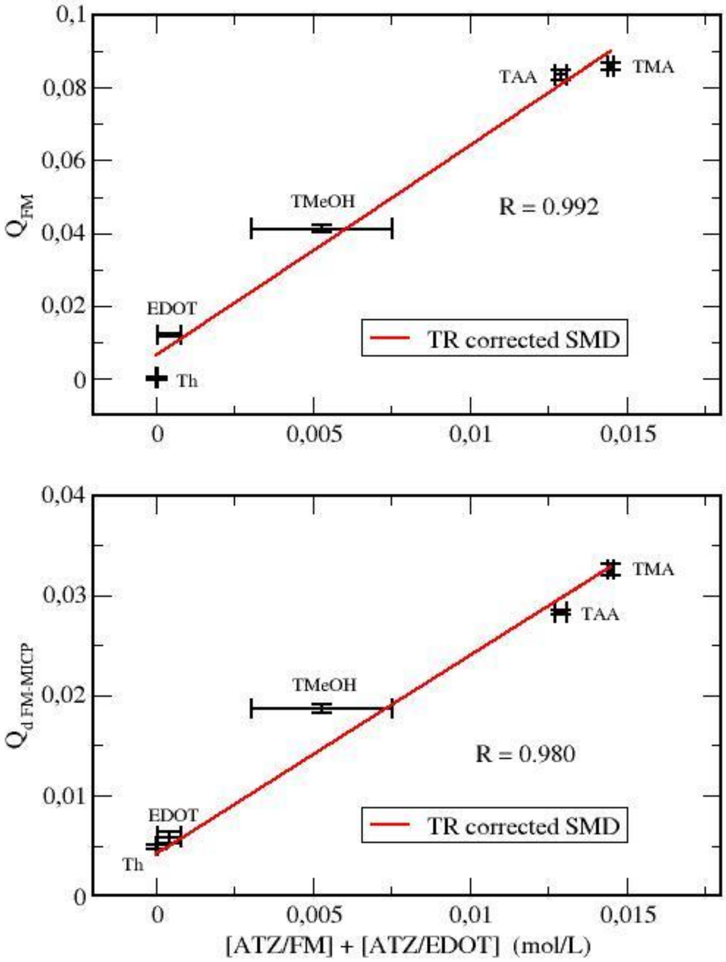

**Figure 4.11** Correlation of the two experimental charges, $Q_{FM}$ (top) and $Q_{d\ FM\text{-}MICP}$ (bottom), with the total concentration of ATZ hetero-dimers, obtained using the most sophisticated calculation of the dimerization free energies ($\Delta_r G_{sol}^{\circ\,TR\,mod\,smd}$). The error bars are defined in the text.

Anyway, the strong correlation of figure 4.11 (top) shows that the number of ATZ molecules embedded in the polymer (related to $Q_{FM}$ value) is the same as (or at least is proportional to) the total number of FM/ATZ and EDOT/ATZ dimers in the solution, before polymerization.

In figure 4.11 (bottom), we have considered the $Q_{d\ FM\text{-}MICP}$ charges obtained from equation 4.2 and electrochemically measured. We have seen, in section 4.2, that these charges are related to the efficiency of the functionalized FM-MICP polymers to detect ATZ targets. It can be seen once again that the correlation with the total concentration of ATZ hetero-dimers ([FM/ATZ] + [EDOT/ATZ]) is strong (R=0.980), but weaker than for the $Q_{FM}$ charge. This strong correlation can be found surprising, because several effects could disturb it:

*i)* The strength of the FM-ATZ interactions should interfere twice: firstly, in determining the number of FM/ATZ pre-polymerization dimers and thus the number of functionalized cavities into the imprinted polymer during the polymerization process; secondly, in determining the efficiency of a given cavity to detect ATZ in the detection process.

*ii)* The dimerization free energies in the functionalized cavities of the polymer are certainly different from those in the acetonitrile solution, and consequently the FM/ATZ concentrations should have different values in the genuine polymer and in the FM-MICP matrix after detection.

*iii)* ATZ molecules diffuse in the polymer at an unknown rate, depending on the nature of the FM-MICP polymer.

The fact that the correlation of figure 4.11 (bottom) is also strong suggests the following mechanism of atrazine detection:

*i)* The ATZ molecules diffuse slowly in the polymer matrix and independently of the nature of the FM-MICP, so that they are mainly collected by the imprinted cavities close to the polymer surface.

*ii)* The imprinted cavities may thus be considered saturated by ATZ molecules in the detection process, so that the number of cavities does not interfere in the detection process.

*iii)* The FM/ATZ dimerization free energies in the polymer matrixes are close to (or at least follow the same law as) the free energies in the acetonitrile solution.

This good correlation shows that the detection of ATZ by FM-MICP polymer is simply related to the strength of the interaction between the ATZ target molecules and the FM functional monomers in the genuine solution. In particular, the number of FM/ATZ dimers in solution is the critical parameter which determines the efficiency of the FM-MICP towards the detection of ATZ.

Meanwhile, non-specific adsorption is presented in the ATZ detection process by FM-MICP, thus the contribution of this kind of interaction should be examined.

### 4.4.2 Evaluation of the non-specific adsorption

While FM-MICP films are electrosynthesized in the presence of ATZ molecules, FM-NICP layers are electrochemically prepared in the absence of target molecules and are thus free from functionalized imprinted cavities able to specifically interact with target molecules. As a consequence, added ATZ molecules can only interact with FM-NICP layers by the way of a non specific adsorption thanks to the interaction with EDOT or FM functional monomers localized close to the polymer surface.

If the non-specific interactions between ATZ molecules and FM-MICP and FM-NICP layers are similar, hence, the detection of ATZ molecules by the FM-NICP allows the evaluation of the contribution of adsorption in the ATZ recognition process by FM-MICP layers, as already proposed.

The detection of ATZ molecules by FM-NICP was already evaluated and quantified by the values of $Q_{d\ FM\text{-}NICP}$ (figure 4.4). In order to elucidate the influence of FM on the non-specific detection of ATZ molecules, the values of $Q_{d\ FM\text{-}NICP}$ were plotted in the figure 4.12 top as a function of the ATZ hetero-dimers concentrations ([FM/ATZ] + [EDOT/ATZ]), calculated from $\Delta_r G_{sol}^{\circ\, TR\, mod\, smd}$ values.

Figure 4.12 top demonstrates that the interaction between ATZ and FM-NICP increases in the order: Th, EDOT, TMeOH, TAA, TMA as expected from the strength of the different functional monomers, supposing that the strength of FM-ATZ interactions in solution and at the solid-liquid interface (copolymer-ACN) are comparable.

The force of FM-ATZ interactions influences the adsorption of ATZ molecules on the FM-NICP surface, therefore adsorption of ATZ over TMA-NICP is translated by high values of $Q_{d\ TMA\text{-}NICP}$. Neverthless, the correlation between $Q_{d\ FM\text{-}NICP}$ and the concentrations sum of ATZ heterodimers (R = 0.87) cannot be considered as good as in the $Q_{d\ FM\text{-}MICP}$ case (R = 0.98). This means that the efficiency of the adsorption over FM-NICP (and eventually FM-MICP) is not only dependent on the FM-ATZ interaction strength.

Indeed, the growth of the copolymers over the electrode is dependent on the nature of FM. The structure and the roughness of these layers are thus different, as well as the specific surfaces onto which ATZ may adsorb. On the other hand, since surface of the polymers is exposed to ACN solvent, the functional groups present at the interface are more or less solvated, depending on their polarity. This will affect the interactions of these functional groups with ATZ molecules during adsorption process.

In summary, the adsorption of ATZ molecules is influenced by:

*i)* the FM-ATZ interaction strength

*ii)* the roughness of FM-NICP and FM-MICP surfaces

*iii)* the solvation of FM-NICP and FM-MICP in ACN

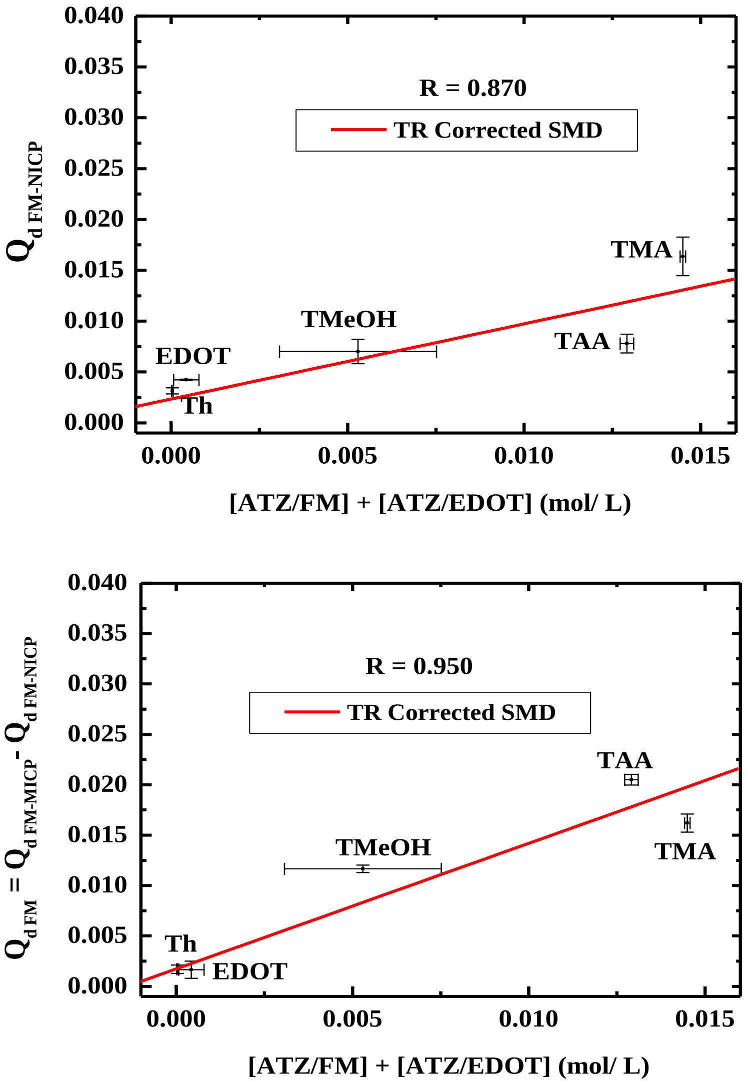

**Figure 4.12** Correlation of the two experimental charges, $Q_{d\ FM\text{-}NICP}$ (top) and $Q_{d\ FM} = Q_{d\ FM\text{-}MICP} - Q_{d\ FM\text{-}NICP}$ (bottom), with the total concentration of ATZ hetero-dimers, obtained using the most sophisticated calculation of the dimerization free energies ($\Delta_r G_{sol}^{\circ TR\,mod\,smd}$). The error bars are defined in the text.

If the non-specific recognition process intervenes in FM-NICP, it must also be considered in the case of FM-MICP layers. In other words, $Q_{d\ FM\text{-}MICP}$ values take into account, in addition to the specific detection of targets, the non specific adsorption of ATZ molecules. Once again, if we assume that, for a given FM functional monomer, ATZ adsorption is similar onto FM-MICP and FM-NICP layers, then subtracting $Q_{d\ FM\text{-}NICP}$ values from those of $Q_{d\ FM\text{-}MICP}$ according to equation 4.4 should give access to specific ATZ detection data ($Q_{d\ FM}$). The real molecular recognition role of the functional imprinted cavities into the polymer matrixes is thus reflected by the value of $Q_{d\ FM}$.

$Q_{d\ FM}$ values are represented as a function of the dimers concentration ([FM/ATZ] and [EDOT/ATZ]) in figure 4.12 bottom, in order to evaluate the influence of the nature of FM on the efficiency of the specific detection by the FM-MICP functionalized cavities.

As expected from the strength of the different functional monomers, the specific detection of ATZ molecules decreases in the following order of functional monomers-based MICP: TAA, TMeOH, EDOT and Th. However, due to the much higher $Q_{d\ TMA\text{-}NICP}$ value comparatively with that of $Q_{d\ TAA\text{-}NICP}$, $Q_{d\ TMA}$ appears lower than $Q_{d\ TAA}$, meaning that ATZ quantitatively adsorbs onto TMA-MICP layers probably due to the poor solvation of TMA-MICP in ACN medium and/or to the high roughness of the TMA-MICP surface.

Therefore, in order to fabricate the "best" sensing layers based on MICP, strong interactions between FM and the template molecules are recommended in the pre-polymerization complex, as well as in the functionalized cavities of the MICP matrix. However, these strong interactions are not sufficient since non-specific adsorption should be minimized. Thus, according to this discussion, TAA-MICP based sensing layer represents the "best" sensing layer in our conditions since it enables the minimization of non-specific adsorption.

## Conclusion

In the present chapter, we experimentally and theoretically studied the influence of the nature of the chemical functionalities of a polythiophene-based Molecularly Imprinted Conducting Polymer (FM-MICP) on its ability to detect atrazine (ATZ) target molecule. Differently functionalized thiophene-based monomers (FM) were used in order to form FM/ATZ pre-polymerization complexes in acetonitrile solvent, leading after electrosynthesis to FM-MICP sensitive layers deposited onto gold substrates and dedicated to the sensing of additional amounts of atrazine. We demonstrated, thanks to electrochemical measurements, the clear effect of the nature of FM functional monomer on the number of ATZ molecular imprints ($Q_{FM}$ values) and on the sensitivity towards ATZ ($Q_{d\ FM\text{-}MICP}$ values) of the FM-MICP layers, which both decrease in the following order of FM functional monomers: TMA, TAA, TMeOH, EDOT and Th. These experimental results were attributed to the strength of the FM-ATZ interaction.

For investigating this hypothesis, we performed DFT/PCM calculations of the free energies of formation in solution of the FM/ATZ dimers. The crude SMD values are very poor, in relation with the poor additive behavior of the PCM solvation energies. We used, therefore, the Wertz formula to introduce an empirical modification of the solvation free energies. The results enable the interpretation of the electrochemical measurements, provided the empirical term only uses the translation rotation part of the gas phase entropy and ignores the vibration part. We could show that a strong correlation exists between the measured electrochemical signals ($Q_{FM}$ and $Q_{d\ FM\text{-}MICP}$ values) and the strength of the interaction between the atrazine and the functional monomers molecules.

In this chapter, we used the PCM method and an empirical correction of the solute entropies. In this way, we could calculate the absolute values of the formation free energies of as much as fourteen dimers with a very reasonable amount of computer time.

The calculated dimerization free energies enabled the calculation of the concentrations of the different FM/ATZ pre-polymerization complexes present in acetonitrile medium before each FM-MICP electrosynthesis. We found that the electrochemical signals ($Q_{FM}$ and $Q_{d\ FM\text{-}MICP}$ values) are well correlated with the concentrations of the FM/ATZ dimers. This good correlation demonstrates that a much elaborated property of the FM-MICP imprinted polymer, as is the detection of targets (quantified by $Q_{d\ FM\text{-}MICP}$) after a complex process of polymer synthesis and washing, can be very simply related to the strength of the interaction between the target molecules and the FM functional monomers in the genuine solution.

Finally, we evaluated the aptitude of ATZ molecules to adsorb onto FM-MICP layers thanks to the measure of ATZ targets sensed by FM-NICP polymers ($Q_{d\ FM\text{-}NICP}$) which were electrogenerated free from specific imprinted cavities.

# References

---

[1] Nicholls, I. A. *Chem. Lett*. 24, 1035-1036, 1995.

[2] Nicholls, I. A. *J. Mol. Recognit*. 11, 79-82, 1998.

[3] Nicholls, I. A.; Adbo, K.; Andersson, H. S.; Andersson, P. O.; Ankarloo, J.; Hedin-Dahlstrom, J.; Jokela, P.; Karlsson, J. G.; Olofsson, L.; Rosengren, J.; Shoravi, S.; Svenson, J.; Wikman, S. *Anal. Chem*. 435, 9-18, 2001.

[4] Nicholls, I. A.; Andersson, H. S.; Charlton, C.; Henschel, H.; Karlsson, C. G. B.; Karlsson, J. G.; O'Mahony, J.; Rosengren, A. M.; Rosengren, K. J.; Wikman, S. *Biosens. Bioelectron.* 25, 543-522, 2009.

[5] Pande, V. S.; Grosberg, A. Y.; Tanaka, T. *Physica D.* 107, 316-321, 1997.

[6] Piletsky, S. A.; Panasyuek, T. L.; Piletskaya, E. V.; Nicholls, I. A.; Ulbricht, M.; *J. Membr. Sci.* 157, 263-278, 1999.

[7] Fu, Q.; Sanbe, H.; Kagawa, C.; kunimoto, K.; Haginaka, *J. Anal. Chem.* 75, 191-198, 2003.

[8] Li, P.; Rong, F.; Xie, Y.; Hu, V.; Yuan, C. *J. Anal. Chem.* 59, 939-944, 2004.

[9] Schwarz, L.; Holdsworth, C. I.; McCluskey, A.; Bowyer, M. C. *Aust. J. Chem.* 57, 759-764, 2004.

[10] Holdsworth, C. I.; Bowyer, M. C.; Lennard, C.; McCluskey, A. *Aust. J. Chem*. 58, 315-320, 2005.

[11] Ogawa, T.; Hoshina, K.; Haginaka, J.; Honda, C.; Tanimoto, T.; Uchida, T. *J. Pharm. Sci.*, 94, 353-362, 2005.

[12] Mierts, S.; Scrocco, E.; Tomasi, J. *Chem. Phys*. 55, 117-129, 1981.

[13] O'Mahony, J.; Karlsson, B. C. G.; Mizaikoff, B.; Nicholls, I.A. *Analyst*. 11, 1161-1168, 2007.

[14] Wang, J. M.; Wolf, R. M.; Caldwell, J. W.; Kollman, P. A.; Case, D. A. *J. Comput. Chem*. 25, 1157-1174, 2005.

[15] Ansell, R. J.; Luah, K. L. *Analyst*. 130, 179-187, 2005.

[16] Andersson, H. S.; Karlsson, J. G.; Piletsky, S. A.; Koch-Schmidt, A. C.; Mosbach, K.; Nicholls, I. A. *J. Chromatogr. A.* 848, 39-49, 1999.

[17] Katz, A.; Davis, M. E.; *Macromolecules*. 32, 4113-4121, 1999.

[18] Svenson, J.; Karlsson, J. G.; Nicholls, I. A.; *J. Chromatogr. A.* 1024, 39-44, 2004.

[19] O'Mahony, J.; Wei, S.; Molinelli, A.; Mizaikoff, B.; *Anal. Chem.* 78, 6187-6190, 2006.

[20] Karlsson, B. C. G.; O'Mahony, J.; Karlsson, J. G.; Bengtsson, H.; Eriksson, L. A.; Nicholls, I. A. *J. Am. Chem. Soc.* 131, 13297-13304, 2009.

[21] O'Mahony, J.; Nolan, K.; Smyth, M. R.; Mizaikoff, B.; *Anal. Chim. Acta*. 534, 31-39, 2005.

[22] Karim, K.; Breton, F.; Rouillon, R.; Piletska, E. V.; Guerreiro, A.; Chianella, I.; Piletsky, S. A. *Adv. Drug Delivery Rev*. 57, 1795-1808, 2005.

[23] Mayes, A. G.; Whitcombe, M. J. *Adv. Drug Delivery Rev*. 57, 1742-1778, 2005.

[24] Piletsky, S. A.; Karim, K.; Piletska, E. V.; Day, C. J.; Freebairn, K. W.; Legge, C.; Turner, A. P. F. *Analyst* 126, 1826-1830, 2001.

[25] Kitchen, D. B.; Decornez, H.; Furr, J. R.; Bajorath, *J. Nat. Rev. Drug Disc.* 3, 935-949, 2004.

[26] Garnier, F.; Korri Youssoufi, H.; Srivastava, P.; Yassar, A. *J. Am. Chem. Soc*. 116, 8813-8814, 1994.

[27] Garnier, F.; Bouabdallaoui, B.; Srivastava, P.; Mandrand, B.; Chaix, C.; *Sens. Actuators B.* 123, 13-20, 2007.

---

[28] Tirapattur, S.; Belletête, M.; Drolet, N.; Leclerc, M.; Durocher, G. *Chem. Phys. Lett.* 370, 799-804, 2003.

[29] Béra-Abérem, M.; Ho, H. A.; Leclerc, M. *Tetrahedron*. 60, 11169-11173, 2004.

[30] Doré, K.; Dubus, S.; Ho, H. A.; Lévesque, I.; Brunette, M.; Corbeil, G.; Boissinot, M.; Boivin, G.; Bergeron, M. G.; Boudreau, D.; Leclerc, M. *J. Am. Chem. Soc.* 126, 4240-4244, 2004.

[31] Ho, H. A.; Leclerc, M. *J. Am. Chem. Soc***.** 126, 1384-1387, 2004.

[32] Tomasi, J.; Menucci, B. ; Cammi, R. *Chem. Rev.* 105, 2999, 2005

[33] Marenich, A. V.; Cramer, C. J.; Truhlar, D. J. *J. Phys. Chem. B* 113, 6378-6396, 2009.

[34] Gaussian 09, Revision A.02, M. J. Frisch, G. W. Trucks, H. B. Schlegel, G. E. Scuseria, M. A. Robb, J. R. Cheeseman, G. Scalmani, V. Barone, B. Mennucci, G. A. Petersson, H. Nakatsuji, M. Caricato, X. Li, H. P. Hratchian, A. F. Izmaylov, J. Bloino, G. Zheng, J. L. Sonnenberg, M. Hada, M. Ehara, K. Toyota, R. Fukuda, J. Hasegawa, M. Ishida, T. Nakajima, Y. Honda, O. Kitao, H. Nakai, T. Vreven, J. A. Montgomery, Jr., J. E. Peralta, F. Ogliaro, M. Bearpark, J. J. Heyd, E. Brothers, K. N. Kudin, V. N. Staroverov, R. Kobayashi, J. Normand, K. Raghavachari, A. Rendell, J. C. Burant, S. S. Iyengar, J. Tomasi, M. Cossi, N. Rega, J. M. Millam, M. Klene, J. E. Knox, J. B. Cross, V. Bakken, C. Adamo, J. Jaramillo, R. Gomperts, R. E. Stratmann, O. Yazyev, A. J. Austin, R. Cammi, C. Pomelli, J. W. Ochterski, R. L. Martin, K. Morokuma, V. G. Zakrzewski, G. A. Voth, P. Salvador, J. J. Dannenberg, S. Dapprich, A. D. Daniels, O. Farkas, J. B. Foresman, J. V. Ortiz, J. Cioslowski, and D. J. Fox, Gaussian, Inc., Wallingford CT, 2009.

[35] Cramer, Ch. J. *Essentials of Computational Chemistry*, Wiley, p. 379, 2004.

[36] Grimme S. J. *Comput. Chem.* 27, 1787-1799, 2006.

[37] Fuentealba, P.; Preuss, H.; Stoll, H.; Szentpaly, L. *Chem. Phys. Lett.* 89, 418, 1989.

[38] Hill, J. G.; Platts, J. A.; Werner, H. J. *Phys. Chem. Chem. Phys.* 8, 4072-4078, 2006.

[39] Curtiss, L. A.; Frurip, D. J.; Blander, M. *J. Chem. Phys.* 71, 2703-2711, 1979.

[40] McQuarrie, D. A. *Statistical Mechanics*, University Science Books, 2000.

[41] Mammen, M.; Shaknovich, E. I.; Deutsch, J. M.; Whitesides, G. M. *J. Org. Chem.* 63, 3821-3830, 1998.

[42] Bell R. P. *Trans. Farad. Soc.* 27, 797, 1931.

[43] Lin, M.; Archirel, P.; Van Oanh, N. T.; Muroya, Y.; Fu, H.; Yan, Y.; Nagaishi, R.; Kumagai, Y.; Katsumura, Y.; Mostafavi, M. *J. Phys. Chem. B* 2011, in press

[44] *Handbook of Chemistry and Physics*, CRC Press, 1994

[45] Sen U. *J. Amer. Chem. Soc.* 102, 2181, 1980.

[46] Siebert, X.; Amzel, M. *Proteins* 54, 104, 2004.

[47] Swanson, J. M. J.; Henchman, R.; McCammon, J. A. *Biophys. J.* 86, 67-74, 2004.

[48] Wertz, D. H. *J. Am. Chem. Soc.* 102, 5316-5322, 1980

[49] Ben Naim, A.; Marcus, Y. *J. Chem. Phys.* 81, 2016, 1984.

[50] Cooper, J.; Ziegler, T. *Inorg. Chem.* 41, 6614, 2002

[51] Lau, J. K. C.; Deubel, D. V. *J. Chem. Theor. Comp.* 2, 103, 2006.

[52] Kua, J. ; Hanley, S. W.; De Haan, D. O. *J. Phys. Chem. A* 112, 66, 2008.

[53] Krtizner, H. E. ; De Haan, D. O. ; Kua, J. *J. Phys. Chem. A* 113, 6994, 2009.

[54] Kua, J. ; Kritzner, H. E. ; De Haan, D. O. *J. Phys. Chem. A* 115, 1667, 2011.

[55] Crowder, G. A.; Cook, B. R. *J. Chem. Phys.* 71, 914-916, 1967.

[56] Murray, C. W.; Verdonk, M. *J. Comp. Aid. Mol. Des.* 16, 741-753, 2002.

# Chapter 5

## Electrochemical and gravimetric coupled transductions for correlated investigations on chemical recognition processes by MICP

Molecularly imprinted conducting polymers, MICP, based sensing layers were synthesized then characterized by different techniques in order to optimize the recognition process of ATZ molecules by these layers. The influence of various functional monomers on the detection process was also investigated by theoretical means correlated with electrochemical sensing results and an evaluation of non-specific interaction was carried out.

In this chapter we will electrosynthesize the MICP sensitive layers onto the sensing zone of surface acoustic wave, SAW, device. Gravimetrical transduction of ATZ molecules detection will be studied and an original coupled electrochemical/gravimetrical transduction, ESAW, will be developed, in order to have better understanding of the parameters that control ATZ recognition process by MICP. Gravimetrical and electrochemical transductions will be simultaneously used to follow-up:

*i)* the kinetics of conducting polymers electropolymerization as well as the doping/un-doping processes.

*ii)* the target molecule extraction and its further recognition by MICP.

*iii)* the relation between mass and structural variations during electropolymerization and sensing processes with the modification of the electrochemical properties of the concerned conducting films.

## 5.1 Introduction

Many studies have been carried out on coupled transduction methods in sensors applications, such as acoustic (quartz crystal microbalance) and optical (surface Plasmon resonance) transductions[1], or on the use of electrochemical quartz microbalance (EQCM) allowing the simultaneous measure of mass and current variations in an electrochemical process. In particular, previous studies[2,3,4,5,6,7,8,9] reported the use of EQCM to investigate conducting polymer performances. However, these devices suffer in this case from their sensitivity to ionic strength, temperature and solutions viscosities and conductivities.

In this chapter, we describe the concept and the use of an original electrochemical surface acoustic wave sensor, ESAW, which appears to be a more interesting candidate since it is able to independently extract the pure mass of a deposited layer. In fact, temperature and viscosity fluctuations are cancelled due to the use of a dual delay line configuration, whereas sensing layer gold metallization makes devices less sensitive to ionic strength and conductivity variations[10].

The original design of such a chemical sensor based on the electropolymerization of “our” polythiophenes-based MICP upon the surface acoustic wave (SAW) sensor sensing area is presented.

## 5.2 Experimental

### 5.2.1 Procedures

Two kinds of conducting polymers were investigated in this chapter:

*i)* Molecularly Imprinted Conducting copolymers, poly(EDOT-co-TAA), (TAA-MICP) noted **MICP**, prepared by electrochemical copolymerization of EDOT and TAA in the presence of ATZ template molecules.

*ii)* Non imprinted conducting homopolymers, polyEDOT, (EDOT-NICP) noted **PEDOT**, electrosynthesized in the absence of ATZ template molecules.

PEDOT films were electrochemically synthesized from $7.5 \times 10^{-3}$ mol $L^{-1}$ of EDOT monomers dissolved in ACN solvent in the presence of $LiClO_4$ (0.1 mol $L^{-1}$).

For MICP preparation, TAA ($30 \times 10^{-3}$ mol $L^{-1}$), used as functional monomer, in addition to ATZ ($15 \times 10^{-3}$ mol $L^{-1}$), used as template molecule, were dissolved in ACN, in the presence of $LiClO_4$ (0.1 mol $L^{-1}$) as supporting electrolyte. A sufficient laps of time of 10 minutes was used for the efficient association, through hydrogen bonds, between TAA and ATZ molecules. Then, EDOT ($7.5 \text{ x } 10^{-3}$ mol $L^{-1}$) used as linker was added before electropolymerization.

PEDOT and MICP electrosynthesis was achieved through chronoamperometry at a constant potential of 1.45 V *vs*. $Ag/AgNO_3$. This technique was used due to the capacities of the actual homemade potentionstat, where 2-steps chronoamperometry technique isn’t functional yet. Electrosynthesis of PEDOT and MICP conducting films was carried out onto the gold ESAW sensing area ($S \approx 0.22$ $cm^2$), which was first cleaned with a piranha solution (98% $H_2SO_4$ / 30% $H_2O_2$ 1:1 v/v) for 30 min and then rinsed with deionised double distilled water (as already indicated in *section 2.2*).

In order to check the sensing properties of MICP towards the target molecules, and eventually to compare them with those of PEDOT, ATZ molecules were first extracted from the matrix of MICP. For this purpose, a continuous flow of an extraction protic solution (methanol and acetic acid, 07:03 v/v) was pumped during 10 min over the sensing area of the ESAW sensor, at a constant flow rate of 0.19 mL $min^{-1}$ with a peristaltic pump. ATZ molecules were then removed from the MICP matrix by breaking the hydrogen bonds linking ATZ to TAA. The obtained functionalized cavities into the washed MICP films were then ready to detect the presence of newly added ATZ molecules.

### 5.2.2 Device and apparatus

The ESAW sensor consists of a delay line fabricated on a 36°rot lithium tantalate ($LiTaO_3$) piezoelectric substrate (see *section 2.5.3*). Chromium/gold (20 nm Cr/80 nm Au) interdigital transducers (IDTs) were structured with a periodicity of $\lambda = 40$ µm, corresponding to an operating frequency of about 104 MHz. The ESAW sensing area (figure 5.1), used also as working electrode for electrochemical measurements, was metalized (20/80 nm Cr/Au) to favor leaky SAW propagation[11,12], and thus the acoustic energy confinement close to surface substrate, making the sensor highly sensitive to any perturbation occurring in the propagating medium. A Teflon fluidic cell was placed on the region between the IDTs to contain solutions and to avoid any short circuit. A pulse excitation technique was used to monitor both amplitude and phase changes versus time. It enables time-of-flight resolved informations to be obtained and spurious reflections to be identified[10]. Copper electrodeposition experiments allowed relating phase variations (in the pulse mode) to the frequency ones (in the double oscillator configuration). A phase shift of 1° is thus equivalent to a 938 Hz frequency shift.

Cyclic voltammetric and amperometric measurements were performed with a homemade potentiostat configuration (see *section 2.6*). The electrochemical system was composed by a three-electrode cell, where grounded gold SAW sensing area was used as working electrode and where coiled Pt and Ag/$AgNO_3$ electrodes were used as counter and reference electrodes, respectively (figure 5.1). Prior to all the experiments, the solutions were purged with argon.

In order to study the electrochemical behavior of synthesized conducting polymers, cyclic voltammograms were recorded, and all cyclic voltammograms were corrected by substracting the background current corresponding to the supporting electrolyte ($LiClO_4$ 0.1 mol $L^{-1}$) in ACN solution.

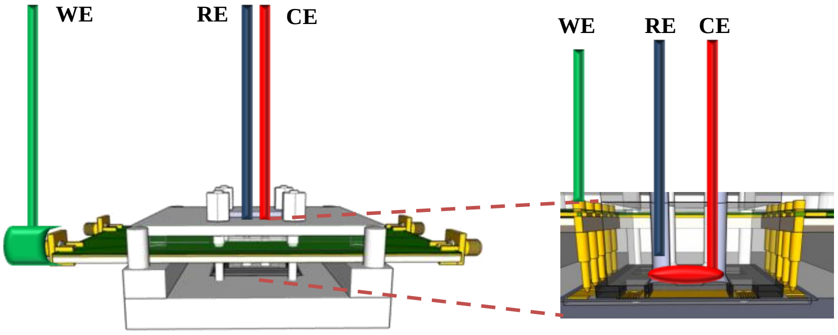

**Figure 5.1** Electrochemical surface acoustic wave, ESAW, device. Sensing area of SAW acts as working electrode (WE), coiled Pt electrode as counter electrode (CE) and $Ag/AgNO_3$ as reference electrode (RE).

Homemade software was developed for monitoring both electrochemical and gravimetric experiments simultaneously. All measurements were achieved at room temperature.

## 5.3 ESAW correlated kinetics investigations

Real time electrochemical/gravimetrical follow up of the different procedures carried out on the sensing layers should, clarify the different parameters that controls the behaviors and the performances of these layers

### 5.3.1 Electropolymerization of MICP and PEDOT: kinetics study and thickness-monitoring

Although the large easiness of electropolymerization of conducting polymers on electrode surfaces, the initial deposition step and the further propagation process are not clearly understood, since the electropolymerization mechanisms generally involve many steps. The polymers are generated by a succession of coupling reactions involving radical cations. Electropolymerization proceeds through successive electrochemical (E) and chemical (C) steps, according to a general $E(CE)_n$ scheme[13,14] The process starts by electrochemical oxidation of the monomer molecules, chemical coupling of the resulting radical cations, reoxidation of the formed oligomers in solution, their further coupling, and so on, leading to the formation of a mixture of oligomers of various molecular weights in the solution phase.

The next step is the nucleation of the polymer phase on the electrode surface, followed by the growth of the primary nuclei through further deposition of polymer molecules from the solution.

In order to check whether both MICP and PEDOT films can be directly electrodeposited onto the gold sensitive area of the ESAW and to highlight the growth kinetics of the conducting films, chronoamperometry was used at a constant potential of 1.45 V *vs.* Ag/$AgNO_3$ to electrosynthesize the films.

The modifications in the phase of the ESAW sensing area (which parallels the current variation) upon the growth of the films by chronoamperometry were used to demonstrate the gravimetrical modifications (figure 5.2). As observed, the current increases first rapidly with time, in both MICP (figure 5.2A top) and PEDOT (figure 5.2B top) cases. This can be attributed to the oxidation of the monomers and to the formation of oligomers of various molecular weights in the solution phase. The simultaneous follow up of the electropolymerization process by ESAW also suggests this argument that was already discussed in ref. 13-14. Indeed, an observation of the phase variations during the MICP (figure 5.2A bottom) and PEDOT (figure 5.2B bottom) electropolymerization processes indicates that, during the first second in both cases, the phase remains constant meaning that no mass is deposited over the sensing area. The calculation of coulombic charges passed in the chronoamperograms during the first second of MICP and PEDOT electropolymerization gives a comparable values (about 10 mC $cm^{-2}$). This indicates that the charge quantities consumed for the formation of MICP and PEDOT oligomers are the same in the two solution phases (during the chemical step).

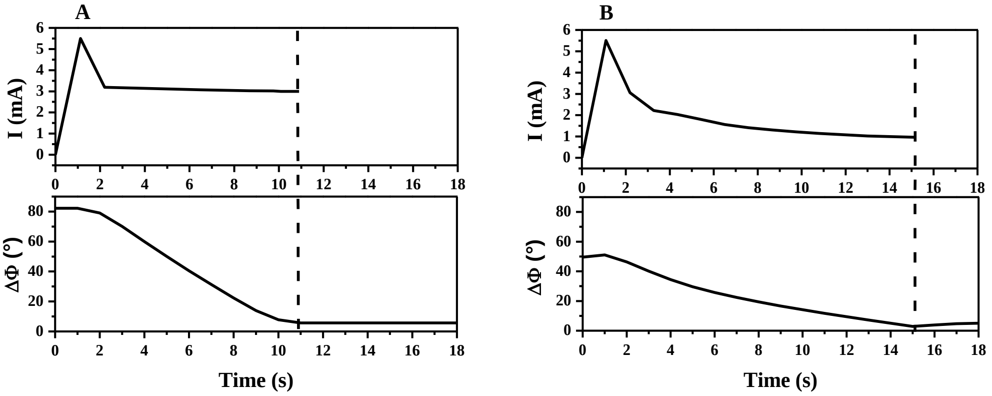

**Figure 5.2.** Simultaneous electrochemical/gravimetrical follow up by ESAW of the electropolymerization at a constant potential (1.45 V *vs.* Ag/$AgNO_3$) of **(A)** MICP, with 11 s time of electrodeposition, and 80° of ΔΦ; **(B)** PEDOT, with 15 s time of electrodeposition and 50° of ΔΦ.

After the first second, for both MICP and PEDOT cases, the current decreases according to an exponential decay law accompanied by a decrease in the phase (figure 5.2). This can be explained by the nucleation and growth of the primary nuclei, which are initially sufficiently small and well separated[15]. Then an overlap of diffusion fields of neighboring nucleation centers upon growth takes place, resulting in a slower decrease in current intensity and a constant decrease in phase, indicating a continuous growth. However, such a decay which is well fitted by an exponential law (figure 5.3) where the current intensity is normalized towards the intensity reached after the first second of electropolymerization, is not in agreement with previous works that reported a current decrease following $1/\sqrt{t}$ relation[16,17,18], (where t represents time). Such a behavior, which has also been reported by A.I. Melato *et al*[19], shows the complexity of the phenomenon taking place near the electrode-solution interface. Under our experimental conditions of relatively high electrode potential, the MICP and PEDOT growth, which seems not to be limited by diffusion phenomena, coexists with the formation of new nucleation centers.

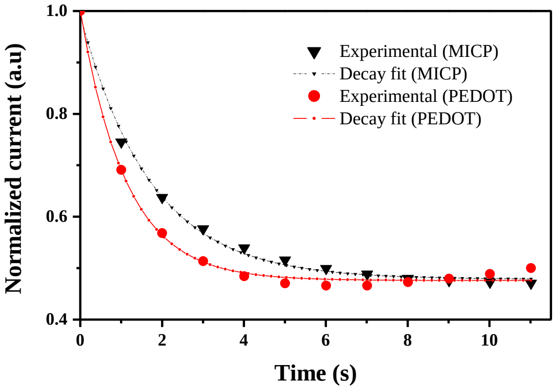

**Figure 5.3.** Current decrease in chronoamperograms of PEDOT and MICP after the first second. Exponential fit of the current intensities decrease.
The currents were normalized towards the current intensity reached at the first second of electrodeposition.

Beyond their similar shape, the main difference between MICP and PEDOT chronoamperograms concerns the time constant, $\tau$, associated to the decreased part of current intensity, which is dependent on the film nature. When considering an exponential decay law, the calculated values, respectively equal to $\tau_{PEDOT} = (1.11 \pm 0.05)$ s and

$\tau_{MICP}$ = (1.74 ± 0.07) s, highlight the fact that the growth mechanism of PEDOT is slightly faster than that of MICP. This can be partly attributed to the higher mobility of the EDOT radical cations present during PEDOT electropolymerization process, when compared to the case of MICP where EDOT molecules coexist with linked TAA-ATZ ones.

In order to determine and to compare the modification of the ESAW gravimetrical response before and after electrodeposition of the MICP and PEDOT films, a measure of the scattering parameters of the transmitted wave ($S_{21}$) of the ESAW device was carried out using the network analyzer. Thus, before and after each electrodeposition the input-output transmission coefficient ($S_{21}$) was measured as a function of frequency, then a follow up, at a constant frequency, of the modulus and the phase variations was carried out beside the electrochemical procedures (see *section 5.4.3*).

Figure 5.4A and B represents the attenuation of ESAW transmitted wave after the electrodeposition of different MICP and PEDOT films respectively. Films were electrodeposited at the same constant potential of 1.45 V *vs.* Ag/$AgNO_3$ with different electrosynthesis times (10, 20, and 30 seconds).

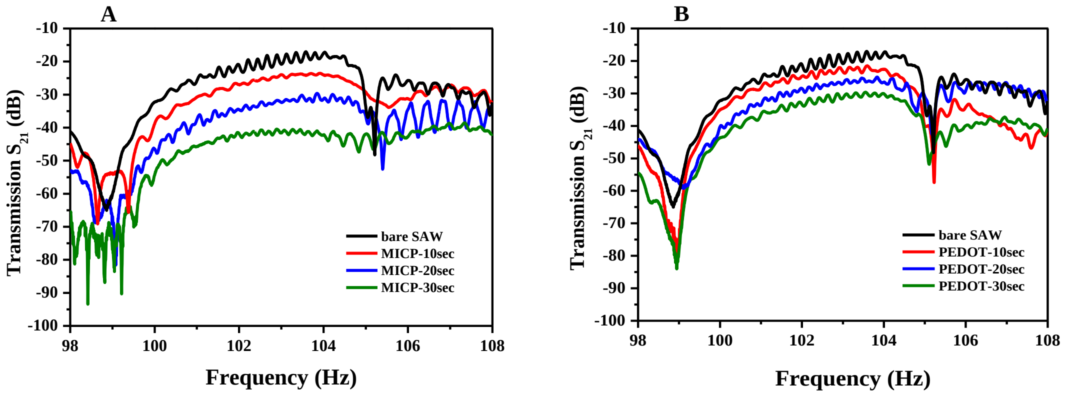

**Figure 5.4.** Frequency response $S_{21}$ of ESAW functional at 104 MHz, of **(A)** bare ESAW surface and of different MICP films; **(B)** bare ESAW surface and of different PEDOT films. All films were electrodepositied at the same constant potential of 1.45 V *vs.* Ag/$AgNO_3$ with different electrosynthesis times 10, 20 and 30 seconds.

Comparing the $S_{21}$ values after the electrodeposition of different films with bare ESAW surface before the deposition process, indicates that the decrease in the transmitted wave amplitude is proportional to the electropolymerization time, thus, with the mass of deposited films. For a given electropolymerization time, the decrease in the $S_{21}$ value was more pronounced in the case of MICP film when compared to PEDOT film, which demonstrates that the deposited mass of MICP film is more important than the mass of PEDOT at the same time of electrodeposition in the implicated conditions.

Thus for a given time, the difference in kinetics of MICP and PEDOT growth, leads to two polymer films of different deposited masses and thicknesses. This was confirmed by the difference in the phase and transmitted wave variations upon electrodeposition of both films at the same conditions (figure 5.2 and figure 5.4). To highlight the relationship between film thickness and electopolymerization duration, various electropolymerization times (from 3 to 100 s) were used. First, charge density $Q$, the main parameter involved in electropolymerization process, is determined from each chronoamperogram. Afterward, the electrosynthesized films thickness, $d$, can be directly calculated from charges values[21], according to Eq 5.1:

$$d = \frac{m\,Q}{2.3\,F\,\rho} \qquad \text{Eq 5.1}$$

where:

$\rho$: the polymer density (~ density of the monomers = 1.334 g $cm^{-3}$)

$m$: the molecular weight of the monomers

$F$: the Faraday's number (~ 96500 C $mol^{-1}$)

The factor 2.3 is related to the number of electrons involved in the polymerization and redox processes[17].

The charges densities as well as the corresponding calculated film thicknesses (from Eq 5.1) are both reported as a function of electropolymerization time on figure 5.5A and figure 5.5B, for MICP and PEDOT respectively.

The variation of $Q$, as a function of time depends on the nature of the conducting polymer. Figure. 5.5A shows that MICP film grows linearly with electropolymerization duration until 60 s (at 60 s thickness was ~ 9µm), whereas PEDOT film thickness in the implied conditions presents a limit value of 1 µm, reached at approximately 60 s (figure 5.5B). This difference is mainly related to the charges quantities which are correlated with the difference in the monomers concentrations in the pre-polymerization solution, and thus with the concentrations of radical cations around the working electrode.

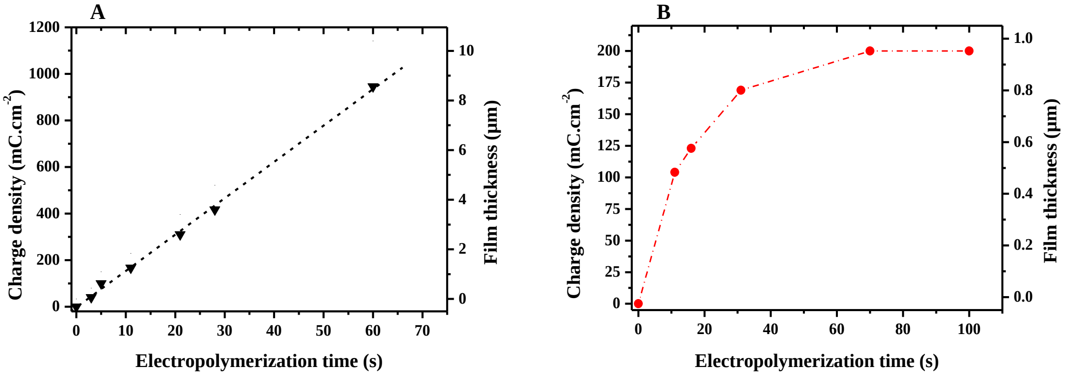

**Figure 5.5.** Charge density and film thickness variations, as a function of electropolymerization time for **(A)** MICP (-▼-) and **(B)** PEDOT (-●-).

Let us note that the so calculated thicknesses are in very good agreement with the values of thicknesses measured by mechanical profilometry techniques (*Section 3.7*) within uncertainties: relative standard deviations are of order of 12% and 4% in the case of MICP and PEDOT respectively.

### 5.3.2 Sensitivity of ESAW to charge transfer

Thanks to chronoamperometry, MICP and PEDOT films can be electrodeposited onto the sensitive area of the ESAW, their thickness being controlled by electropolymerization time. As the developed ESAW allows monitoring both gravimetric and electrochemical transductions simultaneously, the film growth could be followed gravimetrically and the electropolymerization charges, Q, (or the thicknesses) could be well correlated with the phase variations of the surface acoustic wave, $\Delta\Phi$.

However, due to our acquisition card, we are not able, at present, to follow film growth when the electropolymerization duration is lower than 10 s (charge density about 100 mC $cm^{-2}$), except to the detriment of the resolution. Thus, in order to combine both PEDOT and MICP corresponding results, the ESAW sensitivity has to be considered in terms of “charge transfer” (Q) rather than according to film thickness.

The phase variations after electrodeposition of MICP and PEDOT at different times were plotted as a function of the charge transfer upon electropolymerization in figure 5.6.

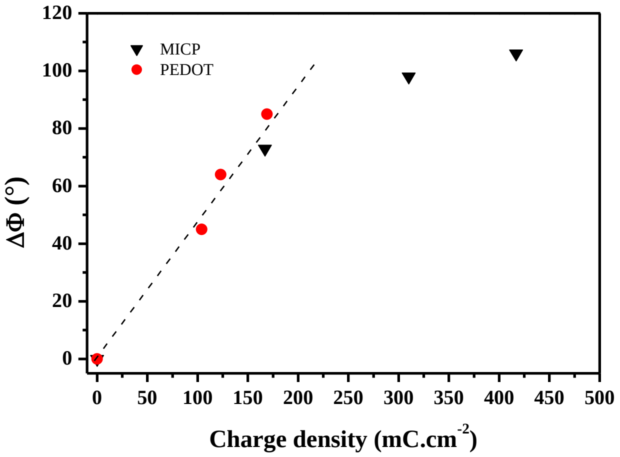

**Figure. 5.6.** Phase variation of ESAW according to charge transfer in MICP (-▼-) and in PEDOT (-●-) electrosynthesized films

For PEDOT, we observe a linear relationship between sensor phase variations and charges densities: about 470 ° $C^{-1}$ $cm^{2}$. The same sensitivity can also be considered for MICP film, up to 250 mC $cm^{-2}$. For higher values, the signal is saturated mostly under the mass effect of deposited film. Indeed, the difference of films thicknesses lead to values of weight ratio MICP/PEDOT included between 3 and 4.6 for electropolymerization durations going from 10 s to 30 s.

### 5.3.3 MICP and PEDOT electrochemical characterizations

The previous results demonstrate that although their growth kinetics is different, both MICP and PEDOT films are directly electrosynthesized onto the sensitive area of the ESAW. In addition, the thickness of the MICP and PEDOT layers is controlled by electropolymerization time. In order to characterize the two kinds of electrosynthesized conducting polymers, electrochemical characterizations were performed.

After electrodeposition of 30 seconds, cyclic voltammetry characterization on MICP and PEDOT films were carried out by scanning the potential between +0.6 and -0.8 V *vs.* Ag/$AgNO_3$ in 0.1 M $LiClO_4$/ACN at a scan rate of 100 mV $s^{-1}$ (figure 5.7A). For both conducting polymers, the current response shows an oxidation peak during doping: at +0.30 V and +0.15 V *vs.* Ag/$AgNO_3$ for MICP and PEDOT respectively. Also, reduction peaks during undoping are observed at -0.30 V and -0.25 V *vs.* Ag/$AgNO_3$ for MICP and PEDOT respectively (figure 5.7A).

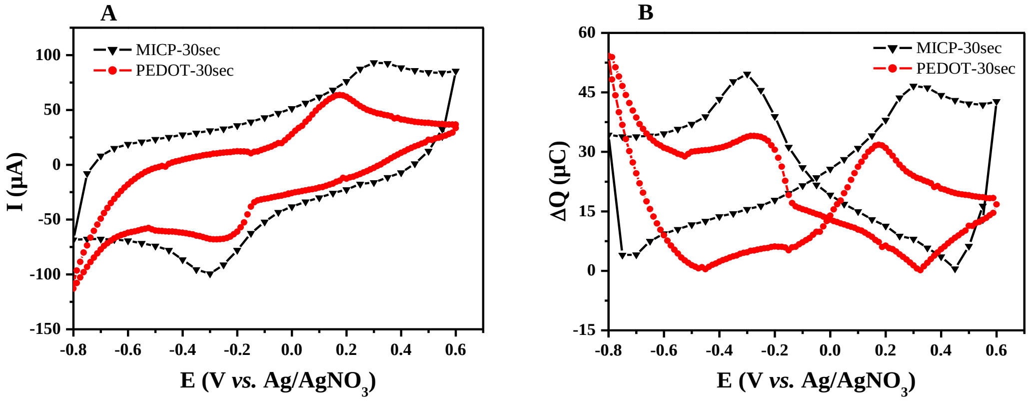

**Figure 5.7. (A)** Cyclic voltammograms at 100 mV $s^{-1}$ in 0.1M $LiClO_4$/ACN of MICP and PEDOT films polymerized during 30 s; charges passed in each voltammogram are: $Q_{PEDOT}$ = 4.68 mC $cm^{-2}$ and $Q_{MICP}$ = 9.86 mC $cm^{-2}$. **(B)** Variation of coulombic charges of MICP and PEDOT as a function of the implied potential

Coulombic charges (ΔQ) variations were calculated from the voltammograms (from the variations of the current intensity at each second) and were plotted *versus* the implied potential, as observed on figure 5.7B. Figure 5.7B reveals that during the same electrochemical process, the amount of involved charges for MICP is higher than that of PEDOT (MICP film thickness is more important than PEDOT thickness). Figure 5.7B demonstrates also that the charges variations during the doping/undoping processes are different for PEDOT and MICP. This behavior was already studied by Hillman et al.[22], only in the case of PEDOT, by using Electrochemical Quartz Crystal Microbalance, EQCM. According to this work, the difference in the charge quantities is referred to the difference in the mechanism involved in the doping/undoping process. P-doping process requires flux of the counter anions to compensate the positive charges on the macromolecular chains, while, undoping process involves solvent flux beside the migration of the counter anions. In addition, the difference in the charges quantities between the doping and undoping processes gives an indication (electrochemical/gravimetric) about the contribution of the solvent in the whole process.

### 5.3.4 Follow-up of doping-undoping processes

Polarization of ESAW–electrolyte system leads to an “electrogenerated concentration gradient” formed in the electrolyte (close to the sensing area of the ESAW). This concept is similar to the diffusion layer introduced first by Nernst in 1904 as a model to explain the time dependent effects of current flow through an electrode (ESAW in our case). In typical cyclic voltammetry (CV), potential variations induce reduction/oxidation of the electro-active layers, related to conducting polymers doping/undoping processes. P-doping or injection of positive charges in the conducting polymer chains upon oxidation is compensated by the diffusion of anions, while the undoping process involves the flux of the solvent beside the migration of the counter anions[9,22]. Doping/undoping process involves thus counter anions and solvent fluxes between conducting polymer macromolecular chains and the electrolyte (region close to the film).

In typical cyclic voltammetry (CV), potential variations *versus* time induce reduction/oxidation of the electro-active layers, which can be related in the case of conducting polymers to the doping and un-doping processes. From a gravimetric point of view, a film doping is thus equivalent to a “mass increase”, whereas un-doping would be comparable to a “mass decrease”. These statements are highlighted by results presented in figure. 5.8, where both voltage and phase were plotted as functions of time in the case of MICP film (electropolymerization time of 30 s).

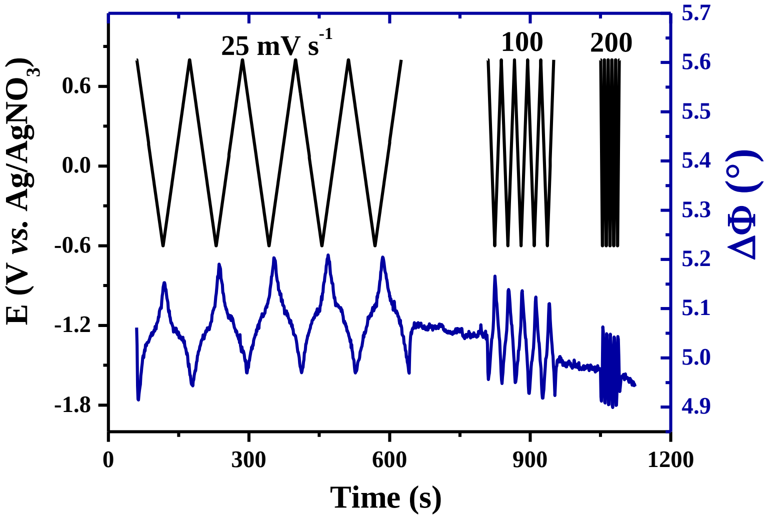

**Figure 5.8.** Voltage and phase variations of MICP film (time of electrodeposition of 30 s) according to time at different voltage scan rates 25; 100, and 400 mV s$^{-1}$.

Figure 5.8 reveals that potential increase (MICP doping) is systematically accompanied by phase values decrease (mass increase) and *vice versa*. Figure 5.8 shows also a series of phase and voltage variations at different scan rates. It appears that phase oscillations magnitude decreases with increasing scan rates. This can be interpreted by considering the diffusion layer thickness over the conducting polymer surface, which depends on the used voltage scan rate.

The aspect of mass variations upon voltammetric cycling can be simplified by considering the "apparent thickness" variation as representative parameter of weight variation. The ESAW response in (CV) configuration is presented in figure 5.9, showing the electric phase variation as well as the charge transfer of MICP film (electrodeposition time of 30 s) according to the applied potential.

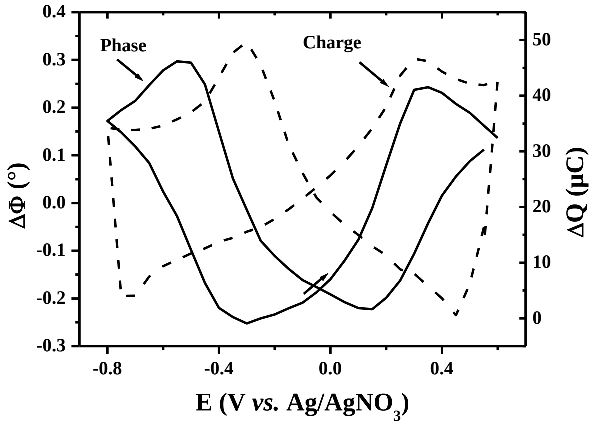

**Figure 5.9.** Phase and charge variations of MICP film (electrodeposition time of 30 s) according to applied potential during cyclic voltammetry acquisitions at a voltage scan rate of 100 mV $s^{-1}$ in 0.1 M $LiClO_4$/ACN

This figure shows the relationship between the two parameters involved in gravimetric and electrochemical transductions. The same behavior has been recorded for different voltage scan rates (table 5.1). Results show that phase variations magnitude increases with decreasing scan rate. According to the concept of "apparent thickness", this can be interpreted as a diffusion layer over the MICP surface, the thickness of which depends upon the used voltage scan rate. Indeed, in slow voltage scans, the diffusion layer grows further from the electrode in comparison with a fast scan. Consequently the "apparent thickness" becomes higher at slow scan rates. Corresponding results are gathered in table 5.1.

**Table 5.1**. Some experimental parameters calculated from ESAW response in the case of MICP film during voltammetric cycling measurements.

| Scan rate (mV $s^{-1}$) | 25 | 100 | 400 |
|---|---|---|---|
| ramp time (s) | 56 | 14 | 3.5 |
| ΔΦ (°) | 0.92 ± 0.10 | 0.52 ± 0.03 | 0.34 ± 0.02 |
| ΔQ (mC $cm^{-2}$) | 1.96 | 1.11 | 0.72 |
| Apparent thickness variation (nm) | 18.8 | 10.6 | 6.9 |
| Relative variation of apparent weight (%) | 1.02 | 0.58 | 0.38 |

## 5.4 MICP-based ESAW transduction

In this section preliminary results of ATZ recognition process by MICP electrodeposited onto the sensing area of the ESAW device is presented. In addition, real time follow up of the extraction and the detection processes is demonstrated.

### 5.4.1 Extraction of atrazine template molecules from MICP matrix

The extraction of atrazine, ATZ, during the washing step lead to the formation, into the polymer matrix of MICP, of recognition cavities which keep the geometrical and functional memory of ATZ molecules. As a consequence, the “washed” MICP layers electrodeposited onto the sensing area of the ESAW device can act as electrochemical as well as gravimetric sensors towards atrazine molecules. However, since no imprinted cavities and no TAA functional monomers are present in the matrix of PEDOT, no noticeable sensing properties are expected in the case of this kind of layers.

Gravimetric transduction and sensing properties of electrodeposited MICP films (thickness ~ 0.3 µm) were first investigated by following ATZ extraction, then by its further injection in the same matrix. The response of PEDOT films (thickness ~ 0.3 µm) to the injection of the extraction solvents was also investigated. In both cases, a continuous flow of the extraction solution was pumped, with a peristaltic pump, over the ESAW sensing area during 10 min at a constant flow rate of 0.19 mL $min^{-1}$.

For MICP films, this step lead to a phase increase corresponding to a mass loss (figure 5.10). In the case of PEDOT, no phase variation was recorded (figure 5.10) indicating that no noticeable degradation of the film occurred. This demonstrates that the mass loss observed for

MICP is not due to polymer alteration but is exclusively due to ATZ removal by the extraction solvents, as already demonstrated.

These gravimetric measurements not only demonstrate the efficiency of the extraction solvents to remove ATZ from MICP but they also allow the determination of the time necessary for the total extraction procedure. Indeed, once the phase signal is observed to be stabilized (figure 5.10 for times higher than 100 s), the extraction process can be considered as definitively finished. As a consequence, an extraction period of 10 min (used in all this work) is found to be largely sufficient for the extraction of ATZ target molecules from MICP matrix whatever the film thickness.

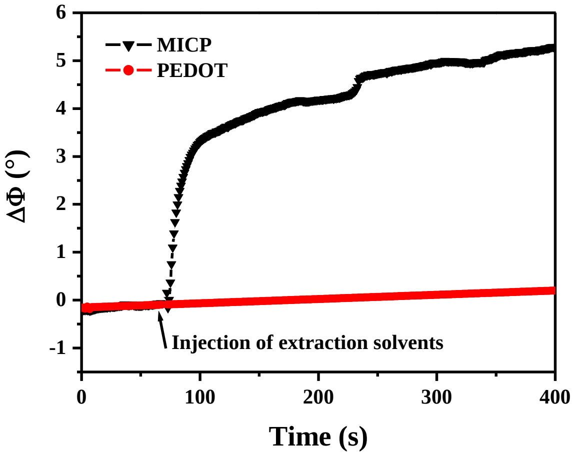

**Figure 5.10.** Phase variations due to the injection of the extraction solvents onto MICP (thickness ~0.3µM) and PEDOT (thickness ~0.3µM) electrodeposited onto ESAW sensing area. The phase increase observed in the case of MICP is attributable to ATZ extraction.

### 5.4.2 Detection of atrazine by MICP

In order to evaluate the sensing properties of washed-MICP towards ATZ target molecules, extraction solutions were drained, replaced by ACN solvent, and the target molecules (at different concentrations of atrazine) were injected in a continuous flow during 600 s over the MICP-covered ESAW sensing area. The pump was then stopped for a period of 3000 s and finally restarted. Corresponding phase variations were recorded after ATZ injection and displayed in particular, as a function of time for a concentration of $10^{-7}$ mol $L^{-1}$ in ATZ molecules (figure 5.11). One can note that the ATZ recognition process by the TAA functionalized MICP which immediately follows ATZ injection and which corresponds to a mass increase, induces an instantaneous phase decrease of about 0.8°. This result confirms the efficiency of the electrosynthesized MICP to sense small amounts of atrazine molecules and the possibility to detect increased concentrations of ATZ (results not shown).

When the peristaltic pump is stopped, the phase remains constant during 500 s, and then it decreases slowly (figure 5.11). By restarting the pump, the phase increases and reaches the same level as that preceding the pump-stop. This indicates that the amount of ATZ molecules, strongly bonded to TAA functional monomers thanks to hydrogen bonds into recognition cavities, remain constant. We assume that the phase variations in the static mode, when the pump is stopped, are only caused by weak non-specific adsorption of atrazine molecules on the MICP surface as discussed in *chapters 3 and 4*. These weak links are easily broken by the mechanical agitation due to the restart of the pump.

We demonstrate here that the MICP-covered ESAW sensing area is not only able to detect very small amounts of atrazine molecules, but it is also able to distinguish between specific and non-specific adsorption processes thanks to the dynamic and static modes of the ESAW sensor.

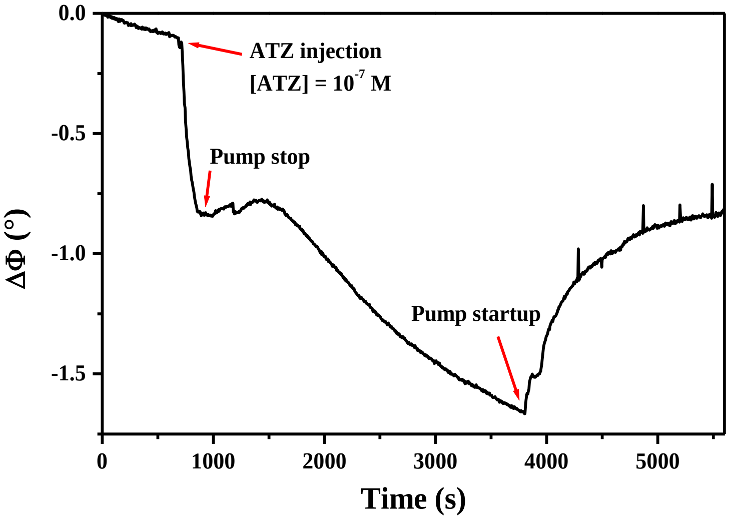

**Figure 5.11.** Follow-up by phase variation measurements in the dynamic and static modes of atrazine specific detection and non-specific adsorption by the “washed” MICP (film thickness ~0.3 µm)

# Conclusion

In this chapter, PEDOT and MICP conducting layers were electrosynthesized onto the gold sensing area of a Surface Acoustic Wave sensor, SAW sensor. The latter serves as basis of three-electrodes cell electrochemical system, where grounded gold SAW sensing area supplied the working electrode. The built device, an Electrochemical Surface Acoustic Wave sensor (ESAW), and homemade software permitted us to carry out simultaneous coupled measurements: gravimetric, amperometric and cyclic voltammetric ones.

Growth and doping/undoping processes of these polymer films were investigated by the developed ESAW sensor. Measurements at various electropolymerization times highlighted a difference between the two polymers electrosynthesis kinetics: MICP films grow linearly with time, whereas PEDOT film thickness presents a limit value of 1 µm, reached at approximately 60 s. This disparity is mainly due to the difference in the monomers concentration in the pre-polymerisation solution, consequently, to charges of electropolymerization.

The electropolymerization process was coupled to gravimetric response i.e. sensor phase. We found a linear relationship between phase variation and charges densities with a sensitivity of 470 ° $C^{-1}$ $cm^2$. The same sensitivity can be considered for the MICP layer, up to 250 mC $cm^{-2}$. For higher thickness values, the signal showed saturation, mostly under the mass effect of deposited film. Indeed, the difference of films thicknesses led to values of weight ratio MICP/PEDOT included between 3 and 4.6 for electropolymerization duration going from 10 s to 30 s.

Using MICP as a sensitive layer of ESAW sensor, for electrochemical and gravimetric combined transductions was applied to atrazine (ATZ) detection. Strongly bonded ATZ molecules (thanks to ATZ - TAA specific recognition) have been highlighted. Besides, we also showed the ability of ESAW to detect, in distinguishable way, weakly adsorbed molecules (by non-specific adsorption) on the MICP surface.

# References

---

[1] R. Schweiss, J.F. Lubben, D. Johannsmann, W. Knoll, Electropolymerization of ethylenedioxy thiophene in micellar aqueous solutions studied by electrochemical quartz crystal microbalance and surface Plasmon resonance. *Electrochim. Acta* 50, 2849-2856, 2005.

[2] B. Deore, Z. Chen, T. Nagaoka,Overoxidized polypyrrole with dopant complementary cavities as a new molecularly imprinted polymer matrix. *Anal. Sci*. 15, 827, 1999.

[3] A. Öpik, A. Menaker, J. Reut, V. Syritski. Molecularly imprinted polymers: a new approach to the preparation of functional materials. *proceedings of the Estonian Academy of Sciences* 58, 3, 2009.

[4] A.R. Hillman, M.J. Swann. General approach to the interpretation of electrochemical quartz crystal microbalance data. 1. Cyclic voltammetry: kinetic subtleties in the electrochemical doping of polybithiophene films. *J. Phys. Chem*. 95, 3271, 1991.

[5] M.J. Henderson, A.R. Hillman, E. Vieil. A combined electrochemical quartz microbalance (EQCM) and probe beam deflection (PBD) study of a poly(O-toluidine) modified electrode in perchloric acid. *J. Electroanal. Chem*. 454, 1, 1998.

[6] A. Rubin, H. Perrot, C. Gabrielli, M.C. Pham, B. Piro. Electrochemical and electrogravimetric behaviors of conducting polymer. Theoritical aspects and application to co-polymer films based on juglone. *Electrochim. Acta*. 55, 6136, 2010.

[7] A. Bund, S. Neudeck. Effect of the solvent and the anion on the doping/dedoping behavior of PEDOT films studied with the electrochemical quartz microbalance *J. Phys. Chem. B* 108, 17845, 2004.

[8] A.R. Hillman, M.A. Mohamoud, *Electrochim. Acta*. Ion, solvent and polymer dynamics in polyaniline conducting polymer films. 51, 6018-6024, 2006.

[9] S. El Sana, C. Gabrielli, H. Perrot. Rate limiting steps of charge transfer at conducting polymers. *Elektrokhimiya* 40, 303, 2004.

**[10]** Bergaoui, Y., Zerrouki, C., Fougnion, J. M., Fourati, N., Abdelghani, A. Sensitivity Estimation and Biosensing Potential of Lithium Tantalate Shear Horizontal Surface Acoustic Wave Sensor, *Sens. Lett.* 7, 1000-1005, 2009.

**[11]** Pardieu E., Cheap H., Vedrine C., Lazerges M., Lattach Y., Garnier F., Remita S., Pernelle C., Molecularly imprinted conducting polymers based on electrochemical sensor for detection of atrazine. *Anal. Chim. Acta.* 649, 236-245, 2009.

[12] G.L. Harding, J. Du. Design and properties of quartz-based love wave acoustic sensors incorporating silicon dioxide and PMMA guiding layers. *Smart Mater. Struct*. 6, 716, 1997.

[13] P. Audebert, P. Hapiot. Fast electrochemical studies of the polymerization mechanisms of pyrroles and thiophenes. Identification of the first steps. Existence of Pi-dimers in solution. *Synth. Met*. 75, 95, 1995.

[14] C.P. Andrieux, P. Audebert, P. Hapiot, J.M. Saveant. Identification of the first steps of the electrochemical polymerization of pyrroles by means of fast potential step techniques. *J. Phys. Chem*. 95, 10158, 1991.

[15] E. Ventosa, J.L. Palacios, P.R. Unwin. Nucleation and growth of PEDOT thin films on highly oriented pyrolytic graphite (HOPG) electrodes. *Electrochem. Commun*. 10, 1752, 2008.

[16] F. Chao, M. Costa, C. Tian. Different steps in electrodeposition of poly(3-methylthiophene) films on platinum electrodes studied by ellipsometry, SEM and AFM techniques. *Synth. Metals* 53, 127, 1993.

[17] H. Randriamahazaka, V. Noël, C. Chevrot, J. Nucleation and growth of PEDOT in acetonitrile on platinum under potentiostatic conditions. *Electroanal. Chem*. 472, 103, 1999.

[18] H. Randriamahazaka, T. Bonnotte, V. Noël, P. Martin, J. Ghilane, K. Asaka, J.C. Lacroix. Medium effects on the nucleation and growth mechanisms during the redox switching dynamics of conducting polymers: case of PEDOT *J. Phys. Chem. B* 115, 205, 2011.

[19] A.I. Melato, A.S. Viana1, L.M. Abrantes. Different steps in the electrosynthesis of PEDOT on platinum. *Electrochim. Acta*. 54, 590, 2008.

[20] E. Tamburry, S. Orlanducci, F. Toshi, M.L. Terranova, D. Passeri. Growth mechanisms, morphology, and electroactivity of PEDOT layers produced by electrochemical routes in aqueous medium. *Synth. Met*. 159, 406, 2009.

[21] L.T. Panasyuk, V.M. Mirsky, A.S. Piletsky, O.S., Wolfbeis. Electropolymerized molecularly imprinted polymers as receptor layers in capacitive chemical sensors. *Anal. Chem*. 71, 4609, 1999.

[22] A.R. Hillman, S.J. Daisley, S. Bruckenstein. Kinetics and mechanism of the electrochemical p-doping of PEDOT. *Electrochem. Commun*. 9, 1316, 2007.

# Conclusion

The increased demand to more performing and accurate chemical sensors leads to the development of new materials dedicated for sensing applications. Functionalized Molecularly Imprinted Conducting Polymers (MICP) represent interesting candidates for the fabrication of such new sensing layers since they present a specific recognition ability and a compatibility with various transduction techniques.

In this context, since few years, LC3B laboratory designs and develops polythiophenes based MICP sensing layers dedicated for the sensitive and specific detection of small non-electroactive organic molecules, such as atrazine. Indeed, in such small molecules, the limited number of potential interactions with the sensing layers complexifies the recognition process, making it less sensitive and less selective.

In this work, profound investigations were carried out on the synthesis, the characterization and the evaluation of the sensing properties towards atrazine of three kinds of differently functionalized conducting polymers-based sensitive layers, PEDOT, NICP and MICP:

*i)* Non-imprinted conducting homopolymers, PEDOT, were synthesized by electropolymerization of EDOT in the absence of atrazine target molecules
*ii)* Non-imprinted conducting copolymers, NICP, were electrosynthesized by copolymerization of EDOT and FM functional monomer (TAA, TMA, TMeOH or Th) in the absence of target molecules
*iii)* Imprinted conducting copolymers, MICP, were prepared by electrochemical polymerization of EDOT or copolymerization of EDOT and FM functional monomer (TAA, TMA, TMeOH or Th) in the presence of ATZ

Characterizations and structural investigations of all these sensing polymer layers were carried out using different surface characterization techniques (AFM, ATR-FTIR, electrochemistry and profilometry) in order to understand the physico-chemistry of the recognition process and with the aim to improve the performance of the polymer layers in both their sensing and transducing (electrochemical and gravimetrical) functionalities. To our knowledge, such a physico-chemical approach is very original in the field of sensors.

We first optimized the synthesis of all the considered sensing layers (PEDOT, NICP and MICP) in acetonitrile solvent. All these layers were electrochemically grown, which enabled a precise control of their thicknesses through the adjustment of the electropolymerization charges. The sensing properties of all layers were quantified through electrochemical measurements (by cyclic voltammetry and square wave voltammetry). The observed dependence of the recognition properties of the conducting layers with their thickness and roughness indicates that the interaction between the target molecules and the sensing groups of the sensor layers takes place, not only at the surface, but also into the bulk of the porous conducting polymer matrixes in a tri-dimensional geometry. However, the involved recognition process appears to be always limited by the diffusion of the target molecules into the polymer matrixes.

In the case of PEDOT, the polymer layers do not favor the recognition process since only weak interactions can be involved between the EDOT units and the atrazine target molecules. On the contrary, the presence of stronger interactions, due to FM residues, in the MICP and NICP layers enables the significant recognition of atrazine through hydrogen-bonds. In comparison with NICP, the superior sensing properties of MICP layers result from the presence of pre-shaped imprinted cavities in their backbones which keep the memory of the atrazine targets.

In addition to their sensitivity, the so-developed MICP electrochemical sensing layers, when used for the detection of atrazine in the optimal conditions, present a low limit of detection ($10^{-9}$ mol $L^{-1}$) and a large dynamic range ($10^{-8}$ to $10^{-4}$ mol $L^{-1}$) as shown by square wave voltammetry measurements. Nevertheless, non-specific adsorption onto the surface of the sensing layers takes place systematically, which affects the specificity and the selectivity of the recognition process.

We experimentally and theoretically studied the influence of the nature of the chemical functionalities (FM) brought by the MICP and NICP sensing layers on their ability to detect atrazine target molecules. In this aim, differently functionalized thiophene-based monomers (FM) were used in order to form FM/ATZ pre-polymerization complexes, leading after electrosynthesis to differently functionalized FM-MICP and FM-NICP sensitive layers.

We demonstrated, thanks to electrochemical measurements, the clear effect of the nature of FM functional monomer on the number of ATZ molecular imprints and then on the sensitivity towards ATZ of the FM-MICP layers, which both decrease in the following order of FM functional monomers: TMA, TAA, TMeOH, EDOT and Th. These experimental results were attributed to the strength of the FM-ATZ interaction.

For investigating this hypothesis, we performed DFT/PCM calculations of the free energies of formation of the FM/ATZ pre-polymerization dimers in acetonitrile solution, with the use of an empirical correction thanks to Wertz formula. We showed that a strong correlation exists between the measured electrochemical signals and the strength of the interaction between the atrazine and the FM functional monomers.

The calculated dimerization free energies enabled the calculation of the concentrations of the different FM/ATZ pre-polymerization complexes present in acetonitrile medium before each MICP electrosynthesis. We found that the electrochemical signals are well correlated with the concentrations of the FM/ATZ dimers. This good correlation demonstrates that a much elaborated property of the MICP imprinted polymer, as is the detection of targets after a complex process of polymer synthesis and washing, can be very simply related to the strength of the interaction between the target molecules and the FM functional monomers in the genuine solution.

We demonstrated that, in order to fabricate the best sensing layers based on FM-MICP, strong interactions between FM and the template molecules are necessary in the pre-polymerization complex and in the functionalized cavities into the MICP matrixes. However, these strong interactions are not sufficient since non-specific adsorption systematically exists and should be minimized. Among all the conducting layers studied in this work, we showed that the TAA-MICP based sensing layers are the best candidates for the preparation of highly sensitive sensors since they offer the best compromise between high level of specific detection and low level of non-specific adsorption.

Finally, in order to validate our sensitive layers, and in particular the TAA-functionalized MICP ones, we used a second type of transduction technique, the gravimetrical transduction of the atrazine recognition process, and we coupled both electrochemical and gravimetrical transductions in an original developed methodology.

In this context, conducting layers were directly electrosynthesized onto the gold sensing area of a Surface Acoustic Wave sensor (SAW sensor). The latter acts as basis of three-electrodes cell electrochemical system, where grounded gold SAW sensing area supplied the working electrode. The built device, an Electrochemical Surface Acoustic Wave sensor (ESAW), and a homemade software allowed us to carry out simultaneous coupled measurements: gravimetric, amperometric and cyclic voltammetric ones.

Thanks to the measurements of acoustic wave variations as a function of electropolymerization time, the developed ESAW sensor enabled not only the study of the kinetics of the sensing layers growth but also the involved doping/undoping processes. Besides, MICP films electrodeposited onto the active surface of ESAW sensor were used as sensitive layers for electrochemical and gravimetric combined transduction of the ATZ molecules recognition event. We demonstrated that, in this configuration, the MICP-covered ESAW are not only able to detect very small amounts of ATZ molecules, but are also able to discriminate between specific recognition and non-specific adsorption processes thanks to the dynamic and static modes of the ESAW sensor.

All this study enabled the development and the evaluation of the performances of differently functionalized Molecularly Imprinted Conducting Polymers as sensitive layers dedicated for the detection of atrazine target molecules. The best sensing layers, TAA-based polythiophenes, present relatively good sensing properties: low detection limit and large dynamic range of detection. These interesting properties result from: i) the presence into the backbones of TAA-MICP of a high number of pre-shaped functionalized cavities. ii) the strength of the interaction between TAA residues and atrazine molecules in acetonitrile solvent. iii) the relatively weak non specific adsorption of atrazine targets at the interface.

Despite the good performances of the MICP-based sensitive layers, these conducting polymers are not perfect and some important problems remain. In particular, the developed MICP are neither reusable nor robust. In this context and in order to modify the structure of the sensitive layers, we can propose the use, during MICP synthesis, of cross-linking monomers based on substituted thiophene molecules like 3,3’-bithiophene. Nevertheless, since cross-linking leads to an important decrease in the conductivity of the conducting polymers, it would be interesting to introduce nano-particles into the structure of the sensing films in order to compensate this conductivity decrease upon structure modification.

We demonstrated that the efficiency of the atrazine detection by the functionalized MICP is related to the strength of the interaction between the target molecules and the FM functional monomers in the genuine solution. Since atrazine molecules interact with TAA residues thanks to hydrogen bonds, it would be difficult to detect atrazine in water. Then, other interaction modes, such as π-stacking interactions, should be used in aqueous solutions to sense atrazine, this would imply the use of monomers bringing hydrophobic functionalities.

On another hand, it would be interesting to choose another small non-electroactive target molecule and to modulate, thanks to theoretical considerations, the nature of the functional monomers and of the solvent in order to underline the influence of the strength of the target/functional monomer interaction on the detection efficiency.

In this study, we presented for the first time an ESAW transduction technique. Nevertheless, complementary investigations should be carried out in order to develop and to optimize the coupled electrochemical/gravimetrical method, taking into account the interesting range of applications of this technique. Improvements on the electrochemical level of the technique are under investigations, such as adding the function of the square wave voltammetry, as well as improving the resolution of the different voltammograms and chronoamperograms.

Finally, variation of the synthesis method of MICP sensing layers is a seducing matter. During this thesis, preliminary experiments (not presented here) were carried out in order to develop a new polymerization method of the conducting polymers based on X-rays and γ-rays radiolysis. This methodology should enable the synthesis of Molecularly Imprinted Conducting Polymers of controlled thickness over both conducting and non conducting substrates.

# Résumé
# en langue française

Dans de nombreux domaines tels que la santé publique, la chimie, l'agro-alimentaire, la sécurité et l'environnement, il est nécessaire de développer de nouvelles technologies de détection afin de pouvoir reconnaître rapidement et quantifier de manière fiable des analytes présents à l'état de traces en matrices complexes.

Les techniques classiques d'analyse bien que fournissant une information souvent fine et complète, s'accompagnent malheureusement de contraintes importantes en termes de logistique, de coût et surtout de temps d'analyse. Au contraire, les capteurs chimiques et biologiques constituent une voie alternative efficace et économique (Figure 1). Les capteurs chimiques miniaturisés pourraient être, dans certains cas, à la base d'un système efficace de détection précoce, avec des avantages notamment en termes de sensibilité, de rapidité, de possibilité d'intégration et d'adaptabilité à un grand nombre d'applications. Néanmoins, le développement des performances de ces capteurs nécessite d'une part la conception de couches de reconnaissance sensibles, sélectives et spécifiques et d'autre part l'émergence de nouvelles technologies de transduction.

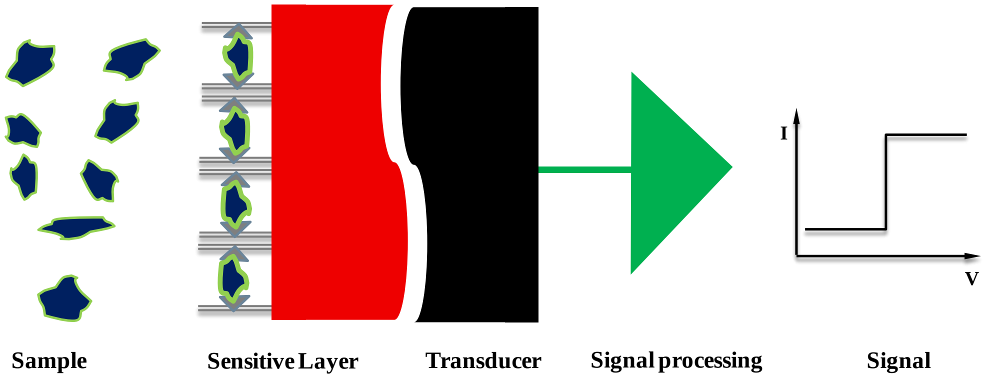

**Figure 1.** Schéma de principe d'un capteur.

Les couches sensibles à base de polymères à empreintes moléculaires (MIP) sont actuellement très utilisées puisqu'elles permettent, grâce à la fonctionnalisation adéquate des matériaux polymères, une détection hautement sélective des molécules cibles en présence desquelles elles ont été synthétisées (Figure 2).

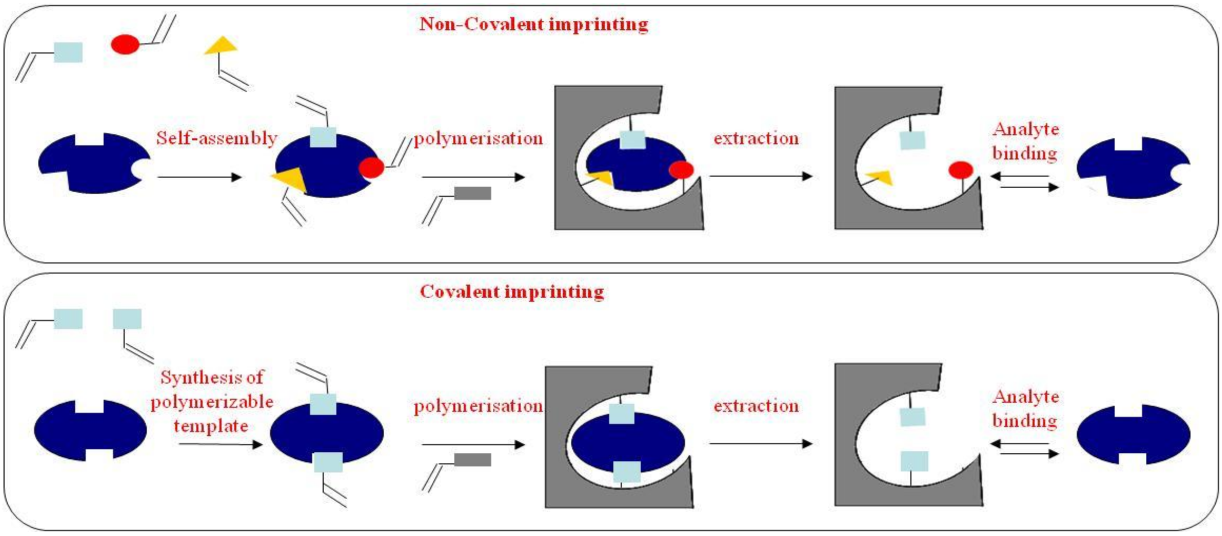

**Figure 2.** Représentation schématique de la procédure d'impression moléculaire.

Les couches sensibles à base de polymères conducteurs (CP) fonctionnalisés (Figure 3) sont également très utilisées puisqu'elles permettent simultanément la reconnaissance de molécules cibles et la transduction électrique du phénomène de reconnaissance. En effet, l'interaction d'un CP fonctionnalisé avec une cible affecte sa conformation spatiale et modifie par conséquent ses propriétés de conduction électrique, comme sa signature électrochimique.

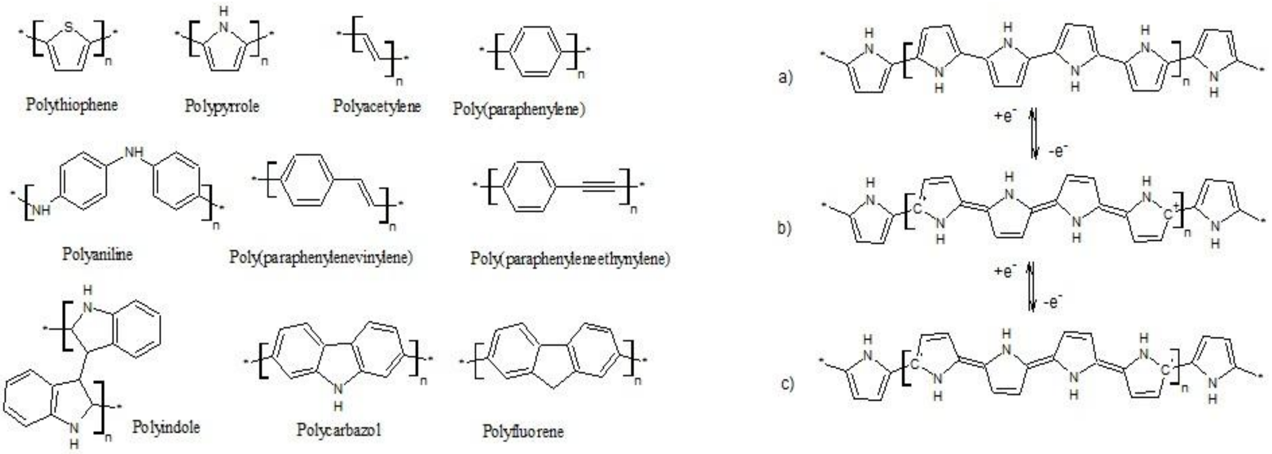

**Figure 3.** Quelques exemples de polymères conducteurs (CP).

Au sein du Laboratoire de Conception de Capteurs Chimiques et Biologiques, LC3B du CNAM, nous avons conçu et développé de manière originale une nouvelle gamme de couches sensibles transductrices : les polymères conducteurs à empreintes moléculaires (MICP). Nous avons également intégré ces MICP au sein de capteurs électrochimiques afin de détecter spécifiquement de petites molécules organiques non-électroactives comme l'atrazine.

Ces polymères conducteurs à empreintes moléculaires (MICP) sont des matrices conductrices synthétisées électrochimiquement en présence des cibles pour la détection desquelles elles sont dédiées (Figure 4). L'extraction des cibles libère au sein des MICP des cavités fonctionnalisées qui gardent la mémoire de la forme et de la distribution spatiale des groupements chimiques des cibles, ce qui permet une reconnaissance moléculaire hautement sélective. Ces matrices possèdent également des propriétés électriques qui leur permettent de transduire électrochimiquement, en temps réel, le phénomène de reconnaissance moléculaire.

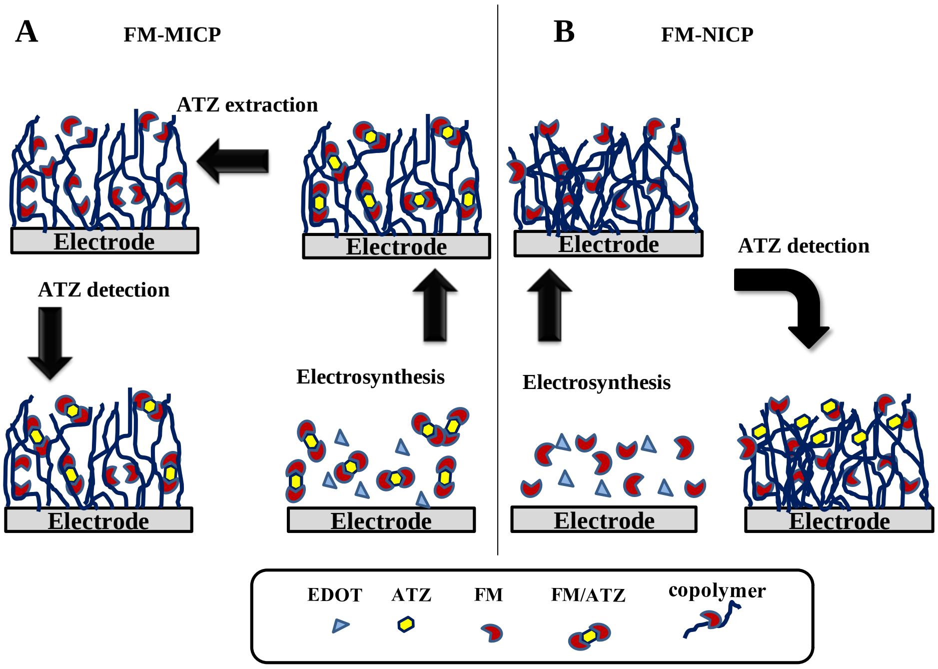

**Figure 4**. Principe de l'électrosynthèse des MICP développé au LC3B.

Dans cette thèse, nous nous sommes investis dans le développement et dans l'optimisation des performances de telles couches sensibles à base de polymères conducteurs fonctionnalisés à empreintes moléculaires, MICP dérivés du thiophène, pour la détection spécifique de l'atrazine, ATZ (Figure 5). Nous avons intégré ces couches sensibles au sein de capteurs électrochimiques et gravimétriques et avons développé une technique menant à une transduction couplée électrochimique / gravimétrique. Nous nous sommes tout particulièrement intéressés à l'influence de la structure et des fonctionnalités chimiques des

MICP d’une part sur la reconnaissance de la cible ATZ et, d’autre part, sur la transduction de cette reconnaissance.

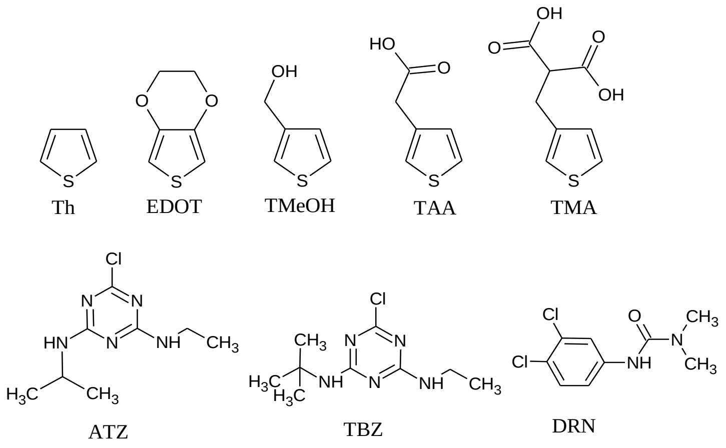

**Figure 5.** Structure chimique des cibles et des monomères fonctionnels, dérivés du thophène, utilisés dans cette thèse.

Nous avons tout d’abord présenté, de manière quelque peu exhaustive, dans le premier chapitre du manuscrit de cette thèse, l’état de l’art sur les capteurs chimiques. Nous avons décrit les différentes méthodes de transduction et présenté les différentes catégories de couches sensibles dédiées à la reconnaissance de petites molécules organiques. En particulier, l’accent a été mis sur les couches sensibles constituées soit de polymères à empreintes moléculaires soit de polymères conducteurs. Cet état de l’art était destiné à mettre en lumière le rôle prépondérant que devraient pouvoir jouer les couches sensibles à base de MICP dans le domaine des capteurs de petites molécules.

Nous avons décrit, dans le second chapitre, les différentes procédures expérimentales que nous avons utilisées au cours de cette thèse pour la préparation des MICP et pour la détection des cibles ATZ. Nous avons présenté également de manière plus brève les méthodes théoriques employées afin d’évaluer la force des interactions qui existent entre les cibles ATZ et les fonctionnalités chimiques des MICP. Par ailleurs, étant donné que cette thèse a nécessité l’utilisation de différentes techniques expérimentales, nous avons jugé utile de décrire les appareillages utilisés durant les caractérisations microscopiques, électrochimiques et spectroscopiques des couches sensibles à base de MICP.

Les résultats expérimentaux sont présentés et discutés à partir du troisième chapitre de la thèse. Dans ce troisième chapitre, nous nous sommes d’abord intéressés à l’optimisation des étapes d’électrosynthèse de MICP à partir de dérivés du thiophène diversement fonctionnalisés (Figure 6) : choix du solvant, des électrodes, du substrat de dépôt, des concentrations, des ratios, des potentiels … Ensuite, partant des conditions expérimentales optimales, nous nous sommes tout particulièrement intéressés à l'influence des propriétés structurales (épaisseur, rugosité, porosité) et fonctionnelles des MICP sur le processus de reconnaissance de l'atrazine et par conséquent sur les performances du capteur.

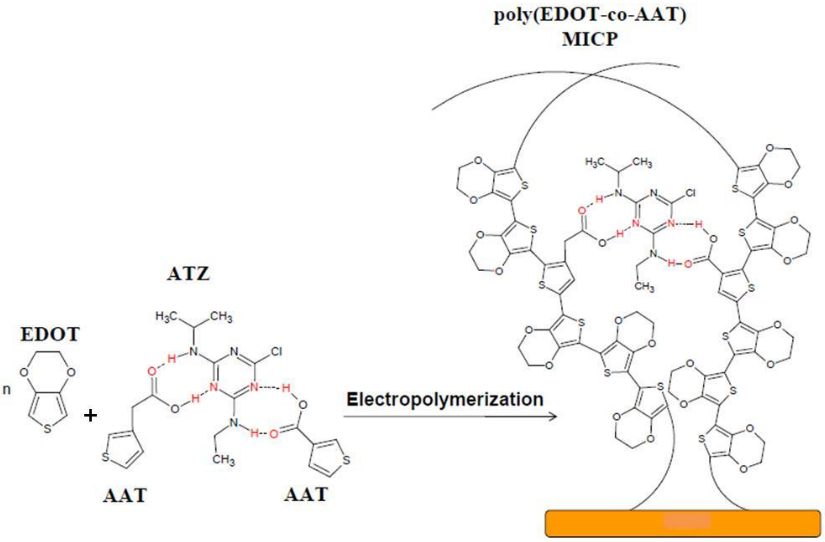

**Figure 6.** Electrosynthèse de MICP par copolymérisation de deux derives du thiophène (EDOT et TAA) en présence de molécules cibles d'ATZ.

Trois types de films polymères, à base de thiophènes fonctionnalisés, ont été électrosynthétisés par chronoampérométrie en 2-étapes sur une électrode métallique :

*i)* Homopolymère non-imprimé, **PEDOT**, synthétisé par électropolymérisation de l'EDOT en l'absence d'atrazine, ATZ**,** utilisée comme molécule cible.

*ii)* Copolymère conducteur non-imprimé, **NICP**, synthétisé par électro-copolymérisation de l'EDOT avec un monomère fonctionnel (Th, TMeOH, TAA ou TMA) en l'absence d'ATZ.

*iii)* Copolymère conducteur à empreintes moléculaires, **MICP**, synthétisé par électro-copolymérisation de l'EDOT avec un monomère fonctionnel (Th, TMeOH, TAA ou TMA) en présence de l'ATZ comme molécule cible.

Les différents films électrosynthétisés ont été caractérisés par voltammétrie cyclique (Figure 7), par spectroscopie infrarouge (Figure 8), par profilométrie optique et par microscopie à force atomique (Figure 9).

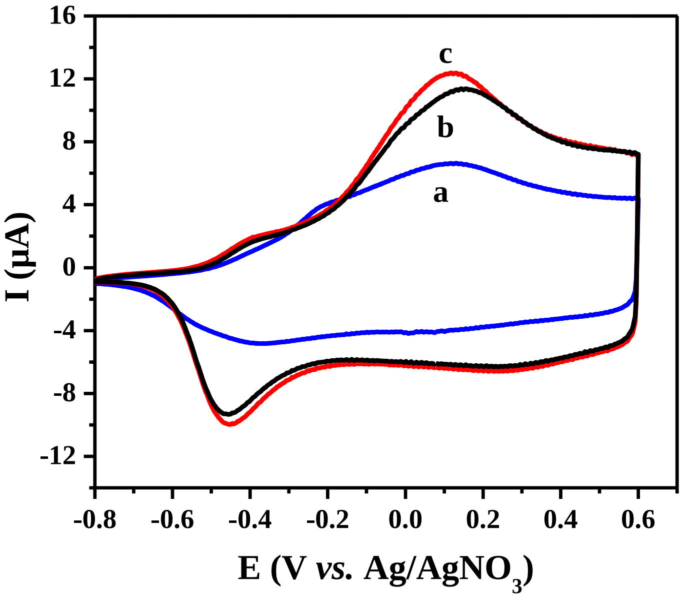

**Figure 7.** Voltammogrammes des films polymères : **(a)** PEDOT, **(b)** MICP, et **(c)** NICP, électrosynthétisés dans l'acétonitrile en présence de $LiClO_4$ comme électrolyte support, à un potentiel de 1,45 V vs. $Ag/AgNO_3$, avec une charge d'électropolymérisation de 100 mC $cm^{-2}$.

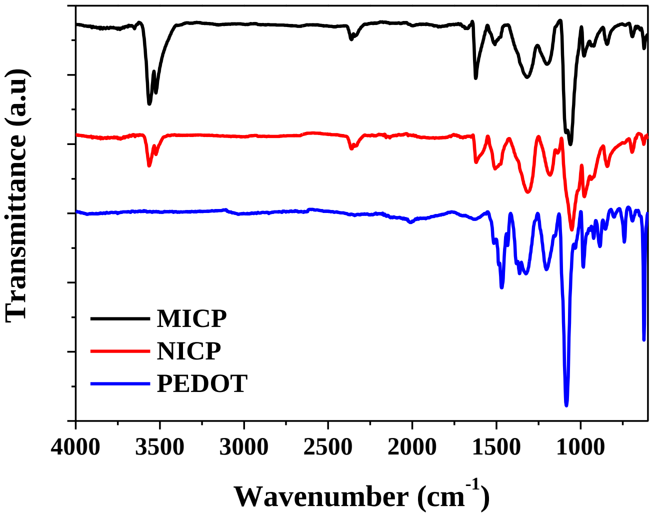

**Figure 8.** Spectres des films de MICP, NICP et PEDOT obtenus par ATR-FTIR. Ces films ont été électrosynthétisés dans l'acétonitrile en présence de $LiClO_4$ comme électrolyte support, à un potentiel de 1,45 V vs. $Ag/AgNO_3$, avec une charge d'électropolymérisation de 100 mC $cm^{-2}$.

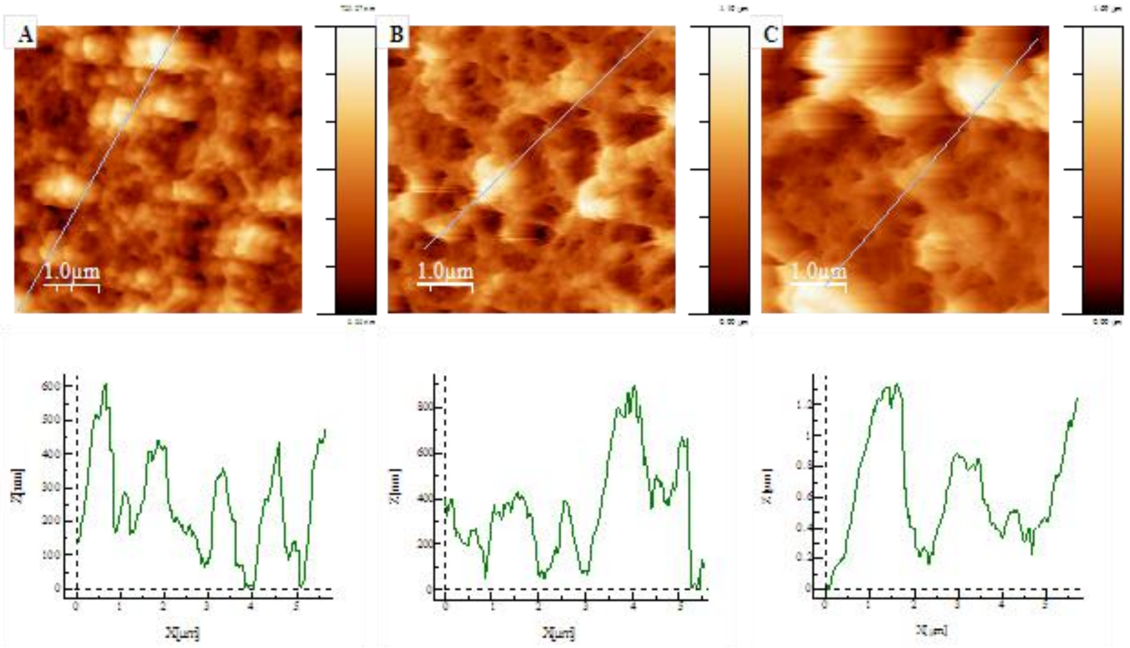

**Figure 9.** Images AFM en mode tapping de : **(A)** PEDOT, **(B)** NICP et **(C)** MICP. Ces films ont été électrosynthétisés dans l'acétonitrile en présence de $LiClO_4$ comme électrolyte support, à un potentiel de 1,45 V vs. Ag/$AgNO_3$, avec une charge d'électropolymérisation de 100 mC $cm^{-2}$.

Les résultats obtenus par les techniques de voltammétrie cyclique (Figure 7) et de spectroscopie infrarouge en mode ATR (Figure 8) démontrent sans ambiguïté que les films de MICP, NICP et PEDOT sont structurellement et chimiquement différents. Ceci démontre également que la copolymérisation de l'EDOT et du TAA a bien lieu dans le cas des copolymères MICP et NICP. Contrairement au PEDOT, ces deux types de polymères sont donc dotés de fonctionnalités de reconnaissance de type TAA. Ce résultat prouve également que de l'atrazine a bien été emprisonnée dans la matrice du MICP, lui conférant ainsi, après extraction des cibles, un rôle de polymère à empreintes moléculaires, possédant des cavités de reconnaissance. La présence de groupements TAA distribués spatialement au sein des cavités de reconnaissance confère ainsi au MICP des propriétés de détection tout à fait intéressantes.

Les résultats obtenus par microscopie AFM (Figure 9) démontrent sans ambiguïté que les films de MICP, NICP et PEDOT sont structurellement différents. Les MICP sont plus poreux et plus rugueux que les films de NICP et de PEDOT. On peut donc s'attendre à ce que les molécules d'atrazine interagissent davantage à la surface des films de MICP et qu'elles y diffusent également plus aisément.

Nous avons démontré par profilométrie optique et par microscopie AFM que la croissance électrochimique des films de MICP, de NICP et de PEDOT s'effectuait couche par couche. Ce résultat démontre qu'il est possible de contrôler l'épaisseur de la couche polymère grâce à l'ajustement de la charge d'électropolymérisation (Figure 10).

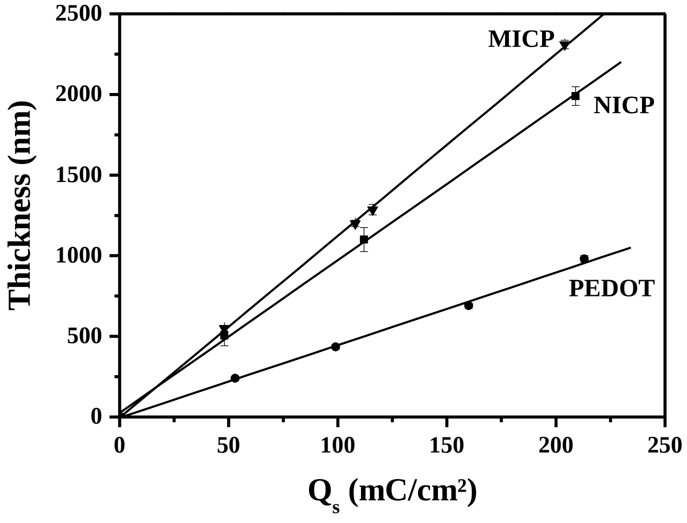

**Figure 10.** Variation de l'épaisseur des films polymères en fonction de la charge d'électropolymérisation ($Q_s$).

Les différents films de MICP, NICP et PEDOT électrosynthétisés dans les conditions décrites précédemment ont ensuite été mis en présence de molécules cibles d'atrazine à une concentration de $10^{-4}$ mol $L^{-1}$. Bien entendu les MICP ont tous été préalablement lavés afin d'en extraire l'atrazine emprisonnée. La détection de l'ATZ additionnelle a pu alors être suivie dans tous les cas grâce à la variation relative de la signature électrochimique de chaque polymère conducteur (Figure 11). Par ailleurs, la détection a pu être quantifiée grâce au calcul de la variation de la charge relative, $Q_r$ déduite des voltammogrammes.

Nous avons étudié l'influence de la nature des films (MICP, NICP et PEDOT) et de leur épaisseur (mesurée par profilométrie optique) sur le processus de détection. Dans tous les cas, la variation de la charge relative due à la détection a été calculée (Figure 12).

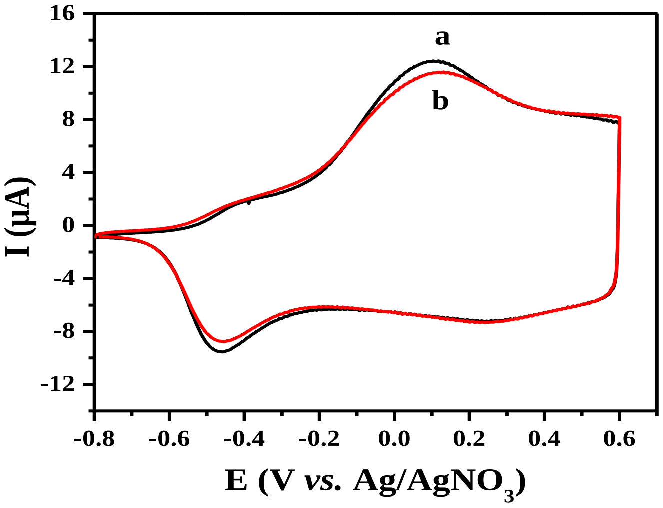

**Figure 11.** Variation de la signature électrochimique d'un MICP après injection de $10^{-4}$ mol $L^{-1}$ d'atrazine. Le MICP a été électrosynthétisé dans l'acétonitrile en présence de $LiClO_4$ comme électrolyte support, à un potentiel de 1,45 V vs. Ag/$AgNO_3$, avec une charge d'électropolymérisation de 100 mC $cm^{-2}$.

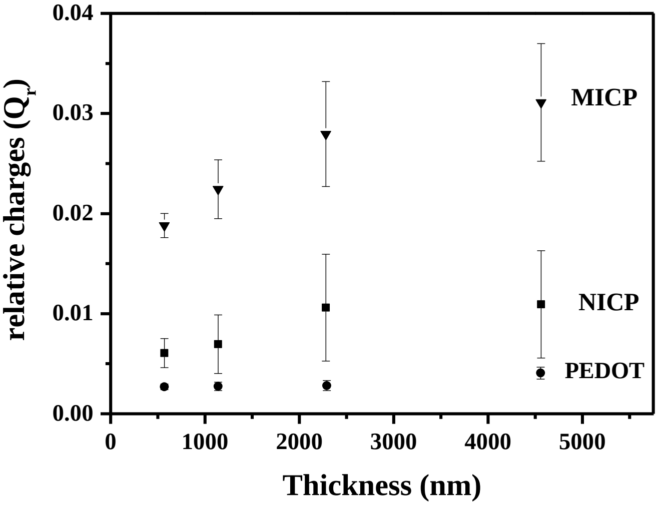

**Figure 12**. Evolution de la charge relative, $Q_r$, en fonction de l'épaisseur du polymère dans le cas des MICP (▼), NICP (■) et PEDOT (●).

L’influence de l’épaisseur des films sur les propriétés de reconnaissance indique que l’interaction entre les molécules cibles d’atrazine et les groupes de reconnaissance ne se situe pas uniquement à la surface des polymères conducteurs, mais se produit aussi en volume, dans une géométrie tridimensionnelle. Cependant, ce processus de reconnaissance 3D semble limité par la diffusion des molécules cibles dans les matrices polymères.

Dans le cas du PEDOT, où aucun groupement TAA n’est présent, la reconnaissance de l’atrazine demeure relativement faible. Cette reconnaissance ne peut cependant être due qu’à de faibles interactions par “π- π” stacking ou par liaisons hydrogène entre les molécules d’atrazine et les résidus EDOT constitutifs du polymère. Au contraire, la présence de résidus TAA dans la structure des copolymères MICP et NICP favorise la diffusion des molécules cibles au sein des matrices polymères et permet leur reconnaissance, via de relativement fortes liaisons hydrogène. Quelle que soit l’épaisseur du film, la détection par le MICP est toujours meilleure que par le NICP. Ceci ne peut résulter que de la présence de cavités fonctionnalisées dans le polymère MICP imprimé. La présence de groupements fonctionnels de type TAA idéalement distribués dans la matrice polymère permet donc une détection optimale des cibles ATZ.

Nous avons utilisé les couches sensibles à base de MICP (fonctionnalisés par les groupements TAA) pour la détection de quantités croissantes de molécules cibles. Comme précédemment, la détection a été quantifiée grâce à la mesure de la charge relative déduite des voltammogrammes (Figure 13).

Les couches sensibles à base de MICP utilisées pour la détection des molécules cibles d’ATZ, en présence desquelles elles avaient été synthétisées, présentent de remarquables propriétés :

- faible limite de détection : $10^{-8}$ mol $L^{-1}$
- large gamme dynamique : $10^{-7}$ à $10^{-4}$ mol $L^{-1}$

Néanmoins, une adsorption non spécifique a toujours lieu à la surface des MICP, et ce en parallèle avec la détection spécifique. Cette adsorption non spécifique, dont la contribution est de l’ordre de 33%, a pu être quantifiée grâce à la variation de la signature électrochimique des NICP une fois mis en présence de molécules cibles d’atrazine. Cette reconnaissance non spécifique affecte la spécificité de la détection en induisant la détection de molécules autres que l’ATZ (Figure 14).

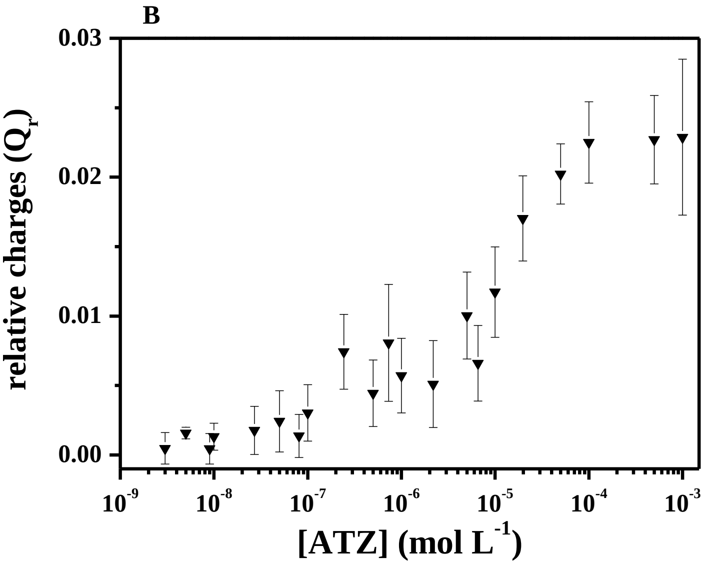

**Figure 13.** Variation de la charge relative, $Q_r$, des MICP (d'épaisseur 1140 nm) en fonction de la concentration d'atrazine.

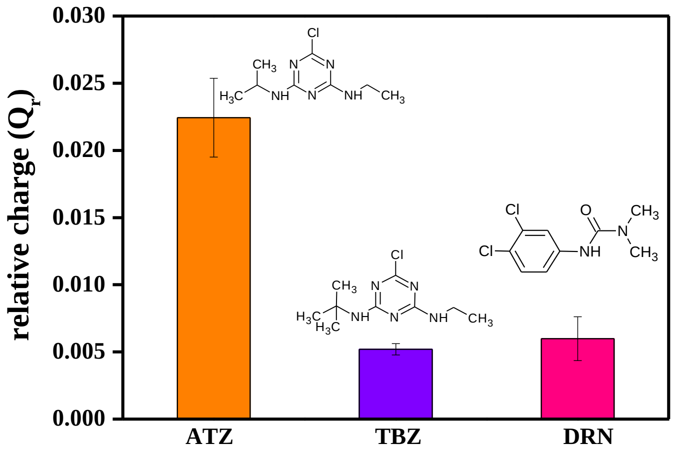

**Figure 14.** Charges relatives correspondant à la détection par le MICP de l'Atrazine (ATZ), de la Terbuthylazine (TBZ) et du Diuron (DRN). La concentration de toutes les molécules injectées est de $10^{-4}$ mol $L^{-1}$.

Afin d'améliorer les performances de notre capteur électrochimique en diminuant sa limite de détection et en élargissant sa gamme dynamique de fonctionnement, nous avons utilisé la voltammétrie à vagues carrées (SWV) en lieu et place de la voltammétrie cyclique (Figure 15).

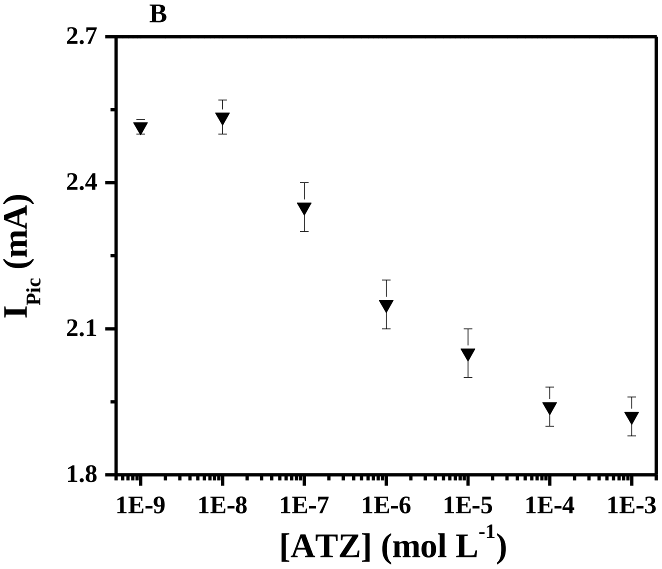

**Figure 15.** Dépendance en fonction de la concentration d'ATZ de l'intensité du courant de pic, $I_{pic}$, mesurée à partir des voltammogrammes à vagues carrées d'un MICP.

L'utilisation de la voltammétrie à vagues carrées (SWV) a permis d'améliorer de manière remarquable les performances des couches sensibles, à base de MICP, intégrées au sein de nos capteurs électrochimiques :

- faible limite de détection : $10^{-9}$ mol $L^{-1}$
- large gamme dynamique : $10^{-8}$ à $10^{-4}$ mol $L^{-1}$

Après avoir étudié l'influence de la structure et de la composition des couches sensibles et après avoir optimisé les performances de nos capteurs électrochimiques à base de MICP, nous nous sommes intéressés dans le quatrième chapitre de la thèse à l'influence des groupements fonctionnels (FM) présents au sein des MICP sur la qualité de la détection. Par ailleurs, la variation des groupements fonctionnels au sein des NICP a également été étudiée afin d'estimer la contribution systématique de l'adsorption non spécifique.

Ainsi, à partir de solutions d'acétonitrile contenant de l'ATZ, molécule empreinte cible en interaction avec des monomères fonctionnels (FM) dérivés du thiophène au sein de complexes de pré-polymérisation FM/ATZ (FM = TMA, TAA, EDOT, TMeOH ou Th (Figure 5)), différentes couches sensibles de type polythiophène (FM-MICP imprimées et

FM-NICP non imprimées) de structures et de fonctionnalités différentes ont été électrosynthétisées sur substrats d'or (Figure 16) et utilisées, après lavage, pour la détection de l'ATZ (Figure 17). La sensibilité de ces couches sensibles a été quantifiée, là encore, par voltammétrie cyclique.

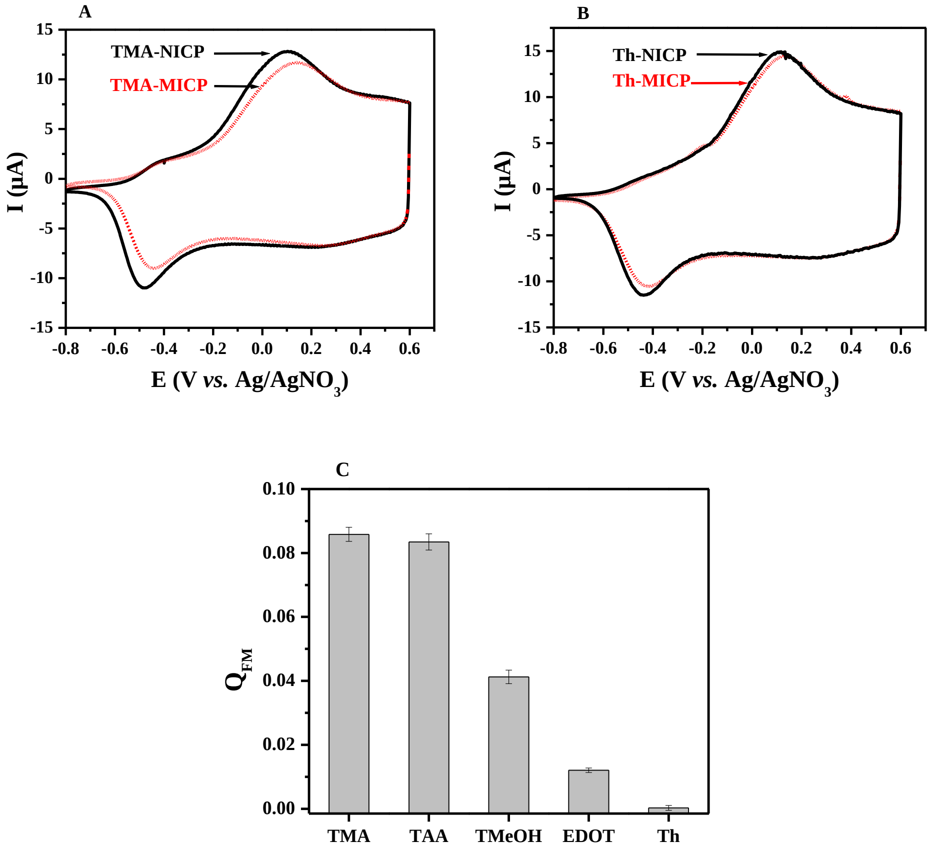

**Figure 16. (A)** Voltammogrammes des TMA-MICP et TMA-NICP (FM = TMA) après électrosynthèse. **(B)** Voltammogrammes des Th-MICP et Th-NICP (FM = Th) après électrosynthèse. **(C)** Charges relatives d'électropolymérisation, $Q_{FM}$, mesurées pour les différents monomères fonctionnels (FM = TMA, TAA, TMeOH, EDOT ou Th).

La différence de signature électrochimique entre les films de FM-MICP (Figure 16) témoigne de leur structure différente et indique sans ambiguïté l'incorporation des groupements fonctionnels, FM, dans les différentes couches sensibles. Par ailleurs, pour un groupement fonctionnel donné, la différence entre les voltammogrammes de FM-MICP et de FM-NICP témoigne de l'incorporation des cibles atrazine dans les cavités des polymères empreintes. Cette différence entre les voltammogrammes ($Q_{FM}$) est indicative de la qualité de l'empreinte moléculaire et reflète donc la force de l'interaction entre FM et ATZ dans le complexe de pré-polymérisation (Figure 16). On en déduit que la qualité de l'empreinte augmente dans l'ordre suivant des FM : Th, EDOT, TMeOH, TAA et TMA.

Afin d'étudier l'influence des groupements FM sur le processus de détection, les différents films FM-MICP ont été mis, après lavage, en présence de $10^{-4}$ mol $L^{-1}$ d'ATZ (Figure 17).

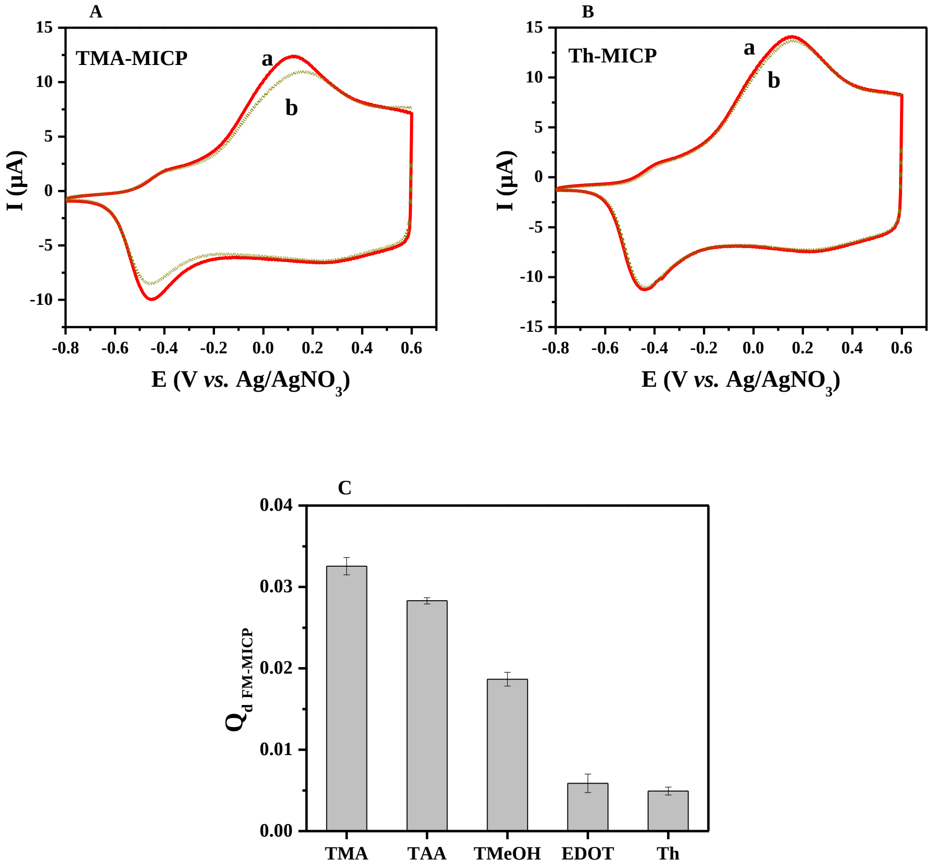

**Figure 17. (A)** Voltammogrammes de TMA-MICP (a) avant et (b) après ajout de $10^{-4}$ mol $L^{-1}$ d'ATZ. **(B)** Voltammogrammes de Th-MICP (a) avant et (b) après ajout de $10^{-4}$ mol $L^{-1}$ d'ATZ. **(C)** Charges relatives de détection, $Q_{d\ FM-MICP}$, mesurées pour les différents monomères fonctionnels (FM = TMA, TAA, TMeOH, EDOT ou Th).

La signature électrochimique des différents FM-MICP est plus ou moins affectée par la présence des molécules cibles d'ATZ. Cette variation qui accompagne l'injection des cibles traduit la reconnaissance plus ou moins importante de l'ATZ par les FM-MICP. La variation dans les voltammogrammes des FM-MICP ($Q_{d\ FM-MICP}$) est donc indicative de la qualité de la détection et reflète la force de l'interaction entre FM et ATZ dans la matrice FM-MICP (Figure 17). On constate que la qualité de la détection augmente dans l'ordre suivant des FM :

Th, EDOT, TMeOH, TAA et TMA. On peut noter que cet ordre est le même que celui relatif à la qualité de l'empreinte.

Les meilleures couches sensibles, en termes de qualité d'empreintes (valeurs des $Q_{FM}$) et de qualité de détection (valeurs des $Q_{d\ FM\text{-}MICP}$), sont les TAA-MICP et TMA-MICP. Néanmoins, une adsorption non-spécifique se produit systématiquement à la surface de ces couches sensibles et affecte par conséquent la sélectivité de la reconnaissance. Il semble raisonnable de penser que les performances des couches TAA-MICP et TMA-MICP résultent d'une forte interaction avec l'atrazine des monomères fonctionnels, TAA ou TMA, d'abord dans les complexes de pré-polymérisation durant l'étape d'électrosynthèse, et ensuite dans les matrices polymères lors de la phase de détection.

Afin de démontrer l'importance de la force de l'interaction entre les FM et l'ATZ sur l'efficacité du processus de reconnaissance, les valeurs absolues des enthalpies libres de formation des dimères FM/ATZ ont été évaluées grâce à des calculs DFT/PCM auxquels une correction semi-empirique a été introduite via l'utilisation de la formule de Wertz.

La géométrie des différents monomères FM et dimères FM/ATZ a d'abord été optimisée dans le vide (Figure 18), l'enthalpie libre de dimérisation en phase gazeuse, $\Delta_r G_g^*$, a été calculée ensuite à l'aide de gaussian09. Les enthalpies libres de solvatation ont été évaluées par une méthode de calculs PCM (formalisme SMD) et ont mené, moyennant différents degrés d'approximations, à différentes expressions des enthalpies libres de dimérisation en solution ($\Delta_r G_{sol}^{\circ\,smd}$, $\Delta_r G_{sol}^{\circ\,TRV\,mod\,smd}$, $\Delta_r G_{sol}^{\circ\,TR\,mod\,smd}$) (Figure 19). Quelle que soit l'approximation utilisée dans nos calculs, les dimères TAA/ATZ et TMA/ATZ sont les plus stables thermodynamiquement dans l'acétonitrile grâce aux fortes interactions par liaisons hydrogène.

Les valeurs des enthalpies libres de dimérisation ainsi calculées nous ont permis d'évaluer les concentrations des différents dimères FM/ATZ présents en solution avant l'électropolymérisation des FM-MICP. Nous avons alors montré que les résultats expérimentaux (valeurs des $Q_{FM}$ et $Q_{d\ FM\text{-}MICP}$) étaient très bien corrélés avec les concentrations des complexes de pré-polymérisation FM/ATZ (Figure 20). Ceci démontre que la qualité des empreintes et de la détection des cibles est directement liée à la force de l'interaction entre les monomères fonctionnels sondes et les molécules cibles.

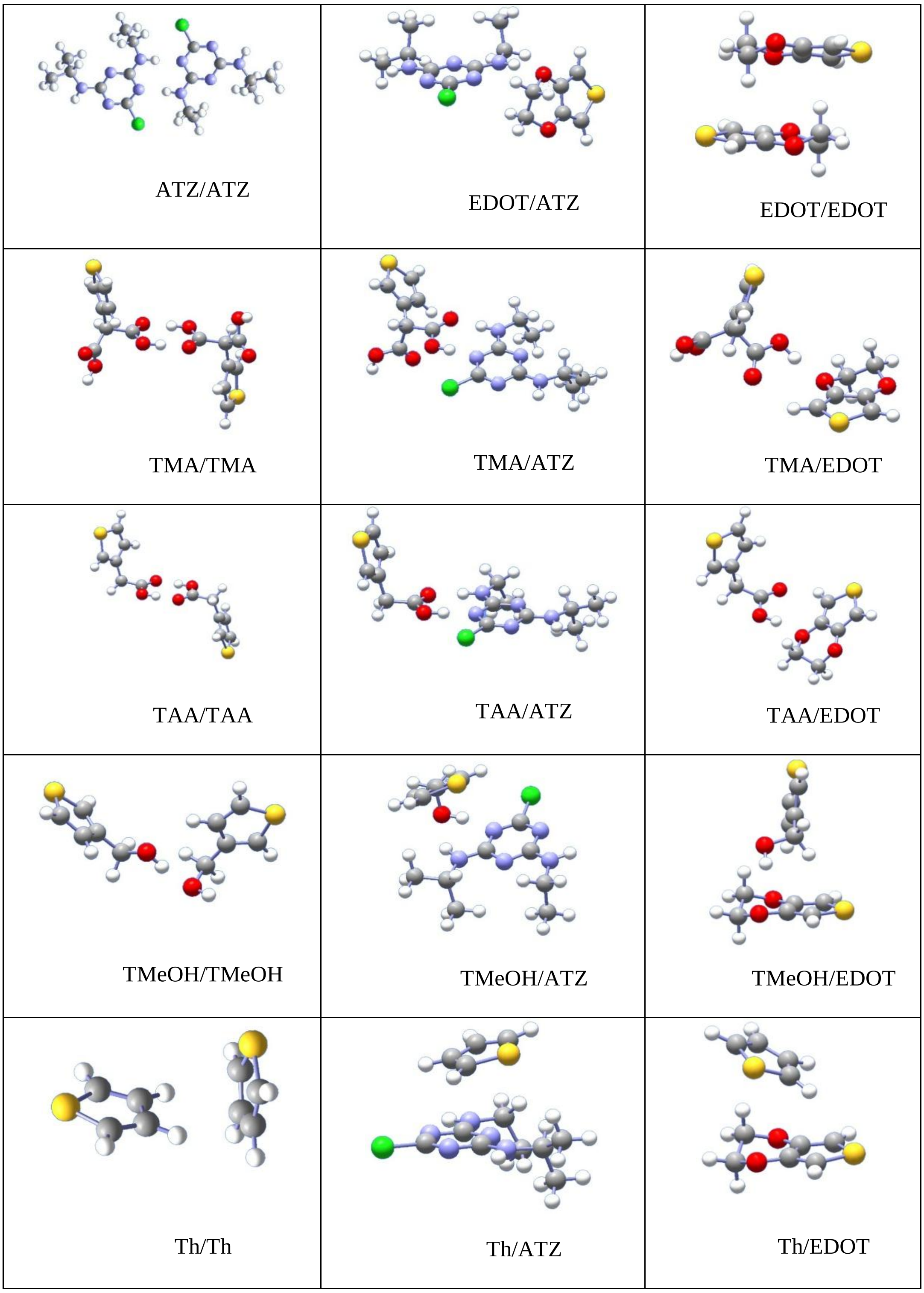

ATZ/ATZ

EDOT/ATZ

EDOT/EDOT

TMA/TMA

TMA/ATZ

TMA/EDOT

TAA/TAA

TAA/ATZ

TAA/EDOT

TMeOH/TMeOH

TMeOH/ATZ

TMeOH/EDOT

Th/Th

Th/ATZ

Th/EDOT

**Figure 18.** Les dimères formés par l'interaction entre l'atrazine (ATZ) et les différents monomères fonctionnels (FM = TMA, TAA, TMeOH, EDOT et Th).

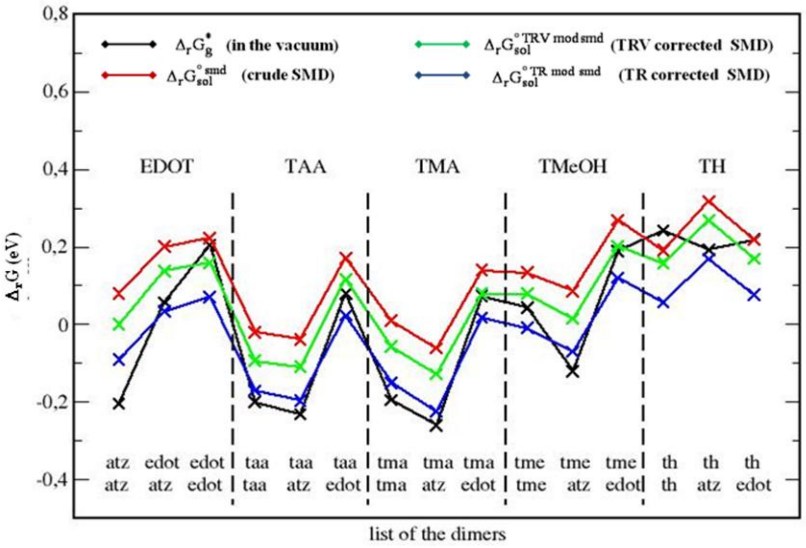

**Figure 19.** Enthalpies libres de dimérisation en phase gazeuse et en solution ( $\Delta_r G_g^*$, $\Delta_r G_{sol}^{\circ smd}$, $\Delta_r G_{sol}^{\circ TRV\, mod\, smd}$ and $\Delta_r G_{sol}^{\circ TR\, mod\, smd}$ ).

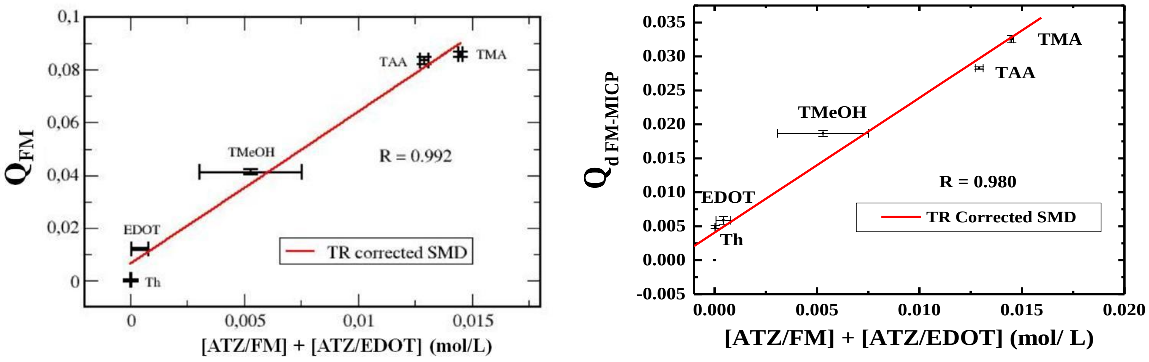

**Figure 20.** Corrélation entre les résultats expérimentaux ($Q_{FM}$ et $Q_{d\ FM\text{-}MICP}$) et les concentrations des différents dimères FM/ATZ.

Les couches sensibles transductrices à base de TAA-MICP et TMA-MICP sont celles qui présentent les meilleures performances en termes de détection de l'atrazine. Néanmoins, l'adsorption non spécifique de l'atrazine est moindre dans le cas des TAA-MICP ; ce qui confère à ce dernier type de couches les caractéristiques optimales pour la détection de l'atrazine.

Nous avons entrepris dans le dernier chapitre de la thèse (chapitre 5) d'électrosynthétiser ces couches optimales à base de TAA-MICP directement sur la couche sensible d'un capteur SAW, à ondes acoustiques de surface, afin de varier d'abord le mode de transduction (gravimétrique au lieu d'électrochimique) et dans l'optique ensuite de développer une détection couplée gravimétrique/électrochimique (ESAW) (Figure 21).

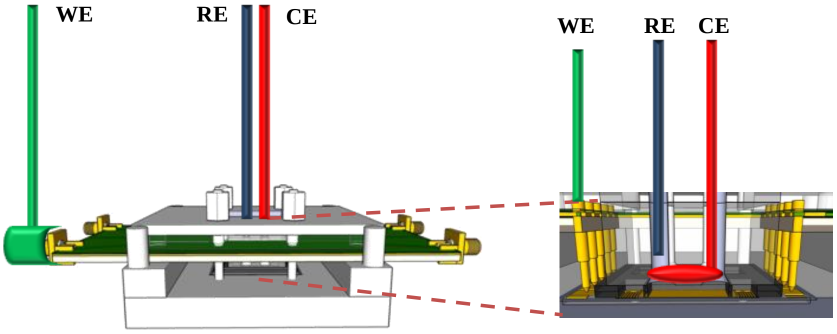

**Figure 21.** Dispositif original de type ESAW développé dans cette thèse. L'électrode de travail correspond à la zone sensible du SAW (WE), un fil de Pt constitue la contre-électrode (CE) et Ag/$AgNO_3$ constitue l'électrode de référence (RE).

Grâce au capteur ESAW que nous avons développé, les processus de croissance (Figure 22), de dopage et de dédopage des couches de TAA-MICP ont ainsi pu être étudiés, de manière parallèle aux mesures électrochimiques, par gravimétrie grâce à la mesure du déphasage de l'onde acoustique (ΔΦ).

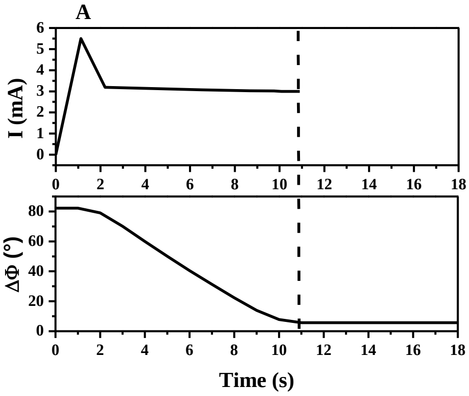

**Figure 22.** Suivi simultané électrochimique/gravimétrique par le capteur ESAW de la croissance à potentiel constant (1.45 V *vs.* Ag/$AgNO_3$) des couches de TAA-MICP.

Les couches de TAA-MICP électrosynthétisées sur la surface sensible du capteur ESAW ont d'abord été lavées afin d'en extraire les molécules cibles d'atrazine emprisonnées. La reconnaissance de molécules additionnelles d'ATZ par les couches polymères électrodéposées sur la surface sensible du capteur ESAW a pu alors être suivie non seulement électrochimiquement, mais aussi par gravimétrie (Figure 23).

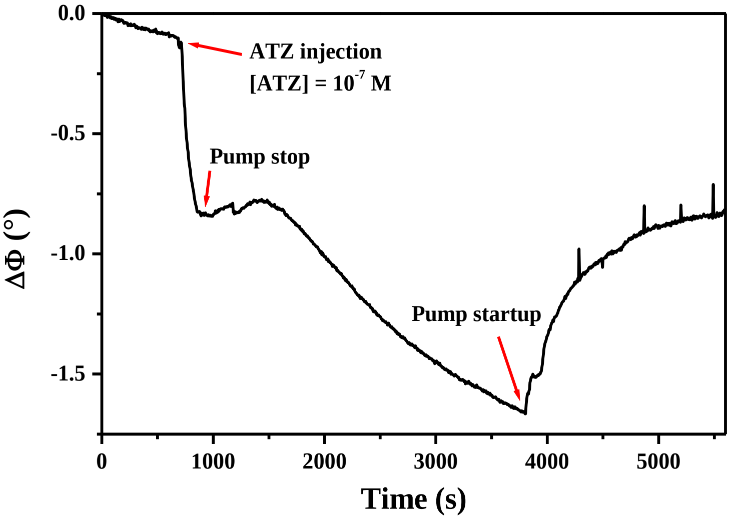

**Figure 23.** Suivi de la variation de phase ΔΦ d'une couche de TAA-MICP lors de l'injection de $10^{-7}$ mol $L^{-1}$ d'ATZ en mode dynamique et en mode statique.

En résumé, l'étude entreprise dans le cadre de cette thèse a permis le développement de différents polymères conducteurs à empreintes moléculaires (MICP) à base de polythiophènes. Ce travail s'est, en particulier, intéressé à l'évaluation des performances de ces polymères en tant que couches de reconnaissance pour la détection spécifique de molécules cibles d'atrazine. Les meilleures couches sensibles transductrices sont celles de TAA-MICP qui ont démontré de remarquables performances aussi bien dans les études électrochimiques que dans les expériences gravimétriques. Les performances de ces couches sensibles résultent de : i) la présence dans leurs matrices d'un grand nombre de cavités fonctionnalisées douées de mémoire moléculaire. ii) la force de l'interaction entre les molécules cibles et les résidus TAA distribués dans les matrices. iii) la relative faible adsorption des molécules cibles aux interfaces.